Large eddy simulation of coupled dispersed phase flows : a statistically-consistent formalism

David Mercier

▶ **To cite this version:**

David Mercier. Large eddy simulation of coupled dispersed phase flows : a statistically-consistent formalism. Chemical and Process Engineering. Université Paris-Saclay, 2020. English. NNT : 2020UPASC022 . tel-03116104

HAL Id: tel-03116104
https://theses.hal.science/tel-03116104v1

Submitted on 20 Jan 2021

HAL is a multi-disciplinary open access archive for the deposit and dissemination of scientific research documents, whether they are published or not. The documents may come from teaching and research institutions in France or abroad, or from public or private research centers.

L'archive ouverte pluridisciplinaire **HAL**, est destinée au dépôt et à la diffusion de documents scientifiques de niveau recherche, publiés ou non, émanant des établissements d'enseignement et de recherche français ou étrangers, des laboratoires publics ou privés.

université
PARIS-SACLAY

Large eddy simulation of coupled dispersed phase flows: a statistically-consistent formalism

Thèse de doctorat de l'Université Paris-Saclay

École doctorale n° 579, Sciences mécaniques et énergétiques, matériaux et géosciences - SMeMaG
Spécialité de doctorat: Énergétique
Unité de recherche: Université Paris-Saclay, CNRS, CentraleSupélec, Laboratoire EM2C, 91190, Gif-sur-Yvette, France.
Référent: : CentraleSupélec

Thèse présentée et soutenue en visioconférence totale, le 18 juin 2020, par

David MERCIER

Composition du jury:

Rodney FOX Professeur, Université d'État de l'Iowa	Président et rapporteur
Cristian MARCHIOLI Professeur, Université d'Udine	Rapporteur et examinateur
Enrica MASI Maître de conférences, Université de Toulouse	Examinatrice
Alexandre RICHARD Maître de conférences, CentraleSupélec	Examinateur
Marc MASSOT Professeur, École Polytechnique	Directeur
Aymeric VIÉ Maître de conférences, CentraleSupélec	Coencadrant
Vincent PLANA Ingénieur, Direction Générale de l'Armement	Invité

Thèse de doctorat

NNT: 2020UPASC022

Acknowledgements

Science and knowledge seldom appear from a blank page. And this thesis is no exception. I would like to take advantage of these few lines to acknowledge some of those who took part in this long adventure. The exhaustivity of the exercise is doomed to fail, but at least I will have tried.
First and for most, I would like to express my gratitude to Aymeric Vié who supervised this very ambitious research project, from the first day to the last, with impressive consistency, patience and empathy.
I would like to express my gratitude to my PhD director, Marc Massot, who considered me for taking part to this challenging adventure. I am thankful for his concern with always ensuring that I had the right resources and contacts to accomplish research of excellent quality.
I would like to acknowledge that the present thesis has been founded by the DGA and supervised by Vincent Plana.
I am especially grateful to Adam Larat, Ludovic Goudenège and Rémi Zamansky for having taken the time and patience to work with me. The research time spent together has meant a lot to the outcome of this work.
I am very thankful to Rodney Fox and Christian Marchioli for reviewing this work very carefully and for their very constructive input. I would also like to thank Enrica Massi and Alexandre Richard who accepted to be members of the jury of this thesis.
I would like to thank the EM2C laboratory and its successive directors, Olivier Gicquel and Sébastien Ducruix for providing me with a great environment to prepare for this PhD. I would like to thank Brigitte Llobel, Nathalie Rodrigues et Noï Lavaud for their great efficiency and kindness. I would also like to thank Jean-Michel Dupays et Sébastien Turgis for their constant support.
I am very grateful to all my fellow EM2C students who marked this adventure of their unique personality.
I would also like to present my gratitude to all the people not cited above whom have contributed to the success of this adventure thanks to their patience, passion and support.
And lastly, I am gratefull to Zeigarnik effect (Zeigarnik (1927)) which undeniably helped me complete this work in the end.

Abstract

The simulation of the polydisperse fuel sprays is of tremendous importance for high-fidelity descriptions of aeronautical burners. To this end, the Eulerian Moment Methods are an interesting strategy, because of their intrinsic statistical convergence. Such methods have been successfully used to represent macroscopic trends such as the flame shape, but there are still some issues to be tackled in order to increase their level of fidelity and prediction.
Among them, the two-way coupling between the spray and the gas phase is critical. Indeed, moment methods used to simulate sprays in burnurs are often based on the Mesoscopic Eulerian Formalism (MEF) of Février et al. (2005), which considers the ensemble-averaged statistics of the disperse phase conditioned to a unique gas phase. This conditioning is required in order to solve the gas phase without any ensemble averaging such as in RANS methods. Unfortunately, if the disperse phase affects the gas phase, this conditioning may be at least impossible and at most strongly restricted.
In this context, the present work investigates the development of a statistical description in the case of a reduced vision of the gas phase, such as the Large Eddy Simulation (LES), and two-way coupling is taking place between the two phases. This solution is interesting for two-way coupled disperse phase flows, as the retro-coupling can occur at the small scales of the flow, with limited impact on the large scales, as suggested by Février et al. (2005). Beyond the usual description of LES, following Pope (2010) and Fox (2003), we consider a statistical framework of LES under which the statistics are taken as ensemble-averaged over the possible unresolved features. To investigate this solution, a numerical framework using synthetic turbulence is developed, based on a superposition of analytic modes. By doing so, the distribution of modes can be easily controlled, thus enabling the generation of fields with identical large scales. This framework is carefully evaluated to ensure statistical and numerical convergence of the measures of interest, such as particle dispersion. Our formalism is then investigated, focusing on the impact of choosing this framework compared to the initial MEF, from the DNS to the RANS limit. We show that the choice of the formalism has a negligible impact on the diffusion regime of particles in turbulence, but still has a clear impact on the initial transport regime, during which all physics could happen in spray combustion. We finally investigate Lagrangian LES models of the literature in this framework and propose some perspective toward two-way LES of turbulent particulate flows.

Contents

Introduction

1 Context

1.1 Turbojets

According to their speed, planes are usually propelled by different kinds of engines. From slow to fast, one can think of turboprop, turbojet and ramjet engines. For current planes, the most usual engine is the turbojet, see Fig. 1 in which the different parts are represented: the air inlet, the compressor, the combustion chambers, the turbine and the exhaust part.

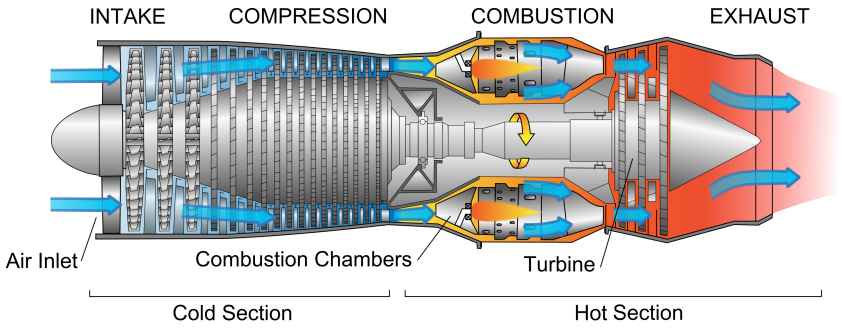

Figure 1. Sketch of a turbojet engine.
By Jeff Dahl, CC BY-SA 4.0, https://commons.wikimedia.org/w/index.php?curid=3235265

In such turbojet, the air ideally follows an open Brayton cycle. The ideal thermodynamic evolution of the gas during an open Brayton cycle is represented in Fig. 2, with steps 1-2-3-4. On the left is the evolution of the pressure against the specific volume, and on the right is the evolution of the temperature against the entropy. The cycle is said to be open because air from the turbojet outlet at step 4 does not loop to the turbojet inlet step 1. The ideal open cycle starts with an isentropic compression through the compressor (steps 1 to 2), then heat is added by an isobaric combustion (steps 2 to 3), and the fluid is accelerated by an isentropic expansion through a nozzle (steps 3 to 4)[1]. Thrust is produced by the difference in velocity between the engine intake and the engine

[1]In a real turbojet, a turbine usually recovers some work between the combustion chamber and the nozzle in order to drive the compressor.

exit. It is to be noticed that the rise of temperature between steps 2 and 3 highlights the gain of enthalpy produced by combustion. Without combustion, the turbojet will not generate any thrust, this is why this element is at the core of a turbojet.

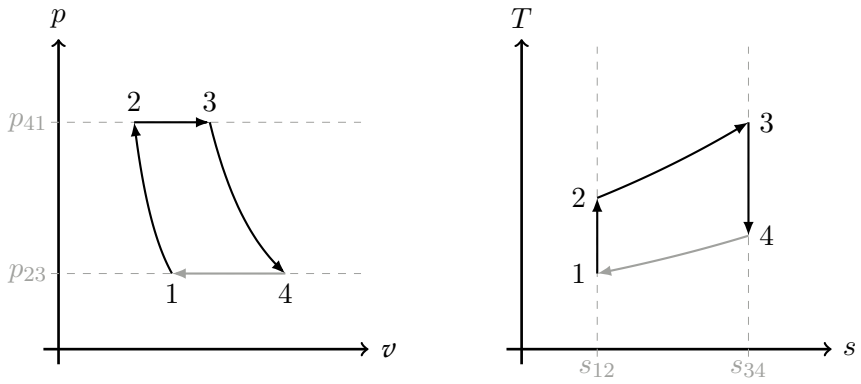

Figure 2. Brayton cycle: Clapeyron diagram (left) and temperature-entropy representation (right). Black arrow indicate the compression (1-2), combustion (2-3) and expansion (3-4). The grey arrows is purely notional, as the cycle is open.

1.2 Aeronautical combustion chambers

In the combustion chamber, the fuel of the engine is burned in order to generate the rise in temperature. Combustion occurs when mixing the hot air of the combustion chamber (Fig. 3) with a fuel vapour. The fuel is injected in the combustion chamber in a liquid form and atomised into small droplets at the contact of intense shear layers of air. These volatile fuel droplets vaporise and produce a fuel vapour which burns at the contact of the hot air inside the combustion chamber.

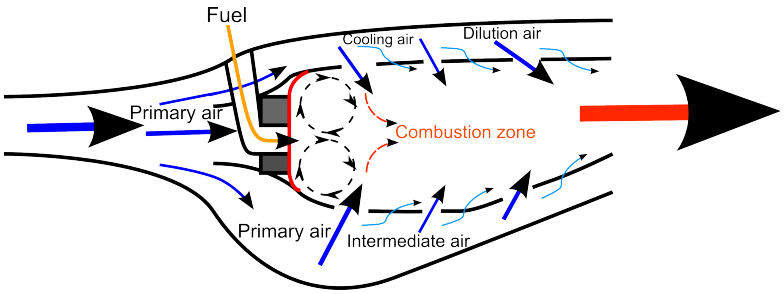

Figure 3. Sketch of a combustion chamber in a turbojet engine.
By SidewinderX, CC BY-SA 3.0,
https://commons.wikimedia.org/w/index.php?crid=8965151

To design a combustion chamber, we can either decide to build real prototypes to evaluate proposed designs, or to make use of numerical simulations to avoid the cost of experimental campaign and designs. Simulations are nowadays used at every level of conception in

the aeronautical field. The modelling and simulation of combustion chambers requires to reproduce several physical phenomena: high-speed aerodynamics, acoustics, fuel injection, combustion, turbulence, radiation... Today, simulation strategies exist for all these phenomena, but being able to simulate with a high precision all of them at the same time is still a hard task. Still, simulations, even at low level of modelling, are now able to give insightful and predictive results in engine-like conditions for global characteristics such as flame shape or overall acoustic behaviour. As an example, Fig. 4 shows the comparison between experiments and numerical simulations for the BIMER burner of the EM2C laboratory (Providakis, Zimmer, Scouflaire, and Ducruix (2012); Renaud, Ducruix, and Zimmer (2017); Cheneau (2019)). In this burner, depending on the flow history, here increasing or decreasing staging factor[2] Results reveal a good description of the flame shape with the numerical simulation for two operating conditions. Interestingly, the numerical simulation is far from being high-fidelity: mono-disperse Eulerian description of the spray, two-step chemistry, coarse mesh... And even with such crude description, the correct flames are retrieved.

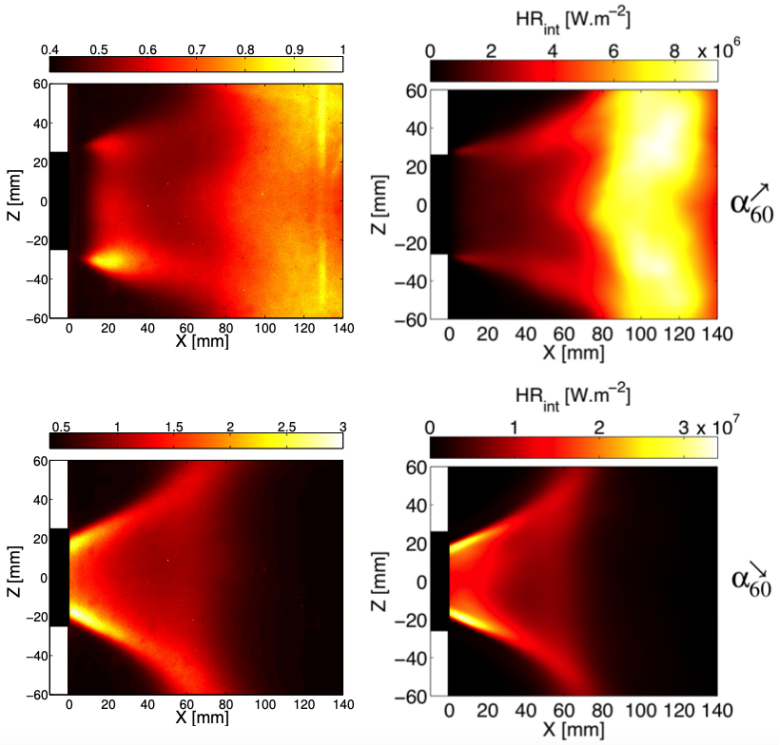

Figure 4. Qualitative comparison between mean image of OH^* in experiments and line-of-sight integrated heat release simulations (Cheneau (2019)) for increasing (top) or decreasing (bottom) staging factor α, for the BIMER combustor (Providakis, Zimmer, Scouflaire, and Ducruix (2012); Renaud, Ducruix, and Zimmer (2017)).

[2]The staging factor α is the ratio between the fuel mass flow rate injected in the pilot stage and the total fuel mass flow rate.

However, there are still situations under which simulations have to be improved, which is the reason why high-fidelity simulations are still required.

1.3 High-fidelity numerical simulations

To reduce pollutant emissions, combustion chambers are now designed with several swirler stages and several injection systems. Furthermore, lean global operating conditions are targeted to reach the optimal conditions for NOx and CO emissions. Such designs are also expected to improve the operability limits of the engine, for instance in high altitude or low temperature. In these extreme conditions, the flame is prone to unstable phenomena, such as high acoustic activity or flame extinction and shape transitions. These events are actually very hard to reproduce with current simulation strategies because they requires the prediction of very fine phenomena that occur at the scales of the smallest turbulent structures. Such physics cannot be captured by crude simulation strategies, and requires high-fidelity simulations. Such high-fidelity simulations are expected to be expensive at first glance, preventing form their use to be on a day-to-day basis for conventional design. Therefore, they are more dedicated to solve design issues under crisis situations for which low-fidelity tools have reached their limits.

2 Numerical simulation of the fuel spray

Providing a high-fidelity simulation of the combustion chamber must rely on a good representation of the spray all along its lifetime. In Fig. 5, the different phases of the spray evolution are depicted.

1. *Primary breakup*: The liquid fuel is injected in the combustion chamber as a liquid core or a liquid sheet, depending on the injection technology. Due to strong aerodynamic stresses on the liquid interface, this coherent liquid core breaks-up into ligaments.
2. *Secondary breakup and transport*: the ligaments continue to break-up. They generate aerodynamically stable droplets which are carried by the turbulent flow field.
3. *Evaporation/Combustion region*: Droplets encounter ambient conditions that are sufficient to lead to their evaporation. This way, they feed the combustion with the gaseous fuel and they thus enable to sustain a flame.

Theses three phases are obviously "porous" is the sense that there is no clear separation, and they can all occur simultaneously. The first phase requires the description of the tortuous interface between the gas and the fluid. At the opposite, droplets can be assumed spherical in the second and third phases. This allows to use a framework similar to kinetic theory, which drastically simplifies the modelling and simulation of these two phases. In the following we give a brief overview of what is done today in simulation for these last two regimes.

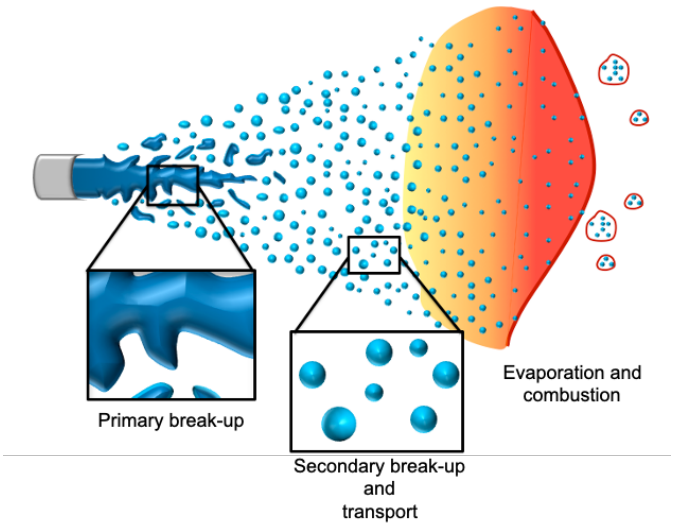

Figure 5. Schematic representation of the different phases of the spray evolution.

2.1 Liquid jet atomisation

The simulation of the primary breakup reviewed here is the source of intense research to be able to correctly capture the creation of the spray (see for instance Chiodi and Desjardins (2017); Vaudor, Ménard, Aniszewski, Doring, and Berlemont (2017); Movaghar, Linne, Herrmann, Kerstein, and Oevermann (2018)), as well as ensuring a good transition between the coherent dense phase and the disperse phase. As an example, Figure 6 shows the simulation of a liquid jet in a high-speed gaseous cross flow (Leparoux, Mercier, Moureau, and Musaefendic (2018)).

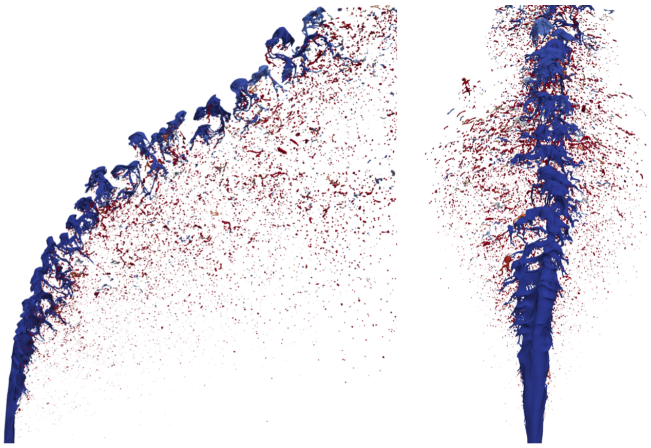

Figure 6. Simulation of a liquid jet in a crossflow simulated with the YALES2 solver (Leparoux, Mercier, Moureau, and Musaefendic (2018)).

his kind of simulations requires large computational resources, as it is requires to sim-

ulates scales of the domain size (centimetres), the nozzle injector (millimetres) down to droplet size (micrometers). Nowadays, simulating on a day-to-day basis such processes inside a realistic combustion chamber is not possible, and such simulations are only aiming at giving input to injection modelling strategies or DNS to verify and/or design reduced order models.
In fact, instead of simulating the atomisation process from the liquid core to the spray, the classical solution for simulating the spray in a combustion chamber is to rely on an injection model that will define the spray characteristic as a consequence of empirical correlations (experimental or numerical). Example of this kind of model is the FIMUR approach (Sanjosé, Senoner, Jaegle, Cuenot, Moreau, and Poinsot (2011); Vié, Jay, Cuenot, and Massot (2013); Hannebique, Sierra, Riber, and Cuenot (2013)), which aims at mimicking a pressure-swirl atomiser, and which has been used successfully in numerous simulations of reactive flows in aeronautical-like burners. This kind of approach is proven to be really useful, but still has to progress as some recent works exhibits a more limited accuracy when external flow has a strong interaction with the nozzle atomisation (Mesquita, Vié, and Ducruix (2018); Vignat, R., Durox, Vié, Renaud, and Candel (2020)).
Another promising solution is to develop new strategies based on various reduced-order models, where the natural approach is a diffuse interface model near the injection nozzle in order to resolve the interface (Cordesse, Remigi, Duret, Murrone, Ménard, Demoulin, and Massot (2020)) and then to couple it to a spray either Lagrangian (Anez, Ahmed, Hecht, Duret, Reveillon, and Demoulin (2019)) or Eulerian model in the disperse phase zone (Cordesse, Remigi, Duret, Murrone, Ménard, Demoulin, and Massot (2020)) in order to capture the details of the polydisperse spray generated through the atomisation process. Such approaches suffer from the transition parameters, that are somewhat arbitrary and rely on a list of assumptions. Some recent progress has been made in order to design a unified Eulerian model able to cope with various zones, including the the mixed zone, and relying on a geometrical approach of the spray polydispersion (Drui, Larat, Kokh, and Massot (2019); Essadki, de Chaisemartin, Laurent, and Massot (2018); Essadki, Drui, de Chaisemartin, Larat, Ménard, and Massot (2019); Cordesse (2020)).
Eventually, whatever the chosen methods, it will result in the generation of a spray composed of small spherical droplets, with various sizes, velocities, temperatures. Furthermore this spray is still coupled to the gas phase, and two-way interactions must be accounted for.

2.2 Evolution of the spray

To describe the spray in combustion chambers, three kinds of approach can be envisaged:

- the deterministic Lagrangian approaches,
- the kinetic-based Lagrangian methods,
- the Eulerian moment methods.

2.2.1 Deterministic Lagrangian approaches

The most widely used method is the point-particle Lagrangian description of the spray: droplets are tracked individually or by small groups in the flow, and their evolution is driven by their exchange with the gas phase through drag force, evaporation and heating. Deterministic Lagrangian simulation are quite easy to implement numerically. However, their associated numerical cost is difficult to balance evenly in the context of parallel computations. Furthermore, the exchange terms between the fluid and the disperse phase need to be treated with care, as information has to be transferred between the singular point particles and the Eulerian mesh of the fluid. Evaluating the gas phase properties to correctly account for the drag force is the source of recent contributions that suggest corrections of the velocity Horwitz and Mani (2016); Ireland and Desjardins (2017); Balachandar, Liu, and Lakhote (2019); Poustis, Senoner, Zuzio, and Villedieu (2019)). Computing the feedback of droplets on the gas phase also requires regularisation to avoid numerical issues, see Capecelatro and Desjardins (2013); Zamansky, Coletti, Massot, and Mani (2016). Eventually, only one realisation of the disperse phase is computed at each time. Therefore, the statistical convergence of the simulation is costly to obtain. Despite these limitations, this strategy has led to numerous successful simulations, in the sense that they retrieve well the experimental results for several configurations. Moreover, the fact that Lagrangian simulations can simulated a unique realisation is sometimes an advantage when it comes to rare events. For example, Fig. 7 presents the simulation of a spray burner using two evaporation models for the droplet (one considering evaporation only, the second switching to isolated combustion when it occurs, Paulhiac (2015)). It can be seen that when a droplet crosses the flame, it leads to a strong local disturbance, here a large heat release rate compared to the the rest of the flame. Such random "catastrophic" events can be reproduced with a deterministic approach, but if the simulation method uses any ensemble-averaging, capturing such phenomena is today hardly achieved.

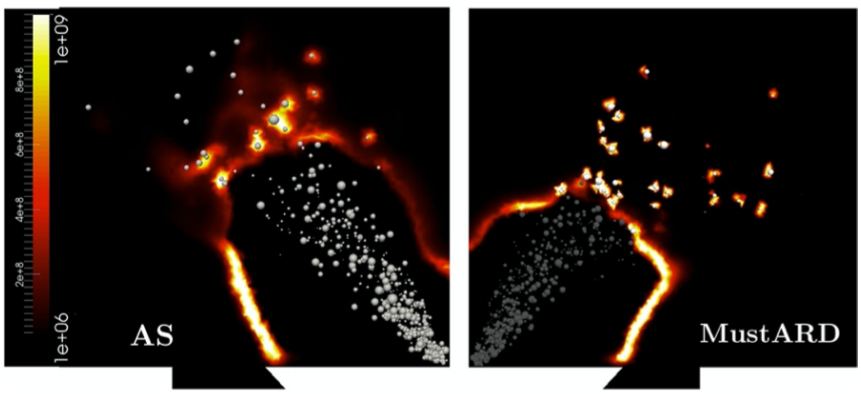

Figure 7. Instanteneous heat release along with droplets in the simulation of a spray burner (Paulhiac (2015)), with two evaporation models (left, "classical" evaporation, right, switching between evaporation and isolated combustion).

2.2.2 Kinetic-based Lagrangian methods

If one is interested in statistically-converged quantities, a solution is to rely on a statistical description of the disperse phase, which objective is to compute the evolution of the Number Density Function (NDF) of the spray. The NDF gives the average number of droplets at a given point in space and time and with given physical properties such as temperature or size for instance. The NDF satisfies a Population Balance Equation (PBE) which describes its evolution in the phase space. At this point, one of the two possible strategies to compute the evolution of the NDF is to use a Lagrangian method, in which elements of the NDF are randomly drawn and are computed according to the PBE. For instance Bini and Jones (2008) develops a Lagrangian Stochastic Model based on the addition of Wiener processes to drive droplet trajectories. They used this strategy to compute sprays of droplets in Bini and Jones (2009). At this point, it is important to point out that identifying what happens in a unique realisation is only possible if the simulation is fully deterministic, either for the gas phase or for the disperse phase. If the Lagrangian method is based on a kinetic description, the simulation cannot guarantee that the local perturbations of the droplets correspond to what happens in a realisation, because designing a forcing that represents turbulence is not straightforward.
Furthermore, even if the kinetic-based Lagrangian methods aim at solving the NDF, they still have the same drawback as the deterministic Lagrangian approaches: a slow convergence of the statistics. This is where Eulerian Moment methods become of interest.

2.2.3 Eulerian moment methods

To the difference of Kinetic-based Lagrangian methods which draw Lagrangian elements in order to reconstruct the NDF in a Monte-Carlo fashion, Eulerian moment methods offer a different strategy for describing the NDF. As their name indicates, moment methods do not consider the whole NDF, but only some of its first moments. These moments can have a physical meaning, such as the overall droplet concentration for instance. With moment methods, each moment is considered for itself, as a field, with its own evolution equations. To the difference of Lagrangian methods for which it is important to ensure that enough particles are drawn in order to converge the statistics of interest, moment methods have the advantage of directly computing the converged moments of the distribution of particle. Moreover, because moment methods share the same Eulerian framework as the gas phase, it is easier to ensure consistent exchange terms between phases and to design strategies for well balanced parallel codes. Compared to Lagrangian approaches, there is only a small community of people that uses the Eulerian moment method for describing the spray in aeronautical combustion chambers. The main reason that limits the diffusion of this method is that they requires a specific attention to numerical methods, as they lead to hyper-compressible fields (de Chaisemartin (2009)). Moreover, describing important features of the spray such as poly-dispersion requires to transport several moments, which makes their use even less straightforward. Despite these difficulties, this method has been used to simulate successfully several burners, even in annular burner context, see Fig. 8 (Lancien, Prieur, Durox, Candel, and Vicquelin (2018)). In terms of engineer, the fact we can easily estimate the computational time, whatever the number of droplets in the simulation, is surely and advantage compared to Lagrangian methods. For example, a flame switching in a Lagrangian simulation could lead to a great increase in droplet number and imbalances between computational cores if the load is not dynamically updated.
To sum up the main strengths of moment methods, which make them of particular interest for applicative simulations are:

- Their intrinsic statistical convergence.
- The ease to couple them with the gas phase, compared to the Lagrangian methods.
- The existence of shared framework with methods describing interface flows, making them a preferred solution for solving the spray from its atomisation to its combustion (Essadki, Drui, de Chaisemartin, Larat, Ménard, and Massot (2019); Essadki, de Chaisemartin, Laurent, and Massot (2018)).

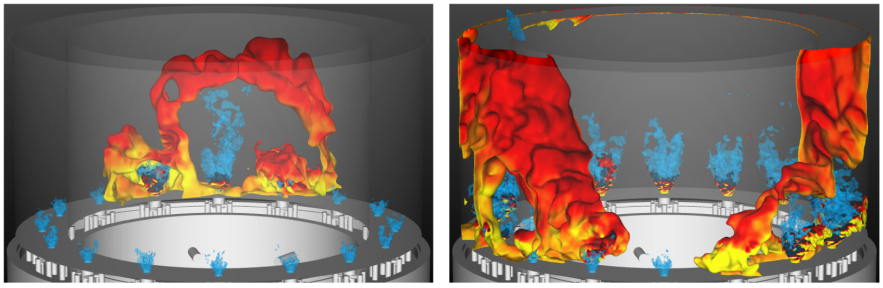

Figure 8. Simulation of the multi-sector MICCA burner of EM2C (Lancien, Prieur, Durox, Candel, and Vicquelin (2018)) using an Eulerian moment method for the spray.

2.3 Some open issues in the spray simulation

Looking at the landscape of possible solutions, it appears that we are today able to get meaningful simulations with the available methods. However there are still some open issues that are still to be tackled:

- *Models for droplet evolution*: whatever the framework for spray evolution is, models such as drag force or evaporation laws are required, and the final result may be highly dependent on the choice of the model. Unfortunately there is not necessary a perfectly predictive model for all possible physics. For instance, in the case of evaporation, there are several model available in the literature, and there are also several ways of implementing the same model, depending on the way the mixture is treated for instance. Furthermore, models are not necessary validated in the conditions that droplets meet during combustion.
- *Two-way coupling in Lagrangian framework*: the coupling between the two-phase may rise different questions depending on the framework of the simulation. For Lagrangian simulations, attention must be given to the way the flow and the particle are coupled, how the gas phase properties are evaluated at the droplet location, how the evolution models are applicable, and how the feedback of the droplet to the carrier phase is computed.
- *Two-way coupling in kinetic descriptions*: for such simulations, Eulerian or Lagrangian, peculiar attention must be given to the targeted statistics which would be impacted by the retro-coupling. For instance, the Mesoscopic Eulerian Formalism (MEF) of Février, Simonin, and Squires (2005), which is the basis of the Eulerian simulations previously presented (Cheneau (2019); Lancien, Prieur, Durox, Candel, and Vicquelin (2018)), considers statistics averaged over several particle phase realisations conditional to a unique gas phase realisation. Such conditioning is possible only if the particles do not affect the gas phase. If so, unfortunately each particles realisation may affect differently the gas phase, preventing from any straightforward conditioning.
- *Subgrid scale modelling*: finally, industrial-like simulations cannot be performed resolving all the turbulent scales and reduction techniques such as Large Eddy Simulation (LES) are required. In this context, modelling the effect of sub-grid

scale on droplet dynamics, but also the sub-grid feedback of these droplets on the carrier phase is mandatory. Today, the simulations are limited to a "global" feedback without sub-grid scale coupling, which requires far more attention, as shown in Letournel, Laurent, Massot, and Vié (2020).

3 A statistically-consistent framework for the simulation of two-way coupled disperse phase flows

The challenge that is addressed in this PhD focuses on the last two issues, and aims at providing a statistical description of coupled disperse phase flows in the context of reduced simulation such as LES.
This focus has been chosen for the following reasons:

- Simulating of a full combustion chamber requires to gather a numerous modelling approaches, which are always embedded into a Large Eddy Simulation framework. This LES framework is always described in classical textbook as the sole filtering operation applied to the evolution equations. However, LES models are always validated against statistical quantities such as temporal or spatial averaged quantities.
- A statistical description is key for the simulation of highly turbulent flow with a large range of time and space scales, as one single realisation would be not representative of the full behaviour of the burner.
- Two-way coupling imposes constraints on the statistical contents of the quantities of interest, as any ensemble-average on the disperse phase will imply an ensemble-averaged on the carrier phase. It is today primordial to push forward statistical method, to investigate the existence of possible bottlenecks or fundamental limitations of such strategies.
- Such research objective is justified at a first glance for Eulerian Moment methods for sprays, but the implications are valid for any physical model coupled with the carrier phase, such as soot description. Conclusions will also hold true for the statistical description of interfacial flows.

To this aim, the present PhD work attempts to combine two elements:

- A statistical description of the disperse phase consistent with two-way coupling.
- A fluid reduction setting a framework where LES is to be found.

Let us briefly present these topics here in order to introduce the problematic of this manuscript.

3.1 Choice of the statistical description

The starting point is to define the statistical characterisation of the resolved fields. The problem at stake is a turbulent disperse phase flow. In such conditions, the number of possible states for the full problem is very large, as it includes all possible spatial distributions of the droplets and all possible s everywhere in the domain. Therefore this choice is critical, as we will obviously not solve all possible states. For the simulation of spray combustion, a possible statistical characterisation is the one suggested by MEF, but as already mentioned, two-way coupling will prevent from using directly such statistics, as they only include the particles. Fortunately, in Février, Simonin, and Squires (2005), the authors conclude with interesting perspectives:

- "*Formally, extension of the MEF to regimes including two-way coupling could be possible via definition of a* ***conditional average using a single realisation of the large-scale fluid flow****, rather than the whole turbulent fluid velocity field as developed in this manuscript*".
- "*The basis of such an approach would take advantage of the fact that for small particle diameters,* ***the direct modification of the fluid flow occurs at very small scales***".
- "*While the smallest scales over a large number of ensembles would differ from one realisation to the next,* ***the large eddies of the fluid flow would exhibit negligible variation****, in turn providing the condition on which to define properties of the particulate phase*".

Considering these perspectives it seems promising to explore conditional averaging on the largest scales of the flow. However, in order to reach conditions where the two phases are coupled, strong assumptions have to be made with respect to the interactions between the disperse phase, the resolved scales of the fluid and the unresolved scales of the fluid. The disperse phase has to affect at most the smallest scales of the fluid, while the impact of the smallest fluid length scales of the flow on the resolved fluid has to be independent of realisations.

3.2 Fluid reduction and large-scale conditioning

Fluid reductions such as LES are commonly used to reduce the computational cost of the simulations, at the price of modelling efforts to recover the effects of sub-grid scales onto the resolved large ones. LES particle models are in general constructed without taking into account the effect of particles on the carrier phase, which unfortunately makes the picture much more difficult:

- Classical models for point particles, such as the drag law, are widely used in a one-way context. However, they often rely on the hypothesis that the particles are much smaller than the smallest length scales of the fluid and that the particle load is negligible (Stokes (1851)). The physical cases where particles produce turbulence often push these approximations to the limit of their validity. In a two-way coupled framework, it is much more difficult to derive consistent models (Horwitz and Mani (2016)).
- Standard reduction techniques for turbulence such as LES are very consistent with the picture given by Richardson of an *energy cascade* (Fig. 1.3). It assumes that energy is generated at the largest scales of the flow and ripples down through wave-numbers to be eventually dissipated at higher frequencies. However, in a two-way coupled context, the mechanisms for energy production, transfer and dissipation in the fluid are different (Letournel, Laurent, Massot, and Vié (2020)). Clusters of particles, of various sizes and shapes, can appear and exchange momentum with the turbulent fluid at a wide range of scales (Zamansky, Coletti, Massot, and Mani (2016)). Therefore, in a two-way coupled, two-phase flow, the traditional hypothesis of energy flowing unidirectionally from lowest wave-numbers to the highest wave-numbers is dubious and cannot be used as a reliable basis for reduced

models.

On top of the physical limitations of existing models, there are numerous issues to be tackled if we want to follow the suggestions of Février, Simonin, and Squires (2005):

- The LES is generally seen as a sole filtering operation. However, here, because of the presence of particles, the sub-grid scale can vary a lot between different realisations. This leads to the idea of considering an ensemble-average over the smallest scales of the flow and immediately rises the issue of performing such an averaging operation.
- If an ensemble-averaging is taken over the small scales, how are the large scales affected by the sub-grid scale averaging?

These questions ask for a broader vision of fluid reductions, which must include the possibility of ensemble-averaging, and which is at the very end at the core of the present PhD work.

4 Outline of the manuscript

The present manuscript is organised in the following way:

- Part I reviews various elements of reduced two-phase flow simulations. On each aspect of the present work, it frames the manuscript in the context of a prolific literature. It identifies key elements that reduced two-phase flow simulations must account for in a broad perspective of successive reduced visions of reality. It also sheds light on the bricks missing for deriving a statistically-consistent formalism for two-way coupled disperse phase flows.
- Part II introduces an extended statistical formalism that we envision as a first step on the road to statistically-consistent, two-way coupled, disperse phase flows simulations. This extended formalism, called Extended Mesoscopic Eulerian Formalism MEF (EMEF), is seen as an extension of the Mesoscopic Eulerian Formalism (MEF) of Février, Simonin, and Squires (2005): it relies on an ensemble average conditioned to the largest scales of the flow. Such conditioning requires a specific attention to the reduction framework. We thus have suggested a general classification for reduction strategies. This classification takes into account both the injective and the self-contained character of a given reduction strategy. The injective quality of a reduction indicates if, for one large-scale flow field, there is only one unique corresponding small-scale flow field. The self-contained quality of a reduction indicates if the evolution of the large scales is independent of the choice of the corresponding residual field. In order to observe the numerical behaviour of the extended mesoscopic Eulerian formalism, a numerical set-up based on Kinematic Simulations (KS) is presented in Chap. 6. Kinematic simulations are synthetic flow fields built from the linear superposition of analytic modes. With kinematic simulations we have full control on the probability distribution of the flow field. This makes the computation of the extended mesoscopic Eulerian formalism possible, by sampling the probability space associated to self-contained large eddy simulations. The numerical set-up is extensively validated in Chap. 7

and 8, to ensure the statistical and numerical convergence of the proposed fluid and computed particle statistics.

- In Part III, we assess the behaviour of the extended mesoscopic Eulerian formalism with numerical simulations. The simulations performed rely on the kinematic simulations presented earlier in this work (Chap. 9). This numerical implementation of the extended mesoscopic Eulerian formalism proves that this theoretical construction is a statistically consistent representation of two-phase flows that can be computed in practice. We show that since the extended mesoscopic Eulerian formalism is a statistic, it does not alter the intrinsic physical properties of the particles, such as their diffusion coefficient. However, we also show that this new formalism offers new statistics for the transport regime. The transport regime is key for the numerical simulation of combustion chambers as it is the main one experienced by fuel droplets from their formation to their vaporisation. The new statistics of the extended mesoscopic Eulerian formalism are intermediate between DNS and RANS, which proves that it is at the level of large eddy simulations. In the last chapter, we review different possible closures for the disperse phase in one-way coupled large eddy simulations (Chap. 10). We show that existing models may clearly differ in the transport part, and that by design, the tested models cannot fit exactly the spectral properties of particle trajectories.

Part I

Turbulent particulate flows

Chapter 1

Turbulent flows

This chapter aims at presenting some modelling aspects of fluids which represent a mandatory step before the conception of two-phase flow models, reduced or not.

- In Sec. 1.1, we start by describing the equations of reference for the fluids we wish to consider in this study: the Navier-Stokes equations (Eq. 1.2).
- In a second time, in Sec. 1.2, we describe turbulence. This is a very difficult task, because this regime is mostly referred to only by some characteristic properties and not by a clear and precise definition. This is partly due to the difficulties raised by the Navier-Stokes equations. Working on a loosely defined object makes the work quite difficult. This is why some time is spent providing our angle on the topic.
- Finally, in Sec. 1.3, we present some properties of interest of turbulence.
  - In Sec. 1.3.1, we describe a very basic and robust reference metric used for the characterisation of turbulence. This metric is constantly used throughout this work: spreading. The spreading characterises the rate at which particles are dispersed. The spreading behaviour of the particles will help us understand the dynamics of our different test cases.
  - In Sec. 1.3.2, we briefly present more advanced characterisations of the turbulence.
    * Particle pair spreading in Sec. 1.3.2.1. This characterisation is respected by the test case used in this work (Fig. 7.10).
    * We briefly evoke intermittency, a more recent and active research topic on the characterisation of turbulence, especially in the context of turbulent disperse phase flows.

1.1 The Navier-Stokes equations

In this section we present the Navier-Stokes equations.

- We start by presenting the variables of interest (Sec. 1.1.1),
- before introducing the system of equations (Sec. 1.1.2),
- and some of its limitations in (Sec. 1.1.3).

1.1.1 A macroscopic representation of the molecules

The Navier-Stokes equations are macroscopic equations which act on macroscopic variables. Establishing a relation between the representation of a fluid in terms of molecules and the representation of a fluid in term of macroscopic variables is quite standard (Drew and Passman (1999), Pope (2000), Chap. 2.1). It is best understood in the context of the kinetic theory of gases (Ferziger and Kaper (1973), Lanford (1981), Chapman, Cowling, and Burnett (1939), Lebowitz (1995)).
Discrete molecules are easily represented in terms of macroscopic variables when (Struchtrup (2005)):

- the ratio of the mean free path of the molecules to a representative physical length scale of the problem is small;
- the ratio of the mean frequency of the motion of the molecules to a representative macroscopic frequency of the problem is large.

This is traditionally characterised in terms of the Knudsen number:

$$\mathrm{Kn} = \frac{\ell_{\text{mean free path}}}{\ell_{\text{physical length}}} = \frac{f_{\text{macroscopic}}}{f_{\text{microscopic}}}. \tag{1.1}$$

When the Knudsen number is very small, the characteristic physical length scale of the problem encompasses many molecules and these particles move fast with respect to the characteristic time scale of the macroscopic problem. The high number of collisions leads to a fast relaxation of the distribution of molecules velocity towards an equilibrium distribution. This distribution can be parametrized only by a limited number of macroscopic quantities, such as the velocity $\boldsymbol{u}_f$, which offer a representative description of the local fluid state. In this continuum mechanics approximation, evolution equations for these macroscopic variables are expressed in the form of partial differential equations such as Navier-Stokes equations that are presented in the next section.

Although Navier-Stokes equations are primarily derived as phenomenological equations, it is possible, with many hypothesis along the way, to establish a path between the Kinetic Theory of gases and incompressible Navier-Stokes equations (Bardos, Golse, and Levermore (1993), Lions and Masmoudi (2001) and Golse and Saint-Raymond (2004)). This derivation is quite complex and out of scope here, however, it is interesting to notice at this point that Navier-Stokes equations are already a first level of reduction of the reality at the molecular level. They offer a statistical description of a discrete set of molecules in terms of the first moments of their velocity distribution. This approach is

similar to the strategy adopted by moment methods for sprays, which offer a statistical description of the first moments of the disperse phase in a Eulerian framework (Sec. 2.4). Let us now introduce the Navier-Stokes equations.

1.1.2 Navier-Stokes equations, a representation of the fluid in the form of a dynamical system

Fluids are everywhere. One of their main characteristic is that they flow under any applied shear stress. They cannot resist to shear stress in a static equilibrium.
According to the case under consideration, different equations for describing a fluid can be adopted, such as the Euler equations, the Navier-Stokes equations, or the Grad equations (see for instance Struchtrup (2005)). In the present document, we are interested in the interactions between inertial particles and turbulence. Turbulence is a phenomenon already present and mostly studied in the context of incompressible flows (Temam (2001)), even if the literature also addresses the modelling of compressible turbulence (see Chassaing, Antonia, Anselmet, Joly, and Sarkar (2002) for instance). The reference equations for studying the turbulence are thus the incompressible Navier-Stokes equations (Eq. 1.2):

$$\nabla_{\boldsymbol{x}} \cdot \boldsymbol{u}_f = 0, \tag{1.2a}$$

$$\partial_t \boldsymbol{u}_f + (\boldsymbol{u}_f \cdot \nabla_{\boldsymbol{x}})\, \boldsymbol{u}_f = -\frac{1}{\rho_f} \nabla_{\boldsymbol{x}} p_f + \nu_f \Delta_{\boldsymbol{x}} \boldsymbol{u}_f, \tag{1.2b}$$

where $\boldsymbol{u}_f$ is the fluid velocity, ρ_f the density and p_f the hydrodynamic fluid pressure.
With the incompressible Navier-Stokes equations, the fluid evolution corresponds to a causal deterministic system. We call this kind of description a *dynamical system.*

Definition 1. A *dynamical system* is a tuple (T, A, Φ), with:

- a monoïd T,
- a set A called phase space
- the evolution function of the dynamical system:

$$\Phi : U \subset T \times A \to A, \tag{1.3}$$

such that

$$\Phi\left(t_2, \Phi\left(t_1, a\right)\right) = \Phi\left(t_2 + t_1, a\right), \quad \forall a \in A, \quad \forall t_1, t_2, (t_1 + t_2) \in I\left(a\right), \tag{1.4}$$

with $I(a) = \{t \in T : (t, a) \in U\}$

In the case of the Navier-Stokes equations,

- the monoïd is $\mathbb{R}^+$, which corresponds to the set of the times t,
- phase space is the set A_f, which corresponds to the set of turbulent flow fields $\boldsymbol{u}_f$,
- the evolution function of the dynamical system is the function Φ_f which gives the evolution of the flow field following Navier-Stokes equations (Eq. 1.2).

With the incompressible Navier-Stokes equations, the fluid is represented by a smooth flow field $\boldsymbol{u}_f$. Indeed, $\boldsymbol{u}_f$ for instance has to be at least twice differentiable in order to be a *physical* (strong) solution of incompressible Navier-Stokes equations. Ensuring this property for long times is not obvious as presented in the next section.

1.1.3 A smooth solution to Navier-Stokes equations

This section largely inspired by Temam (2001) focuses on the viability of smooth representation in the context of Navier-Stokes equations. In order to do this let us first define some terms:

- The *fluid vorticity vector* $\boldsymbol{\omega}$ represents the local spinning motion of the fluid velocity near some point:

$$\boldsymbol{\omega} = \nabla \times \boldsymbol{u}_f = \begin{pmatrix} \frac{\partial u_{f,z}}{\partial y} - \frac{\partial u_{f,y}}{\partial z} \\ \frac{\partial u_{f,x}}{\partial z} - \frac{\partial u_{f,z}}{\partial x} \\ \frac{\partial u_{f,y}}{\partial x} - \frac{\partial u_{f,x}}{\partial y} \end{pmatrix}. \tag{1.5}$$

- The fluid *enstrophy* is defined as the integral of the square of the fluid vorticity vector over a surface S:

$$\mathfrak{E}(\boldsymbol{\omega}) = \int_S \|\boldsymbol{\omega}\|^2 . \mathrm{d}S. \tag{1.6}$$

  It can be interpreted as a type of potential density directly related to the kinetic energy in the flow that corresponds to dissipation effects in the fluid.
- We call a *strong solution* of the Navier-Stokes equations a solution for which the enstrophy is finite at all times.
- We call a *weak solution* of the Navier-Stokes equations a solution for which the enstrophy may become infinite at some instants of time.

From a physical point of view, it is much more natural to work with strong solutions, because they are more intuitive (there is no need for a variational framework to derive them) and because no flow experiment performed up to now has shown infinite enstrophy. However, from a mathematical point of view, it is expected since Leray (1933), Leray (1934a), Leray (1934b) that the vorticity vector of solutions of the Navier-Stokes equations could indeed become infinite. In fact, it is still a research topic today (Buckmaster and Vicol (2019)), and up to now, no one has been able to prove or give a counter-example to the following statement (from Fefferman (2006)):

> *In three space dimensions and time, given an initial velocity field, there exists a vector velocity and a scalar pressure field, which are both smooth and globally defined, that solve the Navier-Stokes equations.*

This lack of knowledge does not come from a lack of effort or interest, as there is a one million dollars prize for whomever gives an answer to this challenge. In the meantime,

as explained by Temam (2001) and briefly summed up in Tab. 1.1, a lot of work has already been done on Navier-Stokes equations.

	Weak solutions	**Strong solutions**
2D	Existence and uniqueness at all times	
3D	Existence at all times Uniqueness?	Uniqueness Existence at all times?

Table 1.1. Current knowledge of existence and uniqueness of Navier-Stokes solutions according to the dimension and to the type of solution (strong or weak).

As physicists, we are especially interested in having the existence of a single solution to Navier-Stokes equations in three dimensions with finite enstrophy (strong solution). We can clearly see in Table 1.1 that this is not the case yet. In three dimensions:

- Either we get a weak solution which exists but can have infinite enstrophy and is not guaranteed to be the unique solution at all times,
- or we get a strong solution which is not guaranteed to exist at all times, but if it does, is unique.

In this work, we are interested in reductions of two-phase flow models. By *reduced model* we mean a model of lower dimension which still capture some elements of the dynamics of the original system. Because we do not fully understand the nature of solutions of Navier-Stokes equations, it is quite difficult to get optimal reduction strategies for the numerical simulation of turbulence (Temam (1991)). This limited understanding makes the present work useful (because there is still a lot to study), but at the same time difficult (because many things are not known for certain).
In the context of practical numerical applications, Navier-Stokes equations are often discretised and computed at a given finite spatiotemporal resolution. Such a strategy has proven satisfactory with respect to experimental observations so far.
The question of weak or strong solutions is at stake when performing numerical solution of Navier-Stokes equations, but also rises when it comes to the description of turbulence. As turbulence is key to the context of this work, let us try to characterise it in the next section.

1.2 Turbulence

Without getting lost into the details of turbulent flows, it is fundamental to get a clear idea of the basic principles underlying how turbulence is understood in this work. Here, we will first characterise some of the properties of turbulence, before describing the so-called inertial range into more details.

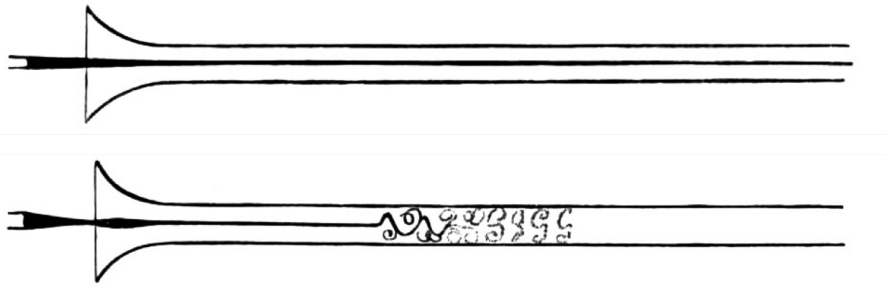

Figure 1.1. Sketches illustrating the influence of the Reynolds number on the flow behaviour from Reynolds (1883). A fluid is flowing in a tube and some ink is injected on the centreline at the entrance of the tube in order to visualise the flow. When the Reynolds number is low (top image), the ink draws a straight line and the regime is called laminar. When the Reynolds number is high (bottom image), the ink is dispersed in eddies after a given point and the regime is called turbulent.

1.2.1 Turbulence, an unstable regime

In the Navier-Stokes equations (Eq. 1.2), aside from the pressure term, the temporal evolution of the fluid velocity is controlled by two terms:

- a term $(\boldsymbol{u}_f \cdot \nabla_{\boldsymbol{x}})\,\boldsymbol{u}_f$ corresponding to the inertial effects of the fluid on its motion, with characteristic dimension $\frac{U_*^2}{L_*}$,
- and a term $\nu_f \Delta_{\boldsymbol{x}} \boldsymbol{u}_f$ corresponding to the effect of viscosity on the fluid dynamic, with characteristic dimension $\frac{\nu_f U_*}{L_*^2}$.

The balance between inertial and viscous effects of a fluid is named the Reynolds number:

$$\mathrm{Re} = \frac{L_* U_*}{\nu_f}, \tag{1.7}$$

with a reference length scale L_*, and U_* a velocity such that $U_* T_* = L_*$, with T_* a reference time scale.

When the Reynolds number is low (top of Fig. 1.1), the viscous term is dominant and the flow regime is called *laminar*. When the Reynolds number becomes large (bottom of Fig. 1.1), the flow regime becomes *turbulent*. Motions appear unstable, erratic and difficult to characterise in terms of shapes or patterns. There is no precise value of Reynolds number which corresponds to a turbulent flow. It depends on each specific case at hand and on the choice of the characteristic scales used to define the Reynolds number. But whatever the case under consideration and the method used to define the characteristic scales of the flow, the flow becomes turbulent as one increases the Reynolds number (Lesne and Laguës (2012), Chap. 9.5.2). Turbulence is a state of the flow which is highly sensitive to initial conditions, with a wide range of scales mixing the fluid (illustration of the wide range of scales, in wave-number space, from experiments Fig. 1.2).

If we now focus on the energy of a turbulent flow, the traditional picture of reference is

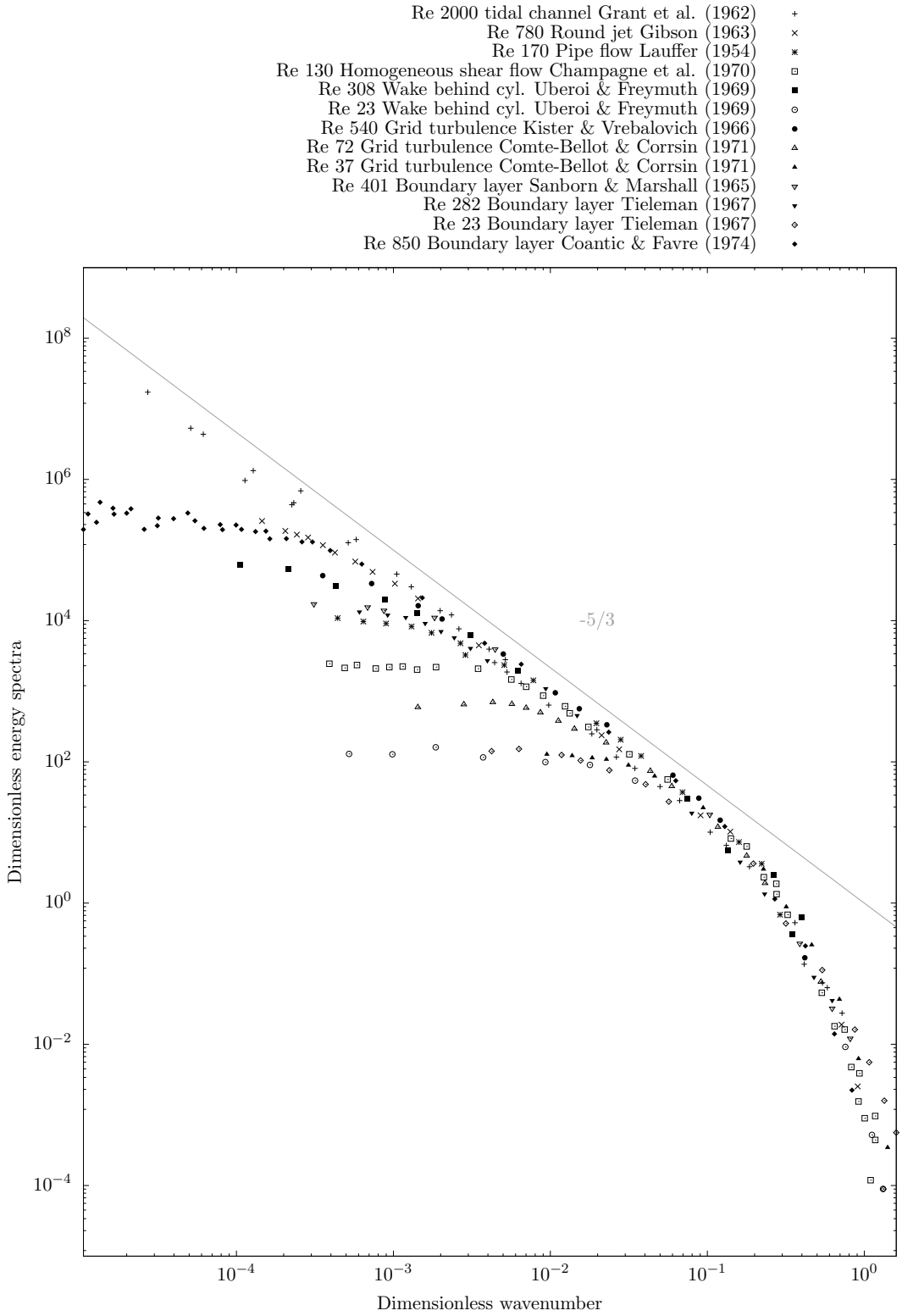

Figure 1.2. Stream wise turbulence energy spectra for various flows (from Chapman (1979)).

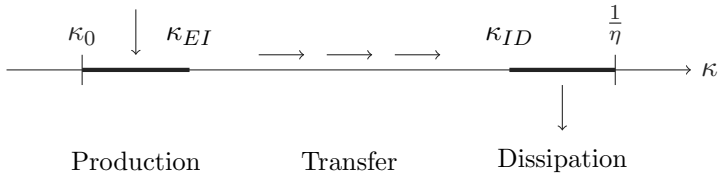

Figure 1.3. Sketch of the principle of the energy cascade described in Richardson (1922), p. 66 (adapted from Pope (2000), Fig. 6.2).

given by the energy cascade (described in Richardson (1922), p. 66, Fig. 1.3). Simply put, energy is injected at low frequencies ($\kappa \in [\kappa_0, \kappa_{EI}]$) through interaction at the boundaries and is dissipated at high frequencies ($\kappa \in [\kappa_{ID}, \kappa_\eta]$) through viscosity. This mechanism defines three different ranges:

- The *energy-containing range* at the lowest wave-numbers ($\kappa \in [\kappa_0, \kappa_{EI}]$) which usually contains most of the fluid kinetic energy and where kinetic energy is also produced.
- The *dissipation range* at the highest wave-numbers ($\kappa \in [\kappa_{ID}, \kappa_\eta]$) which usually dissipates most of the fluid kinetic energy. κ_η is the wave-number associated with the Kolmogorov length scale η:

$$\eta = \left(\frac{\nu_f^3}{\varepsilon}\right)^{1/4} . \tag{1.8}$$

  The Kolmogorov length scale corresponds to the characteristic scale of the smallest turbulent motions.
- In-between is an intermediate range of scales ($\kappa \in [\kappa_{EI}, \kappa_{ID}]$), called inertial range, where energy flows from the energy containing range to the dissipation range.

After having briefly presented the conditions for a fluid to be turbulent in this section, let us now focus on the inertial range which is a specific region of interest of the turbulent flow field for this study.

1.2.2 The inertial range, a quest for universality

In order to apprehend turbulent flows, one is looking for universal properties of turbulence. This is difficult, because a turbulent flow is an open system, far from equilibrium. Navier-Stokes equations being dissipative, energy has to be continuously fed to the system at the largest scales of the flow. Nonetheless, it is expected to have some stable universal properties, independent of the details of the external forcing (Farge (1992)). Following on the average energy cascade picture of Richardson (Fig. 1.3), energy is mostly injected in the flow from the constraints given at the boundaries. These constraints generate large scale motions in the domain, which feed progressively smaller scales in the flow. For very high Reynolds numbers, far away from the boundary conditions, as the energy gets successively transferred from one scale to an other, it somehow loses any information specific to the case (Leslie (1973), p.25). Therefore, behaviour of

the flow becomes in a sense universal. This is the realm of the inertial range. These properties are limited to a given range of scales which is called the universal equilibrium range (Pope (2000), p. 185). The universal equilibrium range encompasses the inertial range and the dissipation range. In the universal range, Kolmogorov (1941) made some key hypothesis, which are at the basis of most of current works on turbulence (see for instance Lesne and Laguës (2012), Chap. 9.5.5 or Pope (2000), Chap. 6.1.2):

- the universal range is statistically isotropic;
- the statistical properties of the inertial range are only function of the dissipation;
- the statistical properties of the dissipative range are only function of the dissipation and the viscosity;

from which a dimensional analysis gives Kolmogorov's law which states that the average energy density spectrum is of the form:

$$E(\kappa) \sim \varepsilon^{2/3}\kappa^{-5/3}, \tag{1.9}$$

with κ the wave-number, ε the rate of dissipation of turbulent kinetic energy and $E(\kappa)$ the average fluid energy density spectrum.
It is possible to observe in Fig. 1.2, which represents stream-wise turbulence energy spectra for various flows, that the relation given by Eq. 1.9 is well verified in practical experiments.
While Navier-Stokes equations are deterministic, characterisation of the inertial range, and of turbulence in general, is usually done in a statistical way. This means that a probability measure can be associated to the turbulent flow. This is what is presented in the next section.

1.2.3 Probability spaces and Navier-Stokes equations

This section presents how to build a probability measure associated to turbulence. It is the necessary foundation of a consistent probabilistic framework for deriving statistical models of the disperse phase consistent with fluid reductions, such as large eddy simulation, and with two-way coupling between phases. Let us start by defining a probability space.

Definition 2. A *probability space* is a tuple $(\Omega, \mathcal{E}, \mathbb{P})$ of three elements:

- the set of possible outcomes Ω,
- the set of events, which is a σ-algebra $\mathcal{E} \subseteq 2^{\Omega}$:
  - $\Omega \in \mathcal{E}$,
  - $\mathcal{E}$ is closed under complements, $\forall e \in \mathcal{E}, \quad (\Omega / e) \in \mathcal{E}$,
  - and $\mathcal{E}$ is closed under countable unions

$$\forall (e_i)_{i\in\mathbb{N}} \in \mathcal{E}^{\mathbb{N}}, \left(\bigcup_{i=1}^{\mathbb{N}} e_i\right) \in \mathcal{E}. \tag{1.10}$$

- and $\mathbb{P}$, the probability measure on $\mathcal{E}$:
  - $\mathbb{P}[\Omega] = 1$ and
  - $\forall (e_i)_{i\in\mathbb{N}} \in \mathcal{E}^{\mathbb{N}}$, such that

$$i \neq j \implies e_i \cap e_i = \emptyset, i, j \in \mathbb{N}, \tag{1.11}$$

$$\mathbb{P}\left[\bigcup_{i=1}^{\mathbb{N}} e_i\right] = \sum_{i=1}^{\mathbb{N}} \mathbb{P}[e_i]. \tag{1.12}$$

Elements of Ω are only individual realisations, whereas $\mathcal{E}$ include individual realisations, but also sets of individual realisations. For any element e in $\mathcal{E}$, $\mathbb{P}[e]$ gives the probability of e.
Let us see how to associate a probability measure $\mathbb{P}$ to turbulence (this section can be found in Drew and Passman (1999), Chap. 9-10).

1.2.3.1 A deterministic dynamical system with random initial conditions

For a deterministic system of equations such as the Navier-Stokes equations, one way to introduce a probability space is through the choice of initial conditions. Let us call A_f the set of turbulent s $\boldsymbol{u}_{f,0}$. In practice, we can consider that $A_f = \mathbb{R}^{3^{\mathbb{R}^3}}$.
We consider that initial conditions are a measurable function which depends on the outcome of a random phenomenon:

$$\begin{array}{rccl} \boldsymbol{u}_{f,0}: & \Omega & \to & A_f \\ & \omega & \mapsto & \boldsymbol{u}_{f,0}(\omega). \end{array} \tag{1.13}$$

Definition 3. A *random variable* Y is a measurable function from a set of possible outcomes Ω to a measurable space.

Therefore, the initial conditions of the fluid $\boldsymbol{u}_{f,0}$ define a random variable.

Definition 4. When it exists, the *expectation* of a random variable Y is given by:

$$\mathbb{E}[Y] = \int_\Omega Y(\omega)\, \mathrm{d}\mathbb{P}[\omega]. \tag{1.14}$$

Definition 5. When it exists, the *conditional expectation* of a random variable Y on $e \subset \Omega$ is given by:

$$\mathbb{E}[Y|e] = \frac{1}{\mathbb{P}[e]} \int_e Y(\omega)\, \mathrm{d}\mathbb{P}[\omega]. \tag{1.15}$$

Definition 6. When it exists, the *variance* of a random variable Y is given by:

$$\mathrm{Var}\left[Y\right] = \mathbb{E}\left[\left(Y - \mathbb{E}\left[Y\right]\right)^2\right]. \tag{1.16}$$

Definition 7. When it exists, the *conditional variance* of a random variable Y on $\boldsymbol{e} \subset \Omega$ is given by:

$$\mathrm{Var}\left[Y|\boldsymbol{e}\right] = \mathbb{E}\left[\left(Y - \mathbb{E}\left[Y|\boldsymbol{e}\right]\right)^2 \middle| \boldsymbol{e}\right]. \tag{1.17}$$

Because $\boldsymbol{u}_{f,0}$ is measurable, we extend the probability measure $\mathbb{P}$ to A_f such that

$$\forall \omega \in \Omega, \quad \mathbb{P}\left[\boldsymbol{u}_{f,0}\left(\omega\right)\right] = \mathbb{P}_0\left[\boldsymbol{u}_{f,0}^{\leftarrow}\left(\omega\right)\right]. \tag{1.18}$$

Therefore, we extend the initial probability measure $\mathbb{P}_0$ to ulterior time:

$$\forall \omega \in \Omega, \forall t \in \mathbb{R}, \quad \mathbb{P}_t\left[\boldsymbol{u}_{f,t}\left(\omega\right)\right] = \mathbb{P}_0\left[\Phi_{f,t}^{\leftarrow}\left(\boldsymbol{u}_{f,t}\left(\omega\right)\right)\right]. \tag{1.19}$$

1.2.3.2 Ergodicity - a probability space for time

The erratic behaviour of turbulence is reminiscent of a chaotic dynamical system. Chaos is *when the present determines the future, but the approximate present does not approximately determine the future* as Edward Lorenz puts it (Danforth (2020)).
Let us present here some definitions to explicit the notion chaos.

Definition 8. The flow Φ of the dynamical system (T, A, Φ) is *sensitive to initial conditions* when, $\forall a_1 \in A, \forall \epsilon \in \mathbb{R}^{+*}, \exists a_2 \in A, \exists a \in \mathbb{R}^{+*}$, s.t.:

$$0 < \|a_2 - a_1\| < \epsilon \text{ and } \|\Phi\left(t, a_2\right) - \Phi\left(t, a_1\right)\| > e^{a.t}\|a_2 - a_1\|. \tag{1.20}$$

Definition 9. The dynamical system (T, A, Φ) is *topologically mixing* when, $\forall \boldsymbol{a}_1, \boldsymbol{a}_2$ non-empty open sets of A,

$$\exists t \in T, \text{ s.t. } \Phi\left(t, \boldsymbol{a}_1\right) \cap \boldsymbol{a}_2 \neq \emptyset. \tag{1.21}$$

Definition 10. Let (T, A, Φ) be a dynamical system. For any point $a \in A$, the set γ_a is called *orbit* through a.

Definition 11. Let (T, A, Φ) be a dynamical system. The point $a \in A$ is *periodic* if it exists $t \in T$ such that $\Phi\left(t, a\right) = a$.

Property 1. *Let (T, A, Φ) be a dynamical system. Let $a \in A$ by a periodic point of the system. Then all points on the orbit through a, γ_a are periodic.*

Definition 12. The dynamical system (T, A, Φ) has *dense periodic orbits* if every point in the space is approached arbitrarily closely by periodic orbits.

Definition 13. A dynamical system is *chaotic* when:
- it is sensitive to initial conditions,
- it is topologically mixing,
- and it has dense periodic orbits.

Because of the very unstable nature of such systems, two different trajectories starting from very close initial conditions always have a very different future. In this context, if one is interested in a representative description of the system, focusing on the evolution of a single trajectory, may not be the most appealing.
The concept of *attractor* provides a solution to such a difficulty.

Definition 14. Let (T, A, Φ) be a dynamical system. The subset $\boldsymbol{a} \in A$ is an *attractor* when:
- $\boldsymbol{a}$ is forward invariant under Φ:

$$\forall a \in \boldsymbol{a}, \forall t \in T, \Phi(t, a) \in A. \tag{1.22}$$

- There exists an open set $B(\boldsymbol{a})$ called basin of attraction of $\boldsymbol{a}$ such that: For any open neighbourhood N of $\boldsymbol{a}$, there is a time $t_0 \in T$ such that $\forall t > t_0$, $\Phi(t, N) \subset B(\boldsymbol{a})$.

An attractor corresponds to the subset of solutions which attracts all the possible trajectories of the system (Temam (2001)). Therefore, if an attractor exists, characterising this set of solutions guaranties to provide representative information about the permanent regime of the flow.
Interestingly, the Navier-Stokes equations in dimension three possess a global attractor (of finite dimension). Because the system is chaotic and the attractor is global, any single trajectory explores all the attractor of the system over time. In the limit of an infinite timespan, the permanent regime of a single trajectory becomes representative of the permanent regime of any trajectory.
This is the reason why it is extremely interesting to study turbulence through the lens of the probability space inferred by the temporal evolution of one given trajectory. Therefore, the temporal evolution of the fluid described by deterministic Navier-Stokes equations calls for a stochastic treatment (Reynolds (1895), Kolmogorov (1941)).
This leads us naturally to a key concept: *ergodicity*.

Definition 15. Let $(A, \mathcal{A}, \mathbb{P})$ be a probability space and (T, A, Φ) be a dynamical system. The dynamical system is *measure-preserving* on the probability space if:

$$\forall \boldsymbol{a} \in \mathcal{A}, \forall t \in T, \mathbb{P}\left[\Phi_t^{\leftarrow}(\boldsymbol{a})\right] = \mathbb{P}[\boldsymbol{a}]. \tag{1.23}$$

Definition 16. Let (T, A, Φ) be a measure preserving dynamical system on the probability space $(A, \mathcal{A}, \mathbb{P})$. Φ is *ergodic* when:

$$\forall t \in T, \forall \boldsymbol{a} \in \mathcal{A}, \quad \Phi_t^{\leftarrow}(\boldsymbol{a}) = \boldsymbol{a} \implies \mathbb{P}[\boldsymbol{a}] \in \{0, 1\}. \tag{1.24}$$

Property 2. *Let (T, A, Φ) be a measure preserving dynamical system on the probability space $(A, \mathcal{A}, \mathbb{P})$. For all integrable f, for almost all $a \in A$:*

$$\mathbb{P}[f(A)] = \lim_{t \to \infty} \frac{1}{t} \int_0^t f(\Phi_t(a))\, dt. \tag{1.25}$$

Therefore, for an ergodic dynamical system, its time average is the same as its average over its probability space. In the case of turbulence theories, the inertial range is often assumed to be ergodic (Farge (1992)). Therefore, this leads to an equivalence for the inertial range of turbulence between:

- the probability measure associated of realizations of the permanent regime, and
- the probability measure built from the temporal evolution of turbulence.

1.2.3.3 Physical probability space and autocorrelation

Following Drew and Passman (1999), Chap. 10.3, the spatial fluctuations of the turbulent field at any given time can also be seen as a random variable. In the context of Kolmogorov (1941) hypothesis, in the inertial range, where turbulence is assumed stationary, homogeneous and isotropic, for quantities which possess a volume average, it is often assumed that

- the spatial averages over large volumes and
- temporal averages

are the same.
This equivalence between spatial and temporal averages is very interesting for building models based on volume averages. It allows to estimate unknown volume averaged quantities in terms of well known time averaged quantities.

1.2.3.4 Turbulence and probability spaces

Therefore, thanks to the ergodicity hypothesis and following many authors (Monin and Yaglom (1971), Chap. 4.4.7, Crowe, Sommerfeld, and Tsuji (1998), Chap. 6.1, Drew and Passman (1999), Chap. III, Pope (2000), 3.8), we will consider that the probability spaces implied by fully developed turbulence over

- realizations,
- time, or
- space

are the same.

1.3 Some properties of turbulence

This section focuses on describing some common properties of turbulence. It goes gradually,

- starting from a very basic, global one-point metric (Sec. 1.3.1), which characterises dispersion,
- then moving to a more advanced but standard, global two-point metric (Sec. 1.3.2.1), which characterises two-point dispersion,
- and finally, a local two-point metric (Sec. 1.3.2.2): intermittency.

Because it is already a vast topic, we will only focus on spreading in this work. The notions and mechanisms of spreading in turbulence are used constantly in the next parts of this manuscript. This is why it is presented quite extensively in Sec. 1.3.1.

1.3.1 Spreading, a basic metric of turbulence

The lack of a full understanding of turbulence does not prevent us from characterising its behaviour on some specific aspects. For instance, the previous section briefly presented considerations on topology (chaotic behaviour) and energy. An other characterisation is done through the spreading of fluid parcels. It is one of the earliest characterisations of turbulence, starting with Reynolds (1883), and treated in the seminal works of Taylor (1921) and Richardson (1926). The spreading of fluid parcels is of interest to this work because in the universal regime of isotropic homogeneous turbulence, spreading is the first order effect of the fluid on particles.

1.3.1.1 Spreading of fluid parcels

In the context of the equations of Navier-Stokes, *fluid parcels* (Landau and Lifshitz (1959), p. 1) are notional particles which move according to the fluid velocity field at their location. They correspond to a Lagrangian description of the fluid. It is interesting to study their behaviour in the context of disperse two-phase flows because in the limit of null inertial, the disperse phase behaves as fluid parcels (Balachandar and Eaton (2010)). A detailed analysis of the behaviour of fluid parcels in a turbulent fluid is given by Falkovich, Gawedzki, and Vergassola (2001) (for shorter material, one can also refer to Eyink (2008), Chap. 5.b.). Since the study of inertial particles done in this work has many similarities with the properties of the fluid parcels in turbulence, some essential properties of fluid parcels in turbulence are stated hereafter.
When using Navier-Stokes equations, deriving the evolution of fluid parcels simply corresponds to the Lagrangian point of view of the fluid. The acceleration of fluid parcels is given by taking the material derivative of the fluid flow field at the location of the parcel.

Although the actual motion of fluid parcels is intrinsically local, one can be interested in deriving some global properties representative of a given flow field. One interesting quantity is the evolution with time of the squared distance of a fluid particle from its

original position:

$$t \in \mathbb{R}^+ \mapsto \|\boldsymbol{x}_p(t+t_0) - \boldsymbol{x}_p(t_0)\|^2, \tag{1.26}$$

with x_p a particle trajectory function of time t, and t_0 a time of reference. For a reference see for instance Pope (2000), Chap. 12.4. This quantity is of prime importance for subgrid modelling of inertial particles because it is usually this quantity that closure models attempt to reproduce in the first place (see Sec. 10).
In fact, instead of considering only $x_p(t+t_0)$, the evolution with time of one particle on one fluid realization, it is possible to consider the quantity:

$$t, t_0, \boldsymbol{x}_{p,0}, \omega_f \mapsto \boldsymbol{x}_{p,t_0,\boldsymbol{x}_{p,0}}(t), \tag{1.27}$$

which is a function of the time t, but also:

- the initial time t_0,
- the initial particle position $\boldsymbol{x}_{p,0} := \boldsymbol{x}_p(t_0)$,
- and the fluid realization ω_f.

Consistently with the probability space associated with turbulence, the deterministic quantity corresponding to the particle position $\boldsymbol{x}_{p,t_0,\boldsymbol{x}_{p,0}}(t)$ can be interpreted as a random variable $\boldsymbol{X}_p(t)$ of initial time, position and/or realization without distinction (Fig. 1.4). This vision makes possible the computation of global properties representative of the flow field.
One such global properties representative of the flow field is the relative mean square displacement:

$$\mathbb{E}\left[\|\boldsymbol{X}_p(t) - \boldsymbol{X}_p(0)\|^2\right]. \tag{1.28}$$

The time evolution of the relative mean square displacement (Eq. 1.29) was studied in particular by Taylor (1921):

$$t \in \mathbb{R}^+ \mapsto \mathbb{E}\left[\|\boldsymbol{X}_p(t) - \boldsymbol{X}_p(0)\|^2\right]. \tag{1.29}$$

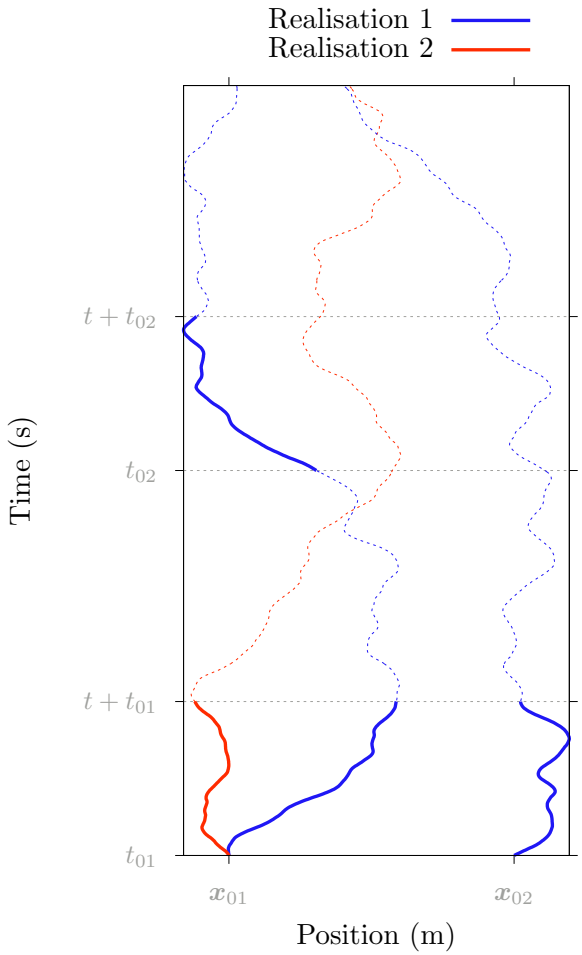

Figure 1.4. Illustration of how ergodicity makes time, space and realizations similar for the statistical study of stationary isotropic homogeneous turbulence.
Statistical properties of the mean square displacement after a time t are the same when considering different initial positions (x_{01} vs x_{02}), or different initial stating times (t_{01} vs t_{02}), or different realizations (- vs -).

1.3.1.2 Short time transport behaviour

If the process $\boldsymbol{X}_p(t)$ is differentiable, of velocity $\boldsymbol{V}_p(t)$, Eq. 1.29 is equivalent to a quadratic function as $t \to 0$:

$$\mathbb{E}\left[\|\boldsymbol{X}_p(t) - \boldsymbol{X}_p(0)\|^2\right] \sim_0 \mathrm{Var}\left[\boldsymbol{V}_p(0)\right] t^2. \tag{1.30}$$

1.3.1.3 Long time diffusive behaviour

When $\int_{t_0}^{t} \mathbb{E}\left[\boldsymbol{V}_p(s).\boldsymbol{V}_p(t_0)\right] \mathrm{d}s$ has a finite limit D as t goes to $+\infty$, the fluid parcel spreading is asymptotically diffusive:

$$\mathbb{E}\left[\|\boldsymbol{X}_p(t) - \boldsymbol{X}_p(0)\|^2\right] \sim_{+\infty} 2Dt. \tag{1.31}$$

The limit D is called the diffusion coefficient of the particle.
The Lagrangian integral time-scale is the characteristic time scale to get to this asymptotic diffusive regime:

$$T_L = \frac{D}{\mathrm{Var}\left[\boldsymbol{V}_p(0)\right]}. \tag{1.32}$$

For times much smaller than the correlation time T_L, the particle velocity has a strong correlation with its initial velocity. On the contrary, for times much longer than the correlation time T_L, the particle velocity is independent of its initial velocity. Therefore, at an observation time scale larger than the correlation time T_L, the particle trajectory can be represented by a sum of independent paths, like a diffusion process. However, with such a representation of a particle trajectory, the strongly correlated short time transport behaviour is lost (Fig. 1.5).

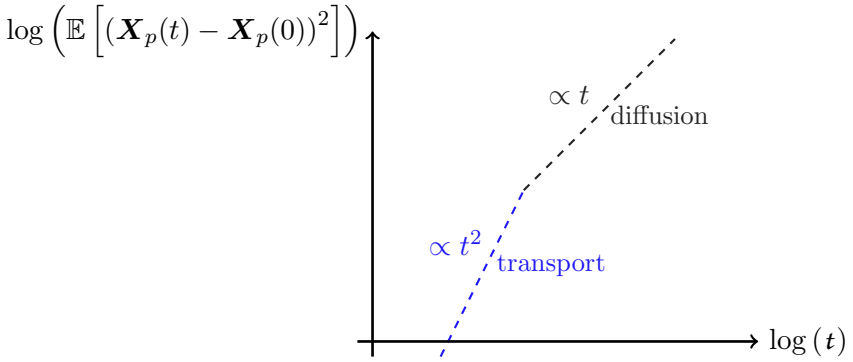

Figure 1.5. Asymptotic spreading behaviour of fluid parcels
Asymptotically short times correspond to a transport regime, whereas asymptotically long times correspond to a diffusion regime.

1.3.2 More advanced characterisations of turbulence

Short time and long time regimes are very important one-point statistics used for the description of turbulence and the design of reduced models. The starting point of a closure model for particles in an industrial context is often to match these statistics, and recovering the correct behaviour of these statistics is already quite involved (Minier and Profeta (2015), Reeks, Swailes, and Bragg (2018)).
However, although fundamental, these regimes do not entirely characterise turbulence. It is quite the opposite. Furthermore, the long time diffusive behaviour describes a regime at a much larger time scale than the largest time scales of particle trajectories, for which practical interest in the case of liquid fuel injection in turbo-reactors may not always be very clear.

1.3.2.1 Fluid parcels pair spreading

One of the fundamental feature of fully developed turbulence is its inertial range. This fluid structure is best explored in terms of two point statistics such as fluid parcel pair dispersion. As noticed by Richardson (1926), in the inertial regime, fluid parcel pair dispersion is a function of the relative distance between the parcels. If one considers two fluid parcels such that $\eta < |\boldsymbol{X}_{p,2}(t) - \boldsymbol{X}_{p,1}(t)| < L$, the scaling given by Kolmogorov (1941) implies Eq. 1.33, with C_0 being Richardson's constant:

$$|\boldsymbol{X}_{p,2}(t) - \boldsymbol{X}_{p,1}(t)|^2 (t) \simeq \mathrm{C}_0 \mathbb{E}[\varepsilon]\, t^3. \tag{1.33}$$

This scaling correspond to a velocity field of very low regularity. More on this can be found in Falkovich, Gawedzki, and Vergassola (2001) or Eyink (2008) for instance.

1.3.2.2 Intermittency

It is difficult to present turbulence scaling without a word on intermittency, which is currently the state of the art in terms of turbulence analysis.
The inertial range, as described by Kolmogorov (1962) possesses properties of self-similarity across time-scales and across length-scales. This behaviour is reminiscent of a fractal object. Describing the inertial range as self-similar is already a good approximation. We will keep with this level of description in this manuscript.
Current works refine this fractal representation by observing that self-similarities in turbulence are not homogeneous. They conclude that turbulence is more adequately described by a multi-fractal object as described in Dubrulle (2019). This is the concept of *intermittency* in turbulence. More details on intermittency can be found for instance in Frisch (1995), Chap. 8.
Among other effects, intermittency has a direct impact on the acceleration distribution of fluid parcels.

- In the context of turbulence as described by Kolmogorov (1962), the acceleration distribution of fluid parcels is close to a normal distribution.
- However, in the context of an intermittent flow, the acceleration distribution of fluid parcels deviate from normality and show heavier tails.

This leads to more precise LES models for particles (see for instance Gorokhovski and Zamansky (2018)).
It is important to keep in mind that intermittency characterises the turbulent flow field at a much higher order than position spreading (high order moments of the acceleration of low inertia particles) and will not be the base of this manuscript (work is currently done on the topic, for instance by Letournel (2022)).

Highlights and conclusions

In this chapter we have introduced the carrier phase for the particles as well as essential notions which will follow us along the manuscript. The carrier phase of reference for this work is given by a turbulent fluid following Navier-Stokes equations. It corresponds to a deterministic dynamical system. It is possible to consider this fluid as a random variable. Thanks to the properties of turbulence, the law of this random variable is obtained indifferently from the temporal evolution of the fluid or from different realisations. With Taylor (1921), we have also reviewed the concept of spreading: fluid particles are dispersed in the flow following an initial ballistic regime before switching to a diffusion regime.

Chapter 2

Modelling of particles in a turbulent flow

In this chapter, we briefly review the available methods to describe droplets or particles dynamics in a turbulent gaseous carrier phase:

- The first section focuses on available methods for describing an individual droplet, from the resolution of its interface to the point-particle approach.
- The second section describes elementary physics of such particulate flows
- The third section presents the interest of a statistical point of view, and how to derive it, leading to the Mesoscopic Eulerian Formalism (MEF).
- The last section shows how to solve a Population Balance Equation using a Macroscopic Moment Method.

2.1 Describing droplets or particles dynamics

In this section, we briefly detail the available solutions to describe a droplet or particle dynamics in a gaseous carrier flow, turbulent or not.

2.1.1 Different levels of modelling

Inside a combustion chamber, liquid fuel droplets can be described by different properties. Usual properties for one droplet would be for instance its shape, its composition field, its temperature field and its velocity field. Many physical phenomena can influence the evolution of each droplet: they can vaporise, they can collide with each other or with surfaces, they can be advected, accelerated, distorted and even broken apart by the surrounding fluid. Furthermore, their enthalpy changes through phase change, conduction, convection and radiation.

Let us briefly present different levels of representation of liquid fluid droplets in numerical simulations ordered by decreasing numerical cost.

- *Resolved interface*: one way to represent a particle is by carefully reproducing

the full particle as a liquid droplet. With such a representation, the particle shape changes with time, due to its interaction with the surrounding fluid (see for instance the work by Ménard, Tanguy, and Berlemont (2007)). Such a strategy is very expensive since it requires to solve the flow inside and outside each droplet, as well as the dynamics of the interfaces along with their jump conditions.

- *Imposed interface*: when a droplet is small enough (small Weber number), its shape is nearly spherical. In this case, it is reasonable to assimilate a droplet to a spherical particle. Its physical extension is only parametrised by the position of its centre of mass and its diameter. The interaction of the particle with the surrounding fluid is done by computing accurately the flow around the particle (see for instance Homann, Bec, and Grauer (2013), Botto and Prosperetti (2012), Chadil, Vincent, and Estivalèzes (2019)).
- *Point-particle simulations*: when the particle is small compared with the length scale of fluid fluctuations, the fluid is assumed to be uniform in the vicinity of the particle. In this case, the particle can be represented only by the position of its center. Because the fluid is not resolved around the particle, and because the particle has a negligible volumetric occupation in the fluid, it is possible to use a simple model for the evolution law of the particle in the fluid. An example of evolution law is given by the Basset-Boussinest-Oseen equation for particles with a small relative velocity with respect to the unperturbed fluid. When the particle is much denser than the surrounding fluid, Basset-Boussinest-Oseen equation becomes Stokes' drag law (Stokes (1851))[1].

The main concern of this work is the interaction of small liquid droplets with gaseous turbulence, we thus restrict ourselves to a point-particle representation. Furthermore, our interest is mainly on the droplets' dynamics. Therefore, we neglect collisions, break-up and vaporisation, leading to a model in which the sole interaction between the gas phase and the disperse phase is through the aerodynamics force, here solely the drag force.

2.1.2 Point-particle modelling under Stokes' drag law

In this section, let us present Stokes' drag law. When one particle q, ($q \in [\![1, \mathrm{N}_p]\!]$) is represented at a time t by a position $\boldsymbol{x}_q(t)$, a velocity $\boldsymbol{v}_q(t)$ and a characteristic relaxation time $\tau_q = \rho_q d_q^2 / (18\mu_f)$, with ρ_q the particle density, d_q the particle diameter and μ_f the fluid cinematic viscosity, the evolution equation of this particle with Stokes' drag law reads:

$$\mathrm{d}_t \boldsymbol{x}_q(t) = \boldsymbol{v}_q(t), \tag{2.1a}$$

$$\mathrm{d}_t \boldsymbol{v}_q(t) = \frac{1}{\tau_q} \left(\boldsymbol{u}_{f@q}(t) - \boldsymbol{v}_q(t) \right). \tag{2.1b}$$

[1] According to the case at hand, it is possible to consider alternate drag laws such as the popular one proposed by Naumann and Schiller (1935) for instance.

In this work, τ_q is the same for all the particles in a given simulation, therefore it is named τ_p. The linear acceleration term in the second equation of Eqs. 2.1 is named Stokes' drag law. It corresponds to the force exerted by a uniform incompressible steady flow of velocity $\boldsymbol{u}_{f@q}$ on a solid sphere of velocity $\boldsymbol{v}_q$. The system of Eqs. 2.1 has to be closed for the quantity $\boldsymbol{u}_{f@q}$. In general, it is taken as the fluid velocity in the vicinity of the particle. In the context of a point particle approximation, this quantity is the fluid velocity at the position of the particle $\boldsymbol{u}_q(t) = \boldsymbol{u}_f(t, \boldsymbol{x}_q(t))$. When one computes Navier-Stokes equations, this quantity is readily accessible. However, when one only computes a reduced vision of the fluid, giving a meaning to Eqs. 2.1 is challenging (Sec. 3.3). Furthermore, these equations are valid in a one-way context, when the fluid velocity $\boldsymbol{u}_f$ is not impacted by the presence of the particle. In a two-way case, $\boldsymbol{u}_f$ is impacted by the presence of the particle. Therefore, this formulation may not hold true (Zeren (2010), Sec. 2.4.1 and 2.4.2, Capecelatro and Desjardins (2013), Horwitz and Mani (2016), Ireland and Desjardins (2017), Zwick and Balachandar (2017), Poustis, Senoner, Zuzio, and Villedieu (2019), Zwick and Balachandar (2020)).
Interestingly, the term $\boldsymbol{u}_f(t, \boldsymbol{x}_q(t))$ induces a coupling between the particle position and the particle velocity. Indeed, if one introduces a corrective model for the particle position (in the form of a Wiener process for instance), it changes the particle trajectory, which impacts on the fluid velocity seen at the position of the particle, therefore changing the particle acceleration and thus modifying the particle position. The same coupling phenomena happens when altering the particle velocity.

2.1.3 Inertial particles as a dynamical system

Similarly to the approach derived for the fluid ruled by the Navier-Stokes equations (Sec. 1.1), the system of the fluid and the particles is a dynamical system. Phase space $A = A_f \times A_p^{\mathrm{N}_p}$ is now given by the conjunction of the fluid state in A_f and the N_p particle states in A_p, with $A_p \subset \mathbb{R}^6$.
The deterministic flow of the dynamical system Φ is now given by Navier-Stokes equations (Eq. 1.2) and the evolutions equations of the particles (Eq. 2.1). For any initial point in phase space $s_0 \in A$, $\Phi_t(s_0)$ is the state of the system after some time $t \in \mathbb{R}^+$.
This modelling choice is interesting because it gives deterministic trajectories for the particles.
However, when particle trajectories in turbulence are chaotic, accurately reproducing the deterministic nature of particle trajectories can be secondary. One may be more interested in more global properties such as the measure of an attractor. Furthermore, adopting a deterministic evolution law for the particles is not always a suitable strategy. As an example, think of Brownian motion for instance (Einstein (1905)).
With discrete particle simulation, one may want to describe each point particle with many different state variables when applicable (such as position, velocity, size, temperature and composition for instance). In the context of this work, the representation of each point particle will only include its position, size and velocity. This minimal descrip-

tion possesses the key quantities controlling the dynamical behaviour of each particle. Therefore, it is a good starting point when designing a consistent two-way coupled LES model.

2.1.4 Eulerian formulation of a Discrete Particle Simulation

The Lagrangian representation of a particle q, ($q \in [\![1, \mathrm{N}_p]\!]$) simply consists in the list of its state variables at a time t. In our case, its position $\boldsymbol{x}_q(t)$, and its velocity $\boldsymbol{v}_q(t)$. In this work, the evolution equations of these variables is given by the evolution equations presented in Sec. 2.1.2 (Eq. 2.1).

The Eulerian representation of the same reality for one particle is given by the *fine-grain* distribution (Pope and Ching (1993)):

$$\forall q \in [\![1, \mathrm{N}_p]\!], \quad f_{q,\mathrm{DPS}} = \delta_{\boldsymbol{x}_q(t)} \delta_{\boldsymbol{v}_q(t)}. \tag{2.2}$$

The evolution equation for $f_{q,\mathrm{DPS}}$ equivalent to Eq. 2.1 is given by (Struchtrup (2005), Chap. 3.1):

$$\forall q \in [\![1, \mathrm{N}_p]\!], \quad \partial_t f_{q,\mathrm{DPS}} + \nabla_{\boldsymbol{x}} \cdot (\mathrm{d}_t \boldsymbol{x}_q \, . f_{q,\mathrm{DPS}}) + \nabla_{\boldsymbol{v}} \cdot (\mathrm{d}_t \boldsymbol{v}_q \, . f_{q,\mathrm{DPS}}) = 0. \tag{2.3}$$

This equation has to be understood in the sense of measures. Note that because we are considering the specific case of collision-less point-particles, Eq. 2.3 does not include a collision kernel. When particles follow the same evolution behaviour as in Eqs. 2.1, by replacing the acceleration in Eq. 2.3, one gets:

$$\forall q \in [\![1, \mathrm{N}_p]\!], \quad \partial_t f_{q,\mathrm{DPS}} + \boldsymbol{v} \cdot \nabla_{\boldsymbol{x}} \left(f_{q,\mathrm{DPS}} \right) + \frac{1}{\tau_p} \nabla_{\boldsymbol{v}} \cdot \Big(\left(\boldsymbol{u}_f \left(t, \boldsymbol{x} \right) - \boldsymbol{v} \right) f_{q,\mathrm{DPS}} \Big) = 0. \tag{2.4}$$

When considering several particles, one has to compute the evolution of the whole family $\left(f_{q,\mathrm{DPS}}\right)_{q \in [\![1,\mathrm{N}_p]\!]}$.

In the one-way coupled context, when the particles do not interact between each other, the *normalised counting measure* (NCM) (Baddeley (2007)):

$$f_{\mathrm{NCM}} = \frac{1}{\mathrm{N}_p} \sum_{q=1}^{\mathrm{N}_p} \delta_{\boldsymbol{x}_q} \delta_{\boldsymbol{v}_q} \tag{2.5}$$

contains as much information as the whole family $\left(f_{q,\mathrm{DPS}}\right)_{q \in [\![1,\mathrm{N}_p]\!]}$ but in only 6 dimensions. f_{NCM} follows the same equation as $f_{q,\mathrm{DPS}}$:

$$\partial_t f_{\mathrm{NCM}} + \boldsymbol{v} \cdot \nabla_{\boldsymbol{x}} \left(f_{\mathrm{NCM}} \right) + \frac{1}{\tau_p} \nabla_{\boldsymbol{v}} \cdot \Big(\left(\boldsymbol{u}_f \left(t, \boldsymbol{x} \right) - \boldsymbol{v} \right) f_{\mathrm{NCM}} \Big) = 0. \tag{2.6}$$

The computation of the normalised counting measure is often done in a Lagrangian manner (see for instance the work presented by Zamansky, Coletti, Massot, and Mani (2014)[2]).

2.2 Dynamics of point-particles in a turbulent flow

In this section, we focus on the dynamics of inertial particle in a turbulent flow.

2.2.1 Non-dimensional numbers

In the context of two-way coupling derived by Letournel, Laurent, Massot, and Vié (2020)), the parameters of the system are:

- for the gas phase, the scale of turbulence can be parametrised by the small scale, unambiguously the Kolmogorov length scale η. We also need a turbulent intensity through the turbulent velocity $\boldsymbol{u}_f$, the molecular viscosity ν_f and the fluid density ρ_f;
- for the disperse phase, the first parameter is the relaxation time τ_p. A stated in Letournel, Laurent, Massot, and Vié (2020), we also need the particle mass m_p and a number density n_0.

In total, we have 7 parameters and 3 fundamental units (mass, time and space). We thus end up with 4 non-dimensional parameters:

- *The turbulent Reynolds number* $\mathrm{Re}_t = \frac{\boldsymbol{u}_f L_t}{\nu}$: it quantifies the intensity of turbulence, but also the scale separation between the small and large ones.
- *The Stokes number based on the Kolmogorov scale* $\mathrm{St}_\eta = \frac{\tau_p}{\tau_\eta}$, which quantifies the ability of particles to react to small scale fluctuations.
- *the mass loading* ϕ, which is a first driver of the impact of the particles on the gaseous carrier phase.
- *the dimensionless particle number* $n_\eta = n_0\eta^3$, which is the number of particle in a small eddy of the turbulence, which is a second driver of the impact of the particles on the gaseous carrier phase.

In the present work, we will focus on regimes for which the particles do not affect the gas phase[3]. Therefore we are only concerned by the effect of Stokes number on particle dynamics.

[2] This work has been performed with a source term from the particles to the fluid. In order to ensure convergence, the punctual source term has been convoluted by a truncated Gaussian kernel before being applied to the fluid phase.

[3] The reader can refer to Letournel, Laurent, Massot, and Vié (2020), Letournel (2022) and references therein for specific studies with two-way coupling.

2.2.2 Segregation and uncorrelated motion

In the one-way coupled case, the only control parameter of the particles is their relaxation time, as the others control the retro-action of the disperse phase on the gas phase. The relaxation time is closely associated to the Stokes number St_η. In the following we detail the impact of the Stokes number by going from the tracer limit to the infinite Stokes number limit.

In the case where τ_p, is close to 0, the Stokes number is also close to 0. The particles closely follow the gas phase. In this situation the behaviour of the particles is similar to the behaviour of fluid parcels. For instance, they share the same dispersion properties as the fluid parcels.

For $0 < \mathrm{St}_\eta < 1$, the particle trajectories tend to depart from fluid particle trajectories. In this situation, the particles are slowly ejected from vortices because of their inertia. However, they are not able to cross the low-vorticity high-strain-rate zones that separates the vortices. Therefore, they accumulate in these separating regions, generating the so-called segregation or preferential concentration (Eaton and Fessler (1994)). In Fig. 2.1, examples of the segregation obtained in the case of frozen turbulence illustrates this effect (de Chaisemartin (2009)).

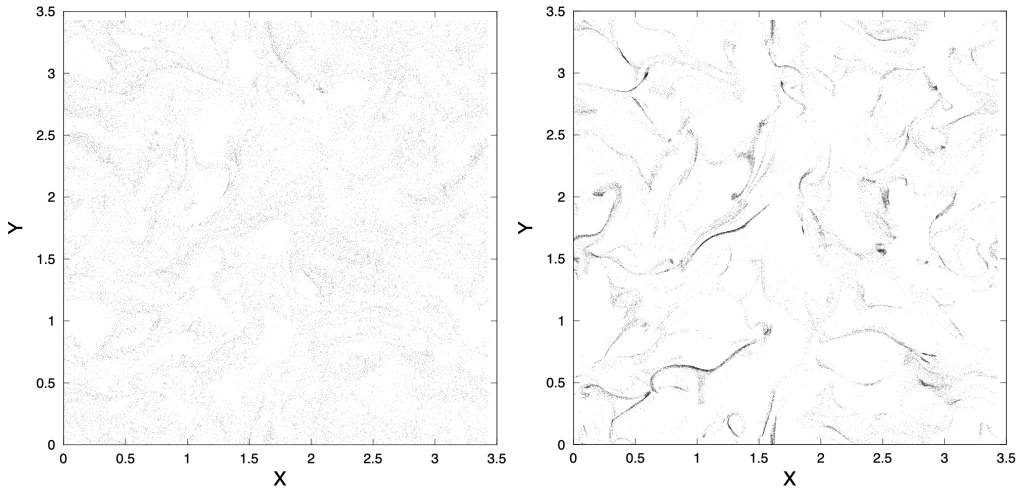

Figure 2.1. 3D frozen homogeneous isotropic turbulence: position of particles for a mid-plane for $\mathrm{St}_\eta = 0.17$ (left) and $\mathrm{St}_\eta = 1.05$ (right).

This effect of preferential concentration is maximum at $\mathrm{St}_\eta \approx 1$. When this limit is crossed, particles are able to cross the high-strain-rate regions. Because particles do not have to accumulate in specific regions anymore, preferential concentration tends to decrease. As the Stokes number increases, the particle velocity is less and less correlated to the local velocity of the carrier phase. Actually, when $\mathrm{St}_\eta > 1$, particles trajectories become very different than fluid parcels trajectories. Inertial particles can come close to

other particles that originate from different vortices and may have had a significantly different trajectory in the flow. In a probabilistic context such as the MEF (See Sec. 2.3), this leads to an increase of the local particle velocity variance or uncorrelated motion (Février, Simonin, and Squires (2005), Sabat, Vié, Larat, and Massot (2019)). In the limit of an infinite Stokes number, the particle energy is mainly given by the uncorrelated motion.

If we look at inertia from a dynamical system perspective, to the difference of fluid particles, which are fully determined with their position at a given time, inertial particles are defined at any time t by both their position and velocity. Therefore, phase-space for inertial particles has twice the dimensions of phase-space for fluid particles. Both fluid and inertial particles are modelled as a deterministic dynamical system. Therefore, for both, their trajectories cannot cross in phase space. This means that fluid particles cannot cross in physical space. However, inertial particles can because their phase space includes velocity. Therefore, they can be at the same point in space with different velocities and still not cross in phase space.

2.3 Average mesoscopic approach

When one is not interested in a unique realisation of the disperse phase, but in converged statistics, he can rely on an average mesoscopic approach which offers a statistical description of the particles. This strategy is of particular interest when the particle concentration is high and tracking individual particles is expensive. In the following, we detail the basis of a average mesoscopic approach. The interested reader can also refer to the work of Subramaniam (2013). The principle of this approach is to compute the evolution of the law of the particles. When this law is a function, it is called a Probability Density Function (PDF). The associated evolution equation is called a Population Balance Equation (PBE).

2.3.1 Probability space

The two-phase flow system is considered as a deterministic dynamical system. For the fluid, we have already defined in Sec. 1.1:

- phase space A_f, which corresponds to the set of all the different fluids possible,
- the fluids $\boldsymbol{u}_f(t,.)$, which belong to A_f,
- $\mathcal{A}_f$, the set of subsets of A_f,
- and the elements of $\mathcal{A}_f$: $\boldsymbol{a}_f$. The variable $\boldsymbol{a}_f$ corresponds to an ensemble of possible fluids.

By analogy, for each particle $q \in [\![1, \mathrm{N}_p]\!]$ we name:

- A_p the phase space of each particle,
- $a_p^{(q)}(t) = \left(\boldsymbol{x}_p^{(q)}(t), \boldsymbol{v}_p^{(q)}(t)\right)$ the state variable at time t,
- $\mathcal{A}_p$ the set of subsets of A_p,
- and $\boldsymbol{a}_p^{(q)} \in \mathcal{A}_p$ an ensemble of particle positions.

Similarly to single phase flows (Sec. 1.2.3), a probability space is introduced in the system with the initial conditions. We consider that the initial conditions of the deterministic dynamical system are random variables of a probability space $(\Omega, \mathcal{E}, \mathbb{P})$. In our case, initial conditions are given by:

- the intial fluid velocity field $\boldsymbol{u}_{f,0} \in A_f$,
- the initial positions and velocities of the N_p particles:
  - $\left(\boldsymbol{x}_{p,0}^{(q)}, \boldsymbol{v}_{p,0}^{(q)}\right) \in A_p$, $q \in [\![1, \mathrm{N}_p]\!]$.

Therefore, the initial conditions are defined in A, with $A = A_f \times A_p^{\mathrm{N}_p}$.
We name Φ the deterministic flow of the dynamical system given by Navier-Stokes equations (Eq. 1.2) and the evolutions equations of the particles (Eq. 2.1).
For any initial point in phase space $s_0 \in A$, $\Phi_t(s_0)$ is the state of the system after some time $t \in \mathbb{R}^+$. Assuming that $\forall t \in \mathbb{R}^+$, Φ_t is measurable, we naturally extend set of random variables to any time $t \in \mathbb{R}^+$, by considering the probability measure:

$$\mathbb{P}_t[s_t] = \mathbb{P}\left[\Phi_t^{\leftarrow}(s_t)\right], \tag{2.7}$$

where $\Phi_t^{\leftarrow}(s_t) = \{s_0 \,|\Phi_t(s_0) = s_t\}$.

2.3.2 Probability Density Functions

In the following, we consider a series of probability density functions (PDF) that are of interest for two-phase flows, based on different measures on the probability space. It is first possible to consider the joint distribution of the particles and the fluid:

$$\begin{aligned}
&\forall t \in \mathbb{R}^+, \quad \forall \boldsymbol{a}_p^{(q)} \in \mathcal{A}_p \text{ with } q \in 1 \dots \mathrm{N}_p, \quad \forall \boldsymbol{a}_f \in \mathcal{A}_f, \\
&\int_{\boldsymbol{a}_p^{(1)} \cup \dots \cup \boldsymbol{a}_p^{(\mathrm{N}_p)} \cup \boldsymbol{a}_f} f_{\mathrm{all}}\left(t, a_p^{(1)}, \dots, a_p^{(\mathrm{N}_p)}, \boldsymbol{u}_f(t,.)\right) \mathrm{d}a_p^{(1)} \dots \mathrm{d}a_p^{(\mathrm{N}_p)} \mathrm{d}\boldsymbol{u}_f = \\
&\qquad\qquad \mathbb{P}_t\left[a_p^{(q)} \in \boldsymbol{a}_p^{(q)} \text{ with } q \in 1 \dots \mathrm{N}_p, \boldsymbol{u}_f(t,.) \in \boldsymbol{a}_f\right].
\end{aligned} \tag{2.8}$$

This distribution f_{all} gives the probability of having each particle at a given position in their phase space, with a given state for the whole fluid. Such distribution has too high a dimensionality, we therefore want to reduce it. We treat by two means: averaging over the particle space, or averaging over the fluid space

2.3.2.1 Fluid space reduction

Let us start by considering reductions along the fluid space. The conditional distribution on a subset $\boldsymbol{a}_f$ of the set of fluids $\mathcal{A}_f$ is given by:

$$\begin{aligned}
&f_{\mathrm{all},\boldsymbol{a}_f}\left(t, a_p^{(1)}, \dots, a_p^{(\mathrm{N}_p)}\right) = \\
&\qquad \frac{\displaystyle\int_{\boldsymbol{a}_f} f_{\mathrm{all}}\left(t, a_p^{(1)}, \dots, a_p^{(\mathrm{N}_p)}, \boldsymbol{u}_f(t,.)\right) \mathrm{d}a_p^{(1)} \dots \mathrm{d}a_p^{(\mathrm{N}_p)} \mathrm{d}\boldsymbol{u}_f}{\displaystyle\int_{A_p^{(1)} \cup \dots \cup A_p^{(\mathrm{N}_p)} \cup \boldsymbol{a}_f} f_{\mathrm{all}}\left(t, a_p^{(1)}, \dots, a_p^{(\mathrm{N}_p)}, \boldsymbol{u}_f(t,.)\right) \mathrm{d}a_p^{(1)} \dots \mathrm{d}a_p^{(\mathrm{N}_p)} \mathrm{d}\boldsymbol{u}_f}.
\end{aligned} \tag{2.9}$$

Specific cases are given by:

- The marginal distribution of the particles f_{all,A_f}. This distribution is obtained by integrating the joint distribution of the particles and the fluid over the whole fluid space.
- The conditional distribution on one fluid $\boldsymbol{u}_f$: $f_{\text{all},\boldsymbol{u}_f}$. Integrating this distribution gives the probability of having all particles at a given state for a unique fluid realization.

2.3.2.2 Particle space reduction

All these distributions consider the whole setting of particles. Let us now try to reduce the dimensionality of the particle space part. In this section, let us consider a fixed subset a_f of the set of fluids $\mathcal{A}_f$.
The marginal distribution of one particle $q \in [\![1, \mathrm{N}_p]\!]$ is given by:

$$f_{a_f}^{(q)}\left(t, a_p^{(q)}\right) = \int_{\bigcup_{d\neq q} A_p^{(d)}} f_{\text{all},a_f}\left(t, a_p^{(1)}, \ldots, a_p^{(\mathrm{N}_p)}\right) \mathrm{d}a_p^{(1)} \ldots \mathrm{d}a_p^{(\mathrm{N}_p)}. \tag{2.10}$$

Computing the distribution of each particle is costly. Therefore, it is customary to consider the average distribution over the particles:

$$f_{a_f}\left(t, a_p\right) = \frac{1}{\mathrm{N}_p} \sum_{q=1}^{\mathrm{N}_p} f_{a_f}^{(q)}\left(t, a_p^{(q)}\right). \tag{2.11}$$

2.3.2.3 Exchangeable particles

Definition 17. We say that particles are *exchangeable* when the joint distribution of a permuted sequence is equal to the distribution of the original sequence:

$$\begin{aligned} &\forall t \in \mathbb{R}^+, \quad \forall a_p^{(q)} \in \mathcal{A}_p \text{ with } q \in 1 \ldots \mathrm{N}_p, \\ &\int_{a_p^{(1)} \cup \cdots \cup a_p^{(\mathrm{N}_p)}} f_{\text{all},a_f}\left(t, a_p^{\sigma(1)}, \ldots, a_p^{\sigma(\mathrm{N}_p)}\right) \mathrm{d}a_p^{(1)} \ldots \mathrm{d}a_p^{(\mathrm{N}_p)} = \\ &\qquad\qquad \int_{a_p^{(1)} \cup \cdots \cup a_p^{(\mathrm{N}_p)}} f_{\text{all},a_f}\left(t, a_p^{(1)}, \ldots, a_p^{(\mathrm{N}_p)}\right) \mathrm{d}a_p^{(1)} \ldots \mathrm{d}a_p^{(\mathrm{N}_p)} \end{aligned} \tag{2.12}$$

for all possible permutations of the indices σ.

If we consider that particles are exchangeable, the expression of f_{a_f} simplifies to:

$$f_{a_f}\left(t, a_p\right) = f_{a_f}^{(q)}\left(t, a_p^{(q)}\right), \tag{2.13}$$

for any $q \in [\![1, \mathrm{N}_p]\!]$. In this case, f_{a_f} does not only give the average distribution of the particles, but the actual distribution of each particles.

2.3.2.4 Exchangeable and independent particles

Definition 18. We say that particles are *independent* when the joint distribution is equal to the product of the marginals:

$$\int_{a_p^{(1)}\cup\cdots\cup a_p^{(\mathrm{N}_p)}} f_{\mathrm{all},a_f}\left(t,a_p^{(1)},\ldots,a_p^{(\mathrm{N}_p)}\right)\mathrm{d}a_p^{(1)}\ldots\mathrm{d}a_p^{(\mathrm{N}_p)} = \int_{a_p^{(1)}\cup\cdots\cup a_p^{(\mathrm{N}_p)}} f_{a_f}^{(1)}\left(t,a_p^{(1)}\right)\ldots f_{a_f}^{(\mathrm{N}_p)}\left(t,a_p^{(\mathrm{N}_p)}\right)\mathrm{d}a_p^{(1)}\ldots\mathrm{d}a_p^{(\mathrm{N}_p)}. \quad (2.14)$$

In the specific case where particles are independent, we can represent the full joint distribution of the particles by the product of the single-particle distributions:

$$f_{\mathrm{all},a_f}\left(t,a_p^{(1)},\ldots,a_p^{(\mathrm{N}_p)}\right) = \bigotimes_{q=1}^{\mathrm{N}_p} f_{a_f}^{(q)}\left(t,a_p^{(q)}\right). \quad (2.15)$$

In the specific case where particles are exchangeable and independent, we can represent the full joint distribution of the particles by the sole single-particle distribution:

$$f_{\mathrm{all},a_f}\left(t,a_p^{(1)},\ldots,a_p^{(\mathrm{N}_p)}\right) = \left[f_{a_f}\left(t,a_p^{(q)}\right)\right]^{\mathrm{N}_p}. \quad (2.16)$$

In this case, the distribution f_{a_f} is enough to give the full joint distribution of the particles.

2.3.3 Mesoscopic Eulerian Formalism

Looking at the reduction of the distribution we have presented f_{a_f}, let us discuss the consequence of these choices. First let us dive into the question of the fluid space reduction: average over all fluid realisation $\boldsymbol{a}_f = A_f$ or conditional on one fluid $\boldsymbol{a}_f = \boldsymbol{u}_f$. Choosing $\boldsymbol{a}_f = A_f$ has the advantage of giving the full statistics of the disperse phase, which is the first reason why we are interested in statistical methods. However there is a drawback to this method: such a distribution leads to a formalism in which the dynamics of the carrier phase will be seen as an ensemble average, thus loosing every realization details. These kind of details will be discussed in the next chapter, but for now, it must be noted that, as the particle dynamics is mainly driven by the carrier force aerodynamic coupling, the most detail in the flow we have, the less effort we have to do in the modelling of the disperse phase.
Therefore, it appears of interest to work with the distribution conditioned to one gas phase realisation $\boldsymbol{u}_f$. This is what the Mesoscopic Eulerian Formalism (MEF) of Février, Simonin, and Squires (2005) is suggesting to do.

Definition 19. The *Mesoscopic Eulerian Formalism* (MEF), as derived in Février, Simonin, and Squires (2005), considers the specific cases of f_{a_f}, where $\boldsymbol{a_f}$ is a fluid $\boldsymbol{u}_f$.

Given one fluid realization $\boldsymbol{u}_f \in A_f$, when the evolution of the fluid is not impacted by the disperse phase, the MEF distribution $f_{\boldsymbol{u}_f}$ follows the same equation as (Eq. 2.3):

$$\partial_t f_{\boldsymbol{u}_f} + \boldsymbol{v} \cdot \nabla_{\boldsymbol{x}} \left(f_{\boldsymbol{u}_f} \right) + \frac{1}{\tau_p} \nabla_{\boldsymbol{v}} \cdot \left(\left(\boldsymbol{u}_f \left(t, \boldsymbol{x} \right) - \boldsymbol{v} \right) f_{\boldsymbol{u}_f} \right) = 0. \tag{2.17}$$

This is an equation in six dimensions which is quite costly to compute on a mesh. Computation of $f_{\boldsymbol{u}_f}$ is usually done with Monte-Carlo simulations. Contrarily to a fluid flow, where one can define a Knudsen number, point particles considered here do not interact between themselves, with collisions for instance. Thus, $f_{\boldsymbol{u}_f}$ is a distribution and can still be a Dirac or a sum of Dirac distributions.

2.4 Macroscopic approaches

In the previously introduced statistical mesoscopic approach, the ending point is a PBE that describes the evolution of the PDF. To solve this PBE, three methods can be envisaged:

- *Direct resolution*: the equation is discretized in the phase space. This method cannot be envisaged for simulations that are multidimensional in space, as at least 6 dimensions must be discretized for the sole space-velocity phase space in 3 physical dimensions. It is only possible for a reduced number of dimensions (1 or 2).
- *Lagrangian sampling*: the PDF is computed by sampling the PDF and tracking these elements using a Lagrangian techniques. Using such strategy is going back to the initial problem of statistical convergence.
- *Macroscopic Moment methods*: instead of tracking the PDF itself, we look at its moments. By doing so, we can solve quantities that leave in the physical space only, thus being easily discretized by classical methods such as finite volume. This is the method that is described here.

Let us first define the moments $\mathcal{M}_k(t, \boldsymbol{x})$ of order k of the PDF (we focus here on the velocity space, but this can be extended to any other state variable of a particle):

$$\mathcal{M}_k(t, \boldsymbol{x}) = \int_{\mathbb{R}^3} \left(\otimes^k \boldsymbol{v} \right) f \left(t, \boldsymbol{x}, \boldsymbol{v} \right) \mathrm{d}\boldsymbol{v}, \tag{2.18}$$

with $\otimes^k$ the tensorial product of order k and The similar notation for the terms $\mathcal{M}_k$ should not be misleading as to their different respective dimensions (the term $\mathcal{M}_k$ is a tensor of order k). A physical insight can be given to moments: the zeroth order moment corresponds to the particle total number density, the first order moment to the

momentum (if multiplied by particle individual mass). It is possible to get an equation for the moments from Eq. 2.17 by integration over the phase space:

$$\partial_t \mathcal{M}_k + \nabla_{\boldsymbol{x}} \cdot \mathcal{M}_{k+1} - \frac{k}{\tau_p} \left(\mathcal{M}_{k-1} \odot \boldsymbol{u}_f \right) = 0, \qquad k \in \mathbb{N}. \tag{2.19}$$

with $\odot$ the symmetric tensor product (which gives to the symmetric part of a normal tensor product). In this equation, we see that for a moment of order k, we need a moment of order $k+1$. So whatever the moment set we solve, we always need an additional moment. Unfortunately, for a given finite moment vector, there is an infinity of possible PDFs. Therefore we need to make some assumptions to close the evolution equations of the moments. Furthermore, such moment system requires attention in terms of numerical, as we need to solve a system of PDEs. The interested reader could refer to Kaufmann, Moreau, Simonin, and Helie (2008); Laurent, Vié, Chalons, Fox, and Massot (2013); Masi and Simonin (2014); Sabat (2016); Sabat, Vié, Larat, and Massot (2019) and references therein.

Highlights and conclusions

- The reference point-particle model of this thesis has been presented, which is limited to Stokes drag.
- Main physics of particles in turbulent flows has been identified.
- The statistical mesoscopic viewpoint has been detailed, with an emphasis on the Mesoscopic Eulerian Formalism (MEF).
- Macroscopic moment methods have been finally briefly presented.

Chapter 3

Reduction strategies for turbulent flows

In this chapter, we present the reduction techniques that are used to make reachable the computation of high-Reynolds-number flows. We first show how the high-dimensionality of turbulent flows makes their computation over-expensive even with the most powerful supercomputer. We then present reduction techniques classically based either on averaging or filtering. We expand the explanations about the Large Eddy Simulation at the core of the present work.

3.1 The high-dimensionality of turbulent flows

> *[...] inasmuch as those who do not understand the nature of things do not verify phenomena in any way, but merely imagine them after a fashion, and mistake their imagination for understanding, such persons firmly believe that there is an order in things, being really ignorant both of things and their own nature. When phenomena are of such a kind, that the impression they make on our senses requires little effort of imagination, and can consequently be easily remembered, we say that they are well-ordered ; if the contrary, that they are ill-ordered or confused. Spinoza (1842), Part 1*

Although turbulent flows have a finite number of degrees of freedom (Temam (2001), p.150), the way they are currently described with the Navier-Stokes equations requires a very large number of dimensions (see Pope (2000), Chap. 9.1.2 for an estimation of the numerical cost of a turbulence computation). High dimensional problems can be investigated with the recent development of computers. However, even with the current computational power available (Fig. 3.1), direct numerical simulation (DNS) of the Navier-Stokes equations for industrial applications is not reachable even for the most powerful supercomputers.
Our current representation of turbulence is too complex to be computed as such. But as Spinoza (1842) puts it, a reality is only as complex as the representation one has of it.

Therefore, this section is dedicated to understanding some classical strategies devised to get some simpler descriptions of turbulent flows, which are more easily computed.
With the Navier-Stokes equations, the fluid is described by its velocity and pressure fields. These fields have a low regularity, with features over a very wide range of scales. This gives this problem a very high dimensionality when represented with conventional quadratures techniques. The numerical computation of these low regularity fields on a mesh requires a large number of cells and makes the computation very expensive.
To get an idea, the left hand-side of Fig. 3.1 represents the amount of time required to compute homogeneous isotropic turbulence (HIT) with $\mathrm{Re}_L = 10^7$ ($\mathrm{Re}_\lambda = 8000$) according to years. An example of a HIT simulation is presented in Fig. 3.2. We have previously seen the Reynolds number as an indicator of the state of the flow -laminar or turbulent, see Sec. 1.2.1-, but it also gives an estimate of the physical dimensionality of the flow (Temam (2001), Chap. 3) and of the numerical cost of the problem (Pope (2000), Sec. 9.1.2)). It is possible to see that the best computers become exponentially faster with time. However, the time deemed reasonable even for research remain out of reach for the time being.
The right hand-side of Fig. 3.1 represents differently the same dilemma. It shows the time needed for the best computers in the world to perform increasingly larger turbulence computations. We see, even to their fullest power, the biggest computers are very limited in the range of turbulence cases they are able to tackle.

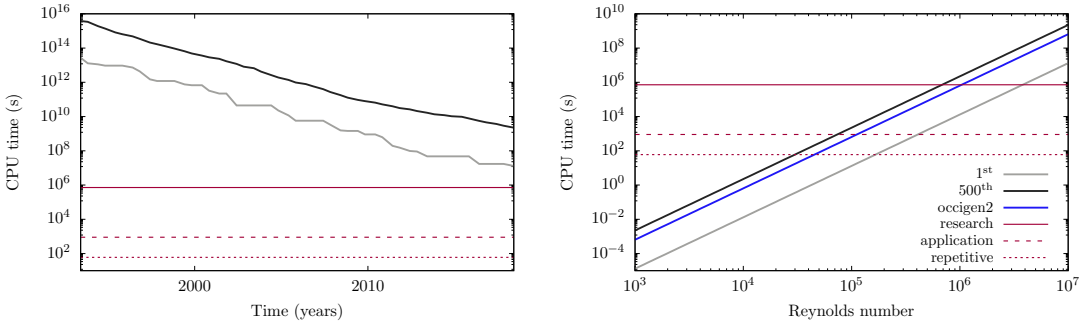

Figure 3.1. On the left, evolution of CPU time (s) with years to compute homogeneous isotropic turbulence at $\mathrm{Re}_L = 10^7$ or $\mathrm{Re}_\lambda = 8000$.
On the right, evolution of CPU time (s) in mai 2018 to compute homogeneous isotropic turbulence according to the Reynolds number.
These figures are drawn following Pope (2000), Eq. 9.12 updated with data from https:www.top500.org
. Times deemed acceptables for research (200 hours), applications (15 minutes) and repetitive computations (1 minute) according to Peterson, Kim, Holst, Deiwert, Cooper, Watson, and Bailey (1989) are indicated as a reference.

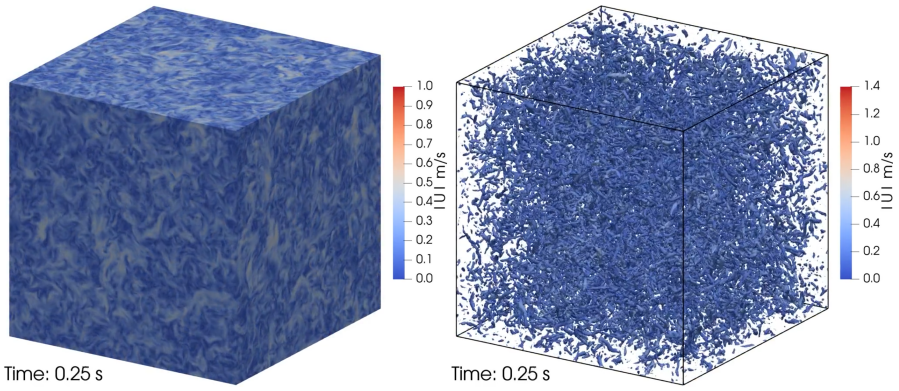

Figure 3.2. Homogeneous Isotropic Turbulence simulated the code OpenFoam (OpenFoam (2008)): velocity field (left) and isosurfaces of Q-criterion identifying the turbulence structure (right).

3.2 Dimensionality reductions for turbulent flows

In order to lower the dimensionality (and thus the numerical cost) of the problem, one strategy is to derive alternate fields with more regularity than the original ones. This is traditionally attempted with operations implying different levels of filtering and/or averaging. With respect to the reference flow described by Navier-Stokes equations, these alternate fields are designated here as a reduced description of the fluid. Standard reduced descriptions do not usually have in mind coupled two-phase flow cases. This is why our challenge is to find a way to create a description of the fluid flow which has a lower dimensionality and is compatible with coupled two-phase scenarii. The difficulty is to keep all the characteristics of the system *essential* for describing its physics. The term *essential* is emphasized because it is function of the properties of the system of interest (existence of symmetries in the geometry, regime of operation, evolution of the energy of the system for instance) and of what is expected as an output of the simulation (time averaged data or time resolved data for instance).
In this following, we present two classical reduction strategies for turbulent flows: Reynolds averaging and Large Eddy Simulation (LES). For the interested reader, Sagaut (2006) is a reference of choice on the matter.

3.2.1 Reynolds averaging

Reynolds averaging is the decomposition of quantities between a mean and a fluctuating part:

$$\boldsymbol{u}_f = G_{\mathrm{Re}}\left(\boldsymbol{u}_f\right) + \boldsymbol{u}'_f, \tag{3.1}$$

with G_{Re} a Reynolds operator, $\boldsymbol{u}_f$ a quantity of interest, and $\boldsymbol{u}'_f = \boldsymbol{u}_f - G_{\mathrm{Re}}\left(\boldsymbol{u}_f\right)$ its fluctuating part.

Definition 20. A *Reynolds operator* G_{Re} is an averaging operator with the following properties:

- G_{Re} is linear.
- $G_{\mathrm{Re}}\left(G_{\mathrm{Re}}\left(\boldsymbol{u}_1\right) \times \boldsymbol{u}_2\right) = G_{\mathrm{Re}}\left(\boldsymbol{u}_1\right) \times G_{\mathrm{Re}}\left(\boldsymbol{u}_2\right)$, with $\boldsymbol{u}_1$ and $\boldsymbol{u}_2$ two quantities of interest.
- G_{Re} commutes with partial derivatives in space and time.

This set of properties allows Reynolds operators to work well with the Navier-Stokes equations. Reynolds decomposition can be done in different spaces. Classical ones are:

- temporal when G_{Re} is a time average,
- or statistical when G_{Re} is the expectation operator.

In the context of this work, we consider the statistical space as being the most general case. Therefore, in the following, we will simply name the equations obtained by statistically averaging Navier-Stokes equations: Reynolds Averaged Navier-Stokes (RANS) (Heinz (2003), Sagaut (2006), Chaouat (2017)). However, when the flow regime is permanent, owing to ergodicity, Reynolds averaged Navier-Stokes equations are identical to time averaged Navier-Stokes equations.
Averaging is interesting because it is a convex operation which smooths out quantities, diminishing the amount of detail and information, thus making computations less expensive. However, it does not offer any control on the resulting regularity of the solution (Pope (2010)). For instance, very fine structures which are constantly present in every flow realization, such as boundary layers, are preserved by averaging. This difficulty is adressed by the Large Eddy Simulation strategy that we present in the next section.

3.2.2 Coarsening - Large Eddy Simulation

RANS is an interesting reduction technique. However, it does not offer an explicit control on the regularisation of the flow field (and thus its associated cost). One of the most straightforward strategy to deal with this difficulty is to start the reduction process by specifying the level of regularization wanted. The method is named Large-Eddy Simulation (LES) in this work.
In LES, the regularisation of the flow field is traditionally perceived as a convolution of the field by a given kernel (Eq. 3.2, Pope (2000), 1.3.2).

$$G_{\mathrm{LES}}(\bullet) := \Delta * \bullet, \tag{3.2}$$

with G_{LES} the reduction operator, Δ a normalised convolution kernel and $*$ the convolution operator. Usually, in physical space, the kernel is either a boxcar, a gaussian or a cardinal sine. They each have their pros and cons:

- The boxcar and the gaussian do not remove all the high frequencies in the field. Thus they do not really regularize the field. Because they preserve some high frequencies, they can lead to aliasing (frequency folding) when represented on a low resolution mesh.

- The cardinal sine acts as a sharp spectral cut-off in wavenumber space. Thus it is effective at regularising the flow. However, it is not local (thus difficult to envision in realistic wall bounded flows for instance) and not positive (a positive value such a density is not guaranteed to preserve its positivity with this kernel).

A detailed discussion about filtering can be found in Pope (2000), Sec. 13.2.

3.2.3 RANS versus LES

To get an idea of the impact of the reduction strategy on the resulting flow, Fig. 3.3 compares three simulations: a DNS (a), an LES (b) and a RANS simulation (c). Compared to DNS, all reduced simulations imply a lost of fine structures. However, comparing RANS to LES, we obviously see that intermediate scale features are kept in the LES, along with an unsteady trend, while the RANS simulation is highly diffuse and in this specific case will not present any unsteadiness.
However, it has to be kept in mind that resolving finer scales and capturing unsteadiness will necessary come with an increased computational cost: while RANS simulations can in some cases be envisaged on a desktop computer and can make use of physical space reductions such as planar symmetry or axisymmetry, LES requires supercomputing because it cannot use any physical space reduction, as the fine scales do not present any symmetry instantaneously, and requires a fine time-space representation.
At this point, it is worth remembering the context of this work: aiming at high-fidelity simulations. For such a perspective, it seems obvious that the preferred strategy would be to go for LES, as it will give us high-resolution statistics along with a way of controlling the level of precision through the adjustment of the filtering length scale.

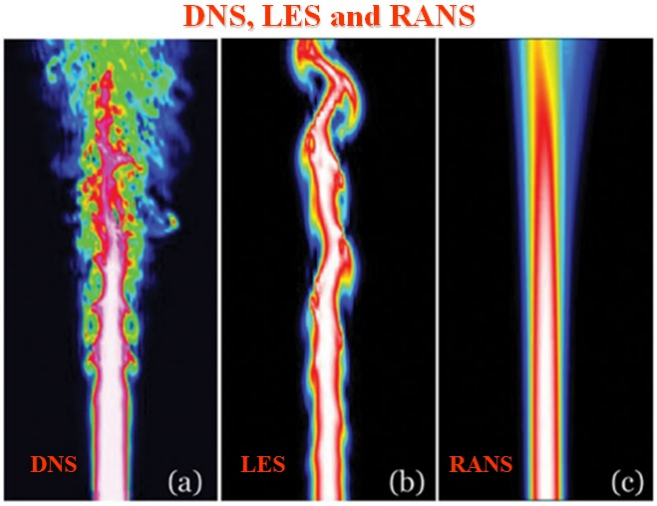

Figure 3.3. Comparison of a DNS (a), LES (b) and RANS (c) simulation of a jet flow (Italian Agency For New Energy Technologies (2006)).

3.3 Equation of the reduced variables and closures

3.3.1 Equation of the reduced variables

In order to compute the evolution of the reduced variables presented above (Sec. 3.2), a classical strategy is to apply the reduction operator directly to the evolution equations of the original variables (Eq. 1.2).
A usual reduction operator G, such as the operator used for RANS: G_{Re}, or the operator used for LES: G_{LES}, is usually assumed to behave like a Reynolds operator (3.2.1) when it comes to commutation with derivatives. Thus, when applied to Navier-Stokes equations, G gives the equalities:

$$\nabla_{\boldsymbol{x}} \cdot G\left(\boldsymbol{u}_f\right) = 0, \tag{3.3a}$$

$$\partial_t G\left(\boldsymbol{u}_f\right) + G\left(\left(\boldsymbol{u}_f \cdot \nabla_{\boldsymbol{x}}\right) \boldsymbol{u}_f\right) = -\frac{1}{\rho_f} \nabla_{\boldsymbol{x}} G\left(p_f\right) + \nu_f . \Delta_{\boldsymbol{x}} G\left(\boldsymbol{u}_f\right). \tag{3.3b}$$

Eq. 3.3 is only the filtered version of Eq. 1.2. What is desired is an evolution equation for the reduced variable $\overline{\boldsymbol{u}}_f = G\left(\boldsymbol{u}_f\right)$. However, starting with Eq. 3.3 and changing variables, we only get the set of unclosed equations Eq. 3.4.

$$\nabla_{\boldsymbol{x}} \cdot \overline{\boldsymbol{u}}_f = 0, \tag{3.4a}$$

$$\partial_t \overline{\boldsymbol{u}}_f + G\left(\left(\boldsymbol{u}_f \cdot \nabla_{\boldsymbol{x}}\right) \boldsymbol{u}_f\right) = -\frac{1}{\rho_f} \nabla_{\boldsymbol{x}} G\left(p_f\right) + \nu_f . \Delta_{\boldsymbol{x}} \overline{\boldsymbol{u}}_f. \tag{3.4b}$$

With the hypothesis taken here for G, the difficult terms remaining in Eq. 3.4 to get a closed equation are the non-linear term $G\left(\left(\boldsymbol{u}_f \cdot \nabla_{\boldsymbol{x}}\right) \boldsymbol{u}_f\right)$ and $G\left(p_f\right)$. In the present context of incompressible flow, closing $G\left(p_f\right)$ is not an issue, as this term only appears as a Lagrangian multiplier that is here to ensure the mass conservation equation. Such term is however of great importance for compressible flows (Garnier, Adams, and Sagaut (2009)).
On the other hand, the inertial term $G\left(\left(\boldsymbol{u}_f \cdot \nabla_{\boldsymbol{x}}\right) \boldsymbol{u}_f\right)$ requires much more attention. Actually, this is this term that contains the non-linearities of the Navier-Stokes equations. It is usually expanded in the form

$$G\left(\left(\boldsymbol{u}_f \cdot \nabla_{\boldsymbol{x}}\right) \boldsymbol{u}_f\right) = \left(\overline{\boldsymbol{u}}_f \cdot \nabla_{\boldsymbol{x}}\right) \overline{\boldsymbol{u}}_f + R\left(\boldsymbol{u}_f\right),$$

where $R\left(\boldsymbol{u}_f\right)$ has to be modelled.
Expressing $R\left(\boldsymbol{u}_f\right)$ in terms of $\overline{\boldsymbol{u}}_f$ is the essence of the closure problem and is discussed in the next section.

3.3.2 Closures for LES models

A very good account on classical closures techniques is presented by Pope (2000), Part II and in Sagaut (2006). They can be roughly sorted in two categories according to the way they are derived.

- **Structural models**, usually start from the exact unclosed expression of the term to model. Each unknown variable is then approximated in terms of the resolved variables (through asymptotic expansions for instance). The advantage of starting from the exact unclosed expression of the term to model is that the resulting closure often shares a similar structure with the exact term.
- **Functional models**, usually start from the expected dynamics of the system and its interactions with the unclosed term. They propose a substitute for the implicit term which has a similar effect on the resolved physics. The advantage of functional models is that they are specifically designed to reproduce the same effect as the exact term on the resolved physic. The disadvantage of functional models is that their expression is not directly derived from an approximation of the expression of the exact term. Therefore, there is not direct connection between the expression of the closure term and the expression of the exact term. In these circumstances, it is may be difficult to guarantee the good behaviour of the closure for the full range of different dynamics the system can experience.

Despite its limitations, the functional strategy is the most widely used in industrial applications, the most famous model being the one of Smagorinsky (1963):

$$R\left(\boldsymbol{u}_f\right) = 2\nu_{\mathrm{SGS}} S_{ij} \tag{3.5}$$

where S_{ij} is the resolved deformation tensor and ν_{SGS} is the turbulent viscosity:

$$\nu_{\mathrm{SGS}} = \left(\mathrm{C}_S \Delta\right)^2 \left|S_{ij}\right|^{-1/2} \tag{3.6}$$

where Δ is the filter scale and C_S the Smagorinsky constant usually taken as $C_S = 0.18$. This model is based on the eddy-dissipation concept, in which the effect of sub-grid scale is expected to be dissipative. This is a key trend in eddy-dissipation model which makes them very powerful for complex simulations as the physical closure helps to stabilize the computation. This model structure is shared with several models in the literature, see for instance Nicoud and Ducros (1999); Nicoud, Toda, Cabrit, Bose, and Lee (2011).

Highlights and conclusions

- The requirements of dimensionality reduction have been highlighted on the HIT case based on computational cost.
- Two reduction techniques have been introduced, and focus has been made on the Large Eddy Simulation because of the ability to control its accuracy.
- Closure methods have been briefly reviewed.

Chapter 4

Reduction strategies for particles in turbulent flows

The previous chapter was dedicated to fluid reductions in the context of single phase flows. We are here interested in reduction technique for disperse phase flows. This chapter is organised as follows:

- The first section (Sec. 4.1) presents the effects of the fluid reduction on the equations of inertial particles.
- The second section (Sec. 4.2) presents an illustration of some of the effects of the fluid reduction on the dynamics of inertial particle, and why these effects justify a non-trivial closure. The quantities observed are particle kinetic energy and particle diffusion coefficient.
- The third section (Sec. 4.3) presents a class of closures which is able to recover the effects of fluid reduction on the particle kinetic energy and particle diffusion coefficient. These closures are also used and studied more extensively in Chap. 10.

4.1 Inertial particle equations under fluid reduction

In this section, let us observe the effect of fluid reduction on the disperse phase. This is the first step before proposing some fluid closure for the disperse phase Sec. 4.3. Reductions in the fluid representation impact the particle evolution equations. This is especially the case for fully resolved particles. But it is also the case for point particles. In the specific case of Stokes' drag law (Eqs. 2.1), the fluid velocity at the position of the particle is used to compute the particle acceleration. When the fluid representation is reduced (see Sec. 3.3), this velocity is not readily accessible anymore. Ideally, if the fluid regularisation operator G was invertible, one would want to get:

$$d_t \boldsymbol{x}_p(t) = \boldsymbol{v}_p(t), \tag{4.1a}$$

$$d_t \boldsymbol{v}_p(t) = \frac{1}{\tau_p} \left(G^{-1} \circ G \circ \boldsymbol{u}_f \left(t, \boldsymbol{x}_p(t)\right) - \boldsymbol{v}_p(t) \right), \tag{4.1b}$$

with $\boldsymbol{x}_p(t)$ and $\boldsymbol{v}_p(t)$ respectively the particle position and velocity at time t, $\boldsymbol{u}_f\left(t, \boldsymbol{x}_p(t)\right)$ the fluid velocity at the position of the particle, and τ_p the characteristic inertial time of the particle.
However, in reality, we do not know how to inverse the fluid regularisation operator G, especially when reducing the number of degree of freedom that represent the fluid (such as a coarser mesh). Expressing $\boldsymbol{u}_f\left(t, \boldsymbol{x}_p(t)\right)$ in terms of regularized field and fluctuation, one gets:

$$\boldsymbol{u}_f\left(t, \boldsymbol{x}_p(t)\right) = G \circ \boldsymbol{u}_f\left(t, \boldsymbol{x}_p(t)\right) + \boldsymbol{u}_f\left(t, \boldsymbol{x}_p(t)\right)'. \tag{4.2}$$

The regularised fluid $G \circ \boldsymbol{u}_f\left(t, \boldsymbol{x}_p(t)\right)$ is a known quantity. However, the reduced fluid simulation does not give the residual fluid velocity $\boldsymbol{u}_f\left(t, \boldsymbol{x}_p(t)\right)'$. Thus, the goal of reduction techniques for particulate flows is to retrieve this fluctuations, but not only. Actually, what is required is the history of fluctuations along the particle path, which is different from the fluid path when inertia effects take place. To highlight this requirements, we must look at the integrated equations of the particle evolution:

$$\boldsymbol{x}_p(t+\Delta t) = \boldsymbol{x}_p(t) + \int_t^{t+\Delta t} \boldsymbol{v}_p(\tau)\mathrm{d}\tau, \tag{4.3a}$$

$$\begin{aligned}\boldsymbol{v}_p(t+\Delta t) =& \boldsymbol{v}_p(t) + \frac{1}{\tau_p}\int_t^{t+\Delta t} \left(G \circ \boldsymbol{u}_f\left(\tau, \boldsymbol{x}_p(\tau)\right) - \boldsymbol{v}_p(\tau)\right)\mathrm{d}\tau \\ &+ \frac{1}{\tau_p}\int_t^{t+\Delta t} \boldsymbol{u}_f\left(\tau, \boldsymbol{x}_p(\tau)\right)'\mathrm{d}\tau,\end{aligned} \tag{4.3b}$$

Therefore, we not only need to reconstruct the instanteneous spatial structure of the fluid, but also its time evolution.
In order to understand the impact of $\boldsymbol{u}_f\left(t, \boldsymbol{x}_p(t)\right)'$, on the dynamic of inertial particles, let us observe in the next section what happens when $\boldsymbol{u}_f\left(t, \boldsymbol{x}_p(t)\right)'$ is taken to be 0.

4.2 Diffusion of inertial particles under fluid reduction

In this section, we propose to observe the impact of $\boldsymbol{u}_f\left(t, \boldsymbol{x}_p(t)\right)'$, on the dynamic of inertial particles. This is done in the following setting:

- the fluid reduction operation is assumed to remove the smallest spatial scales of the flow field,
- the dynamics of the resolved scales is not impacted by the reduction operation (the study is done by filtering *a posteriori* on a resolved fluid simulation). This lets us focus on the particles, without having to consider the potential influence of a fluid closure.

The impact of fluid reduction on the behaviour of inertial point particles has already been widely studied (Armenio, Piomelli, and Fiorotto (1999), Yamamoto, Potthoff, Tanaka,

Kajishima, and Tsuji (2001), Fede and Simonin (2006), Gorokhovski and Zamansky (2018)). A key quantity defining the dynamics of interital particles is diffusion (see Sec. 1.3.1.3). It is a metric of reference in this work and it is constantly observed throughout Parts II and III. Furthermore, diffusion is a quantity strongly affected by some classical closures presented in this work (see Sec. 10), therefore, the diffusion of small inertial particles is expected to be strongly altered by the fluid flow reduction operation. This is why we briefly present here the impact of fluid flow reduction operation on the diffusion of small inertial particle. The article by Fede and Simonin (2006) already proposes an extensive study of the impact of the fluid flow reduction operation on the diffusion of small inertial particles. This is why it is used as a reference in this section. Because dispersion of the particle is driven by their kinetic energy (on diffusion, see Sec. 1.3.1.3) we start by presenting the impact of filtering the fluid on the level of kinetic energy of the disperse phase before presenting its impact on particle dispersion.

4.2.1 Simulation set-up

Fede and Simonin (2006) studied the impact of removing the small scales of a DNS on the dynamics of small collisional particles. Their carrier phase of reference is a box of homogeneous isotropic turbulence forced by a stochastic spectral scheme by Eswaran and Pope (1988). They modelled particles as inertial collisional point particles with the drag law from Naumann and Schiller (1935). No retroaction from the disperse phase to the carrier phase is taken into account. They assessed the influence of the higher wavenumbers of the fluid flow on the disperse phase behaviour by computing the evolution of the disperse phase on the reduced fluid. For this study it is considered that the fluid given by a LES is exactly the spatially filtered field of a fluid DNS. They performed several computations with different levels of reduction of the fluid and different levels of inertia of the particles.

4.2.2 Effect of reducing the fluid on inertial particle kinetic energy

The study by Fede and Simonin (2006) shows the effects of closing the particle evolution equations directly with the reduced fluid on the disperse phase behaviour. This is illustrated in Fig. 4.1.

- The left hand-side of Fig. 4.1 represents the disperse phase kinetic energy (normalised by disperse phase kinetic energy for fluid DNS) with respect to the filtered fluid kinetic energy (normalised by DNS fluid kinetic energy) for different Stokes numbers. It can be seen Fig. 4.1 that filtering has a strong impact on the particle properties, such as kinetic energy. The amount of energy removed from the disperse phase varies linearly with the amount of energy not represented in the reduced description of the flow.
- The right hand-side of Fig. 4.1 represents the disperse phase kinetic energy (normalised by disperse phase kinetic energy for fluid DNS) with respect to particle inertia for one level of fluid filtering. It can be seen that the linear coefficient varies as a decreasing function of the Stokes number. It is close to 1 for a Stokes number

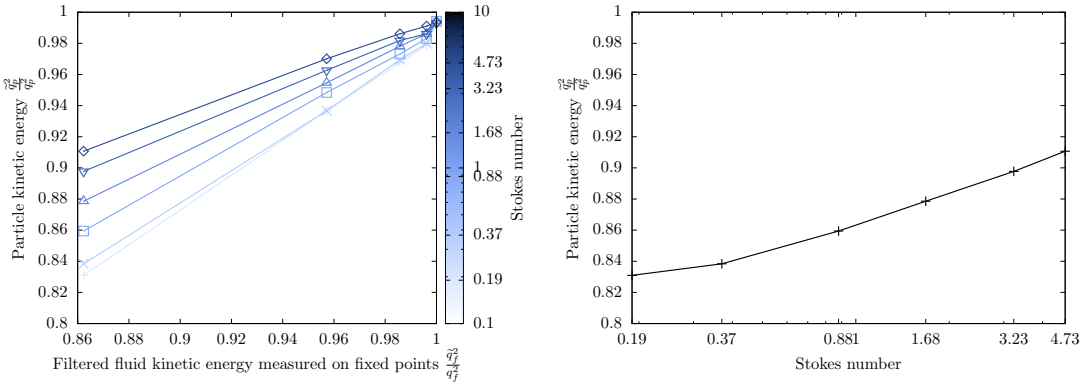

Figure 4.1. On the left, particle kinetic energy (normalised by disperse phase kinetic energy for fluid DNS) as a function of the filtered fluid kinetic energy measured at fixed locations (normalised by DNS fluid kinetic energy).
On the right, particle kinetic energy (normalised by disperse phase kinetic energy for fluid DNS), as a function of Stokes number, for 86% of filtered fluid kinetic energy.
Data from Fede and Simonin (2006).

based on Kolmogorov time scale around 1. For a Stokes number of 1, when the fluid reduction removes 20% of the fluid energy, the disperse phase kinetic energy is also decreased by 20% (20% is the guideline given by Pope (2000) for energy filtering in LES).

Let us now observe the effect of reducing the fluid on inertial particle diffusion coefficient.

4.2.3 Effect of reducing the fluid on inertial particle diffusion coefficient

The left hand-side of Fig. 4.2 presents the impact of filtering on the diffusion coefficient of the inertial particles for different Stokes numbers. The behaviour of the diffusion coefficient of the disperse phase with filtering seems more complex than the behaviour of the kinetic energy. The diffusion coefficient of the particles of high Stokes number does not appear to be affected by the filtering. However, the diffusion coefficient of low inertia particles seems to be linearly affected by the filtering.

Still in Fede and Simonin (2006), the right hand-side of Fig. 4.2 shows a non-monotonous dependency of the diffusion coefficient on the Stokes number. This observation is different from the results presented by Reeks, Swailes, and Bragg (2018) for whom diffusion is not influenced by the particle inertia.

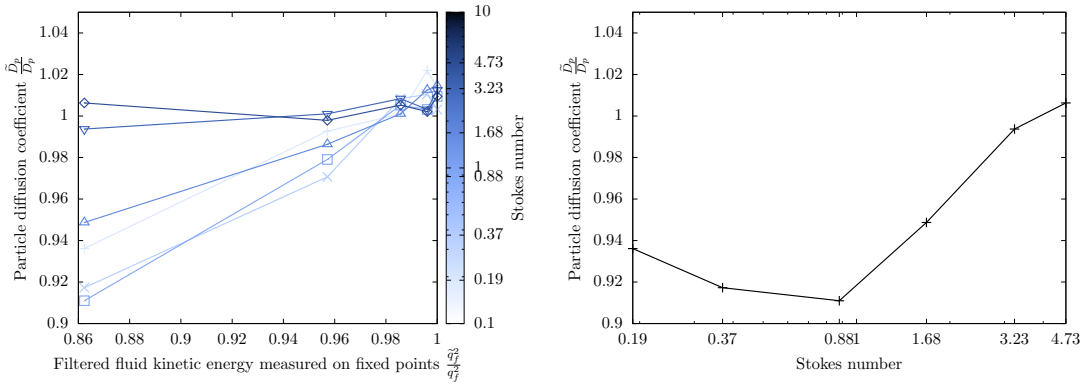

Figure 4.2. On the left, particle diffusion coefficient (normalised by the diffusion coefficient en DNS) as a function of the filtered fluid kinetic energy measured at fixed locations. Each line represents a different of Stokes numbers.
On the right, particle diffusion coefficient (normalised by the diffusion coefficient en DNS) as a function of Stokes number for 86% of filtered fluid kinetic energy.
Data from Fede and Simonin (2006).

4.3 Closures techniques for the Point-Particle Lagrangian trajectories

After having presented how fluid reduction alters the inertial particle behaviour in the previous section, let present here some strategies to recover a correct particle dynamics. In the literature, different models are derived in order to reproduce the resolved particle dynamics when only the reduced fluid flow is available. Extensive reviews of these models can be found in Kramer (2001), or in Marchioli (2017). Following Kramer (2001), it is possible to sort these models in two classes:

- Eulerian closures,
- and Lagrangian closures.

Let us briefly present here some examples for each of these two classes. For Lagrangian closures, we focus on stochastic modelling because this class of stochastic closures are used in Chap. 10, to close the disperse phase equations according to the formalism derived in Chap.5.4.

4.3.1 Eulerian fluid reconstructions

Some strategies try to reconstruct a fully resolved velocity field for the particles to evolve on. This is the Eulerian class of reconstruction. It is interesting because it preserves the correlation in the driving force of neighbouring particles. Meaning that different particles at the same location and experience the fluid velocity. Let us briefly evoke some of them here.

4.3.1.1 Approximate deconvolution

With this strategy one tries to recover the original fluid flow field. This is done by inverting as much as possible the effects of the reduction operator on the fluid field. However, if the fluid flow reduction is a true reduction operation (not injective), some of the fluid flow information is lost when performing the reduction. Therefore, this technique does not create any information about the resolved fluid from the reduced fluid (otherwise, no reduction would have been performed) However it is able to ensures that the energy spectrum of the reduced fluid is close to the energy spectrum of the resolved fluid on the wave-numbers they share in common. For more on approximate deconvolution techniques, see for instance Shotorban and Balachandar (2007), Kuerten (2006) or Wang, Zhao, and Ihme (2019)).

4.3.1.2 Kinematic simulation

With this strategy, the sub-grid fluid is reconstructed by a sum of independant modes. This approach is developped in Fung, Hunt, Malik, and Perkins (1992), Khan, Luo, Nicolleau, Tucker, and Lo Iacono (2010), Ray and Collins (2014), and Zhou, Wang, and Jin (2018). In this work, the fluid flow field is generated with this strategy (see Sec. 6.1).

4.3.1.3 Fractal interpolation

Similarly to Germano identity, this strategy uses the fractal understanding of the inertial range to propose a reconstruction of the higher wave-numbers of the fluids such as in Scotti and Meneveau (1999), Salvetti, Marchioli, and Soldati (2006), Marchioli, Salvetti, and Soldati (2008) and Knorps and Pozorski (2018).

4.3.2 Lagrangian fluid closures

In this section let us evoke the Lagrangian class of reconstruction. We focus on some strategies that treat inertial particle trajectories as a stochastic process, with Langevin equations of different orders (Langevin (1908), Pope (2000), Chap. 12.3), because this is what is used in Chap. 10 (Minier and Profeta (2015)).
In the models presented here, the influence of the unresolved fluid is not treated as a four dimensional field any more, but only as a stochastic process seen along each particle trajectory. This is a natural extension of standard modelling techniques. Let us briefly draw a parallel here.

- From physical particles, was derived the mesoscopic approach (Sec. 2.3). The mesoscopic approach does not describes individual physical particles any more, but rather the evolution of a law. One drawback of such modelling is that it assumes that particle trajectories are not correlated between each other (other than though the fluid). Therefore, the mesoscopic approach loses a level of correlation in the description of the system.
- Then, from the mesoscopic approach where trajectories are deterministic, to a closure in the form of a stochastic processes, one also loses a level of correlation in

the description of the system. This time, it is related to the temporal evolution of individual particle trajectories.

With this stochastic vision, different particles can be at the same point in phase-space and experience different evolutions. This means that the particles computed with this technique are not the particles of one fluid, but all the particles of an ensemble of different fluids. This ensemble of fluids could be for instance all the fluids which share the same reduction. This vision is already consistent with the formalism introduced in Chap. 5.4. Let us now present these models by increasing dimensionality (these models can be found with more details in Minier and Peirano (2001), Eq. 353 and Heinz (2003), p.92). Because we only use these models here for Monte-Carlo simulations, they are presented in a Lagrangian form. However, it is also possible to derive the Eulerian equation giving the evolution of the probability law of the particles (the Fokker–Planck equation).

4.3.2.1 One variable diffusion model

The first model presented is the simplest one. It focuses only on the particle position. It describes particles with only one variable: their physical position. The closure consists in compensating for the missing fluid energy with the addition of a Wiener process to the particle trajectory. A Wiener process is a continuous stochastic process with normally distributed and independent increments. For closing the one variable model, it is interesting to use a Wiener process process as a closure because it mimics the dispersive effect of the unresolved turbulent flow field on the particle position. One of the limitations of this closure is that it is not possible to differentiate the particle position to get a particle velocity any more.

$$\mathrm{d}\boldsymbol{X}_1(t) = \overline{\boldsymbol{u}}_f\left(t, \boldsymbol{X}_1(t)\right)\,\mathrm{d}t + \sigma_1 \mathrm{d}\boldsymbol{B}_t \tag{4.4}$$

This description is used for instance in Taylor (1921), Batchelor (1952), Tchen (1959), Mols and Oliemans (1998) and Shotorban and Balachandar (2007).

4.3.2.2 Two variables diffusion model

The second model adds some complexity to (Eq. 4.4). With this model, particles are described by their position and velocity. The missing fluid energy is accounted for at the level of the particle velocity. Its form is very close to the original linear model for inertial particles (Eqs. 2.1). Adopting the two equations model Eq. 4.5 only has an interest over the one equation model Eq. 4.4 when the relaxation time scale τ_{V2} is large in comparison with the smallest time scales of the reduced fluid $\overline{\boldsymbol{u}}_f$.

$$\mathrm{d}\boldsymbol{X}_2(t) = \boldsymbol{V}_2(t)\,\mathrm{d}t, \tag{4.5a}$$

$$\mathrm{d}\boldsymbol{V}_2(t) = \frac{1}{\tau_{V2}}\left(\overline{\boldsymbol{u}}_f\left(t, \boldsymbol{X}_2(t)\right) - \boldsymbol{V}_2(t)\right)\,\mathrm{d}t + \sigma_2 \mathrm{d}\boldsymbol{B}_t. \tag{4.5b}$$

Derivations of this model are presented, for instance by Reeks (1977), or Bini and Jones (2008)

4.3.2.3 Three variables diffusion model

The three variables model keeps the same strategy, but goes one step further. The aim is to better reproduce the particle trajectory statistics. Adopting the three equations model Eq. 4.6 has most interest over the two equations model Eq. 4.5 when

- τ_{V3} and τ_{U3} are of the same order of magnitude, to justify modelling by a third order,
- and both τ_{V3} and τ_{U3} are large in comparison with the smallest time scales of the reduced fluid $\overline{\boldsymbol{u}}_f$.

In the case where τ_{V3} and τ_{U3} are different by an order of magnitude, this third order model is very well represented by a second order model (Eq. 4.5), with $\tau_{V2} = \tau_{V3} + \tau_{U3}$. With this perspective in mind, it is important to note that in the second order model model, τ_{V2} does not have to be τ_p, but rather a characteristic time which is specific to the behaviour of the inertial particle within the reduced fluid.

$$\mathrm{d}\boldsymbol{X}_3(t) = \boldsymbol{V}_3(t)\,\mathrm{d}t, \tag{4.6a}$$

$$\mathrm{d}\boldsymbol{V}_3(t) = \frac{1}{\tau_{V3}}\left(\boldsymbol{U}_3(t) - \boldsymbol{V}_3(t)\right)\,\mathrm{d}t, \tag{4.6b}$$

$$\mathrm{d}\boldsymbol{U}_3(t) = \frac{1}{\tau_{U3}}\left(\overline{\boldsymbol{u}}_f\left(t, \boldsymbol{X}_3(t)\right) - \boldsymbol{U}_3(t)\right)\,\mathrm{d}t + \sigma_3 \mathrm{d}\boldsymbol{B}_t. \tag{4.6c}$$

Derivations of this model are presented, for instance by Minier, Peirano, and Chibbaro (2004), Fede, Simonin, Villedieu, and Squires (2006), Shotorban and Mashayek (2006), Vinkovic, Aguirre, Ayrault, and Simoëns (2006) and Minier and Profeta (2015).

4.3.2.4 More advanced models

Ultimately, this class of stochastic trajectory closures can be used to reproduce state of the art statistical trajectory properties such as intermittency characteristics like in Bini and Jones (2007), Gorokhovski and Zamansky (2014) or Zhang, Legendre, and Zamansky (2019). Note that intermittency is mostly relevant for fluid parcels or very low inertia particles, because it disappears as inertia increases. However, because statistical trajectory closure strategies only reproduces average particle trajectory statistics, they can never take into account effects of the local fluid structure on neighbouring particles such as particle pair separation and segregation.

4.4 Reduced statistical description of disperse phase flows

The previous sections were focusing on the Lagrangian evolution of particles. Here we are interested in their statistical description. Therefore, we work with a PDF and its

balance equation, which is an evolution equation in time and space. In this section, we first investigate the impact of reduction on the PBE, and then we look at solutions for macroscopic moment methods.

4.4.1 Reduced PBEs

Let us consider a PBE:

$$\partial_t f + \boldsymbol{v} \cdot \nabla_{\boldsymbol{x}} f + \frac{1}{\tau_p} \nabla_{\boldsymbol{v}} \cdot \left(\left(\boldsymbol{u}_f \left(t, \boldsymbol{x} \right) - \boldsymbol{v} \right) f \right) = 0. \tag{4.7}$$

Here two solutions for considering reductions can be envisaged. Like for the Lagrangian particle trajectory, the first solution is to consider that the fluid velocity is decomposed in two components:

$$\partial_t f + \boldsymbol{v} \cdot \nabla_{\boldsymbol{x}} f + \frac{1}{\tau_p} \nabla_{\boldsymbol{v}} \cdot \left(\left(G \circ \boldsymbol{u}_f \left(t, \boldsymbol{x} \right) - \boldsymbol{v} \right) f \right) = -\frac{1}{\tau_p} \nabla_{\boldsymbol{v}} \cdot \left(\boldsymbol{u}_f \left(t, \boldsymbol{x} \right)' f \right). \tag{4.8}$$

To close this equation we need to recover the fluid fluctuations, but apparently no effort is required for the disperse phase, as it is still fully resolved, in the sense that such equation could generate structures as fine as possible, as there is no reduction to avoid such details. However it must be kept in mind that the constructed fluctuations must belong to a unique fluid realisation.
Another solution is to directly filter the PBE:

$$\begin{aligned} \partial_t G \circ f + \boldsymbol{v} \cdot \nabla_{\boldsymbol{x}} G \circ f + \frac{1}{\tau_p} \nabla_{\boldsymbol{v}} \cdot \left(\left(G \circ \boldsymbol{u}_f \left(t, \boldsymbol{x} \right) - \boldsymbol{v} \right) G \circ f \right) = \\ - \frac{1}{\tau_p} \nabla_{\boldsymbol{v}} \cdot \left(G \circ \left(\boldsymbol{u}_f \left(t, \boldsymbol{x} \right) f \right) - G \circ \boldsymbol{u}_f \left(t, \boldsymbol{x} \right) G \circ f \right). \end{aligned} \tag{4.9}$$

This is this solution that has been adopted in the literature. Actually, there is two works that investigated the filtering of the PBE:

- Pandya and Mashayek (2002) who uses an analogy with the work of Reeks (1991) based on Lagrangian History Direct Interaction (LHDI);
- Zaichik, Simonin, and Alipchenkov (2009) which is based on the work of Zaichik (1999) that considers a Gaussian process to close the equation.

The two methods give the following closed form:

$$\begin{aligned} \partial_t G \circ f + \boldsymbol{v} \cdot \nabla_{\boldsymbol{x}} G \circ f + \frac{1}{\tau_p} \nabla_{\boldsymbol{v}} \cdot \left(\left(G \circ \boldsymbol{u}_f \left(t, \boldsymbol{x} \right) - \boldsymbol{v} \right) G \circ f \right) = \\ \nabla_{\boldsymbol{v}} \cdot \left(\mu \nabla_{\boldsymbol{v}} G \circ f + \lambda \nabla_{\boldsymbol{x}} G \circ f \right). \end{aligned} \tag{4.10}$$

In which is exhibited a phase space diffusion due to the subgrid scales. Both methods end with the derivation a macroscopic moment methods based on the filtered PBE.
To the author's knowledge, the previous statistical methods have not been used to simulate turbulent disperse phase flows, and are limited to theoretical derivations. Another solution also investigated in the literature was to use a Lagrangian Filtered Mass Density Function (Innocenti, Marchioli, and Chibbaro (2016)), but it has not reached the application level.

4.4.2 Reduced Moment methods

There is another solution to derive a reduced statistical model: filtering the moment equations, in analogy with reduced strategies for gaseous flows. Here are two works that investigated this idea:

- Shotorban and Balachandar (2007) suggested a filtered version of the equilibrium model of Ferry and Balachandar (2001); Ferry and Balachandar (2002). In this model, the sole number density equation is transported, and the turbulent transport is modelled through a diffusion-like closure, in analogy with what is done for turbulent scalar transport.
- Moreau, Simonin, and Bédat (2010) filtered the moment equations derived from the MEF: droplet number density, momentum and internal energy. To close the equations, they use approximations inspired from gaseous compressible flows, as the moment equations exhibited a similar structure.

Highlights and conclusions

- The inertial particle equations under fluid reduction has been presented
- The impact of fluid reduction on the particle dynamics has been highlighted
- Lagrangian modelling techniques focuses on the reconstruction of the accurate trajectories, without specific attention on the corresponding statistical description
- Reduced statistical methods have also been presented, which always end with diffusion-like closures, either in the phase space or in the physical space.
- None of the presented methods have been derived in the context of two-way coupled flows

Part II

Extended formalism and related numerical strategy

Chapter 5

General reduction framework and introduction of a new MEF formalism adapted to LES

As we have seen in Sec. 3.3, working with the reduced variables leads us to an unclosed equation, for which we presented classical closures in Sec. 3.3.2. These closures rely on some key properties of the reduced variables which are bound to be different in a strongly coupled two-phase flow.
In order to move forward, let us propose a formalism for the concept of reduction. This new formalism will help us understand the classical reductions performed in the literature for single phase flows and two-phase flows. We will then envision designing a consistent reduction operation for strongly-coupled two-phase flows in the context of LES under the MEF. This will lead us to a new MEF formalism that we propose to evaluate according to some metrics that will be defined. Eventually, we present the expected behaviour of these metrics.

5.1 General reduction framework

To put in a broader perspective the reduction techniques, we propose a description in terms of dynamical system.
In this work, the system of reference is a deterministic dynamical system D_{ref}. It is made of:

- a flow field, solution of the Navier-Stokes equations (Eq. 1.2),
- and a set of inertial point-particles, following Stokes' drag law (Eq. 2.1).

For simplicity, in this section, we will consider the system *autonomous* (independent of time). This is only to make notations lighter, as the same reasoning could be extended to non autonomous systems.
The space of all the possible states of D_{ref} is called *phase space*. Let us name it $\mathcal{S}_{\text{ref}}$. In our context, a point in phase space describes the whole system. It is made of:

- the fluid, described at each time by a velocity field $\boldsymbol{u}_f$,
- and the set of inertial point-particles, described at each time by a family of positions and velocities $(\boldsymbol{x}_{p,i}, \boldsymbol{v}_{p,i})_{i\in[\![1,\mathrm{N}_p]\!]}$.

Therefore, elements of $\mathcal{S}_{\mathrm{ref}}$ are in $\mathbb{R}^{3+3+2\cdot\mathrm{N}_p}$.
We name Φ_{ref} the flow associated to D_{ref}:

$$\forall t \in \mathbb{R}^+, \text{ if } s_{\mathrm{ref}} \in \mathcal{S}_{\mathrm{ref}}, \quad \begin{array}{l}\Phi_{\mathrm{ref}}(s_{\mathrm{ref}}, t) \text{ is the state of the system solution of } D_{\mathrm{ref}},\\ \text{with initial condition } s_{\mathrm{ref}}, \text{ after a time } t.\end{array} \tag{5.1}$$

The flow is the function which gives the evolution of any point in phase-space $\mathcal{S}_{\mathrm{ref}}$ through the dynamical system D_{ref} after some time t.
Let us now introduce a reduction operator on the phase space $\mathcal{S}_{\mathrm{ref}}$ of the dynamical system D_{ref}:

$$\begin{aligned}\mathfrak{G}\colon \mathcal{S}_{\mathrm{ref}} &\to \mathcal{S}_{\mathrm{red}}\\ s_{\mathrm{ref}} &\mapsto \mathfrak{G}\left(s_{\mathrm{ref}}\right),\end{aligned} \tag{5.2}$$

with $\mathcal{S}_{\mathrm{red}} = \mathfrak{G}\left(\mathcal{S}_{\mathrm{ref}}\right)$. $\mathfrak{G}$ can be a reduction operator of the fluid velocity field like in Sec. 3.3.1, or of the disperse phase, or of both. It is defined on the phase space $\mathcal{S}_{\mathrm{ref}}$. Therefore, it does not act on the temporal dimension of the system (it does not include time averages for instance). We are aware that it is not representative of all the reduction techniques available in the literature, but it is enough to work with those presented in this manuscript, and is in accordance with the classical LES methods, which solely act on the physical space.
Because $\mathfrak{G}$ is defined on the phase space, it does not automatically give a new dynamical system. It only transforms the phase space. In the general case, it is necessary to define new evolutions equations associated with the new phase space $\mathcal{S}_{\mathrm{red}}$. Different options are possible, according to the case at hand. Let us review them in the following section.

5.1.1 Injective reduction operator

The simplest case is when $\mathfrak{G}$ is injective. $\mathfrak{G}$ is said *injective* when:

$$\forall \left(s_{\mathrm{ref},1}, s_{\mathrm{ref},2}\right) \in \mathcal{S}_{\mathrm{ref}}^2, \quad \mathfrak{G}\left(s_{\mathrm{ref},1}\right) = \mathfrak{G}\left(s_{\mathrm{ref},2}\right) \implies s_{\mathrm{ref},1} = s_{\mathrm{ref},2}. \tag{5.3}$$

Note that the injectivity of $\mathfrak{G}$ relies:

- on the transformation performed by $\mathfrak{G}$: $\zeta \mapsto \mathfrak{G}\left(\zeta\right)$,
- but also on the domain of $\mathfrak{G}$: $\mathcal{S}_{\mathrm{ref}}$.

The same transformation can be injective on a domain and non injective on an other: take for instance $x \mapsto \|x\|$ which is not injective on $\mathbb{R}$ but is injective on $\mathbb{R}^+$.

When $\mathfrak{G}$ is injective, it is possible to define the inverse of $\mathfrak{G}$ as a function:

$$\begin{aligned}\mathfrak{G}^{-1}\colon \mathcal{S}_{\mathrm{red}} &\to \mathcal{S}_{\mathrm{ref}}\\ s_{\mathrm{red}} &\mapsto s_{\mathrm{ref}},\end{aligned} \tag{5.4}$$

where $\mathfrak{G}^{-1} \circ \mathfrak{G} = \mathrm{Id}$. Note that the inverse $\mathfrak{G}^{-1}$ is a theoretical construction and does not always have an explicit expression.

When $\mathfrak{G}$ is injective, it is simple to define a new flow $\Phi_{\mathrm{red,inj}}^{\mathcal{S}_{\mathrm{ref}},\mathfrak{G}}$ on $\mathcal{S}_{\mathrm{red}}$ such that:

$$\forall t \in \mathbb{R}^+, \quad \forall s_{\mathrm{red}} \in \mathcal{S}_{\mathrm{red}}, \quad \Phi_{\mathrm{red,inj}}^{\mathcal{S}_{\mathrm{ref}},\mathfrak{G}}(s_{\mathrm{red}}, t) = \mathfrak{G} \circ \Phi_{\mathrm{ref}}\left(\mathfrak{G}^{-1}\left(s_{\mathrm{red}}\right), t\right). \tag{5.5}$$

However, if $\mathfrak{G}^{-1}$ is not explicitly known, $\Phi_{\mathrm{red,inj}}^{\mathcal{S}_{\mathrm{ref}},\mathfrak{G}}$ is only a formal construction and it does not give an explicit formulation for the associated dynamical system $D_{\mathrm{red,inj}}$.

When $\mathfrak{G}$ is injective, $\mathcal{S}_{\mathrm{red}}$ and $\mathcal{S}_{\mathrm{ref}}$ have the same cardinality. Therefore, $\mathfrak{G}$ is not really a reduction operator in the sense that it does not remove information from solutions of the system of reference.

5.1.2 Non-injective reduction operator

This leaves us with the interesting case where $\mathfrak{G}$ is not injective. This means that:

$$\exists \left(s_{\mathrm{ref},1}, s_{\mathrm{ref},2}\right) \in \mathcal{S}_{\mathrm{ref}}^2, \quad \text{such that } \mathfrak{G}\left(s_{\mathrm{ref},1}\right) = \mathfrak{G}\left(s_{\mathrm{ref},2}\right) \text{ and } s_{\mathrm{ref},1} \neq s_{\mathrm{ref},2}. \tag{5.6}$$

Now, two cases are possible.

5.1.2.1 The reduced system is self-contained

The first case is when the reduction $\mathfrak{G}$ of the system $\mathfrak{G}$ is self-contained. We say that the reduced system is *self-contained* when:

$$\begin{aligned} &\forall \left(s_{\mathrm{ref},1}, s_{\mathrm{ref},2}\right) \in \mathcal{S}_{\mathrm{ref}}^2, \\ &\quad \mathfrak{G}\left(s_{\mathrm{ref},1}\right) = \mathfrak{G}\left(s_{\mathrm{ref},2}\right) \implies \Big(\forall t \in \mathbb{R}^+, \quad \mathfrak{G} \circ \Phi_{\mathrm{ref}}\left(s_{\mathrm{ref},1}, t\right) = \mathfrak{G} \circ \Phi_{\mathrm{ref}}\left(s_{\mathrm{ref},2}, t\right)\Big). \end{aligned} \tag{5.7}$$

This means that different points in phase space can have the same image by the reduction operator. However, if they do share the same reduction at one time, they will keep on sharing the same reduction at ulterior times.
Note that the fact that the reduction operator $\mathfrak{G}$ is self-contained depends on:

- the transformation performed by $\mathfrak{G}$: $x \mapsto \mathfrak{G}\left(x\right)$,
- the domain of $\mathfrak{G}$: $\mathcal{S}_{\mathrm{ref}}$,
- and also the reference flow Φ_{ref}.

In this case, because $\mathfrak{G}$ is not injective, the preimages of $\mathfrak{G}$ given by the operator $\mathfrak{G}^{\leftarrow}$ are not in $\mathcal{S}_{\mathrm{ref}}$ any more, but in the power set of $\mathcal{S}_{\mathrm{ref}}$: $\mathcal{P}\left(\mathcal{S}_{\mathrm{ref}}\right)$. $\mathfrak{G}^{\leftarrow}$ gives a subset of $\mathcal{S}_{\mathrm{ref}}$. However, thanks to the self-contained property (Eq. 5.7), for all t in $\mathbb{R}^+$, for all s_{red} in $\mathcal{S}_{\mathrm{red}}$, the set $\mathfrak{G} \circ \Phi_{\mathrm{ref}}\left(\mathfrak{G}^{\leftarrow}\left(s_{\mathrm{ref}}\right), t\right)$ is reduced to only one element.
Therefore, when the system is self-contained, it is still possible to define a new flow $\Phi_{\mathrm{red,s-c}}^{\mathcal{S}_{\mathrm{ref}},\mathfrak{G},\Phi_{\mathrm{ref}}}$ on $\mathcal{S}_{\mathrm{red}}$ such that:

$$\forall t \in \mathbb{R}^+, \quad \forall s_{\mathrm{red}} \in \mathcal{S}_{\mathrm{red}}, \quad \Phi_{\mathrm{red,s-c}}^{\mathcal{S}_{\mathrm{ref}},\mathfrak{G},\Phi_{\mathrm{ref}}}(s_{\mathrm{red}}, t) = \mathfrak{G} \circ \Phi_{\mathrm{ref}}\left(\mathfrak{G}^{\leftarrow}\left(s_{\mathrm{red}}\right), t\right). \tag{5.8}$$

$\Phi_{\mathrm{red,s-c}}^{\mathcal{S}_{\mathrm{ref}},\mathfrak{G},\Phi_{\mathrm{ref}}}$ is a formal construction. This flow does not give an explicit formulation for the associated reduced and self-contained dynamical system $D_{\mathrm{red,s-c}}$.

5.1.2.2 The reduced system is not self-contained

When the reduction $\mathfrak{G}$ is not self-contained:

$$\begin{aligned}&\exists\,(s_{\mathrm{ref},1},s_{\mathrm{ref},2})\in\mathcal{S}_{\mathrm{ref}}^2 \text{ and } t\in\mathbb{R}^+,\\ &\text{ such that } \mathfrak{G}\,(s_{\mathrm{ref},1})=\mathfrak{G}\,(s_{\mathrm{ref},2}) \text{ and } \mathfrak{G}\big(\Phi_{\mathrm{ref}}\,(s_{\mathrm{ref},1},t)\,\big)\neq\mathfrak{G}\big(\Phi_{\mathrm{ref}}\,(s_{\mathrm{ref},2},t)\,\big).\end{aligned}\tag{5.9}$$

We call a system which is not self-contained, *uncontained*. In this case, the reduction operation does not lead to a single evolution of the reduced system. Therefore, it is not possible to simply define a reduced dynamical system like in the other cases.
For the reduced system, one gets a set of different possible evolutions going in different directions:

$$\forall t\in\mathbb{R}^+,\quad \forall s_{\mathrm{red}}\in\mathcal{S}_{\mathrm{red}},\quad \mathfrak{G}\circ\Phi_{\mathrm{ref}}\left(\mathfrak{G}^{\leftarrow}\left(s_{\mathrm{ref}}\right),t\right).\tag{5.10}$$

5.1.3 Summary of the possible impact of the reduction operation on deterministic dynamical system

We have seen in the beginning of this chapter that it is possible to sort the reduction operators of dynamical systems according to their effect on the dynamical system. The different scenario are summed up in Tab. 5.1:

- The first aspect, represented by the rows of the table, focuses on the impact of the reduction operator on phase space. It distinguishes operators which are invertible in phase space from those which are not. Usually, if the operator corresponds to a reduction, it is not an injective function of phase space.
- The second aspect, represented by the columns of the table, deals with the interaction of the operator on the original dynamic of the system. If the original evolution of the original system is still adapted to the reduced variable, the system is self-contained. Otherwise, building a consistent system of the reduced variable is not straightforward and needs some investigations.

		Possible evolution(s) of a reduced representation	
		one	**many**
Number of realisation(s) with the same reduced description	**one**	injective	
	many	non-injective self-contained	non-injective uncontained

Table 5.1. Possible evolutions of the phase space of a deterministic dynamical system when applying an arbitrary reduction operator.

In the next section, we present the classical reduction operations of single and two phase flows under the light of the reduction formalism we have introduced.

5.2 Classification of usual reduction strategies for turbulent two-phase flows

In this section, we propose to review the reduction operation performed in some classical contexts: starting with single phase turbulence, before moving to two-phase flows in one-way and two-way coupled contexts.

5.2.1 Reduction of single phase turbulence

In the context of single phase turbulence, the most consistent vision is that current reductions techniques are self-contained (McComb (1990), Chap. 1.5.1). Although this choice corresponds to what would be expected from ideal reductions (Langford and Moser (1999)), it is not obvious from an experimental perspective. Indeed, Akbari and Montazerin (2013), show that, conditioning to the locally resolved scales the effect of the unresolved scales on the resolved scales, does not give a unique value but a whole distribution. Nonetheless, some authors try to give a theoretical justification to the self-contained vision by resorting for instance to the theory of renormalisation (Yakhot and Orszag (1986)). Other authors focus on providing new reduction formalisms which are naturally self-contained (Pope (2010)). In the context of this work, we will assume that we can work with a non-injective self-contained representation of the flow field. This is exactly the object which is built in Chap. 6 for the study performed in Chap. 9. Since we are interested in the dynamics of two-phase flows in the context of this work, let us now present the reductions performed in this scenario.

5.2.2 Reduction of disperse two-phase flows

In this section, we present the nature of the equations on the reduced variables in the context of disperse two-phase flows.

5.2.2.1 With no retroaction of the particles on the fluid

In the context of turbulent disperse two-phase flows with no retroaction of the particles on the fluid, the type of the fluid reduction is the same as in single phase flows.
There are two reduction cases:

- The reduction operation is applied to both phases, as in Shotorban and Balachandar (2007); Moreau, Simonin, and Bédat (2010):
- The reduction operator only acts on the fluid field and does not alter the phase space of inertial particles (Marchioli (2017)): in this case, the level of description of the disperse phase is not reduced. However, the dynamics of the disperse phase can be impacted because of the forcing term coming from the fluid phase which is altered by the reduction operation (Sec. 4.1).

Therefore, reducing the model of the fluid phase, even with a self-contained fluid field reduction, can lead to a model for the disperse phase which is uncontained. This is why, in this work, we propose a new representation of the disperse phase which is guaranteed to remain contained, even for LES. This representation is presented in Sec. 5.4.

5.2.2.2 With two-way coupling

We have seen in the previous section that even a self-contained fluid reduction leads to a model for the disperse phase which is uncontained. In the context of two-way coupling, the disperse phase retroacts on the fluid dynamics, and in some extreme in cases, the fluid is even entirely driven by the dynamics of the particles (Capecelatro, Desjardins, and Fox (2016a) and Zamansky, Coletti, Massot, and Mani (2016)). Therefore, following the disperse phase evolution, the fluid phase also becomes uncontained. Modelling two-way coupling presents a difficulty of the same nature as one-way LES. Because one-way LES involves less equations to close, we will start with this scenario in Sec. 5.4.

After having briefly presented how usual reduction techniques for two-phase flows can be sorted according to the reduction framework presented in Sec. 5.1, we now propose to see how to derive the mesoscopic Eulerian formalism in the context of LES, and suggest what could be done in the context of two-way coupled LES.

5.3 Derivation of the mesoscopic Eulerian formalism in the context of reduced two-phase flows

The objective of this research project was to derive an average mesoscopic description of the disperse phase compatible with LES and strong two-way coupling. In this section, we present how we approached this challenge. Let us start by presenting the one-way coupled context before moving on the the two-way coupled scenario.

5.3.1 With no retroaction of the particles on the fluid

In a one-way coupled scenario, the fluid evolution is independent to the level of description of the particles.
However, for the disperse phase, it is a different story. Let us derive again the mesoscopic formalism in the context of a reduced fluid. For simplicity, let us consider that particles are exchangeable. When the fluid is fully resolved the MEF distribution, is the conditional law of one particle on one fluid realisation.
A classical fluid reduction is assumed self-contained, but cannot reasonably be injective (Sec. 5.2.1). Therefore, when one computes a reduced fluid, it is not possible to have access to one fluid realisation, but only to a set of fluid realisations $\mathfrak{G}^{\leftarrow} \circ \mathfrak{G}(\boldsymbol{u}_f)$. Therefore, it is not possible to derive the classical MEF distribution.
At this point, two strategies are possible:

- Use a representation of the disperse phase at the mesoscopic level different from the MEF, such as a stochastic processes (Bini and Jones (2008)). This option has not been chosen in the work performed here and remains to be explored.
- Extend the definition of MEF to make it compatible with fluid reductions. This is the strategy chosen in this work. Let us present it briefly in the next few lines.

The MEF is based on the conditional law of one particle on one fluid realisation. As presented in Février, Simonin, and Squires (2005), extending the MEF consists in taking the conditional law of one particle on a set of fluid realisations:

Definition 21. The *Extended Mesoscopic Eulerian Formalism* (EMEF) considers the specific cases of f_{a_f}, where a_f is the fluid ensemble determined by $\mathfrak{G}^{\leftarrow} \circ \mathfrak{G}(\boldsymbol{u}_f)$, i.e. the ensemble of possible fluids that share the same reduced description.

It is an extension of the MEF introduced by Février, Simonin, and Squires (2005) in order to take into account weak two-way coupling. It is a very interesting object because it has an unambiguous definition on the reduced flow field $\mathfrak{G}(\boldsymbol{u}_f)$, even when the fluid reduction is not injective. This is different from the standard MEF which is based on a full unique fluid realisation of the case. However, computing the evolution of the distribution of the EMEF is difficult because it is the average evolution of the distribution

of the MEF on all the different fluids from the set $\mathfrak{G}^{\leftarrow} \circ \mathfrak{G}(\boldsymbol{u}_f)$. Therefore, theoretically, we need to know all the different fluids of the set $\mathfrak{G}^{\leftarrow} \circ \mathfrak{G}(\boldsymbol{u}_f)$ in order to compute the evolution of $f_{\mathbf{a}_f}$. This is quite different from the usual MEF. As a consequence, in the following of this work, starting Chap. 6, we propose to build a numerical set-up in order to investigate the behaviour of the EMEF, and how it differs form the MEF.
Let us now present the challenges we would encounter when adding two-way coupling to the mix.

5.3.2 With two-way coupling

With two-way coupling, deriving the MEF becomes even more difficult to derive because the disperse phase retroacts on the fluid. Each particle realization leads to a different fluid evolution. These discrepancies are enhanced with time by the mixing nature of the turbulence. Realisations of the fluid and of the disperse phase are strongly interconnected. It is not possible to consider them individually anymore.
In this context two options are readily possible:

- One option is to consider a global average formalism for both phases. This is a RANS approach (for deriving such models, see for instance Emre, Fox, Massot, De Chaisemartin, Jay, and Laurent (2014), Emre (2014), Fox (2014), Capecelatro, Desjardins, and Fox (2016a) and Capecelatro, Desjardins, and Fox (2016b)).
- The other option would be to avoid using any averaging in the formalism and try to model the evolution of one realisation of the system, with point-particle simulations and a stochastic closure for instance (Pai and Subramaniam (2012)), or even using an Eulerian formalism (Goudenège, Larat, Llobell, Massot, Mercier, Thomine, and Vié (2019)).

Some refuse to limit their horizons to these two restrictive perspectives and try to find a way to extend the MEF to two-way coupling in the spirit of LES, in-between DNS and RANS. Here are some options:

- Zeren (2010) considers a conditional average over close initial particle positions. This allows realizations to have a similar structure for initial times. This structure being consistent throughout realizations, it is preserved by the averaging process of the MEF. However, due to the mixing nature of turbulence, the average is likely to make the simulation become closer to RANS averages as time increases.
- Février, Simonin, and Squires (2005) propose to take a conditional average over the large scales of the flow (similarly to the approach proposed by Pope (2010) in a single phase context). Indeed, with the traditional scaling of the Kolmogorov energy spectrum in mind (Sec. 1.2.2), the largest scales of the flow contain most of the energy and can be thought to be more stable to the effect of the small particles. However, with two-way coupling, the energy spectrum is altered and energy transfers are modified so that standard turbulence characterisations such as Kolmogorov hypothesis are not guaranteed to be reasonable any more. In particular, this strategy is not reasonable in the context of the works of Capecelatro, Desjardins, and Fox (2016a) and Zamansky, Coletti, Massot, and Mani (2016), where the small particles are the source of all the flow energy and interact with the fluid energy at

all the scales through the formation of large clusters.

Eventually, there is still the option to represent both phases at a mesoscopic level, but which does not rely on the hypothesis of the MEF. It was not an option in the context of this work, but it could be an promising strategy for deriving LES models for coupled two-phase flow. Let us however present some examples of such alternatives:

- One of the possibilities is to consider both phases as a stochastic processes at the mesoscopic level. This is maybe the simplest option for capturing the dynamics of strongly diverging configurations, evolving far from the mean.
- An other possibility is to consider mesoscopic visions of two-phase flows derived from Euler-Euler simulations (resolved interface simulations and imposed interface simulations). In this case, as explained in Pai and Subramaniam (2009), the mesoscopic density f_{EE} representing the disperse phase is the probability of liquid presence function of time and space. Conveniently, this approach is valid, even when the hypothesis necessary to consider point particles are not valid any more (Eaton (2009)). However, a clear formalism does not guarantee closed equations, and expressions for the source terms still have to be derived (such as in the work of Tenneti, Garg, and Subramaniam (2011) for instance).

We have seen in this section that extending the MEF outside of the context of DNS is not obvious. There is still a long way to go before proposing a MEF framework able to withstand strongly coupled LES simulation. In the perimeter of this work, we will focus on studying the extension of the MEF to LES in a one-way coupled presented in Sec. 5.3.1.

In the next section let us present how we envision to analyse this new formalism in this work.

5.4 Investigation of the Extended MEF in one-way coupled LES

The mesoscopic Eulerian formalism (MEF) has been derived in the context of one-way coupled fully-resolved simulations (Février, Simonin, and Squires (2005)). Extending the mesoscopic formalism to LES is not straightforward. One of the biggest difficulties is to ensure consistency between the spatial reduction operation of the fluid and the statistical average operation of the dispersed phase. This is already a challenge for one-way coupled cases. In this section:

- we present metrics of interest for understanding the difference in behaviour between the MEF and the EMEF introduced in Sec. 5.3.1,
- we describe the results expected from this study.

5.4.1 Metrics of interest

Two metrics are defined here:

- First, we define a metric for measuring on each scenario, how different the local definition of the EMEF is different from the usual MEF (Sec. 5.4.1.1).
- Then, we define a metric for assessing how far is the resulting distribution given by the EMEF from the distribution given by the MEF (Sec. 5.4.1.2).

5.4.1.1 Metric for the reduction operation

Here we define a metric for understanding on each set of fluids, how far the definition of the EMEF is from the MEF.
Both the MEF and the EMEF distribution are written f_{a_f}. The difference is in the cardinality of a_f. In the context of the MEF, a_f represents only one fluid $\boldsymbol{u}_f$, whereas in the context of the EMEF, a_f can represent any probable set of fluids. Therefore, one of the way to characterize the distance between the MEF and the EMEF is in terms of the relative energy of the set a_f with respect to the reduced flow field corresponding to the set a_f. The average energy k of a fluid $\boldsymbol{u}_f$ is given by:

$$k\left(\boldsymbol{u}_f\right) = \frac{\displaystyle\int_{\text{time}} \int_{\text{space}} ||\boldsymbol{u}_f(t,\boldsymbol{x})||^2 \,\mathrm{d}t\,\mathrm{d}\boldsymbol{x}}{\displaystyle\int_{\text{time}} \int_{\text{space}} \mathrm{d}t\,\mathrm{d}\boldsymbol{x}}, \tag{5.11}$$

with *time* and *space* intervals of sensible extension with respect to the phase space A_f and the time span of evolution of the fluid. When the set of the sub-grid scales is centred, $\mathbb{E}\left[a_f - \mathfrak{G}\left(a_f\right)\right] = 0$. Hence, expanding the expression of the average energy of the set of fluids a_f, one gets:

$$\mathbb{E}\left[k\left(a_f\right)\right] = \mathbb{E}\left[k\left(a_f - \mathfrak{G}\left(a_f\right)\right)\right] + k\left(\mathfrak{G}\left(a_f\right)\right). \tag{5.12}$$

In order to clarify the notations:

- The set of fields $a_f - \mathfrak{G}\left(a_f\right)$ corresponds to the set of the sub-grid scales, or unresolved flow field, or lowest eddies.
- The field $\mathfrak{G}\left(a_f\right)$ correspond to the resolved flow field or largest eddies.

We propose to consider that the size of a_f is measurable in terms of the proportion of unresolved energy:

$$\frac{\mathbb{E}\left[k\left(a_f - \mathfrak{G}\left(a_f\right)\right)\right]}{\mathbb{E}\left[k\left(a_f\right)\right]}. \tag{5.13}$$

The complementary term is the proportion of resolved energy:

$$\frac{k\left(\mathfrak{G}\left(a_f\right)\right)}{\mathbb{E}\left[k\left(a_f\right)\right]}. \tag{5.14}$$

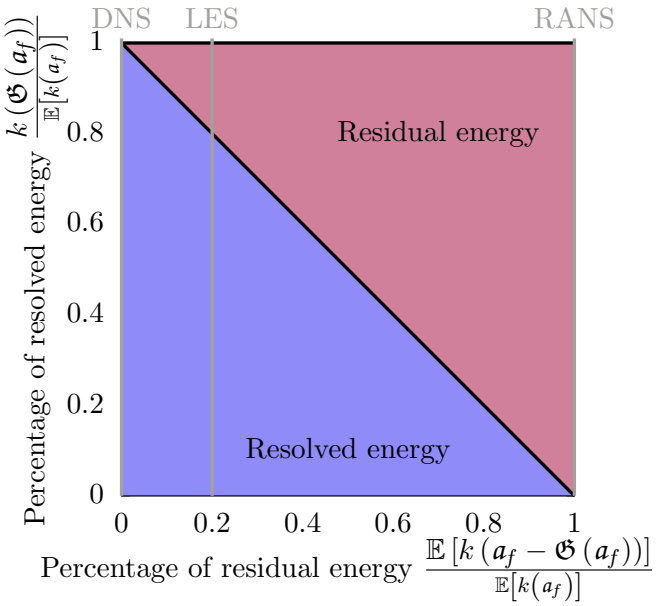

Figure 5.1. Energy in the fluid with respect to the residual fluid energy.

Extending the MEF to non-injective LES is quite interesting because it offers a complete formalism of which DNS and RANS are only limit cases[1]. DNS corresponds to a LES with 100% of the energy of the flow in the reduced flow field, whereas RANS corresponds to a LES with 0% of the energy of the flow in the reduced flow field (Fig. 5.1).
Now that we have proposed a metric for assessing how different is the definition of the EMEF from the MEF, let us define a metric for assessing how different are the resulting distributions of these two formalisms.

5.4.1.2 Metric of the resulting distribution

For assessing the impact of non-injective LES on the MEF, one needs a metric to assess the difference. For combustion applications, knowing the position of the droplets is one of the most important quantities, because it controls where the fuel vaporises hence where the localization of the flame. Thus, when investigating the extended MEF, special focus will be given to particles position.
The main difference between, the MEF in a DNS context, and the extension of the MEF to LES, is that the EMEF distribution represents a set of particles affected by a variety of different fluids sharing the same reduced description. The plurality of sub-grid scales implied by non-injective LES is expected to act primarily as a dispersive force on the particles. If particles were not affected by sub-grid scales, it is likely that there would not be much difference between the EMEF distribution and a standard MEF distribution. However, since inertial point-particles are affected by sub-grid scales removal (Chap. 4),

[1]For reference, Pope (2000), p. 560 Table 13.1 considers that 80% of the total energy has to be resolved by the large scales of the flow for LES.

it appears relevant to think that the EMEF could lead to a different distribution than the standard MEF.
As an illustration of this concept, on can have a look at the contrast between both sides of Fig. 5.2.

- The left of Fig. 5.2 represents the MEF paradigm. It this case, only one fluid realization is involved. The available information is enough to give one and only one deterministic trajectory for each particle. Time evolution of non-colliding inertial point particles with Stokes drag law is bijective in time.
- By contrast, the right of Fig. 5.2 represents the EMEF paradigm. In this case, a set of different fluid flows is involved. This example represents a finite discrete set of ten fluid flow fields. With the Kinematic Simulations used for this work, this set is an infinite set of finite dimension. In the case of real turbulence, this set is not known. For the sake of being consistent with the theme of LES, the synthetic fluids presented here share 80% of their lower modes, which accounts on average for 80% of their energy. As observed on the right of Fig. 5.2, for one given initial particle, there is not one single trajectory, but a set of different trajectories.

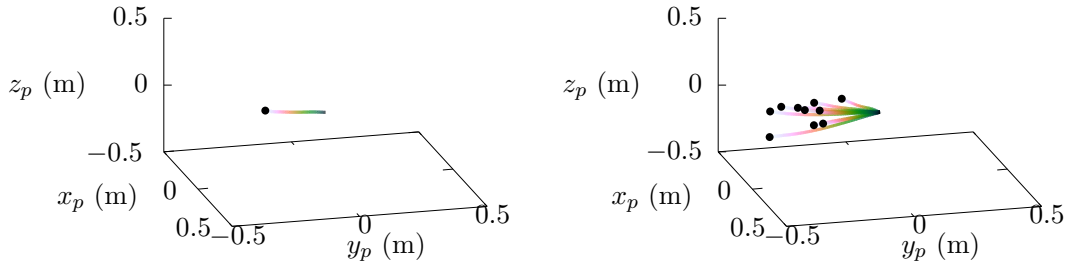

Figure 5.2. The beginning of the trajectory of one inertial particle ($\tau_p = 1$s) on one fluid on the left and on ten different fluids conditioned by 80% of their energy (synthetic fluids, presented in Sec. 6.1, of 200 modes, meaning that the 160 lowest wave-numbers modes are constants across fluids) on the right. The initial particle velocity is taken as the fluid velocity at the particle position.

As observed in Fig. 5.2, one of the main difference between the MEF and the EMEF is that the EMEF is more dispersive than the MEF. This is only a visual observation.
Thus, the first quantity of interest which is studied here in the context of non-injective LES is the particle relative position variance. This is a very standard property widely studied when trying to characterise the behaviour of particles in a flow (Taylor (1921)). Investigating this property is very consistent with the objective of this work, as standard closure models for particle behaviour in LES usually have a major effect on dispersion (see for instance models given by Minier and Peirano (2001) or Reeks (1991)).

Now that we have defined a metric for measuring the difference between the EMEF and the MEF and a metric for measuring the distance between the evolution of the resulting

distributions, let us discuss what we expect to observe with respect to these quantities in the next section.

5.4.2 Expected results - *A priori* study in the case of fluid parcels

It is interesting to start by performing a small *a priori* study on fluid parcels to get an idea of what is likely to happen. Following on the work of Taylor (1921) (see Sec. 1.3.1.1), the behaviour of the relative fluid parcel position variance is expected to exhibit two regimes: an inertial regime and a diffusion regime. In the inertial regime, the fluid parcel relative position variance is a direct function of the initial fluid parcel velocity variance $\mathrm{Var}\left[\boldsymbol{V}_f(0)\right]$ (cf. Eq. 1.29):

$$\mathbb{E}\left[\|\boldsymbol{X}_f(t) - \boldsymbol{X}_f(0)\|^2\right] \sim_0 \mathrm{Var}\left[\boldsymbol{V}_f(0)\right] t^2.$$

If one considers one fixed position in the domain, for a DNS, particle trajectories are deterministic, the local fluid velocity is known, so $\mathrm{Var}\left[\boldsymbol{V}_f^{\mathrm{DNS}}(0)\right]$ is equal to 0 (left of Fig. 5.1). Thus, there is no dispersion. On the opposite, for a RANS computation, except for its mean, nothing is known about the local fluid velocity (right of Fig. 5.1). Thus, $\mathrm{Var}\left[\boldsymbol{V}_f^{\mathrm{RANS}}(0)\right]$ encompasses all the energy of the flow and is equal to whole fluctuations of the flow $\mathrm{Var}\left[\boldsymbol{V}_f\right]$. As implied by its formalism, non-injective LES is in-between. The amount of resolved energy accounts for deterministic motion, whereas the amount of unresolved energy acts as a dispersive force on the fluid parcels. It corresponds to the slope of the initial ballistic regime of dispersion $\mathrm{Var}\left[\boldsymbol{V}_f(0)\right]$.
In the case of non-injective LES, only 80% of the fluid energy is known at a particle location (Pope (2000), p. 560 Table 13.1). The remaining 20% are not only not resolved, but also not specified by the residual field. This is very different from DNS, where the residual scales are unique. This implies that the MEF extended to non-injective LES is forced by a for which 20% of the energy is unknown and not fixed. Therefore, contrarily to DNS, the non-injective LES derivation of the MEF has to take into account a stochastic dispersive force implied by this range of different residual velocity fields possibly accounting for the unresolved energy. As such, when 20% of the fluid energy is unresolved, we have seen in Chap. 4 that it could also alter the disperse phase energy up to 20%. Therefore, following Taylor (1921), a non-injective LES derivation of the MEF could be up to 20% more dispersive than the MEF in DNS.
It is expected that standard MEF behaves differently than its extension to non-injective LES. It is very important to assess this difference precisely in order to characterise MEF in non-injective LES simulations cases and pave the way to coupled cases. Furthermore, in the perspective of deriving closures for reduced simulations, properly apprehending the reference behaviour of the quantity to close is essential.
The next chapters of this work are dedicated to defining the setup for investigating the evolution of the MEF in the context of non-injective LES. Although the evolution at the initial time for fluid particles are quite clear with Taylor analysis, mixed effects of long time behaviours, inertia and filtering can be quite complex. Therefore, a numerical setup was devised in order to be able to investigate these effects.

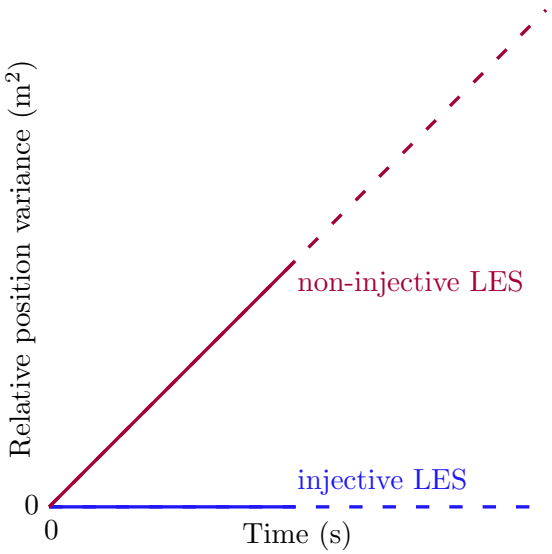

Figure 5.3. Impact of non-injective LES on the MEF on relative position variance of an initial Dirac distribution as predicted by Taylor. Injective LES (in blue) and non-injective LES (in red).

Highlights and conclusions

In this chapter, we have introduced a new formalism in order to understand the challenges of designing an average mesoscopic model for strongly coupled two-phase flows in the context of LES. We have found that, before introducing the two-way coupling, it was already necessary to introduce a new mesoscopic formalism in order to have a consistent LES approach for two-phase flow. This new formalism is reference under the name EMEF in the context of this work. In order to assess the effect of adopting this new paradigm for the disperse phase, we propose two metrics:

- the energy of the unresolved flow fields for measuring the distance between the definition of the EMEF and the definition of the usual MEF,
- and the spatial variance of the respective distributions of the EMEF and of the MEF for assessing the effect of these two different definitions on the actual evolution of the resulting distributions.

In the end, we have presented from an *a priori* analysis the relation that we expect between these two metrics of interest: we expect the spatial variance of the distribution to be positively correlated with the energy of the unresolved flow field. This is what we propose to confirm in the following of this work.

Chapter 6

Numerical set-up for investigation

For numerically characterising the impact of the extension of the MEF to non-injective LES (introduced in Sec. 5.3.1), a probability space of fluids for performing the conditional averaging operation is needed.

- Ideally, one would want to work with turbulent solutions of the Navier-Stokes equations. However, today, to our knowledge, there is no explicit formulation of the probability space associated to turbulent solutions of the Navier-Stokes equations.
- A solution could be to build an empirical measure. However, the dimensionality of turbulent solutions of the Navier-Stokes equations is very large (Sec. 3). Therefore, it seems unreasonable to converge such an empirical measure in the perspective of this work.
- The strategy chosen in this work is to resort to a model of the probability space of turbulence. The model giving the set of turbulent flows comes from Kraichnan (1970). In this work, the probability measure we chose to consider on this set has been derived from numerical simulations of the Navier-Stokes equations by Hunt, Buell, and Wray (1987).

Such simulations are named Kinematic Simulations (KS) in the literature and are already widely studied although not in the context of non-injective LES. Let us review here some examples of the literature.

- Some studies focus on the fluid field given by the KS, such as:
  - Kraichnan (1970) studied the diffusion and directed-interaction approximation of fluid particles in 2 and 3 dimensions for different energy spectrum.
  - Fung, Hunt, Malik, Perkins, Vassilicos, Wray, Buell, and Bertoglio (1991), Murray, Lightstone, and Tullis (2016) investigated Eulerian and Lagrangian statistics of the flow field given by Kinematic Simulations.
  - Fung and Vassilicos (1998), Thomson and Devenish (2005) and Bec, Biferale, Lanotte, Scagliarini, and Toschi (2010) studied fluid particle pair dispersion.
- Other studies used KS to study the effects of a turbulent-like flow on inertial particles:
  - Reeks (1980) studied Eulerian direct interaction.
  - Maxey (1987), Wang and Maxey (1993) and Stafford, Swailes, and Chakraborty

(2016) studied the gravitational settling of aerosol particles.
- Fung and Vassilicos (1991) studied the fractal dimensions of lines advected by the flow.
- Bec (2003), Fung and Vassilicos (2003), Bec, Biferale, Cencini, Lanotte, Musacchio, and Toschi (2007), Ijzermans, Meneguz, and Reeks (2010) studied the fractal clustering of inertial particles.

We present the selected fluid in Sec. 6.1 and then detail its numerical implementation in Sec. 6.2.

6.1 Selected fluid

In this section, let us present the fluid used for kinematic simulation.

Definition 22. Let $\kappa_{\min}, \kappa_{\max}$ and k be positive real numbers such that $\kappa_{\min} < \kappa_{\max}$. We define k_0 such that:

$$k_0 = \kappa_{\min}^{-2/3} - \kappa_{\max}^{-2/3}, \tag{6.1}$$

and

$$k' = k/k_0. \tag{6.2}$$

Let $\mathrm{N}_\kappa \in \mathbb{N}^+$. For $n \in [\![1, \mathrm{N}_\kappa]\!]$, we define:

- the array $\boldsymbol{a}_n \in \mathbb{R}^3$:
  - of norm $\|\boldsymbol{a}_n\| \sim \mathcal{N}^{\mathrm{R}}\left(0, \frac{2k}{\mathrm{N}_\kappa}\right)$, with $\mathcal{N}^{\mathrm{R}}$, the folded normal distribution,
  - and of direction random on a sphere.
- the array $\boldsymbol{\kappa}_n \in \mathbb{R}^3$:
  - of norm

$$\|\boldsymbol{\kappa}_n\| = \left(\kappa_{\min}^{-2/3} - ((n-0.5)/\mathrm{N}_\kappa).k_0\right)^{-3/2}, \tag{6.3}$$

  - and of direction random on a circle orthogonal to $\boldsymbol{a}_n$.
- $\varphi_n \sim \mathcal{U}(0, 2\pi)$, with $\mathcal{U}$ the uniform distribution.
- $\omega_n \sim \mathcal{N}\left(0, (a\|\boldsymbol{\kappa}_n\|)^2 k\right)$, with $\mathcal{N}$ the normal distribution, and $a = 0.4$.

The *synthetic flow field* is given by:

$$\mathtt{u}_f(t, \boldsymbol{x}) = \sum_{n=1}^{\mathrm{N}_\kappa} \boldsymbol{a}_n \cos\left(\omega_n t + \boldsymbol{\kappa}_n \cdot \boldsymbol{x} + \varphi_n\right). \tag{6.4}$$

Let $E_{\text{continuous}}$ be the energy spectrum of the form:

$$\kappa \in \mathbb{R}^+ \mapsto \begin{cases} 2k'/3.\kappa^{-5/3} & \text{for } \kappa_{\min} < \kappa < \kappa_{\max}, \\ 0 & \text{otherwise,} \end{cases} \tag{6.5}$$

Remark. *Instead of $E_{continuous}$, we could have chosen the model spectrum of Pope (2000), Chap. 6.5.3. A simpler choice has been made for this work. As the focus is on LES, it implicitly assumes that one is most likely to be confronted with a turbulent flow at very high Reynolds number (large range of scales, vast inertial range). Furthermore, ideally, the flow reduction has to remove flow scales in a regime considered as universal (inertial and dissipation ranges). Thus only a flow similar to the inertial range is considered in this work.*

Now, let us state some properties of our flow field.

Property 3. *The numbers $\mathfrak{k}_n = \left(\kappa_{min}^{-2/3} - ((n-1)/N_\kappa)).k_0\right)^{-3/2}$, $n \in [\![1, N_\kappa]\!]$ subdivide the energy spectrum $E_{continuous}(\kappa)$ in N_κ intervals of equal energy.*

Proof.

$$\begin{aligned} \int_{\kappa_{\min}}^{\mathfrak{k}_n} E_{\text{continuous}}(\kappa)\,\mathrm{d}\kappa &= 2k'/3 \cdot \frac{1}{-2/3}\left[\kappa^{-2/3}\right]_{\kappa_{\min}}^{\mathfrak{k}_n} \\ &= k' \cdot \left(\kappa_{\min}^{-2/3} - \mathfrak{k}_n^{-2/3}\right) \\ &= k' \cdot \left(\kappa_{\min}^{-2/3} - \left(\kappa_{\min}^{-2/3} - ((n-1)/\mathrm{N}_\kappa).k_0\right)\right) \\ &= \frac{(n-1).k}{\mathrm{N}_\kappa} \end{aligned} \tag{6.6}$$

Therefore, for $n \in [\![1, \mathrm{N}_\kappa]\!]$

$$\int_{\mathfrak{k}_{n-1}}^{\mathfrak{k}_n} E_{\text{continuous}}(\kappa)\,\mathrm{d}\kappa = \frac{k}{\mathrm{N}_\kappa} \tag{6.7}$$

□

Property 4. *The total energy of the spectrum $E_{continuous}$ is k.*

Proof.

$$\begin{aligned} \int_{\kappa_{\min}}^{\kappa_{\max}} E_{\text{continuous}}(\kappa)\,\mathrm{d}\kappa &= 2k'/3 \cdot \frac{1}{-2/3}\left[\kappa^{-2/3}\right]_{\kappa_{\min}}^{\kappa_{\max}} \\ &= k' \cdot \left(\kappa_{\min}^{-2/3} - \kappa_{\max}^{-2/3}\right) \\ &= k \end{aligned} \tag{6.8}$$

□

Property 5. *The modes $\|\boldsymbol{\kappa}_n\|$ of the fluid (Eq. 6.4) represent a quadrature of the energy spectrum $E_{continuous}$ at the barycentre of segments of constant energy.*

Proof. For $n \in [\![1, \mathrm{N}_\kappa]\!]$, the wave-number of average energy on the interval $[\mathfrak{k}_{n-1}, \mathfrak{k}_n]$ is:

$$\|\boldsymbol{\kappa}_n\| = \left(\kappa_{\min}^{-2/3} - ((n-0.5)/\mathrm{N}_\kappa).k_0\right)^{-3/2} \tag{6.9}$$

$$\int_{\mathfrak{k}_n}^{\|\boldsymbol{\kappa}_n\|} E_{\text{continuous}}(\kappa)\,\mathrm{d}\kappa = \frac{1}{2}\cdot\frac{k}{\mathrm{N}_\kappa} \tag{6.10}$$

□

Property 6. *The flow field has null divergence.*

Proof.

$$\nabla_{\boldsymbol{x}} \mathtt{u}_f = \sum_{n=1}^{\mathrm{N}_\kappa} \boldsymbol{\kappa}_n \cdot \boldsymbol{a}_n \sin\left(\omega_n t + \boldsymbol{\kappa}_n \cdot \boldsymbol{x} + \varphi_n\right). \tag{6.11}$$

Because $\boldsymbol{\kappa}_n$ is chosen orthogonal to $\boldsymbol{a}_n$,

$$\boldsymbol{\kappa}_n \cdot \boldsymbol{a}_n = 0, \tag{6.12}$$

therefore,

$$\nabla_{\boldsymbol{x}} \mathtt{u}_f = 0. \tag{6.13}$$

□

Property 7. *The flow field is statistically homogeneous.*

Proof. Let us consider $\boldsymbol{z} \in \mathbb{R}^3$.

$$\begin{aligned} \mathtt{u}_f(t, \boldsymbol{x}+\boldsymbol{z}) &= \sum_{n=1}^{\mathrm{N}_\kappa} \boldsymbol{a}_n \cos\left(\omega_n t + \boldsymbol{\kappa}_n \cdot (\boldsymbol{x}+\boldsymbol{z}) + \varphi_n\right) \\ &= \sum_{n=1}^{\mathrm{N}_\kappa} \boldsymbol{a}_n \cos\left(\omega_n t + \boldsymbol{\kappa}_n \cdot \boldsymbol{x} + (\boldsymbol{\kappa}_n \cdot \boldsymbol{z} + \varphi_n)\right). \end{aligned} \tag{6.14}$$

Let a call $\Delta\varphi_n = \boldsymbol{\kappa}_n \cdot \boldsymbol{z}$. Because φ_n are independent random variables uniformly distributed on $[0, 2\pi]$, $\Delta\varphi_n + \varphi_n$ are independent random variables uniformly distributed on $[\Delta\varphi, 2\pi + \Delta\varphi]$. Because cos is 2π-periodic, the random field $\mathtt{u}_f(t, \boldsymbol{x}+\boldsymbol{z})$ has the same distribution as the random field $\mathtt{u}_f(t, \boldsymbol{x})$. □

Property 8. *For each wave-number $\|\boldsymbol{\kappa}_n\|$, the distribution of frequencies directly follows the work of Ijzermans, Meneguz, and Reeks (2010), where the spectral components of the energy spectrum are chosen in order to respect the numerical simulations performed by Hunt, Buell, and Wray (1987).*

Proof. By definition of the distribution of the wave-numbers of the synthetic fluid. □

Property 9.

$$\int_{\kappa_{min}}^{\mathfrak{k}_n} E_{continuous}(\kappa)\,\mathrm{d}\kappa = \mathbb{E}\left[\sum_{m=1}^{n} \frac{1}{2}\boldsymbol{a}_m^2 \boldsymbol{\delta}_{|\boldsymbol{\kappa}_m|}\right]. \tag{6.15}$$

Proof.

$$\begin{aligned}\mathbb{E}\left[\sum_{m=1}^{n} \frac{1}{2}\boldsymbol{a}_m^2 \boldsymbol{\delta}_{|\boldsymbol{\kappa}_m|}\right] &= \sum_{m=1}^{n} \frac{k}{\mathrm{N}_\kappa}\boldsymbol{\delta}_{|\boldsymbol{\kappa}_m|} \\ &= \frac{n.k}{\mathrm{N}_\kappa}.\end{aligned} \tag{6.16}$$

□

Remark. *the synthetic flow field is such that its spectral representation is very hollow. It only has energy on one wave-vector $\boldsymbol{\kappa}_n$ in one direction per wave-number κ_n. Only a limited number of wave-numbers are represented. They are scattered in a geometric fashion. Similarly to Ijzermans, Meneguz, and Reeks (2010), each mode carries on average the same amount of energy $\frac{k}{N_\kappa}$, with k the total amount of fluid energy on average.*
The hollowness of the synthetic flow field allows to represent of a vast range of fluid scales with a very limited amount data. This property is very useful when investigating LES.

Property 10. *The case has only two dimensionless parameters.*

Proof. The free physical parameters of the fluid are the minimal wave-number $\kappa_{\min}$, the maximal wave-number $\kappa_{\max}$ and the total energy k. Therefore, the only free physical parameters of the two-phase flow simulation are $\kappa_{\min}$, $\kappa_{\max}$, k and τ_p. With Buckingham π theorem it is possible to make only two dimensionless parameters from these variables. □

In this work, we have chosen to express them in terms of Stokes numbers:

- one for the largest scales of the flow: $\mathrm{St}_{\mathrm{large}} = \tau_p \kappa_{\min}/\sqrt{k}$,
- and one for the smallest scales of the flow: $\mathrm{St}_{\mathrm{small}} = \tau_p \kappa_{\max}/\sqrt{k}$.

In the following, we will mostly consider the Stokes number based on the largest scales of the flow: $\mathrm{St} = \mathrm{St}_{\mathrm{large}}$.
To get a idea of the fluid in physical space, the left hand-side of Fig. 6.1 represents the intensity of the fluid velocity field along a plane, and the right hand-side of Fig. 6.1 represents a particle trajectory on this fluid.

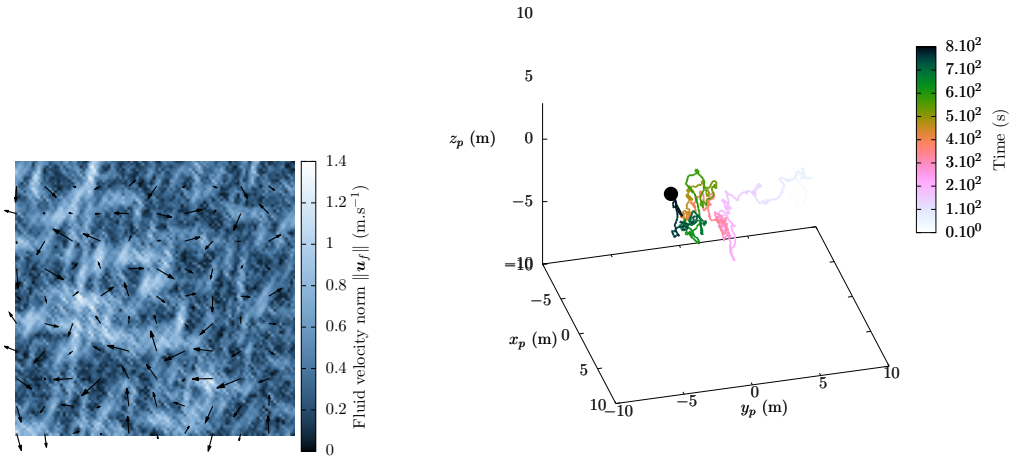

Figure 6.1. On the left hand-side, colormap of the intensity of the fluid velocity field in the plane $z = 0$ superimposed to a quiver plot of fluid velocities projected on the plane $z = 0$.. On the right hand-side, example of a fluid particle trajectory
Fluid of 200 modes with wave numbers between 1m^{-1} and 10000m^{-1} and total energy of $1\text{m}^2.\text{s}^{-2}$. The size of the colormap presented here is 1m×1m.

6.1.1 Limitations of the chosen synthetic fluid

For someone who would want to study turbulence, the main limitations of the synthetic fluid chosen are that:

- The fluid does not follow Navier-Stokes equations, which are usually the reference for turbulence simulation,
- The Eulerian spectrum of the synthetic fluid is sparse by construction of the synthetic fluid, which is not the case for real turbulence.
- Correlations are imposed a priori to the fluid from the work of Hunt, Buell, and Wray (1987). We do not expect to get more correlations in the fluid than the ones we have already included in the design of the fluid.
- The average spectra is fixed to follow Kolmogorov's law. Therefore, it is not straightforward to simulate phenomena which are likely to have an impact on the turbulent spectra, such as coupling.

For more works on the ability of Kinematic Simulations to reproduce some properties of turbulence, it is possible to refer to Thomson and Devenish (2005) and Nicolleau and Aly (2012).
These limitations, stated in the general sense, do not affect the work presented here. Indeed, this study does not intend to provide fundamentally new understandings of turbulence. The focus is on providing some understanding on the implications of a non-injective fluid reduction on the derivation of a MEF for inertial particles. For this study,

a flow similar to fluid turbulence and easily compatible with non-injective self-contained reductions is devised. The synthetic flow field is only here for illustration purposes. The choice of this synthetic flow field helps to present illustrations in a context similar to turbulence. In fact, *a posteriori*, any sort of mixing flow with a known probability space would have been enough to derive the results presented in Chap. 9.

6.2 Numerical implementation

In this section, the choice of architecture for the code used in this work is presented. It is implemented in `Fortran 90`.

6.2.1 Numerical integration of particle trajectories

Numerical integration is done with Euler-Maruyama or fourth order Runge-Kutta schemes, depending on the case at hand. Stochastic integration is done with the Euler-Maruyama scheme. Deterministic integration is done preferably with the fourth order Runge-Kutta scheme, except when comparison with a stochastic case is needed.
Forward Euler method is a first order integration technique for ordinary differential equations (ODE), whereas Runge-Kutta method (RK4) is fourth order. That is why RK4 integration is used preferably to Euler integration in the context of ODE.
For stochastic differential equations (SDE), accuracy of numerical schemes is specified in terms of laws. The Euler-Maruyama method converges with strong order 1/2 to the true solution. Under specific conditions on the SDE, higher order algorithms exist, but they are not used in the context of this work. The maximum theoretical strong order is 1 (Rüemelin (1982)).

6.2.2 Parallelisation

The code aims at computing efficiently statistics of the trajectories of particles on synthetic fluids. A synthetic fluid is made of a number of modes N_κ. These modes are labelled as *small eddies* (SE) or *large eddies* (LE) according to the choice of the amount of energy resolved by the large scales. The small eddies represent represent the portion of the fluid which is removed by the regularisation operation, while the large eddies represent the reduced flow field. For the simulation, statistical parameters are given, such as the number of particles N_p, the number of large scales N_{LE}, and the number of small scales N_{SE} to be computed in the simulation. The total number of synthetic fluids for the simulation is then $\mathrm{N}_{\mathrm{SE}} \times \mathrm{N}_{\mathrm{LE}}$. The total number of particle trajectories is given by $\mathrm{N}_p \times \mathrm{N}_{\mathrm{SE}} \times \mathrm{N}_{\mathrm{LE}}$.
Each particle trajectory requires access to the corresponding synthetic fluid and to the state variables of the particle. Information for each fluid is quite large ($9 \times \mathrm{N}_\kappa$ double precision real numbers, with N_κ up to 200) compared with that of the particles. Indeed each particle is represented by $3 \times 5 \times 6$ (dimensions $\times$ number of state variables $\times$ (current state + number of increments + future state)) double precision real numbers for RK4 scheme or by $3 \times 5 \times 2$ double precision real numbers for Euler-Maruyama

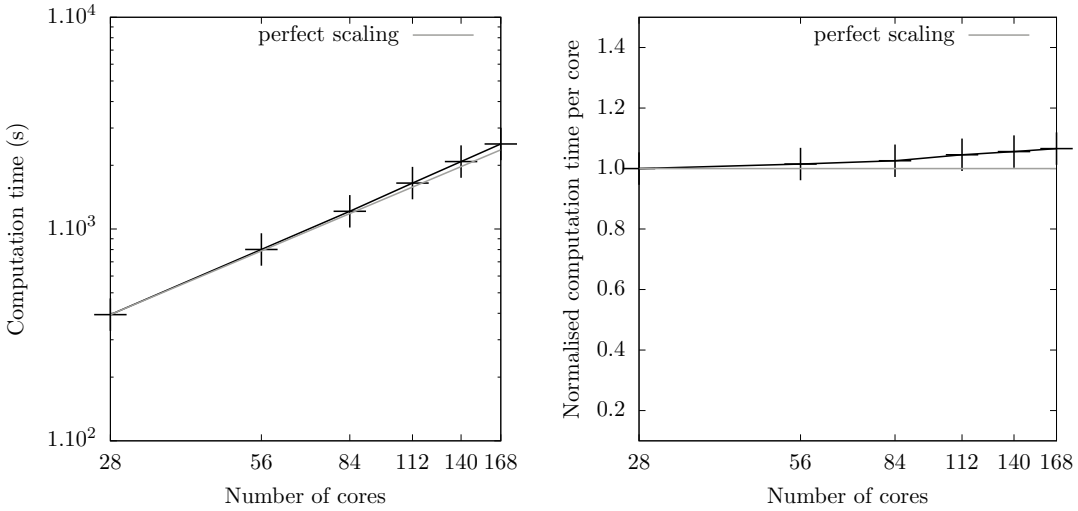

Figure 6.2. Parallel scaling of the computation of 16 particles on different numbers of cores. With a constant number of 8 fluids per core. Fluids of 200 modes and computation of 1000 integration time steps. Parallelisation in the dimension of the fluids. Reference time taken for one core (28 cores).

scheme. Therefore parallelisation is done in the dimension of the fluids first and 6.2), and next in the dimension of the particles and 6.3). This strategy naturally degenerates to a parallelisation only on the particles when the number of fluids falls to 1.
When parallelisation is done only in the dimension of the fluids , several fluids on the same core can share the same large scales/small scales. Therefore, in a memory optimisation strategy, it could be useful in the future to gather the fluid parameters which are the same for different fluids on a given core (this problematic is similar to the work done by de Chaisemartin (2009)).
By default, not much communication between the processes is needed during the computation (except for data processing). The number of particle trajectories is quite large and they evolve independently from each other. Therefore, MPI is quite an obvious choice for parallelisation (as opposed to an OpenMP strategy in this context).
Parallelisation is performed with a message passing interface (`MPI`) and works seamlessly on computers as different as a personal workstation (with a maximum of 4 core/job), Moulon mésocentre (with a maximum of 240 core/job) and the national cluster Occigen (tested with a maximum of 2800 core/job).

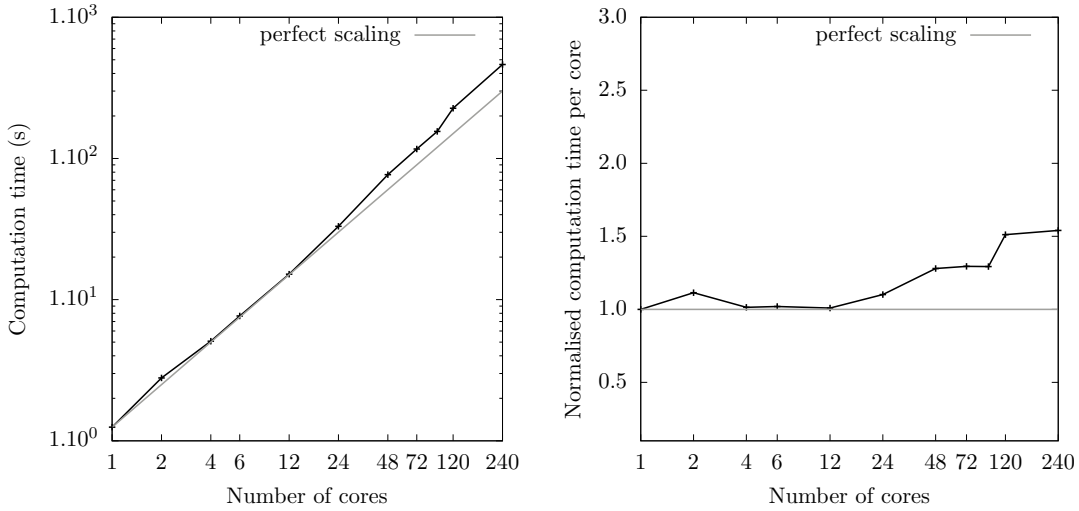

Figure 6.3. Parallel scaling of the computation of 256 particles per cores for different numbers of cores on 1 fluid of 100 modes for 1000 time steps. Parallelisation in the dimension of the particles.

6.2.3 Random number generation

For the numerical simulations, the random number generator chosen is `ran2` presented in Press, Flannery, Teukolsky, and Vetterling (1989). Each process has to start from a different point in the sequence of pseudo-random numbers, so that processes do not get overlapping sequences (Fig. 6.4). If different processes use the same numbers in the sequence of pseudo-random numbers, their evolution is correlated. Therefore, this is to be avoided. For the time being, each process iterates through the sequence of pseudo-random number until it reaches a region where it is guaranteed that there will not be any overlapping during the simulation (among other things, this is function of the number of particles on each core and of the number of integration time steps the simulation is required to perform). This implies that each core has a different initial workload according to the region it aims for in the sequence of pseudo-random number. Optimisations exists for better balancing this initial workload and could be implemented in the future of this work. For more insight on how to optimise number generation for parallel processes, one can have a look for instance at L'Ecuyer (2015).

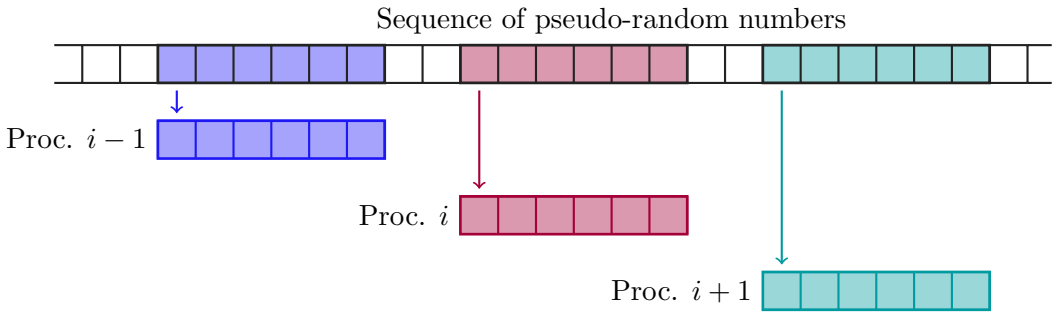

Figure 6.4. Illustration of pseudo-random number management in a parallel context. Each process uses a non-overlapping regions of the sequence of pseudo-random numbers given by a given pseudo-random number generator (for this purpose, the algorithm `ran2` is used in this work).

6.2.4 Data processing

The two main data processing integrated to the parallelised code are:

- variance of particle state variables,
- and power spectral densities along particle trajectories.

In order to get converged quantities, the constraints are quite different. The convergence of time resolved variances of the disperse phase requires the computation of a very large set of particles during the time of interest. On the contrary, the convergence of power spectral densities on wide range of time scales requires the computation of a limited number of particles for an extended amount of time.
Computation of the variance of particle state variables is done across cores on the fly, only for some time steps of interest, with the expanded formula which is very easy to parallelise (Eq. 6.17):

$$\mathrm{Var}\,(X) = \mathbb{E}\left[X^2\right] - \mathbb{E}\left[X\right]^2, \tag{6.17}$$

with X a random variable. This numerical strategy could be upgraded for more stability (Chan, Golub, and LeVeque (1982)). Indeed, computing a large sum of small floating point variables is not recommanded for numerical precision.

Computation of power spectral densities is done using fixed length arrays of various resolution. In order to get the spectral content of particle trajectories over a wide range of scales and at an affordable cost, different arrays collect data points along particle trajectories at various constant frequencies (multiples of the integration frequency, see Fig. 6.5). This data is windowed according to the analysis to be performed (Scholl (2016)). Windowing consists in convoluting the original signal by a normalised kernel. It aims to attenuate the effects of observing an permanent signal only during a finite time-span. Each window has its pros and cons: a square window preserves the energy of the signal, a flattop window preserves the energy in modes, and a Hann window is a good compromise for *a priori* observation of the signal.

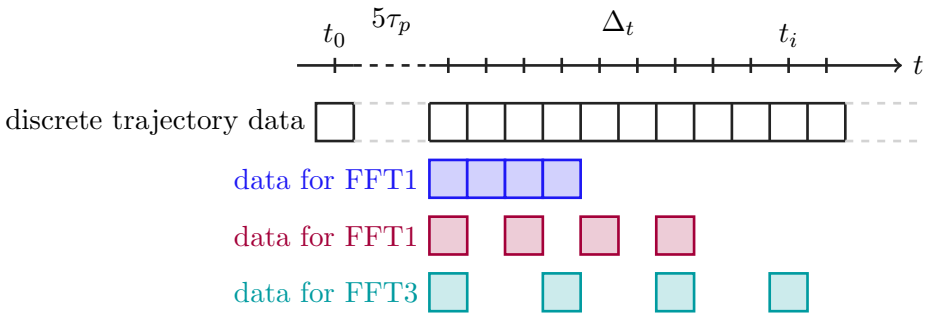

Figure 6.5. Chosen strategy for computing the discrete Fourier transform of a signal over a wide range of scales at a reasonable cost.

Fourier transform is then performed over each array with a fast Fourier transform algorithm. The data from several windows can be averaged in order to increase the signal to noise ratio.
Power spectral densities are used here to study the permanent regime. In order to do so, computations are run during $5\tau_p$ before collecting any data for the computation of the Fourier transforms.
Further optimisation could be envisioned with the parallelisation of the fast Fourier transform algorithm. When possible, it could also be desirable to increase the integration time step when the high frequency Fourier transform is already performed and only the low frequency content of trajectories remains to be sampled. Furthermore, it could be possible to optimise the size of the arrays used for storing the data used as input for the FFT algorithm so that is consistent with the fast memory available on each core for a given cluster.

Highlights and conclusions

- We have presented a numerical set-up adapted to the study of the EMEF proposed in Chap. 9.
- This numerical set-up is based on kinetic simulations of turbulence, which fluid:
  - presents properties similar to turbulence such as a power spectral density following the scaling of Kolmogorov and,
  - also allows an explicit access to the whole probability space associated to the fluid, which is crucial for studying the EMEF.
- Because we envision to compute converge statistics over a large number of dimensions, we presented a numerical implementation of the numerical integration of inertial particles on a compiled code adapted to parallel computing.

Chapter 7

Characterisation of the behaviour of the fluid

The objective of this chapter is to characterize the dispersive behaviour of the flow field given by Kinematic Simulations (KS). It is useful because KS are subsequently used to compute the evolution of inertial particles in Chap. 8 and eventually to study the EMEF in Chap. 9. We focus our analysis on three aspects:

- *The similarity of KS with the picture of turbulence given by Kolmogorov.* This is mainly asserted by the reproduction of an average distribution of energy close to the scaling of the inertial range given by Kolmogorov. This is investigated by representing the power spectral density of the flow field, and also confirmed indirectly by the observation of particle pair dispersion.
- *The one-point dispersive properties of the field.* The corresponding quantities are the temporal evolution of variance of tracers, the Lagrangian fluid velocity autocorrelation and the autocorrelation time scale. These metrics correspond to the quantities observed in the analysis of the EMEF conducted in Chap. 9.
- *The characteristic scales of the dynamics of the flow field.* This is for instance the case of the autocorrelation time scale or of the average power spectral density which gives an average representation of the relative magnitude of the scales of the flow field.

Some works (such as Kraichnan (1970) and Murray, Lightstone, and Tullis (2016)) have already presented some results of dispersion in a flow field given by KS. However, to our knowledge, an extensive study focused on the influence of the sampling range and sampling frequency of KS on the dispersive properties of the flow field has not been conducted in the literature.

Therefore, in this chapter we observe the following properties of the flow field in this order, according to the number of modes of KS:

- the power spectral density,
- one-point dispersion,
- and two-points dispersion.

7.1 Influence of the range and number of modes used in the representation of the fluid

In this section, we present the power spectral density of the flow field for different ranges and numbers of fluid modes. The objective is to get:

- a range of modes which is wide enough to be convincingly representative of the spectrum of fully developed turbulence,
- a number of modes large enough to cover this spectrum and still but remains computationally tractable.

7.1.1 Range of modes

We first investigate the influence of the range of modes $]\kappa_{\min}, \kappa_{\max}[$ used for representing the fluid on the norm of the wave-numbers κ_n, for $n \in [\![1, \mathrm{N}_\kappa]\!]$ (Eq. 6.3). When keeping $\kappa_{\min} = 1.\mathrm{m}^{-1}$, the range of modes $]\kappa_{\min}, \kappa_{\max}[$ is controlled by the value of $\kappa_{\max}$.
Fig. 7.1 represents the influence of the range of fluid wave-numbers, given by the value of $\kappa_{\max}$, on a fixed number N_κ of ten modes. Asymptotes are represented in dotted lines and $\kappa_{\max}$ is represented with a lighter shade. We can see that when $\kappa_{\max}$ increases, the norm of the fluid modes κ_n, for $n \in [\![1, \mathrm{N}_\kappa]\!]$ also increases. When $\kappa_{\max}$ goes towards infinity, each κ_n tends towards a fixed limit represented in Fig. 7.1 with dashed lines. Because $\kappa_{\mathrm{N}_\kappa}$ tends towards a finite limit when $\kappa_{\max}$ goes to infinity, this means that the range of higher wave-numbers of the range $]\kappa_{\min}, \kappa_{\max}[$ not represented by fluid modes in the KS $[\kappa_{\mathrm{N}_\kappa}, \kappa_{\max}]$ diverges as $\kappa_{\max}$ increases. This is perfectly consistent in terms of energy, because the scaling of the power spectral density in $\kappa^{-5/3}$ makes the energy of the range $[\kappa_{\mathrm{N}_\kappa}, \kappa_{\max}]$ very small. However, it has a strong impact in terms of the regularity of the flow field because it constrains the magnitude of the higher wave-numbers.

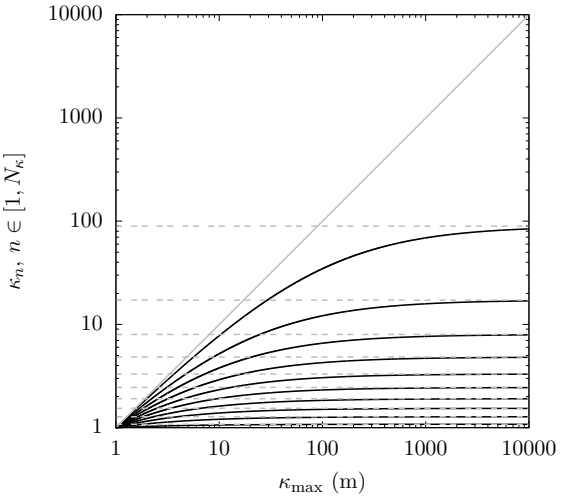

Figure 7.1. Influence of the range of fluid wave-numbers on the modes (here for 10 modes). Asymptotes are represented in dotted lines, and the first bisector with a lighter shade.

Now, let us observe the impact of range of modes $]\kappa_{\min}, \kappa_{\max}[$ on the power spectral density of the velocity of fluid parcels along their trajectory. It is represented in Fig. 7.2 for different ranges of fluid wave-numbers: 2, 10, 10^2, 10^3, 10^4 and 10^5, each represented in a distinct sub-figure. In this figure, the number of modes in the KS is kept constant and equal to N_κ =200. The lines in blue are computed for only one realisation of the KS field whereas the lines in black represent an average over several KS realisations. Blue lines are represented in order to visualise the variability of the power spectral density to individual KS realisations. Therefore, blue lines are naturally more tortuous than their black counterparts. For numeral tractability, each PSD is represented by the combination of different PSD computed at different resolutions and represented by the superposition of different lines of the same colour. It is possible to see their respective extremities pointing out of the superposition of the other levels of resolution. It is considered that these deviations are caused by the finite time span of the samples. In order to mitigate this effect, the samples are convoluted by a Hann window.
We observe that as the range of fluid wave-numbers is increased, the range of velocity fluctuation experienced by a fluid parcel also increases. When the range of fluid wave-numbers becomes large enough, above a decade, the scaling in $\kappa^{-5/3}$ starts to appear clearly in the PSD. Above three decades, the scaling in $\kappa^{-5/3}$ extends to the highest wave-numbers of the particle trajectory at the given resolution of the particle trajectory chosen for this figure. This is why for the following simulations, a range of four decades is usually considered.

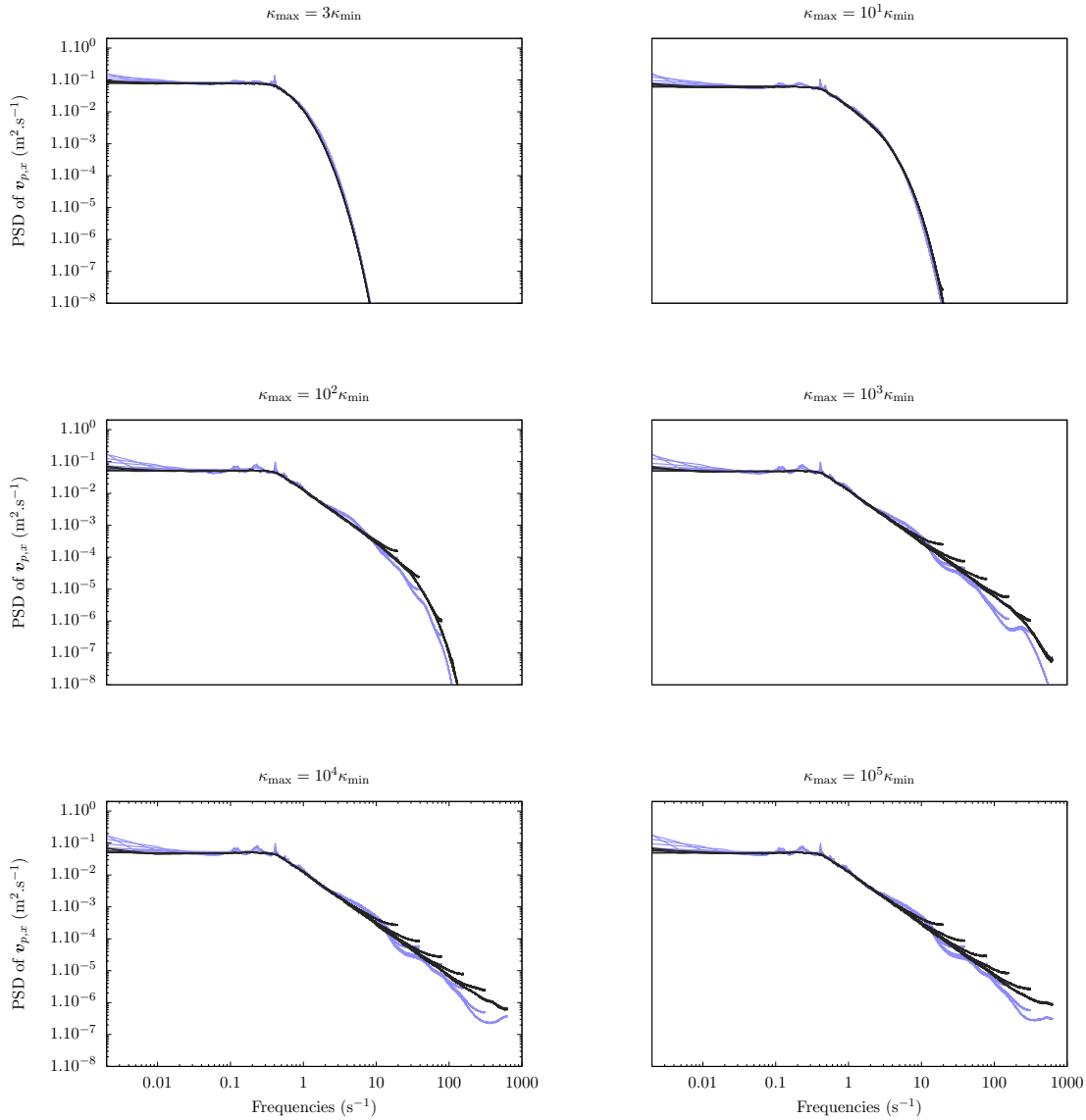

Figure 7.2. Influence of the range of fluid wave-numbers (indicated above each graph $\{2,10,10^2,10^3,10^4,10^5\}$) on the power spectral density of the velocity of a fluid parcel along its trajectory on 240 fields in black (and of 240 particles on 1 fluid in blue) of energy $1m^2.s^{-2}$ for 200 modes wave-number averaged 10 times. Graph shows the superposition of 6 PSD of 2^{14} points with Hann windowing of different resolutions in order to get a visualisation of a wide spectrum range. Trajectories computed with RK4 integration and a time step of $8.10^{-4}s$.

7.1.2 Number of modes

After having observed the influence of the range of the wave-numbers on the amplitude of the modes and on the PSD of the flow field, let us now look at the influence of the number of modes on the value of wave-numbers given by Eq. 6.3. Studying the influence of the number of modes of KS as also been performed in Fung and Vassilicos (1998) and Fung and Vassilicos (2003), although these articles are more focused on particle pair dispersion and particle segregation respectively.
Figure 7.3 represents the influence of the number of modes on the mode wave numbers. For this figure, the range of modes $]\kappa_{\min}, \kappa_{\max}[$ is chosen as $]1, +\infty[$. As can be observed on the left of Fig. 7.3 there is no convergence with the number of modes. This is better seen on the right of Fig. 7.3 which represents the norm of the wave-number of the first mode κ_1 and the last mode $\kappa_{\mathrm{N}_\kappa}$ according to the number of modes N_κ used for the representation of the fluid.

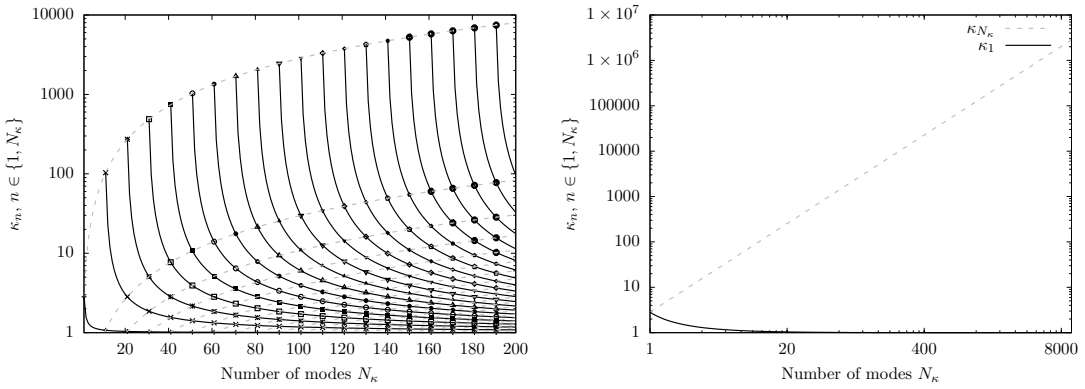

Figure 7.3. On the left: Influence of the number of modes on the mode wave numbers with $\kappa_{\max} = \infty$. In full lines with symbols are the n^{th} modes, whereas in dotted lines are the N_κ-n^{th} modes. Only modes with an index multiple of 10 are represented here.
On the right: Influence of the number of modes on the mode wave numbers with $\kappa_{\max} = \infty$. Here are only represented the first mode (in continuous black line) and the last mode (in dashed grey line).

Similarly to the Fig. 7.2, Fig. 7.4 represents the PSD of the velocity of fluid parcels along their trajectory. It is represented in Fig. 7.4 for different numbers of fluid modes: respectively 1, 4, 10, 25, 50, 100 and 200, each represented in a distinct sub-figure. In this figure, the range of modes in the KS is kept constant and equal to as $]\kappa_{\min}, \kappa_{\max}[=]1, +\infty[$. The lines in blue are computed for only one realisation of the KS field whereas the lines in black represent an average over several KS realisations.
We observe that for a very low number of modes (1, 2, 4), the shape of the PSD is difficult to converge. As the number of fluid wave-numbers is increased, from 10 modes onwards, the scaling in $\kappa^{-5/3}$ appears more clearly. Simultaneously, the range of velocity fluctuation experienced by a fluid parcel also increases and the scaling in $\kappa^{-5/3}$ extends well into the higher frequencies of the PSD. The PSD are more oscillatory at high wave-

numbers because they are much sparser as the wave-number increases. For 50 modes, the scaling in $\kappa^{-5/3}$ already extends over more than two decades. This is why for the following simulations, we will always consider sets of modes with at least 20 modes in them. This means that in order conduct an analysis of the EMEF for with different percentages of fluid energy resolved, by steps of 10% of the total energy, we consider an overall KS with a total of 200 modes.

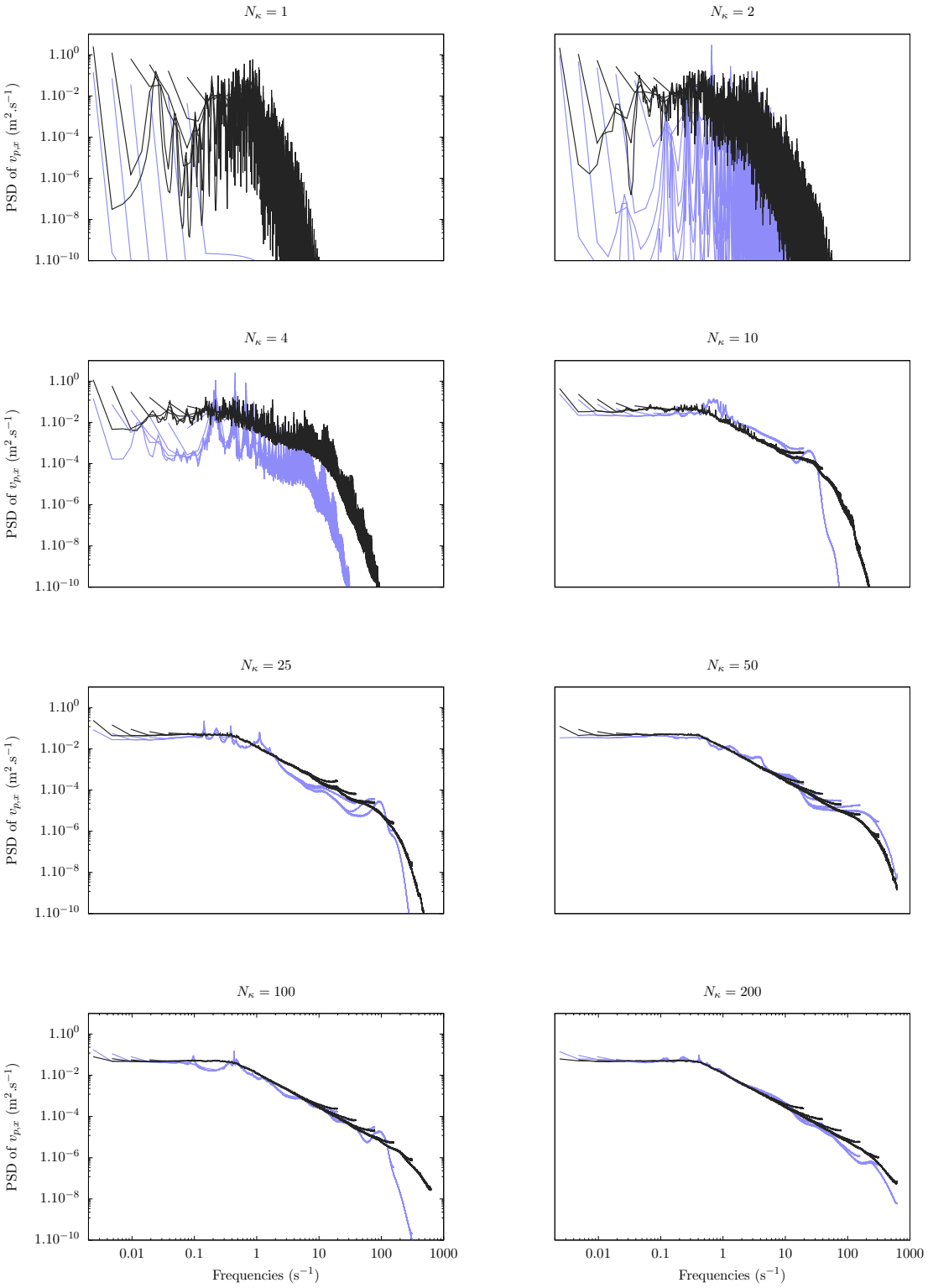

Figure 7.4. Influence of the number of fluid modes (indicated above each graph {1,4,10,25,50,100,200}) on the power spectral density of the velocity of a fluid parcels along its trajectory on a fluid of energy $1m^2.s^{-2}$ wave-number range between $1m^{-1}$ and 10^4m^{-1} averaged 10 times. In black lines, a particle on 240 different fluids. In blue lines, PSD of 240 particles on one fluid realization. Graph shows the superposition of 6 PSD of 2^{14} points with Hann windowing of different resolutions in order to get a visualisation of a wide spectrum range. Trajectories computed with RK4 integration and a time step of 8.10^{-4}s.

7.2 Fluid representation and scrambling behaviour

Definition 23. We consider that the flow field is *scrambling* for particles of finite inertia when:

- particle trajectories are sensible to initial conditions on this flow field,
- and particle trajectories are diffusive for long times.

These two properties are expected from turbulent flows (Taylor (1921), Farge (1992)) and impact the results presented in Chap. 9. Therefore, we investigate the influence of the number and the range of modes of the KS on these aspects. This chapter is only about the fluid, hence, the results presented in this section only focus on fluid particles. Results about inertial particles are presented in the next chapter.
In the case where the fluid is limited to only one mode, the case is one-dimensional, and not scrambling (Goudenège, Larat, Llobell, Massot, Mercier, Thomine, and Vié (2019)). As the number of mode increases, the flow becomes more and more intricate. It is expected that it can lead to a scrambling behaviour (as in Fung and Vassilicos (1998) for instance).
It is interesting to note that an alternate strategy to scrambling could have been to work with Arnold-Beltrami-Childress flow (ABC flow), which is known to be chaotic, and use it as a base element of kinematic simulations instead of simple sines. However, it has a super-diffusive behaviour which is not consistent with standard diffusive characterisations of turbulence. Therefore, we stick to standard KS for this work.
In order to find an adequate number of modes in the KS to get a diffusive behaviour of the particles, Fig. 7.5 presents the dispersion of tracers for different numbers of modes. Let us first present the figure and analyse the results observed. On the left of Fig. 7.5, logarithmic scales are chosen in order to distinguish the different regimes of the dispersion of the disperse phase. In this figure, three regimes can be observed:

- In the first regime (approximatively from 0s to 1s), dispersion is quadratic with time. This corresponds to a time when the motion of the tracers is still correlated to their initial velocity. It corresponds to the short time transport behaviour. From this figure, we deduce that this regime is not affected by the number of modes of the KS.
- After 1s, particles start to be dispersed at a linear rate. A linear dispersion rate is characteristic of diffusion. It corresponds to an erratic motion of the particles. Particle motion is not correlated to their initial state any more. This is exactly the kind of behaviour we are expecting from turbulence and that we are looking for in these KS.
  Observing Fig. 7.5, it appears that the time span of this regime is directly impacted by the number of modes of the fluid. When the fluid is represented by a very low number of modes (1, 2 or 3), diffusion is quasi non-existent. As the number of fluid modes increases (from 7 onwards), the diffusion regime exists for a longer time span. This behaviour is well understood when considering that the diffusion regime is representative of the erratic movements of the flow. When the fluid is

made of a low number of modes, its field is very simple, structured and correlated; far from scrambling. The fluid velocity seen by the particles is not intricate enough to lead to convincing diffusion. As the number of fluid modes increases, it resembles more and more closely a field which could lead to decorrelated motions. Therefore, the fluid particles tend to behaves as such for longer time spans.

- The last dispersion regime observed is again quadratic in time (transport), and lasts forever. From Fig. 7.5, its behaviour is also clearly a function of the number of fluid modes involved. As the number of modes increases, it appears later. Nonetheless, whatever the number of fluid modes tested, it is always present. This means that there is always a tiny amount of the particle energy which is correlated along the particle trajectory. Transport always becomes predominant with time, no matter how small its magnitude is, relative to the actual particle velocity. This is because correlation in time along a particle trajectory leads to a quadratic effect on the measure of dispersion represented in Fig. 7.5, as opposed to diffusion which is linear. This final transport regime is at a scale much larger than the largest scales of the flow. To our current knowledge, it is not referenced in the literature nor of interest for practical applications. Therefore, it is not the object of study of this work, which focuses mostly on the first two dispersion regimes: initial transport and diffusion. In the following, we take a number of fluid modes high enough so that during the timespan of observation, only the first two regimes are present: transport followed by diffusion.

The right of Fig. 7.5 represents exactly the same quantities as the left side, but with linear scales. This figure is here to stress out that although on the left of Fig. 7.5, the regimes of dispersion get closer to one-another as the number of fluid modes is increased, the actual dispersion does not converge as illustrated on the right of Fig. 7.5. Therefore, in the following, when studying models, each comparison will be done on the basis of one fluid representation, with a given number of modes.

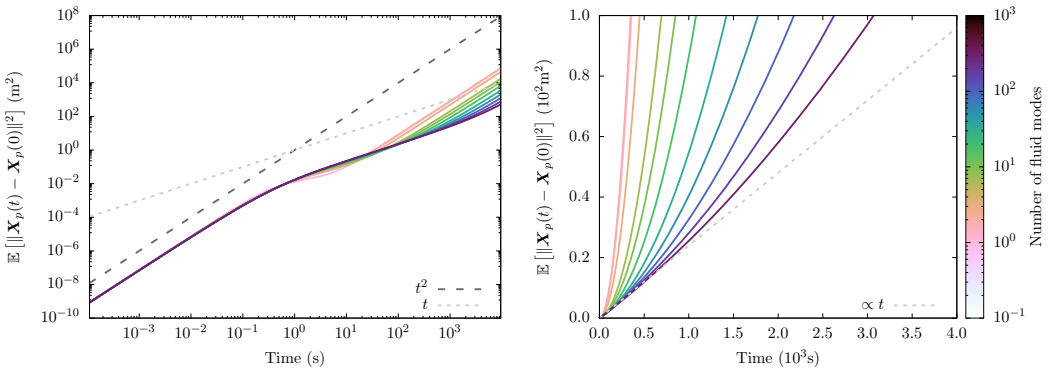

Figure 7.5. Evolution of the average dispersion of N_p=1024 fluid parcels over 1200 different fluids of different number of modes N_κ (indicated on the graph) between $\kappa_{\min} = 1$ m^{-1} and $\kappa_{\max} = 10^5$ m^{-1}, for a constant total fluid energy. Time step integration of dt=10^{-4}s.

Fluid parcel motion can sometimes be characterised by an autocorrelation time along

their trajectories.

Definition 24. When the integral of the autocorrelation of the particle velocity

$$R_{\boldsymbol{V}_p}(t) = \frac{1}{\mathrm{Var}\left[\boldsymbol{V}_p\right]} \int_{t_0}^{t} \mathbb{E}\left[\boldsymbol{V}_p(s)\boldsymbol{V}_p(t_0)\right] \mathrm{d}s \tag{7.1}$$

has a finite limit when t goes to $+\infty$, this finite limit is called *autocorrelation time*.

This autocorrelation time gives the average time it takes for a fluid parcel to be entirely uncorrelated from its initial velocity. It is the characteristic time of diffusion. For more on this measure and related concepts, one can have a look at Pope (2000), Appendix E and F.

In the case chosen here, we have already seen in Fig. 7.5, representing the dispersion of the particles by the flow field, that the final diffusion regime is always transport, which means that fluid particles always stay correlated to their initial state, although the magnitude of this correlation decreases as the number of modes in the KS increases. Therefore, the autocorrelation time of such fluid particles is not well defined (it is infinite).

In spite of these strict and theoretical considerations, let us nonetheless observe the autocorrelation of the velocity of fluid parcels along their trajectory. This quantity is represented in Fig. 7.6 for different numbers of modes: 1, 2, 4, 10, 25, 50, 100 and 200. The autocorrelation represented in Fig. 7.6 is simply computed as the inverse Fourier transform of the PSD in Fig. 7.4. We observe in Fig. 7.6 that the autocorrelation starts at 1, decreases rapidly, and then converges to a strictly positive constant in all the cases. Therefore, $R_{\boldsymbol{V}_p}$ diverges as t goes to $+\infty$ (Fig. 7.7). This is the reason why the autocorrelation time has no meaning in this case in the strict sense.

Even when the fluid is represented by 200 modes, $R_{\boldsymbol{V}_p}$ diverges (Fig. 7.7).

However, the speed of this divergence is directly related to the number of modes in the fluid (left of Fig. 7.8).

On the right of Fig. 7.8 (and also in Fig. 7.7), it is possible to identify two behaviours in the evolution of $R_{\boldsymbol{V}_p}(t)$. The first one starts at $t = 0$s and is marked by a very strong increase for $t = 0.25$s. After 0.25s, there is a breaking point and $R_{\boldsymbol{V}_p}(t)$ increases linearly at a slower pace. This change in behaviour corresponds to the time when $R_{\boldsymbol{V}_p}(t)$ converges towards a constant positive value (Fig. 7.8). This is a characteristic time of the fluid. It corresponds to the time when the dispersion regime changes from transport to diffusion.

The impact of the range of fluid modes in the temporal evolution of $R_{\boldsymbol{V}_p}(t)$ is represented in Fig. 7.9. This figure shows that the value of $R_{\boldsymbol{V}_p}(t)$ at the breaking point converges when increasing the range of wave-numbers for the modes representing the fluids. Therefore, this characteristic time of the fluid converges as the fluid range of representation increases.

The section was the opportunity to observe the scrambling characteristic of the flow from a frequency perspective. The results corroborate the observation of the previous section which focused on diffusion. We observe that strictly speaking, the particles have an infinite autocorrelation time. The divergence of $R_{\boldsymbol{V}_p}(t)$ with time is slower as the

number of modes increases. However, form a physical perspective, it is reasonable to consider that it is possible to define a time characteristic of the autocorrelation of the fluid particle velocity. The value of this time is around 0.25s for 200 modes (Fig. 7.7).

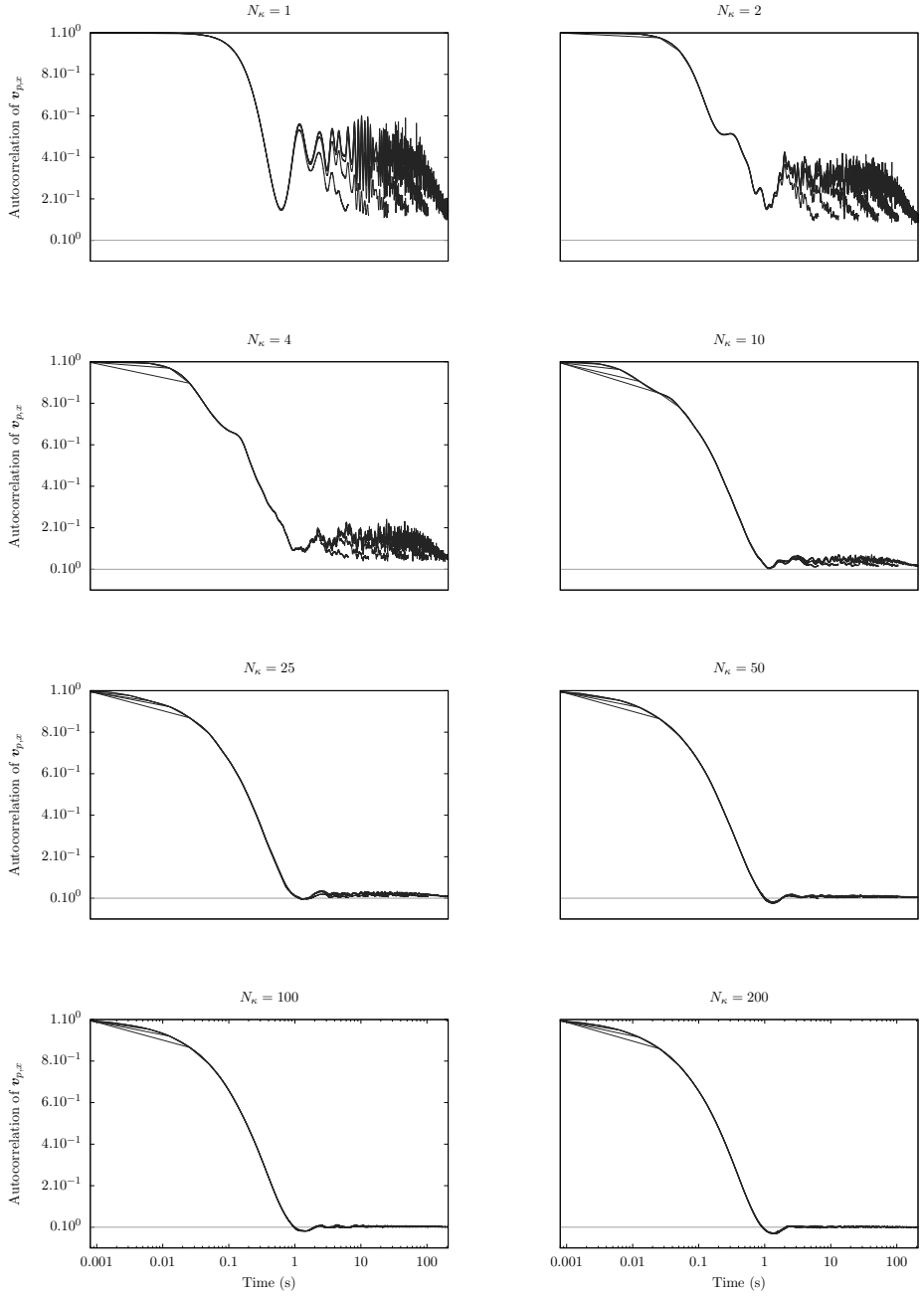

Figure 7.6. Influence of the number of fluid modes (indicated above each graph {1,2,4,10,25,50,100,200}) on the autocorrelation of the velocity of a fluid parcels along their trajectory on a fluid of energy $1\text{m}^2.\text{s}^{-2}$ wave-number range between 1m^{-1} and 10^4m^{-1} averaged 10 times. Graph shows the superposition of 6 autocorrelation of 2^{14} points with Hann windowing of different resolutions in order to get a visualisation of a wide range. Trajectories computed with RK4 integration and a time step of 8.10^{-4}s. For statistical consistency, autocorrelation of a particle on 240 different fluids is averaged.

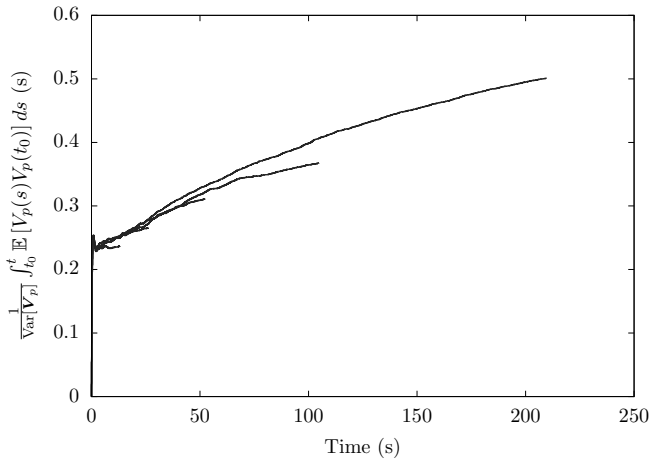

Figure 7.7. Evolution of $R_{\boldsymbol{V}_p}$ against time, on a fluid of 200 modes. Graph shows the superposition of 6 curves of different resolutions in order to get a visualisation of a wide range. Trajectories computed with RK4 integration and a time step of 8.10^{-4}s. For statistical consistency, autocorrelation of a particle on 240 different fluids is averaged.

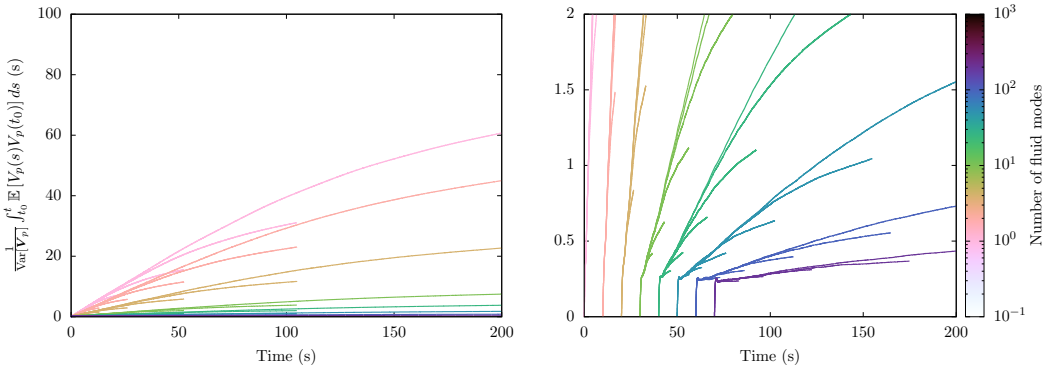

Figure 7.8. Evolution of the quantity $R_{\boldsymbol{V}_p}$ against time, for different numbers of fluid modes (1, 2, 4, 10, 25, 100 and 200). On the right curves are increasingly shifted on the x-axis with to the number of fluid modes, in order to get a better visualisation of the breaking point. Graph shows the superposition of 6 curves of different resolutions in order to get a visualisation of a wide range. Trajectories computed with RK4 integration and a time step of 8.10^{-4}s. For statistical consistency, autocorrelation of a particle on 240 different fluids is averaged.

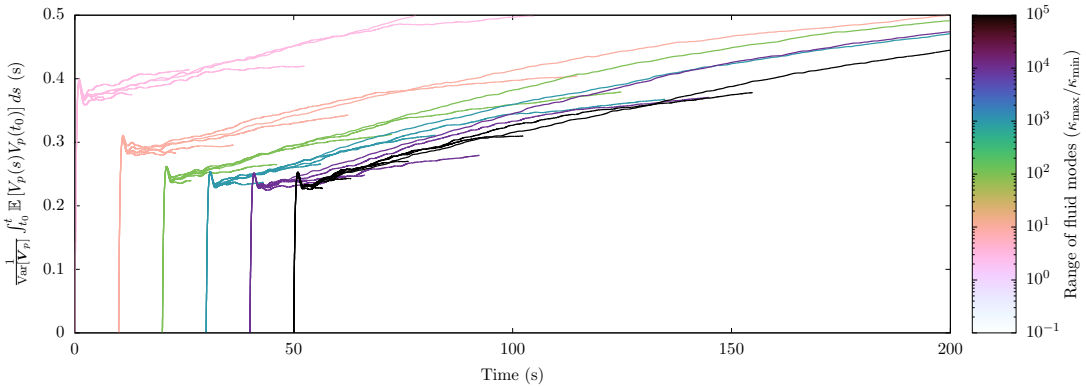

Figure 7.9. Evolution of the quantity $R_{\boldsymbol{V}_p}$ against time, for different range of fluid modes ($\kappa_{\max}/\kappa_{\min} \in \left\{3, 10, 10^2, 10^3, 10^4, 10^5\right\}$) represented by 200 modes. On the right curves are increasingly shifted on the x-axis with to the number of fluid modes, in order to get a better visualisation of the breaking point. Graph shows the superposition of 6 curves of different resolutions in order to get a visualisation of a wide range. Trajectories computed with RK4 integration and a time step of 8.10^{-4}s. For statistical consistency, autocorrelation of a particle on 240 different fluids is averaged.

7.3 Convergence and scaling in the inertial range

The frequency content of a turbulent flow can be divided into three ranges: energy containing range, inertial range and dissipation range (Pope (2000), Fig. 6.1). In this study, the main focus is on the inertial range because

- it is assumed universal (contrarily to the energy containing range),
- it represents most of the universal range (made of the inertial and of the dissipation range) for high Reynolds numbers. In the limit of infinitely high Reynolds numbers (fully developed turbulence), the universal range only consists of the inertial range: the dissipation range disappears.

The inertial range has some invariant properties across scales (similarly to a fractal object). For more on fractals, one can refer to Bishop and Peres (2016). This auto-similarity properties make the inertial range very interesting and at the same time difficult to deal with. Recent studies characterise these scaling more precisely with multi-fractal descriptions in order to take into account effects such as intermittency (Mandelbrot (1974), Frisch and Parisi (1985), Meneveau and Sreenivasan (1987)). For this study, we will first start by working with a simple fractal description of the inertial range following Richardson (1922). With this description, the energy spectrum density of the inertial range scales as $E(\kappa) \propto \kappa^{-5/3}$, $\kappa \in [\kappa_{EI}, \kappa_{ID}]$ and its velocity fields scales as:

$$\|\boldsymbol{u}_f(t, \boldsymbol{x}_1) - \boldsymbol{u}_f(t, \boldsymbol{x}_2)\| \leq C \|\boldsymbol{x}_1 - \boldsymbol{x}_2\|^{\frac{1}{3}}, \quad \kappa_{EI} < \|\boldsymbol{x}_2 - \boldsymbol{x}_1\|^{-1} < \kappa_{ID}, \tag{7.2}$$

with C a real constant. These scaling are only limited to the inertial range. They lead to characteristic behaviour. For instance, the temporal evolution of the mean square distance between two fluid elements is cubic in the inertial range (Fung and Vassilicos (1998), Eq. 1). This is verified in the KS chosen in this work.

Fig. 7.10 presents the temporal evolution of the mean square distance between two fluid elements for different numbers of fluid modes (left) and for different ranges of fluid modes (right). It is indeed possible to observe a range of times for which the mean square distance between two fluid elements scales as the cube of time. However, observing this regime requires to have a sufficient number of modes (at least 100) and a sufficiently large mode spanning (over 10^4). The terminal regime seems not strongly affected for the time span we have observed here.

When the Reynolds number becomes infinite (Onsager (1949)), the dissipation range disappears and the velocity field becomes 1/3-Hölder continuous. For reference, standard Brownian motion is 0.5-Hölder continuous. To get a better feeling of what a 1/3-Hölder continuous velocity field means, Fig. 7.11 represents sample paths of processes with regularity.

These processes should be compared with actual particle trajectories Fig. 7.12.

Almost-all trajectories of such a 1/3-Hölder continuous process are locally Hölder continuous. However, they are almost nowhere differentiable. Thus, they cannot be the strong solution of a partial differential equation (such as Navier-Stokes equations for instance). For comparison, bounded differentiable functions are 1-Hölder continuous, which is more regular (or smooth) than 1/3-Hölder continuous functions. As explained

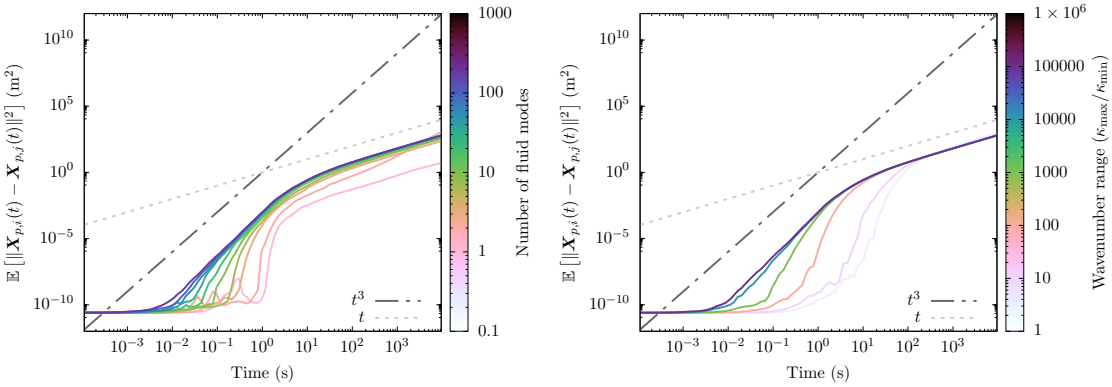

Figure 7.10. Left: Temporal evolution of the mean square distance between two fluid elements for different numbers of fluid modes ($N_\kappa \in \{1, 2, 3, 7, 10, 18, 32, 56, 100, 178, 316\}$) on a range $\kappa_{max}/\kappa_{min} = 10^5$. Distance between 1024 parcels initially in a cube of length 10^{-5}m, averaged over 1200 fluids.
Right: Temporal evolution of the mean square distance between two fluid elements for different ranges of fluid modes ($\kappa_{max}/\kappa_{min} \in \{3, 10, 10^2, 10^3, 10^4, 10^5\}$) represented by 200 fluid modes. Distance between 1024 parcels initially in a cube of length 10^{-5}m, averaged over 1200 fluids.

in Falkovich, Gawedzki, and Vergassola (2001), Chap. II.C.2, it is difficult to consider deterministic particle trajectories in this case. This is due to a problem of limits referred to as *spontaneous stochasticity* and that we propose to briefly sketch out in the following lines (Eyink (2008), Chap. 5d).
Let us take a characteristic example of *spontaneous stochasticity* which deals with the dispersion of the law of one particle in turbulence. Let us consider that the particle has an initial probability distribution bounded in space. Whenever the support of the distribution is initially non-singular, it gets extended by turbulence. Here, two limits are of specific interest.

- The limit of fully developed turbulence ($\mathrm{Re} \to \infty$).
- The limit when the diameter of the law goes to 0 (Dirac distribution).

If one considers first the limit of the particle law to a Dirac distribution, one gets the deterministic trajectory of one particle in a turbulent field with a finite Reynolds number. Taking afterwards the limit $\mathrm{Re} \to \infty$ is not expected to change the deterministic nature of the trajectory of this particle.
However, if we do the opposite and start by considering the action of fully developed turbulence on the law of one particle with a finite extension, it always gets dispersed by turbulence, whatever the initial finite size of the law. Therefore, considering the limit of a law of size zero (Dirac distribution) can difficultly lead to a deterministic trajectory. This is the concept of *spontaneous stochasticity*, where the initial Dirac distribution of a particle gets dispersed by the low regularity of fully developed turbulence.

Both limits are physically consistent. In order to avoid conceptual difficulties, the work done here is presented as much as possible without taking any of the above-mentioned

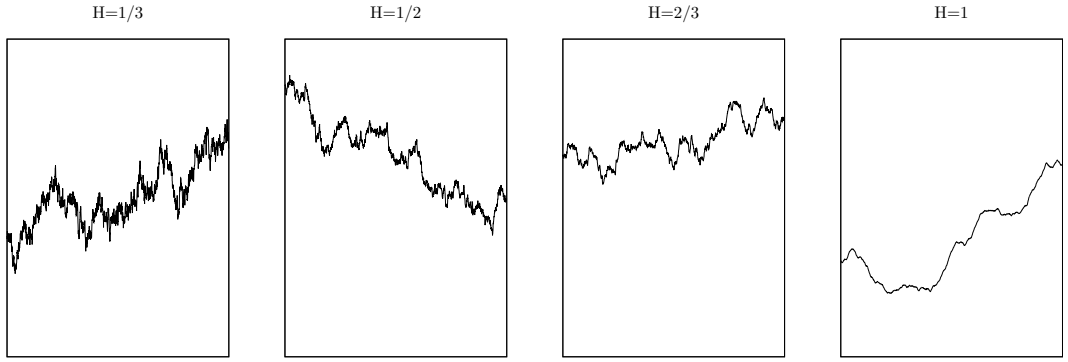

Figure 7.11. Illustration of the concept of regularity with sample paths of fractional Brownian motion with different values of the Hurst exponent H. They intend to represent different levels of Hölder continuity as a fractional Brownian motion admits a version whose sample paths are almost surely Hölder continuous of order strictly inferior to its Hurst exponent.

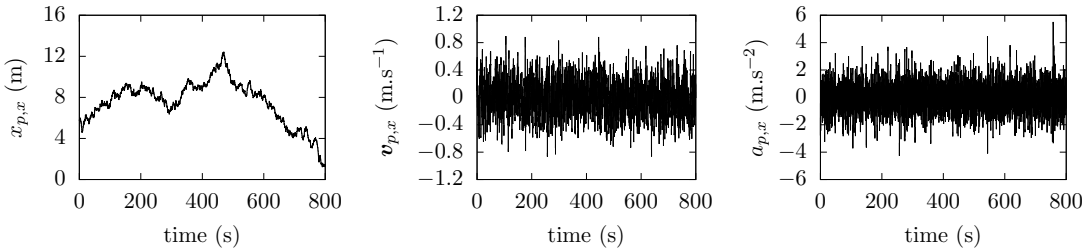

Figure 7.12. Example of a fluid particle trajectory on a synthetic fluid of 200 modes with total energy of $1\text{m}^2.\text{s}^{-2}$ and minimal wave-number of 1m^{-1} Integration time step of 8.10^{-4}s with RK4 integration scheme. From left to right, are represented one component (x) of the parcel position, velocity and acceleration.

limits. Most computations will only involve statistical properties of the particles, where spontaneous stochasticity does not present any conceptual difficulties. The law of the particles is described with an initial law of finite extension and the fluid is represented with a high but finite Reynolds number. The choice of working with a finite Reynolds number is actually imposed by the finite resolution inherent to the numerical representation of the fluid as a finite set of modes.
When computing individual particle trajectories, the number of modes representing the synthetic fluid and the range of these modes is fixed. Then the time step is decreased in order to get converged deterministic particle trajectories. Thus, by first setting the fluid field, and then decreasing the time step, particles are confronted with a continuous velocity field which is not 1/3-Hölder continuous at the time scale of integration. This prevents spontaneous stochasticity. This deterministic behaviour is consistent with what would be obtained for a finite Reynolds number turbulence, where the inertial range is bounded (by the dissipation range).

Highlights and conclusions

In this chapter, we have observed the influence of the number of modes and the range of these modes on the characteristics of the flow field given by KS. After studying the behaviour of fluid parcels through different angles:

- the PSD and the autocorrelation of their velocity,
- and their one and two-points dispersions,

we have found that a fluid of 200 modes spread across four decades allows to get:

- a PSD with a convincing scaling in $\kappa^{-5/3}$ extending over a wide range and easy to converge,
- interesting regimes of transport and diffusion of the fluid parcels.

It was shown that whatever the number of modes in the KS, the velocity of fluid particles always keeps a positive level of correlation with itself leading to a long time transport behaviour of the dispersion of the particles. For what is commonly described in the literature about turbulence we would not expect this regime to exist. Therefore, in the following, we chose to focus our study on time ranges which do not involve this last transport regime.

Chapter 8

Particle trajectories

In the previous chapter, we have studied the effect of the parameters of the KS on the properties of the resulting flow field. We have seen that for 200 modes spread across 4 decades, the KS shows very interesting properties such as a wide PSD following the inertial scaling of turbulence described by Kolmogorov and a clear diffusion regime.
Because we want to study the statistical description of inertial particles in turbulent flow, this section focuses more on the convergence of the description of inertial effects and on the impact of inertia on the dynamics of the disperse phase.

We start by studying the numerical convergence with respect to the integration time-step.

- We present first the convergence of an individual particle trajectory,
- before looking at the convergence of averaged quantities such as the PSD and particle velocity variance.

After having presented the convergence of the numerical integration scheme, we present the convergence of statistical estimators such as the particle position variance in the dimension of the particles and in the dimension of the fluids.
In numerical simulations, ensuring the convergence of the quantities of interest is very standard. The specificity of this work is that the number of different quantities to converge in order to ensure convincing results is quite large:

- As seen in the previous chapter, the number of fluid modes has to be large enough to obtain diffusion.
- As presented in this chapter, the time step has to be small enough for numerical integration,
- the number of inertial particles has to be large enough for statistical convergence,
- and the number of fluids has to be large enough for statistical convergence.

The main difficulty is that each dimension impacts the others. Changing the number of fluid modes changes the frequencies of the flow, thus the resolution needed for temporal integration of particle trajectories. However, because the fluid is better defined with more modes, it decreases the number of fluids and particles required for statistical convergence. Therefore, convergence has been approached as an iterative process in this

work. This coupled process is not highlighted in this manuscript, because for clarity, we have chosen to always present the results of convergence along one dimension with all other dimensions already converged.
The high dimensionality of the space involved by this configuration has rapidly required the development of a MPI code in order to tackle the computations needed. This code has already been presented in Chap. 6.

The second section of this chapter is dedicated to the impact of inertial on the behaviour of the particles. We present how particle variances and PSD are affected by inertia. Having these scaling in mind is important because the results presented in the following chapters only consider one inertia of reference.

8.1 Convergence of particle trajectory with numerical time step

Let us present the convergence of particle trajectories with the numerical integration time-step. It has been seen in the previous section (Sec. 7.3) that the limit behaviour of a point density on a fractal field is not very clear. The auto-similar energy spectrum is discretized by a finite number of smooth modes (Sec. 6.1). Therefore, the fluid is represented by a smooth field (consistent with the smallest scales of turbulence in the limit of the hydrodynamic regime). Let us observe convergence of particle trajectories with respect to numerical integration time step on this smooth field.

8.1.1 Error on the final particle position

This section focuses on the deterministic convergence with the integration time step of one particle trajectory on one fluid field.
Fig. 8.1 presents particle trajectories integrated with a fourth order Runge-Kutta scheme (Hairer, Nørsett, and Wanner (1987), Ch. II) for different integration time steps according to equation Eqs. 2.1. The fluid velocity along the trajectory is computed analytically (more on the expression of the fluid Sec. 6.1).
As explained in the previous section (Sec. 7.3), each fluid realization is smooth, with a finite maximum wave-number and frequency. This is the direct consequence of its representation by a finite sum of smooth modes. On this smooth field (curvature bounded by L), for any finite time $T > 0$, the error $E := \|\boldsymbol{x}_{p,\Delta t}(T) - \boldsymbol{x}_p(T)\|$ on each particle trajectory is expected to converge to zero as the integration time step Δt goes to zero (Hairer, Nørsett, and Wanner (1987), p. 160, Th. 3.4), with C a positive constant:

$$\|E\| \leq \Delta t^4 \frac{C}{L} \left(\exp(LT) - 1\right). \tag{8.1}$$

However, given a particle and a fluid field, for any integration time step $\Delta t_1 > 0$ (even two orders of magnitude smaller than the smallest time scale of the flow in Fig. 8.1),

for any positive number $B_1 > 0$, there is a time $T_1 > 0$ for which the position of the numerical particle $\boldsymbol{x}_{p,\Delta t_1}(T_1)$ cannot be guaranteed to be less than B_1 away from the position of the exact particle $\boldsymbol{x}_p(T_1)$: $\|\boldsymbol{x}_{p,\Delta t_1}(T_1) - \boldsymbol{x}_p(T_1)\| \not\leq B_1$ (Hairer, Nørsett, and Wanner (1987), p. 160, Th. 3.4). The reasoning is valid for any numerical integration scheme when the integrated numerical error of the numerical scheme becomes larger than Kolmogorov scale after some finite time.
If one wants to assess the long time behaviour of particles (for diffusion regime of fluid parcels for instance, see Sec. 1.3.1.1), the cost of point-wise convergence can become astoundingly expensive. However, for such long times, one may not be interested in the actual position of each particle, but on the statistical properties of some particular behaviour (Février, Simonin, and Squires (2005)). It is key to observe how these quantities of interest converge with the time step (Sec. 8.2). This is what is done in the following sections. Aside from the mere practical ease, such a strategy is all the more relevant with respect to the previous section (Sec. 7.3) which illustrates the difficulty of considering a point particle by itself, without any statistical treatment.

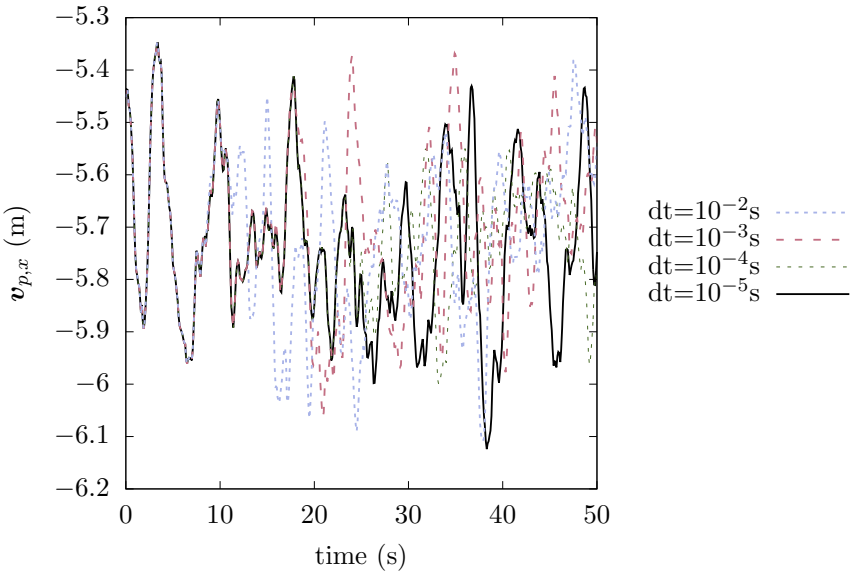

Figure 8.1. Time evolution of one velocity component of one particle trajectory for different integration time steps (in the legend) on one synthetic fluid. Time integration with analytical evaluation of the fluid velocity and Runge-Kutta scheme of order four. Relaxation time constant of the particle $\tau_p = 1\text{s}$. Synthetic fluid of 200 modes between $\kappa_{\min} = 1.\text{m}^{-1}$ and $\kappa_{\max} = 100\text{m}^{-1}$. The fluid realization represented in the figure has $3.9\,10^{-4}\text{s}^{-1} < \frac{1}{2\pi}\omega_i < 2.7\,10^{-1}\text{s}^{-1}$, and $1.1\,10^{1}\text{s}^{-1} < |\boldsymbol{\kappa}_i|/|\boldsymbol{a}_i| < 8.7\,10^{4}\text{s}^{-1}$, $i \in [\![1, \text{N}_\kappa]\!]$.

8.1.2 Metrics for stationary processes

As seen previously (Eq. 8.1) no finite time step can guarantee that a particle trajectory is within a given error bound for arbitrarily long times. In Fig. 8.1, the particle trajectory drifts away as time increases, no matter how small the time step. For a constant error bound, as the time horizon increases, the time step rapidly decreases and the computational cost skyrockets (Fig. 8.5). Therefore, convergence based on particle position is quite impractical for asymptotically long time simulations. Furthermore, one may not be particularly interested in the precise position of one particle (which meaning can be questioned in this context, Sec. 7.3) but rather on statistical properties of particle trajectories. It is crucial to ensure that these statistical properties are converged, whether the actual particle trajectories are themselves converged or not. In permanent regime, one important physical property of a particle trajectory the reproduction of its frequency content. Here, we associate this property to the term *resolved*. A numerical particle trajectory is said well resolved when its frequency content is well reproduced and poorly resolved in the alternate case.
Fig. 8.2 represents the Fourier transform of one particle trajectory for different integration time steps. The simulation setup is the same as the one of Fig. 8.1. It is clearly seen (Fig. 8.2) that as the time step is decreased from 10^{-1}s to 10^{-2}s, more physical elements of the trajectory frequency spectrum are recovered (steadily decreasing energy spectrum on the left side of the graph). However, as one decreases the time step further (from 10^{-4}s to 10^{-5}s for instance), the increase in the energy of the signal recovered becomes negligible. This increase in the numerical cost of the simulation improves the precision of the particle position, but it does not add any physics to the frequency content of its trajectory. Thus, in this case, the physical properties of the trajectory can be assumed to be well resolved for a time step of 10^{-3}s or even 10^{-2}s, even though these time steps do not ensure a converged trajectory for arbitrarily long times.

If one has a specific metric in mind, convergence can be even faster. For instance, one can observe in Fig. 8.3 the velocity variance of one component of one particle trajectory for different integration time steps. Even though the trajectory does not have all the frequency content expected from the converged case, as with an integration time step of 10^{-1}s for instance (for the frequency content, see in Sec. 8.2), a given metric of interest can be already converged (see Fig. 8.3).
Based on these results, in this work, convergence is assessed for each result with respect to the specific metric studied.

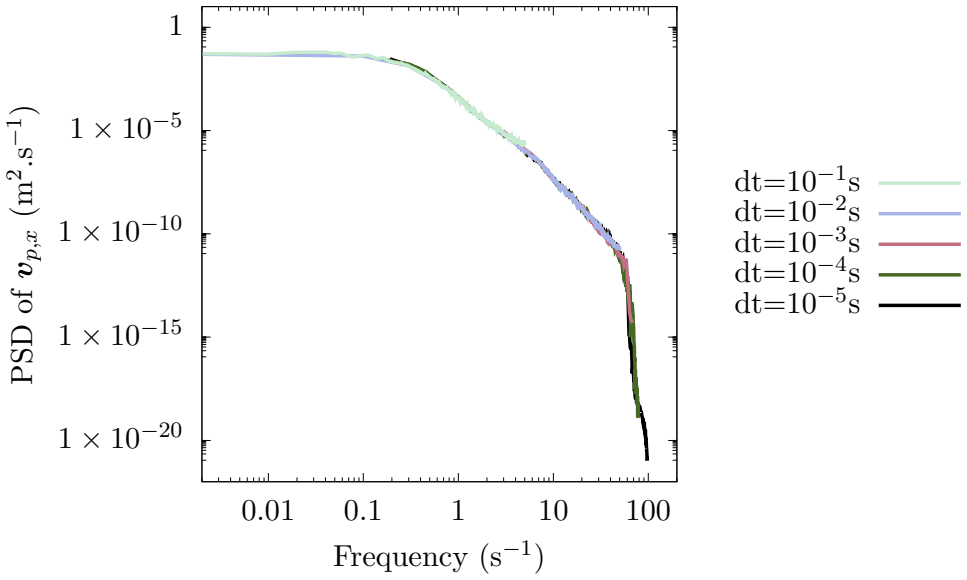

Figure 8.2. PSD of a particle velocity trajectory on a fluid for different integration time steps (10^{-1},10^{-2},10^{-3},10^{-4},10^{-5}). Time integration with analytical evaluation of the fluid velocity and Runge-Kutta scheme of order four. Relaxation time constant of the particle $\tau_p = 1\mathrm{s}$. Synthetic fluid of 200 modes between $\kappa_{\min} = 1.\mathrm{m}^{-1}$ and $\kappa_{\max} = 100\mathrm{m}^{-1}$. The fluid realization represented in the figure has $3.9\,10^{-4}\mathrm{s}^{-1} < \frac{1}{2\pi}\omega_i < 2.7\,10^{-1}\mathrm{s}^{-1}$, and $1.1\,10^{1}\mathrm{s}^{-1} < |\boldsymbol{\kappa}_i|/|\boldsymbol{a}_i| < 8.7\,10^{4}\mathrm{s}^{-1}$, $i \in [\![1, \mathrm{N}_\kappa]\!]$. Fourier transform was performed on the signal, with Hann windowing, between times $t = 10\,\tau_p$ and $t = 100\,\tau_p$ so as to focus on the long time permanent regime. 100 PSD of the same particle trajectory are averaged in the plot.

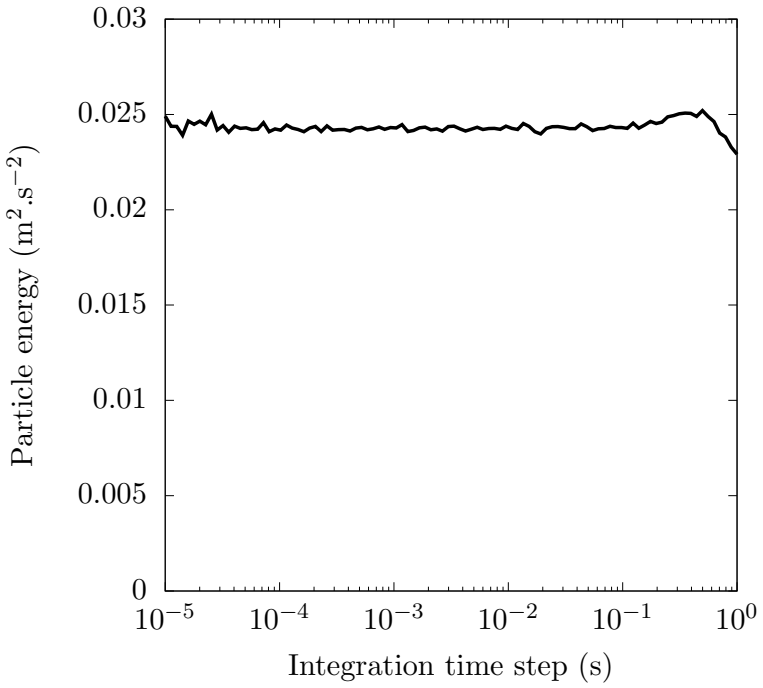

Figure 8.3. Velocity variance of one component of one particle trajectory according to the integration time step on one synthetic fluid. Time integration with analytical evaluation of the fluid velocity and Runge-Kutta scheme of order four. Particle time relaxation constant of $\tau_p = 1s$. Synthetic fluid of 200 modes between $\kappa_{\min} = 1.\mathrm{m}^{-1}$ and $\kappa_{\max} = 100\mathrm{m}^{-1}$. The fluid realization represented in the figure has $3.9\,10^{-4}\mathrm{s}^{-1} < \frac{1}{2\pi}\omega_i < 2.7\,10^{-1}\mathrm{s}^{-1}$, and $1.1\,10^{1}\mathrm{s}^{-1} < |\boldsymbol{\kappa}_i|/|\boldsymbol{a}_i| < 8.7\,10^{4}\mathrm{s}^{-1}$, $i \in [\![1, \mathrm{N}_\kappa]\!]$.

8.1.3 Numerical convergence of average quantities

Previous results were on the trajectory of only one particle on only one fluid. However, in the context of this work, several particle evolutions are computed on several fluids taken at random on a distribution of fluids (defined in Sec. 6.1). Although each fluid is smooth with a fixed maximum frequency, pulsations $(\omega_n)_{n\in[\![1,\mathrm{N}_\kappa]\!]}$ are taken from a centred normal distribution. Thus, for $n \in [\![1, \mathrm{N}_\kappa]\!]$, whatever $B_2 > 0$, it is sure that among all possible fluids, an infinity of fluids has modes with pulsations higher than B_2: $\mathbb{P}(\omega_n > B_2) > 0$. In other words, although for each fluid, the frequency range is bounded, the frequency range of the set of fluids is unbounded. As the error on particle trajectory is directly dependant on the fluid frequency, this implies that for any number $B_3 > 0$ and for any positive time interval $T_3 > 0$, there is no time step $\Delta t_3 > 0$ small enough to ensure that $\|\boldsymbol{x}_{p,\Delta t_3}(T_3) - \boldsymbol{x}_p(T_3)\| \leq B_3$ for all fluids.
In this spirit, Fig. 8.4 treats convergence as a statistical quantity. It is different from Fig. 8.1 where only one particle trajectory is computed on one fluid. For different integration time steps, Fig. 8.4 presents the percentage of particle trajectories which have always been at less than $1/\kappa_{\max} = 0.01\mathrm{m}$ away from the trajectory computed with a time step of $\mathrm{dt}_0 = 0.004\mathrm{s}$. This figure is to understand with the assumption that the trajectory computed with time step of $\mathrm{dt}_0 = 0.004\mathrm{s}$ is close to the exact trajectory (which is consistent with the results presented in Fig. 8.1).

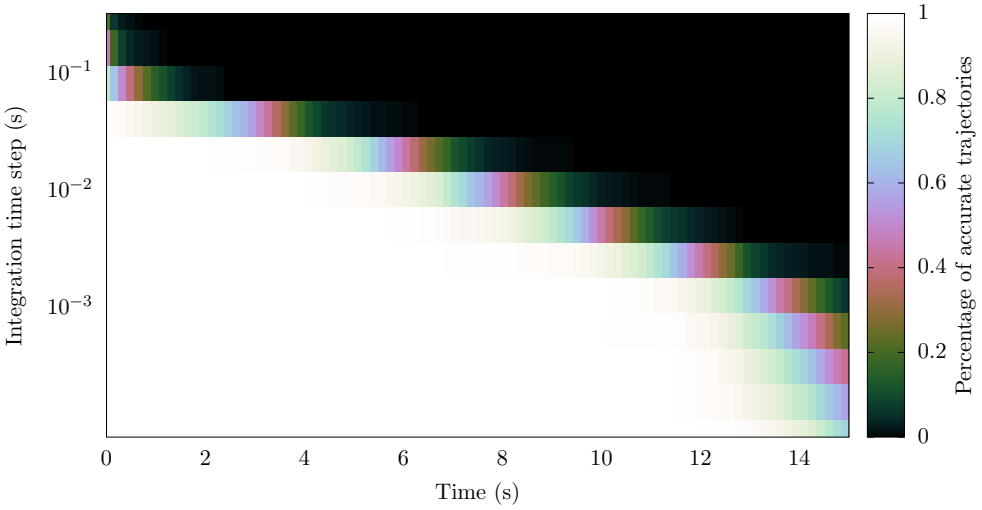

Figure 8.4. Time evolution of the percentage of particle trajectories which have always been at less than $1/\kappa_{\max} = 0.01\mathrm{m}$ of the trajectory computed with time step of $\mathrm{dt}_0 = 2.10^{-5}\mathrm{s}$, for different integration time steps. Computed for a particle on 1024 different fluid flows. Time integration with analytical evaluation of the fluid velocity and Runge-Kutta scheme of order four. Particle time relaxation constant of $\tau_p = 1s$. Synthetic fluid of 200 modes between $\kappa_{\min} = 1.\mathrm{m}^{-1}$ and $\kappa_{\max} = 100\mathrm{m}^{-1}$.

Similarly to the deterministic case, it is possible to consider different metrics in a statistical setting (Fig. 8.5). One still observes that the convergence drastically depends on

the metric observed. For instance, Fig. 8.5 which represents the variance in position of one particle for 2^{19} different initial positions on one fluid is converged for dt=0.1s, on a time span of 40 s, although Fig. 8.4 clearly shows that for this time resolution, a significant proportion of individual particle trajectories differ from the converged trajectories as soon as t =4s. The metrics represented in Fig. 8.5 start to diverge as the integration scheme becomes of the scale of the largest scales of the system (Δt=1s). The velocity of the particles is very badly represented (on the right of Fig. 8.5, the particle velocity variance is under-estimated) and this has a direct impact on the relative dispersion of the particles (on the left of Fig. 8.5) which is slower than for converged computations.

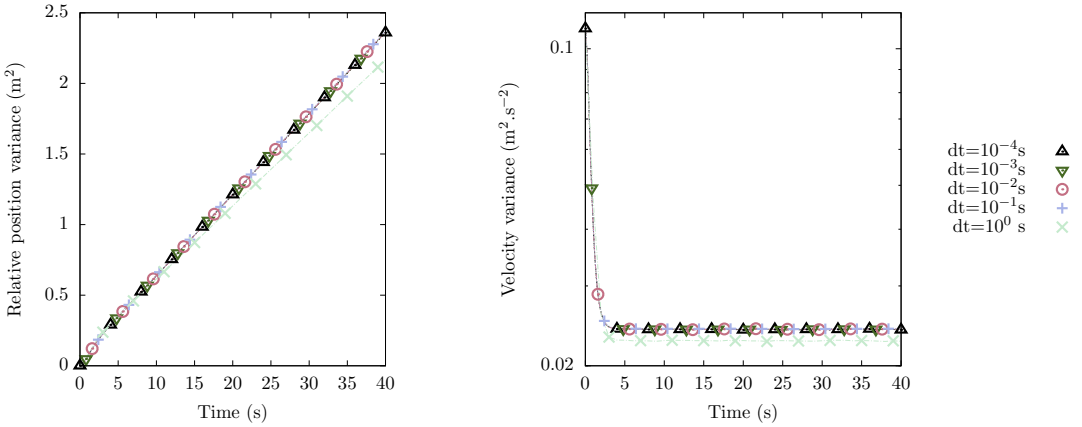

Figure 8.5. Time evolution of the variance in position of 2^{19} particles on one fluid for different integration time steps. Time integration with analytical evaluation of the fluid velocity and Runge-Kutta scheme of order four. Particle time relaxation constant of $\tau_p = 1s$. Synthetic fluid of 200 modes between $\kappa_{\min} = 1.\mathrm{m}^{-1}$ and $\kappa_{\max} = 100\mathrm{m}^{-1}$.

8.2 Statistical convergence

Previous section (Sec. 8.1) is focused on convergence with the numerical integration time step. This section focuses on statistical convergence.

The concept of statistical convergence is very important when working with a phenomenon modelled as a random variable (or with some numerical/experimental results one wants to consider as a random variable). For a reference on Statistics, one can have a look at Freedman, Pisani, and Purves (1978) for instance. For estimating a property (referred to as a parameter) of this random variable one can try to design a sequence of estimators $\left(\widehat{\theta}_n\right)_{n\in\mathbb{N}}$. An estimator is a statistic (function of the sample data). One of the key desired properties of the sequence of estimators is that they converge in probability towards the parameter θ one wants to estimate. This is called consistency:

$$\lim_{n\to\infty} \mathbb{P}\left(\left|\widehat{\theta}_n - \theta\right| < \epsilon\right) = 1, \quad \forall \epsilon > 0. \tag{8.2}$$

In this section, the random variable taken as an example is the particle position $\boldsymbol{X}(t)$. The parameter chosen for illustration is the particle position variance. What is investigated in this section is how estimators of particle position variance converge and give a satisfactory result. The expression of the sample variance of the particle position is computed as:

$$\widehat{\mathrm{Var}}_{\widehat{\mathrm{N}}_p,\widehat{\mathrm{N}}_f}(t) = \frac{1}{\widehat{\mathrm{N}}_{\widehat{\mathrm{N}}_p,\widehat{\mathrm{N}}_f}} \sum_{f=1}^{\widehat{\mathrm{N}}_f} \sum_{p=1}^{\widehat{\mathrm{N}}_p} \sum_{i=1}^{3} \left(\left[\boldsymbol{X}_i(t) - \boldsymbol{X}_i(0) \right] - \widehat{\mathrm{Mean}}_{\widehat{\mathrm{N}}_p,\widehat{\mathrm{N}}_f}(t) \right)^2, \quad (8.3)$$

with

$$\widehat{\mathrm{Mean}}_{\widehat{\mathrm{N}}_p,\widehat{\mathrm{N}}_f}(t) = \frac{1}{3\,\widehat{\mathrm{N}}_p\,\widehat{\mathrm{N}}_f} \sum_{f=1}^{\widehat{\mathrm{N}}_f} \sum_{p=1}^{\widehat{\mathrm{N}}_p} \sum_{i=1}^{3} \left[\boldsymbol{X}_i(t) - \boldsymbol{X}_i(0) \right], \quad (8.4)$$

$\boldsymbol{X}_i(t)$ the component along the direction i of the position $\boldsymbol{X}(t)$ at time t, and

$$\widehat{\mathrm{N}}_{\widehat{\mathrm{N}}_p,\widehat{\mathrm{N}}_f} = \max\left(1, 3\,\widehat{\mathrm{N}}_p - 1\right) \max\left(1, \widehat{\mathrm{N}}_f - 1\right), \quad (8.5)$$

$\widehat{\mathrm{N}}_p > 0$ and $\widehat{\mathrm{N}}_f > 0$.
This expression gives an isotropic measure of the dispersion. With the sample variance $\widehat{\mathrm{Var}}_{\widehat{\mathrm{N}}_p,\widehat{\mathrm{N}}_f}$, one wants to compute the limit as $\widehat{\mathrm{N}}_p$ and $\widehat{\mathrm{N}}_f$ go to infinity. Fig. 8.6 illustrates the dependency of $\widehat{\mathrm{Var}}_{\widehat{\mathrm{N}}_p,\widehat{\mathrm{N}}_f}$ on $\widehat{\mathrm{N}}_p$ and $\widehat{\mathrm{N}}_f$. It represents the convergence of sample variance (Eq. 8.3) with respect to $\widehat{\mathrm{N}}_p$, for $\widehat{\mathrm{N}}_f = 1$ on the left and with respect to $\widehat{\mathrm{N}}_f$, for $\widehat{\mathrm{N}}_p = 1$ on the right.

- On the left, we observe convergence with $\widehat{\mathrm{N}}_p$. Lines are superposed when $\widehat{\mathrm{N}}_p > 1000$. Interestingly, the initial behaviour is uneven. This is because convergence is done with only one fluid. It is the trace of the temporal evolution of the fluid itself.
- On the right, we observe convergence with $\widehat{\mathrm{N}}_f$. Lines are superposed when $\widehat{\mathrm{N}}_p > 100$. Convergence is much faster than when working with particles on the same fluid. Furthermore, the evolution of the converged variance is initially much smoother and satisfactory with respect to what is expected from theory (Taylor (1921)).

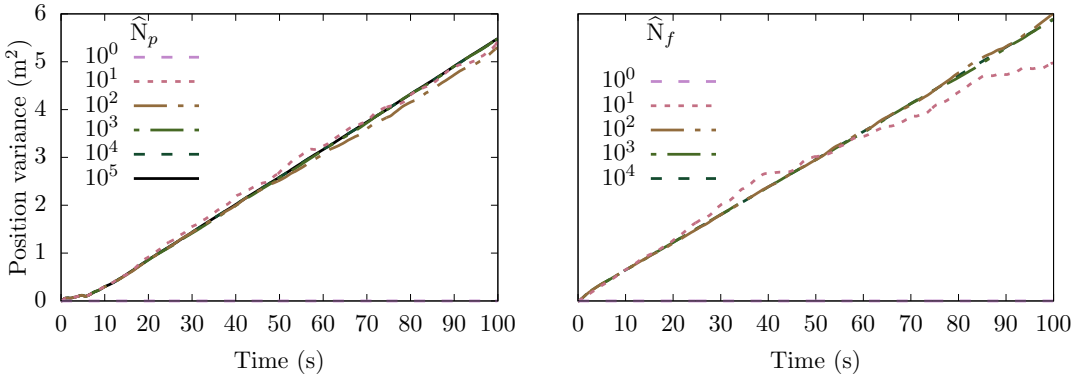

Figure 8.6. On the left: Time evolution of the variance of the dispersion of one particle starting on different fluids. Time integration with analytical evaluation of the fluid velocity and Runge-Kutta scheme of order four, with time step of 0.1s. Particle time relaxation constant of $\tau_p = 1s$. Synthetic fluid of 200 modes between $\kappa_{\min} = 1.\mathrm{m}^{-1}$ and $\kappa_{\max} = 10^5\mathrm{m}^{-1}$.
On the right: Time evolution of the dispersion of one particle for different samplings of the initial positions law (in the legend) on one fluid. The initial position law of the particle is uniform in a cube of $10^{-15}\,\mathrm{m}^3$. Time integration with analytical evaluation of the fluid velocity and Runge-Kutta scheme of order four, with time step of 0.1s. Particle time relaxation constant of $\tau_p = 1s$. Synthetic fluid of 200 modes between $\kappa_{\min} = 1.\mathrm{m}^{-1}$ and $\kappa_{\max} = 10^5\mathrm{m}^{-1}$.

8.3 Influence of the Stokes number

In this section, let us investigate the relation between the fluid and the particles.
Fig. 8.7 shows the impact of the particle inertia on second order moments of an ensemble of inertial particles. As observed on the left figure, inertia does not change asymptotic dispersion behaviours. The initial transport behaviour and the final diffusion evolution are unchanged. The only impact is on the transition between these two regimes which happens later for high inertia particles which manifest a resonance between transport and diffusion regimes. This resonance corresponds to the increase of the ballistic time with particle inertia. This is confirmed when observing the left of Fig. 8.8, which shows an affine evolution for particle dispersion of any inertia. Furthermore, the linear coefficient is the same for any inertia (plotted on the right of Fig. 8.8). This result is also observed in the model proposed by Reeks, Swailes, and Bragg (2018). However, the offset of the dispersion observed in Fig. 8.8 changes according to inertia. This is readily explained by the duration of the ballistic regime which differs with particle inertia (see the resonance Fig. 8.7).
Fig. 8.7 also presents the impact of particle inertia on the temporal evolution of the velocity variance. It is shown to have two major impacts :

- one on the long time asymptotic value of particle velocity variance,
- the other on the characteristic time associated with the temporal evolution of the velocity variance.

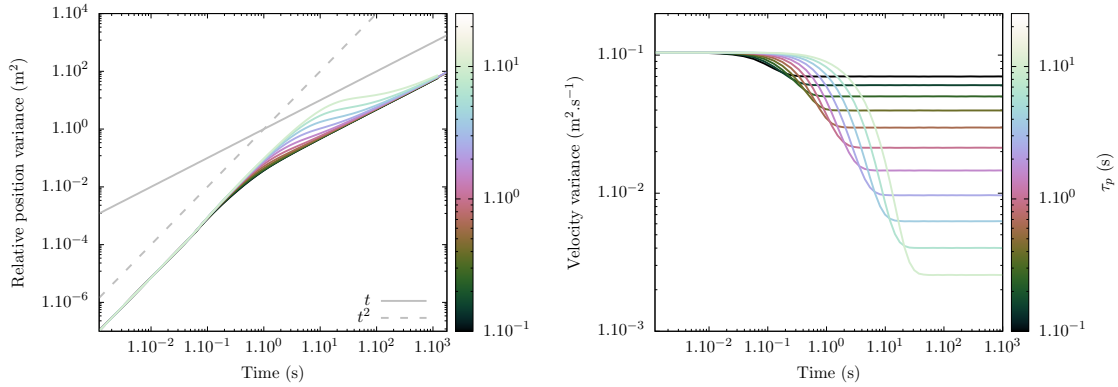

Figure 8.7. Evolution of second order moments of N_p=1024 particles averaged over 1200 different fluids of 200 modes N_κ between $\kappa_{\min} = 1$ m^{-1} and $\kappa_{\max} = 10^5$ m^{-1}, with relaxation time τ_p. On the left, relative position variance, and and on right, velocity variance. Particle time relaxation constant of τ_p indicated in the graphs. Maximal integration time step of dt=0.01s.

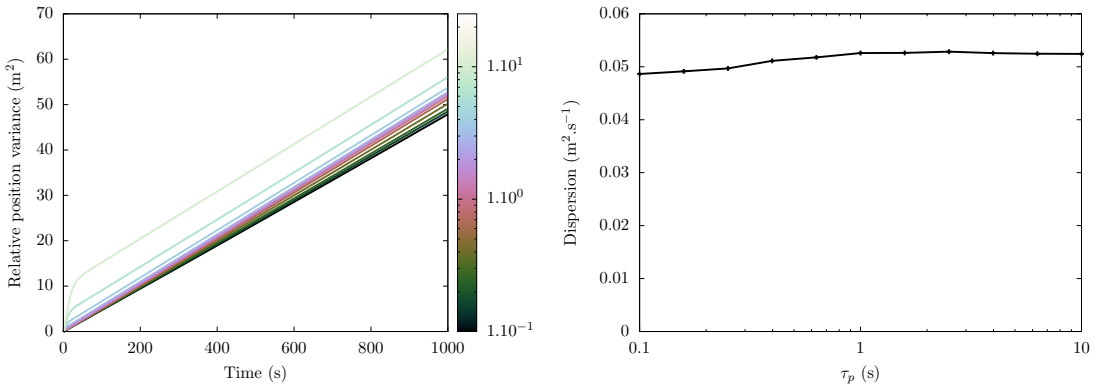

Figure 8.8. On the left, evolution of the relative position variance of N_p=1024 particles averaged over 1200 different fluids of 200 modes N_κ between $\kappa_{\min} = 1$ m^{-1} and $\kappa_{\max} = 10^5$ m^{-1}. Particle time relaxation constant of τ_p indicated in the graphs. Maximal integration time step of dt=0.01s. On the right, slope of the relative position variance according to particle inertia τ_p.

Let us now briefly review these impacts.
Fig. 8.9 presents the asymptotic value of the particle velocity variance according to particle inertia on the left. It is seen on the left of Fig. 8.9 that the asymptotic value of particle velocity variance decreases steadily as the particle inertia increases. The average velocity variance of the particles along their trajectory is the same as the velocity variance of an ensemble of particles taken at a given time. This is a very strong property. It is consistent with the scrambling behaviour of particle trajectories on the fluid. One particle trajectory is somehow representative of all the particle trajectories possible on the fluid. Furthermore, particle velocities are not correlated with fluid velocity realizations

(to the limitation of the tiny residual correlation measurable Fig. 7.9).
Otherwise, the two variances would be different, as it can be seen by applying the law of total variance Eq. 8.6 (the term $\mathrm{Var}\left[\mathbb{E}\left[\boldsymbol{V}_p\,|A_f\,\right]\right]$ has to be very small).

$$\mathrm{Var}\left[\boldsymbol{V}_p\right] = \mathbb{E}\left[\mathrm{Var}\left[\boldsymbol{V}_p\,|A_f\,\right]\right] + \mathrm{Var}\left[\mathbb{E}\left[\boldsymbol{V}_p\,|A_f\,\right]\right] \tag{8.6}$$

Remarkably, the fluid velocity variance seen by particles is insensitive to particle inertia (on the right of Fig. 8.9).

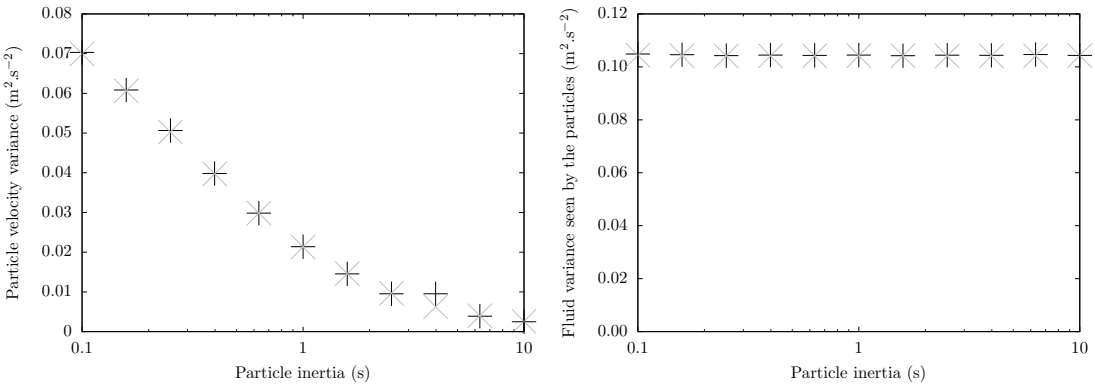

Figure 8.9. Second order moment of particle velocity (on the left) and of fluid velocity seen by particles (on the right) according to inertia computed along particle trajectories (black +) and for a ensemble of particles on an ensemble of particles (grey x).

The second aspect is the characteristic time of particle velocity variance fluctuations. In Fig. 8.10 which represents on the left the particle velocity autocorrelation with respect to particle inertia, it is seen that inertia increases particle velocity autocorrelation. We recover well the scaling proposed by Tchen (1947) and Hinze (1975) (also in Zeren (2010)) (Eq. 8.7):

$$\tau_v \simeq \tau_p + \tau_u. \tag{8.7}$$

Namely that the particle velocity autocorrelation time is close (in a sense let to the appreciation of the reader) to the sum of the particle relaxation time and of the autocorrelation time of the fluid seen by the particles. Interestingly, inertia has no impact on the fluid velocity seen by the particles autocorrelation time (on the right of Fig. 8.10).
The particle velocity variance and the particle velocity autocorrelation time are one point statistics which allow the estimation of the asymptotic diffusive behaviour of the particles. Fig. 8.11 represents the asymptotic dispersion observed in Fig. 8.8, alongside the asymptotic dispersion estimated exclusively with particles velocity and autocorrelation time. This property is very useful for building models. Indeed, if the model respects the particle energy and the particle autocorrelation time, it is bound to give the correct asymptotic diffusion.

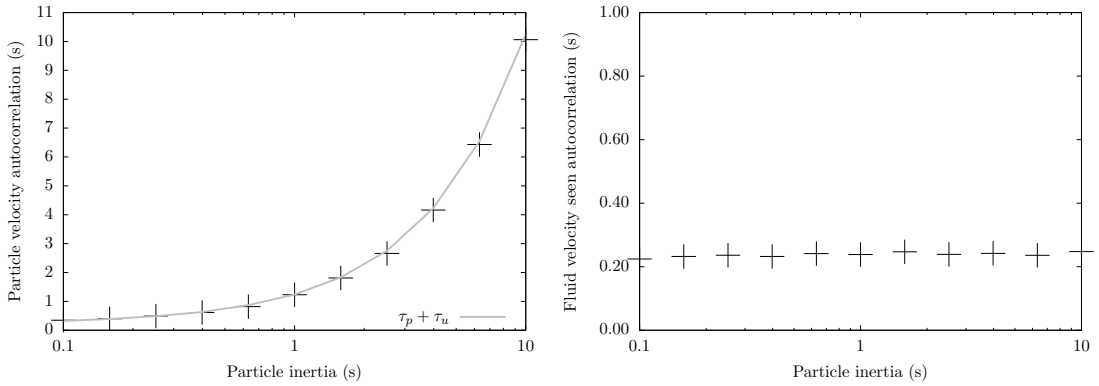

Figure 8.10. Autocorrelation of particle velocity (on the left) and of fluid velocity seen by particles (on the right) according to inertia computed.

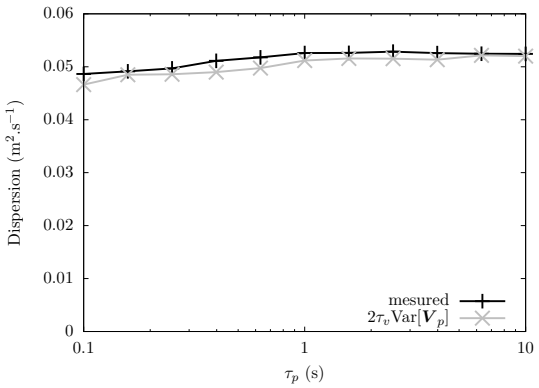

Figure 8.11. Asymptotic dispersion observed Fig. 8.8 alongside the asymptotic dispersion estimated with particles velocity and autocorrelation time.

Fig. 8.12 shows the transfer function vision of the signal experienced by the particles following Hinze (1975). From top to bottom are represented on Fig. 8.12 the power spectral density (PSD) of the fluid velocity seen by the particle, its velocity and its position. They represent different levels of signal integration. The initial signal is given by the fluid velocity seen by the particle. It does not appear to be influenced by the particle inertia. Given its variance $\mathrm{Var}[u_{p,x}]$, and its autocorrelation time τ_u, the simple expression $\mathrm{PSD}^*(u_{p,x})$ of the power spectral density (PSD) of $u_{p,x}$ (Eq. 8.8) approximates well with the asymptotes for low and high frequencies of $\mathrm{PSD}(u_{p,x})$. This expression was found empirically. The measured and approximated power spectral density of the fluid velocity seen by the particle are represented in Fig. 8.12.

$$\mathrm{PSD}^*(u_{p,x})\,(\omega) \simeq \frac{3}{5}\frac{\mathrm{Var}\,[u_{p,x}]}{\left(1+\frac{5}{3}\tau_u\omega\right)^{5/3}}. \tag{8.8}$$

In order to get the particle velocity power spectral density, one only needs to low-pass

filter the fluid velocity seen by the particle, with a low pass filter of characteristic time τ_p. This gives Eq. 8.9, which fits well with the measured power spectral density of the particle velocity represented Fig. 8.12.

$$\mathrm{PSD}^*(\boldsymbol{v}_{p,x})\,(\omega) \simeq \frac{1}{(1+\tau_p\,\omega)^2}\frac{3}{5}\frac{\mathrm{Var}\,[\boldsymbol{u}_{p,x}]}{\left(1+\frac{5}{3}\tau_u\omega\right)^{5/3}}. \tag{8.9}$$

In order to get the particle position power spectral density, one only needs to integrate the fluid velocity seen by the particle. This gives the expression Eq. 8.10, which fits well with the measured power spectral density of the particle position represented Fig. 8.12.

$$\mathrm{PSD}^*(x_{p,x})\,(\omega) \simeq \frac{1}{\omega^2}\frac{1}{(1+\tau_p\,\omega)^2}\frac{3}{5}\frac{\mathrm{Var}\,[u_{p,x}]}{\left(1+\frac{5}{3}\tau_u\omega\right)^{5/3}}. \tag{8.10}$$

With Fig. 8.12, the reader can easily understand that the linear Stokes drag law allows for an easy and straightforward relation between the fluid behaviour and inertial particle trajectories. Therefore, when the linear Stokes drag law is valid, the main challenge for reproducing the energy spectrum of inertial particles comes directly from turbulence. Turbulence is difficult because of its characteristic energy profile which we have difficulties in incorporating easily in standard particle models. Indeed, the energy profile proportional to frequencies to the power $-5/3$ is characteristic of a low regularity field. In order to reproduce such behaviour, the simplest method is to use fractional Brownian motion. However, the use of fractional Brownian motion is computationally expensive and not straightforward in complex simulation as it requires particle increments to be dependent of themselves in the past (which is easy to do) and the future (which is more problematic).

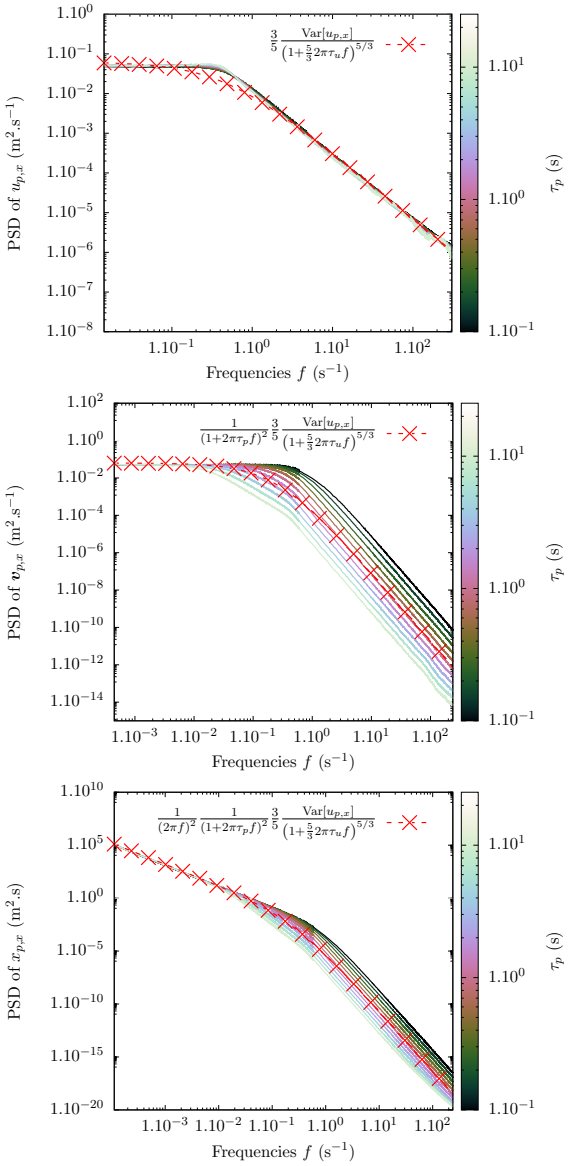

Figure 8.12. PSD of 200 particle trajectories for different relaxation times τ_p in the legend. Fluid of energy $1\mathrm{m}^2.\mathrm{s}^{-2}$ wave-number range between $1\mathrm{m}^{-1}$ and $10^5\mathrm{m}^{-1}$ averaged 10 times. Graph shows the superposition of 10 PSD of 2^{14} points with Hann windowing of different resolutions in order to get a visualisation of a wide spectrum range. Trajectories computed with RK4 integration and a time step of 8.10^{-4}s.
Approximated PSD for $\tau_p = 1$s are represented on overlay with dotted line and crosses.

Highlights and conclusions

In this chapter, we have studied the convergence of particle trajectories and particle statistics.

- We have seen that trying to converge the actual physical position of the particles for arbitrary long times is illusory. However, this work only focuses on describing statistical quantities representative of the behaviour of the particles which may be converged for a much larger time step. For instance, the particle velocity variance is converges for $\Delta t \leq 0.1$s (Fig. 8.3) and the PSD of the particle velocity is converged for $\Delta t \leq 0.01$s (Fig. 8.2).
- We have also studied the convergence of statistical estimators. The estimator chosen for the particle position variance is converged:
  - on one KS for more that 1000 realisations of one particles,
  - and for one particle on more that 100 KS realisations.

  These values are used when presenting statistical results.
- We have also studied the impact of inertia on the behaviour of the particles governed by Stokes drag law. We have shown that the scaling proposed by Tchen (1959) and Hinze (1975) coincide very well with the results obtained numerically.

  It was also shown that:
  - inertia increases the duration of the initial transport regime,
  - and that inertia does not alter the diffusion coefficient.

  Although the first point is very well documented in the literature, the second point was unclear. Eventually, we have presented some models which reproduce very well the influence of inertia on the PSD of the particles.

Part III

Statistically consistent LES of particle laden flows

Chapter 9

Numerical study of the influence of the level of fluid reduction on the EMEF

In the previous part, we have proposed an extended formalism for the statistical description of turbulent particulate flows. In order to investigate this formalism, we have also designed a numerical framework based on synthetic flow fields. The use of synthetic flow fields enables an explicit control of the probability space, which is essential for studying the extension of the MEF to LES.
In this chapter, we present a numerical investigation of the extension of the MEF presented in Sec. 5.3.1. The work is organised as follows:

- We start by introducing the specific set-up based on KS, which makes the study of the EMEF possible.
- Secondly, with this set-up, we observe the numerical results of this formalism which has never been applied before.
- Eventually, we discuss the implications of these observations.

9.1 Objective of the numerical study of the EMEF

In this section, we first present the context chosen in this chapter for performing numerical simulations of the EMEF. Let us recall the definition EMEF distribution in the context of LES.
LES involves a fluid field $\boldsymbol{u}_f$ and a reduction operator $\mathfrak{G}$. Computing a LES gives the evolution of the reduced flow field $\mathfrak{G}(\boldsymbol{u}_f)$. This reduced flow field corresponds to the set of fully resolved flow fields $\mathfrak{G}^{\leftarrow} \circ \mathfrak{G}(\boldsymbol{u}_f)$. In the context of a probability space, the MEF distribution $f_{\boldsymbol{u}_f}$ is defined as the average particle distribution over only one fluid field $\boldsymbol{u}_f$. In contrast, the distribution of the extension of the MEF to LES $f_{\mathfrak{G}^{\leftarrow}\circ\mathfrak{G}(\boldsymbol{u}_f)}$ is defined as the average particle distribution over the entire set of fluid fields $\mathfrak{G}^{\leftarrow} \circ \mathfrak{G}(\boldsymbol{u}_f)$. In order to get access to $f_{\mathfrak{G}^{\leftarrow}\circ\mathfrak{G}(\boldsymbol{u}_f)}$, we need:

- a fluid $\boldsymbol{u}_f$, defined as a random variable on a probability space,
- a reduction operator on the fluid $\mathfrak{G}$,
- and an easy access to the pre-image of the reduction operation on the fluid $\mathfrak{G}^{\leftarrow} \circ \mathfrak{G}(\boldsymbol{u}_f)$.

For the current study, we have chosen the following conditions:

- In order to have access to the pre-image of a reduced flow field, the fluid $\boldsymbol{u}_f$ is given by the field of KS, as presented in Chap. 6.
- KS also provides an explicit probability space to work with.
- For simplicity, the reduction operator $\mathfrak{G}$ is a sharp cut-off filter.

In the following, based on this set-up, the objective is to compare the reference evolution of each formalism. Considering that the differences between these formalisms lie in the dimensions over which averaging is performed, we schematically represent these dimensions in Fig. 9.1. In this figure, each formalism is represented by a different box. This box gathers the dimensions over which an average is taken in the formalism considered. Each column represents a random variable of the probability space: the large scales of the flow, the small scales of the flow, and the initial position of the particles. Each line corresponds to a realisation. Therefore, when the box gathers multiple lines, it means that the formalism corresponds to the expectancy over all realisations of the corresponding random variable. Having that in mind, let us recall the different formalisms by successive increases of the probability space:

- The DPS has no ensemble-average: it is a unique realisation.
- The MEF has an ensemble-average over the particle initial positions.
- The self-contained LES considers an ensemble-average over the particle positions and the small scales of the flow.
- Finally, the RANS formalism considers the ensemble-average over the full probability space.

In this chapter, we want to investigate the differences in the results of each of these formalisms, in order to see what is the impact of the choice of the probability space. Before heading to the results, we first present the chosen fluid in our numerical framework.

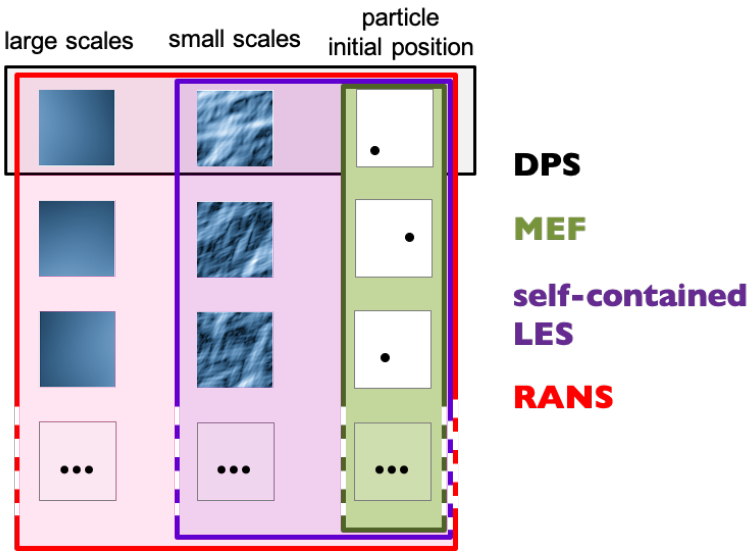

Figure 9.1. Schematic representation of the different possible formalisms embedded in the EMEF: DPS (black box), MEF (Green box), self-contained LES (purple box) and RANS (red box). Each column represents a random variable corresponding to the large scales (left), the small scales (centre) and the particle initial positions (right).

9.2 Choice of the fluid

Based on the outcomes of the previous part, we have chosen a fluid of reference that ensures statistical convergence over the metrics of interest. The parameters of the chosen fluid are listed in Tab. 9.1. These parameters give a fluid with the properties summed up in Tab. 9.2.

Physical name	Symbol	Value
Number of modes	N_κ	200
Total average Eulerian energy	k	1. $m^2.s^{-2}$
Minimum of the range of wave-numbers	κ_{min}	10. m^{-1}
Maximal of the range of wave-numbers	κ_{max}	$10.^5$ m^{-1}

Table 9.1. Free parameters chosen for the fluid for Part. III

Physical name	Value	Reference
Fluid velocity variance	0.1 $m^2.s^{-2}$	Fig. 8.9
Autocorrelation time of the fluid	0.25 s	Fig. 7.7

Table 9.2. Properties of the fluid chosen for Part. III

Now, in the context presented Sec. 9.1, let us show with the following figures, different elements of the set $\mathfrak{G}^{\leftarrow} \circ \mathfrak{G}(\boldsymbol{u}_f)$, for one given field $\boldsymbol{u}_f$. These figures illustrate the sets of fluids used for assessing the behaviour of the EMEF in the next section.
Let us start with Fig. 9.2, which is a visual illustration of two fields. The top graph represents the fully resolved fields of two different realisations conditioned on the same reduced scales presented in the second graph. The residual scales are on the bottom graphs. They are entirely de-correlated between both realisations.
Now let us have a look at the modes themselves. The amplitudes of the modes of two different realisations $\boldsymbol{u}_{f,1}$ and $\boldsymbol{u}_{f,2}$ of a KS according to the amplitude of the wave number of the modes are represented in Fig. 9.3. Each realisation is represented by a different colour, respectively black and red. These two realisations share the same reduction: $\mathfrak{G}(\boldsymbol{u}_{f,1}) = \mathfrak{G}(\boldsymbol{u}_{f,2})$, therefore they both belong to the set $\mathfrak{G}^{\leftarrow} \circ \mathfrak{G}(\boldsymbol{u}_{f,1})$. We say that they are conditioned on their largest scales. The vertical grey line on the graph corresponds to the cut-off frequency of the reduction operator $\mathfrak{G}$. Hence, the amplitudes of the largest scales have the same values for both realisations: the value of the points to the left of the grey line are equal. However, although the amplitudes of the smallest scales still follow the same probability law, they are independent for each realisation: the values of the points to the right of the grey line are different.
Fig. 9.4 represents the frequencies of two different realisations of a fluid conditioned on its largest scales. Similarly to Fig. 9.3, it illustrates the principle of conditioning: the frequencies of the largest scales have the same values for both realisations whereas the amplitudes of the smallest scales are independent of each other.
Finally, Fig. 9.5 is a 1D cut of the fields presented in Fig. 9.2. It helps to get a better visualisation of the velocity profiles. The first row presents two different velocity profile realisations conditioned on their lowest scales presented on the graph of the second row. The two graphs of the third row present the residual velocity profiles of both realisations. It clearly illustrates that a fluid particle or an inertial particle will "see" the same large scales, but will encounter different small scale fluctuations, which is at the core of the construction of our formalism.

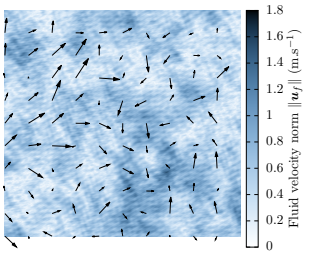

One fluid realization.

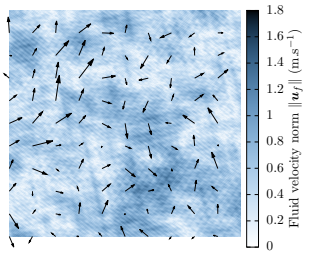

A second fluid realization.

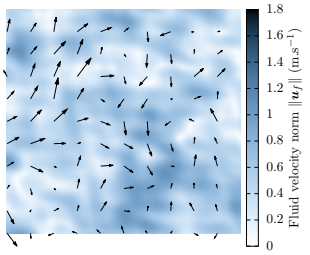

Lower frequency modes shared between the two fluid realisations.

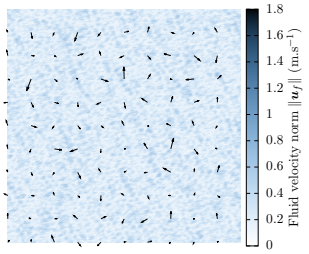

Higher frequency modes, specific to the first realisation.

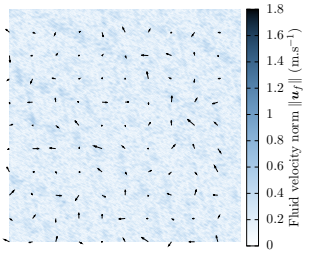

Higher frequency modes, specific to the second realisation.

Figure 9.2. Colormaps of the intensity of self-conditioned fluid velocity fields in the plane $z = 0$ superimposed to a quiver plot of fluid velocities projected on the plane $z = 0$. Fluid conditioned by 80% of its lower wave-number modes. The two realisations share the lower frequency modes (80% in energy) and have their own lower frequency modes (20% in energy). The size of the domain is 1m×1m.

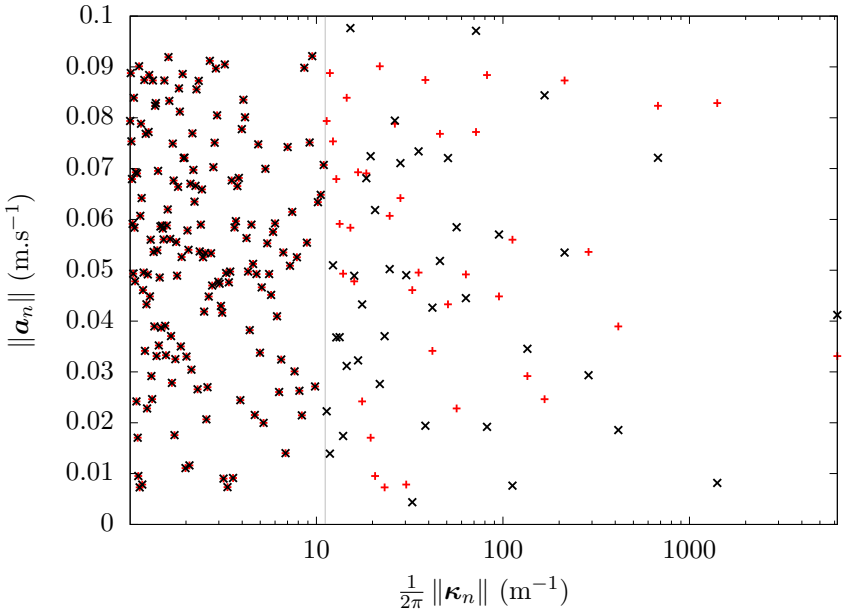

Figure 9.3. Two fluid realisations: amplitudes of the modes against the wavenumber. The two realisations are represented respectively in black and red, conditioned on the largest scales, representing on average 80% of the total energy of the fluid.

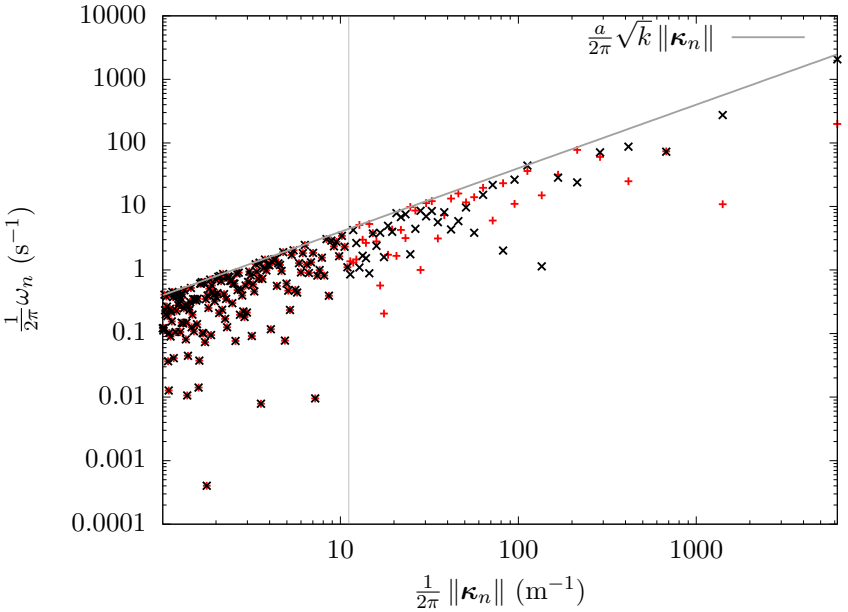

Figure 9.4. Two fluid realisations: frequencies of the modes against the wavenumber. The two realisations are represented respectively in black and red, conditioned on the largest scales, representing on average 80% of the total energy of the fluid.

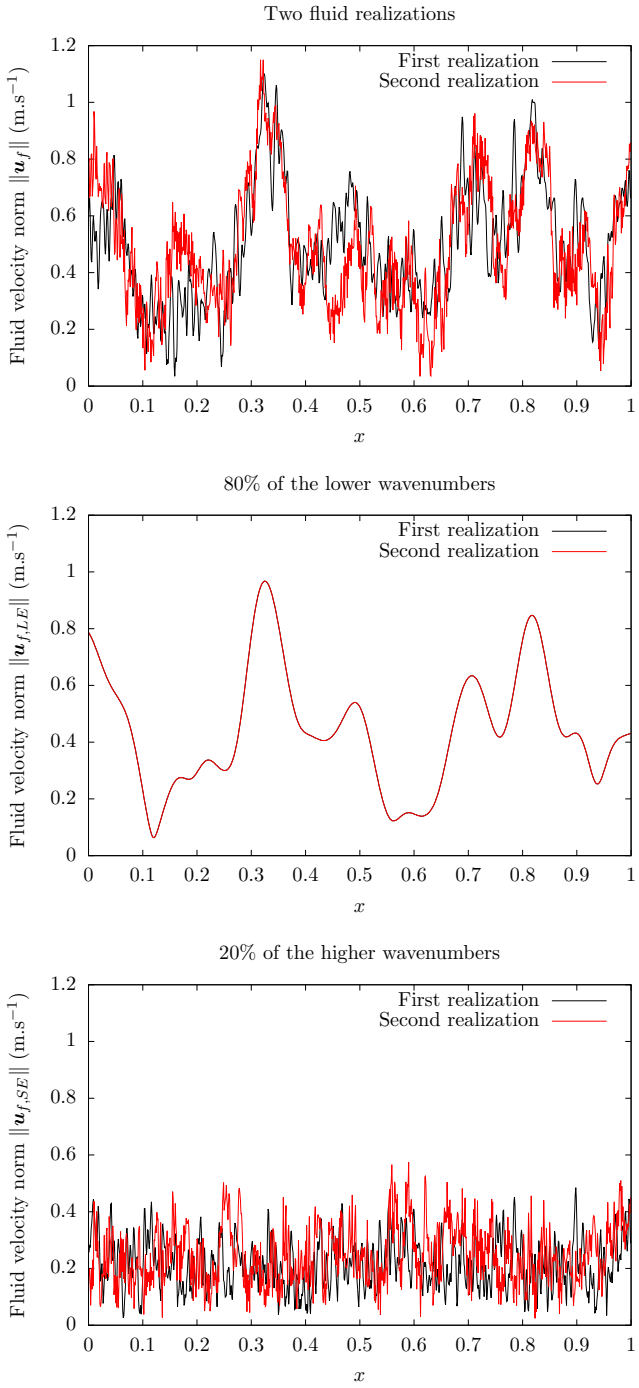

Figure 9.5. Intensity of self-conditioned fluid velocity fields on the line $y = 0$ and $z = 0$. Fluid conditioned by 80% of its lower wave-number modes.

9.3 Influence of the level of fluid reduction on the EMEF

This chapter presents numerical illustrations of the EMEF introduced in Sec. 5.3.1, based on the influence of the fluid reduction level. The objective is to get an idea of the behaviour of reference of the MEF when extended to LES with the EMEF. Once this behaviour is known it is possible to design closure models, which reproduce this behaviour (Chap. 10).

We focus on second order moments of the particle distribution in space and velocity and compare the results given by the EMEF for different levels of fluid reduction. We observed in Sec. 5.4.1.2 (Fig. 5.2) that the EMEF tends to disperse the particle positions. That is why we have chosen the variance as a measure of particle dispersion and as a metric to compare the disperse phase evolution under the EMEF.

The metric of interest is the sample variance of particle relative positions, which is the expectancy of the squared relative displacement of each particle of each realisation with respect to its initial position. In the following, we first present a result of spreading of particles for a given sub-grid scale energy. We then investigate the impact of the probability space on the EMEF distribution, and we look further at the origin of the observed trends through the particle velocity variance and the decomposition of the sample variance of particle relative positions.

9.3.1 Expected spreading of particle

The left-hand side of Fig. 9.6 represents the time evolution of the sample variance of the particle relative positions under the EMEF. One observes that the sample variance of particle relative positions under the EMEF is a monotonously increasing function of time. It is one characterisation of the spreading of the distribution of particles. This is consistent with Fig. 5.2 which shows sample trajectories being dispersed by different self-conditioned fluid realisations.

Adopting a log-log scaling on the right side of Fig. 9.6, we find back the traditional fluid regimes identified by Taylor (1921):

- At initial times, particles are still correlated to their initial conditions. It is the initial transport regime, characterised by a slope of 2.
- As time goes by, their motion becomes more erratic and the transport regime is replaced by diffusion, identified by a slope of 1.

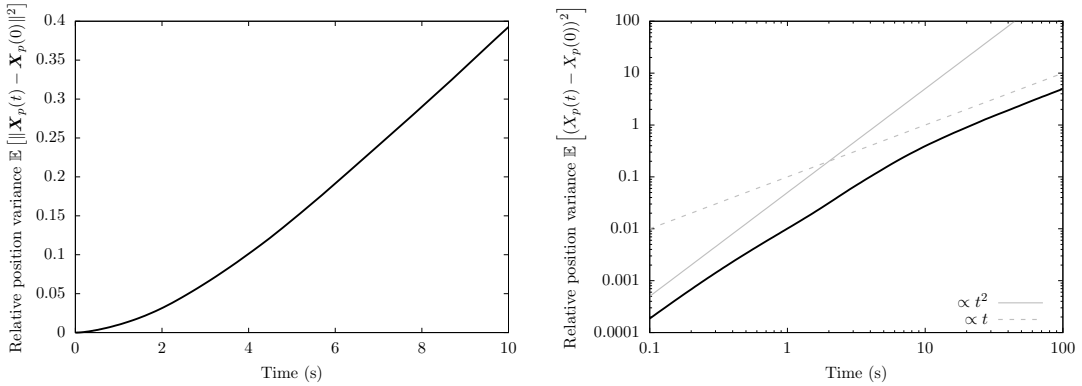

Figure 9.6. Time evolution of the sample variance of particle relative positions under the EMEF, with linear (left) or log (right) scales.
Relative variance of one physical particle position on 240 sub-grids, averaged over 240 large eddies. The sub-grid amounts for 20% of the total fluid energy. Particle relaxation time scale of 1s. Initial particle velocity set to fluid velocity.

9.3.2 Influence of the random subspace on the spreading of inertial particles

Fig 9.7 presents the behaviour of the time evolution of the sample variance of particle relative positions under the EMEF for different levels of fluid resolution:

- For 0% of resolved energy, the simulation is RANS. All possible particle trajectories over realisations are averaged. No conditioning is performed.
- For 100% of resolved energy, the simulation is a DNS. Only one particle trajectory is computed. There is no dispersion. It is in this context that the traditional MEF is defined (Sec. 2.3.3).
- For intermediary percentages of resolved energy, the dispersion represented corresponds to the EMEF. The particle evolution is represented by the distribution of all possible trajectories on all the fluids, which share the same large scales.

Interestingly, the limit case of DNS is a degenerate case as it does not present any dispersion. On the opposite, as soon as some strictly positive amount of statistical averaging on the fluid is involved in the definition of the MEF, the evolution of the particle distributions are quite similar (on the right of Fig 9.7): they all fall into the very standard pattern: a transport regime followed by a diffusion regime. Two important conclusions can be drawn at this point:

- The transport regime appears to be directly influenced by the amount of resolved fluid energy. Following Taylor (1921) analysis, the increase in relative particle position variance in the transport regime is directly proportional to the particle velocity variance.
- The diffusion regime is not affected by the percentage of resolved energy. The only difference is in the time needed to reach this regime, which is increasing when increasing the amount of unresolved scales.

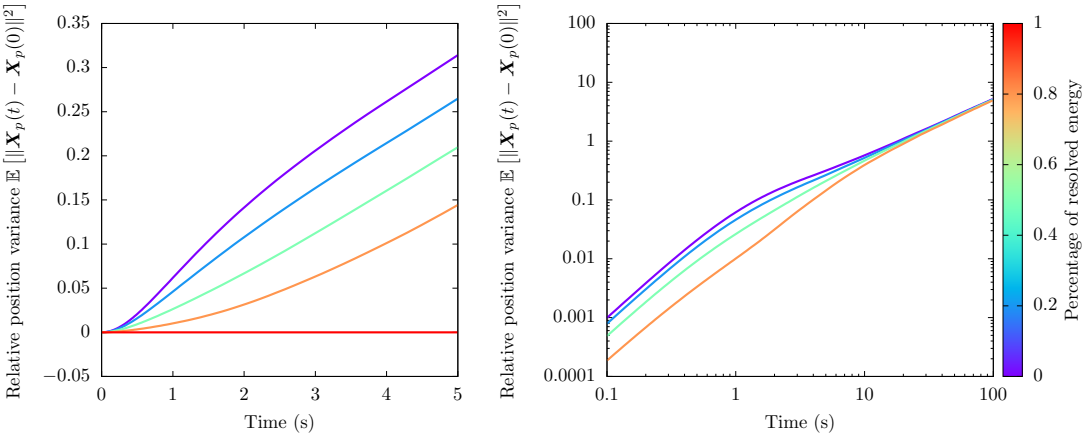

Figure 9.7. Time evolution of the sample variance of particle relative positions with EMEF. Relative variance of one physical particle position on 240 sub-grids, averaged over 240 large eddies. Different amounts of fluid energy resolution are represented (0, 20, 50, 80 and 100%). Particle relaxation time scale of 1s. Initial particle velocity set to fluid velocity.

9.3.3 Particle velocity variance

To better understand the origin of such trends, let us have a closer look at the particle state. First, Fig. 9.8 represents the fluid velocity variance associated with one point in space. On the right, when 100% of the fluid energy is resolved, there is no uncertainty in the fluid field. It is perfectly determined at each given position in space. This is true, even to the limit case of low regularity fields such as the ones presented 7.11. This is the context of fluid DNS.
On the opposite, on the left, 0% of the fluid energy is resolved. This corresponds to a situation where the fluid realisation is undefined. This is the entirely statistically averaged scenario of the isotropic context presented here. It is equivalent to RANS for NS equations. At one given point in space, the fluid velocity in not known at all. The uncertainty in the fluid velocity amounts to the entire fluid energy.
The level of resolution of the fluid does not have to be binary. It is possible to continuously vary the fluid resolution from 0 to 1. By increasing the fluid resolution, the fluid field becomes more and more defined. Uncertainty is decreased progressively from a RANS state, to a DNS state. These intermediate states correspond to what is commonly named LES for NS equations.
Initially starting from the fluid velocity distribution of variance presented Fig. 9.8, inertial particles evolve in time. The temporal evolution of particle velocity variance is presented Fig. 9.9. Aside from the DNS case, all particle velocity variances converge to the same stationary velocity for long times. The combination of two factors explain this behaviour :

- The fluid is mixing the particles. Therefore, changing the fluid ever so slightly, drastically changes the particle trajectory. This is why, after some time, the particle distribution is dispersed in physical space, progressively forgetting its initial

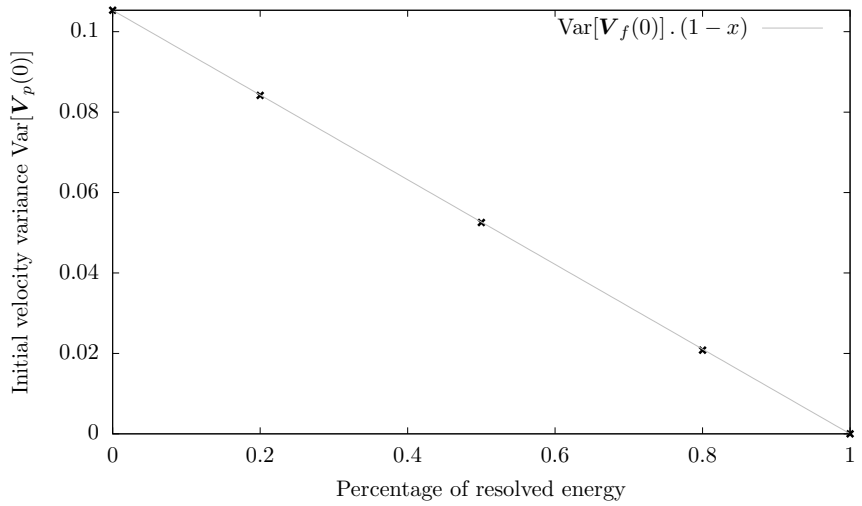

Figure 9.8. Initial particle velocity variance under the EMEF according to the amount of resolved energy, with our choice of KS.
240 sub-grids, averaged over 240 large eddies. Initial particle velocity set to fluid velocity.

conditions.

- The second factor is that all sample particles evolve on fluids with the same physical characteristics. The fluids are not filtered. They all have similar statistical properties. For instance, they have the same energy, same autocorrelation time, and same energy spectrum. The only difference is the size of the statistical set of fluids associated with the particle distribution.

Therefore, after some time, sample particles forget their initial conditions and sample different regions of different fluid with the same statistical properties. On average and after some time, the statistical properties sampled by the particles do not depend on the size of the set of fluids chosen, as long as this set contains more that one element.
This explanation of the convergence of long time particle velocity variance observed on the right of Fig. 9.9, helps us understand the right hand side of Fig. 9.7 better: it was observed in the log-log scale representation of the particle sample variance (Fig. 9.7), that all dispersive distributions fall back on the same diffusion regime. Indeed, the reasoning above highlights that on average, particle trajectories evolve with the same statistical properties whatever the size of the set of fluids chosen. The diffusion regime is only defined by such statistical properties which are velocity variance and autocorrelation time. This is why we observe that the diffusion coefficient of the terminal regime is identical, whatever the size of the set of fluids chosen, as long as it is greater than 1 (size 1 is DNS where the fluid is certain).

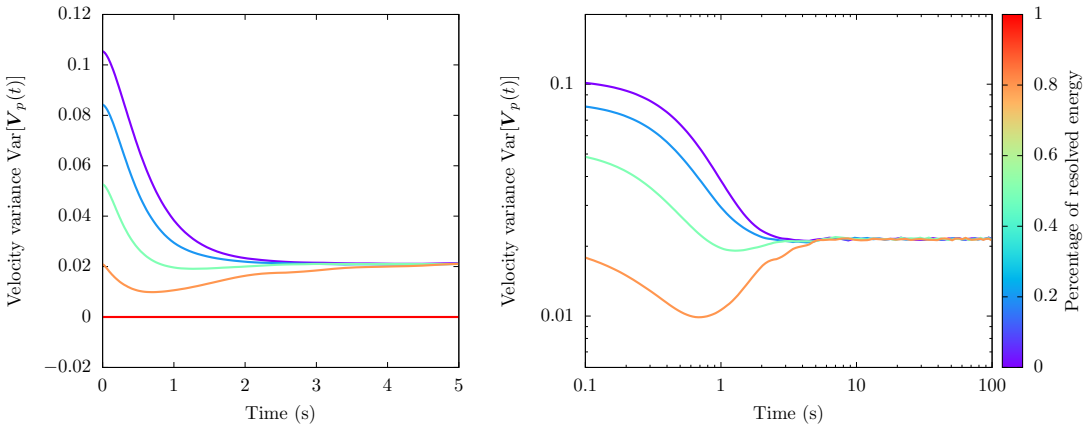

Figure 9.9. Time evolution of the sample variance of particle velocity under the EMEF. Relative variance of one physical particle position on 240 sub-grids, averaged over 240 large eddies. Different amounts of fluid energy resolution are represented (0, 20, 50, 80 and 100%). Particle relaxation time scale of 1s. Initial particle velocity set to fluid velocity.

9.3.4 Decomposition of the sample variance

Let us first note that although all positive levels of fluid reduction lead to a diffusion regime with the same diffusion coefficient, the sample variance of the particle relative positions is still function of the level of fluid reduction. Indeed, the sample variance of the particle relative positions depends on the integrated effect of the initial transport regime which is affected by the size of the set of fluids implied by the reduction operation $\mathfrak{G}^{\leftarrow} \circ \mathfrak{G}(\boldsymbol{u}_f)$.

Let us get a bit more insight on the physical dispersion of the distribution of particles by decomposing the relative position variance of sample particles between resolved scales (LE) and unresolved scales (SE). This is done in Fig. 9.10 by applying the law of total variance (Eq. 8.6). With this decomposition, the law of total variance reads:

$$\mathrm{Var} = \mathrm{Var} \circ \mathbb{E}\left[\cdot \,|\mathrm{LE}\right] + \mathbb{E} \circ \mathrm{Var}\left[\cdot \,|\mathrm{LE}\right], \tag{9.1}$$

with $\circ$ the composition operator. Let us present these different terms:

- Var represents the overall variance of all particles on all possible fluids.
- $\mathrm{Var} \circ \mathbb{E}\left[\cdot \,|\mathrm{LE}\right]$ represents the variance of the mean particle position conditioned on a resolved field. For one reduced fluid field, there is a set of fluid sharing the same reduced field. This creates an ensemble of different fluids conditioned on a common characteristic: the reduced field. Sample particle trajectories go in different directions according to the residual fluid field. However, they can be correlated through the resolved fluid scales which are common to all the sample trajectories. One way to assess this correlation is to observe the evolution of the mean position of sample particles. This quantity is null on average because it is algebraic and the distribution of fluids is isotropic on average. But its variance gives an idea of its order of magnitude.

- $\mathbb{E} \circ \mathrm{Var}\left[\,\cdot\,|\mathrm{LE}\right]$ is the average dispersion of particles over all sets of self-conditioned fluids. It is the quantity we have been interested in so far, because it characterises the growing uncertainty of the particle position of the EMEF distribution which is absent in the standard MEF. The increase of $\mathbb{E} \circ \mathrm{Var}\left[\,\cdot\,|\mathrm{LE}\right]$ is caused by the uncertainty of the unresolved fluid field.

We observe in Fig. 9.10 that during the initial inertial regime, the term $\mathrm{Var} \circ \mathbb{E}\left[\,\cdot\,|\mathrm{LE}\right]$ represents most of the overall variance Var. During this period of time, sample particle velocities are still correlated to their initial conditions. As they originate from the same physical location, they initially undergo exactly the same resolved fluid field. This resolved fluid field gives them a mean motion measured by the quantity $\mathrm{Var} \circ \mathbb{E}\left[\,\cdot\,|\mathrm{LE}\right]$. After the ballistic regime, particles lose the correlation to their initial position. They get dispersed by the added effects of the fluctuating sub-grid scales across realisations and the chaotic nature of their trajectories. Therefore, the term $\mathrm{Var} \circ \mathbb{E}\left[\,\cdot\,|\mathrm{LE}\right]$ does not increase further.

By complementarity, the evolution of the term $\mathbb{E} \circ \mathrm{Var}\left[\,\cdot\,|\mathrm{LE}\right]$ is the exact opposite. Because at the beginning of the dispersion, sample particles are correlated to their initial condition, and thus to the resolved scales, the motion is characterised by synchronised transport, and diffusion is absent. However, after some time, sample particle motions become erratic and $\mathbb{E} \circ \mathrm{Var}\left[\,\cdot\,|\mathrm{LE}\right]$ starts to increase steadily. At this stage, it becomes the major contribution to the overall variance Var.

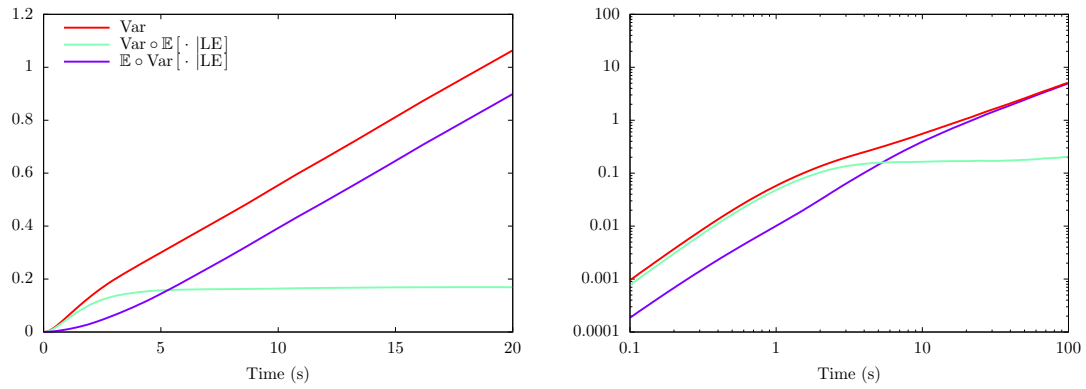

Figure 9.10. Decomposition of the variance of particles over different realisations according to the law of total variances.
Relative variance of one physical particle position on 240 sub-grids, averaged over 240 large eddies. For 80% resolved fluid energy. Particle relaxation time scale of 1s. Initial particle velocity set to fluid velocity.

To conclude, we have presented in this section the impact of LES on the extended MEF distribution. We have shown that reducing the fluid prevents a deterministic treatment of particle trajectories. As soon as the fluid is not perfectly known, particle have to be treated as distributions. A specific quantity of interest if the spatial variance of this distribution. It characterises the uncertainty of the particle position caused by the reduction of the fluid. It is crucial in a context where we would want to enforce coupling

because it corresponds to the location in the fluid where the coupling would take place:

- For short times, in the ballistic regime, the increase in the spatial variance of the distribution of the particle is directly proportional to the level of reduction of the fluid.
- For long times, in the diffusion regime, the main contributor to the growth of uncertainty in the particle position is turbulence itself.

9.4 About the limitations of our study

Let us review the hypothesis considered in this work and the implication of the observations made in the previous section. We have seen that the EMEF offers a unified description of particles distributions from DNS up to RANS. This is made possible by gradually changing the set of fluids associated to the particle distribution. It is possible to assert that in the context where this work was conducted, switching from a DNS physical particle trajectory to the behaviour of a particle with some uncertainty in the fluid has a very strong impact on the particle distribution. This impact is proportional to the fluid uncertainty for times close to initial conditions. For these early times, physical correlation still takes into account the initial statistical correlation. However, for long times, uncertainty growth is directly controlled by the physical properties of turbulence itself, whatever the initial amount of fluid resolution. The behaviour is the same for all the cases including some positive amount of uncertainty.
At this point, it is important to look back at the hypothesis we used in order to derive these observations, so that we can assess their impact on the results observed in the previous section.

- **Stability of the large scales.** In the case presented here, with kinematic simulations, the fluid was in a way ruled out. The largest scales of the flow were assumed to be stable in time whatever the different choices of the smallest scales. If we were to work with NS this stability would be removed. There is no formalism yet able to take into account this instability in the context of NS equations although some ideas have already been suggested by Pope (2010). As we have seen in the previous section, increasing the uncertainty of the fluid description is only bound to increase the dispersion of the distribution of the particles in position.
- **Independence of the small scales.** In the case presented here, the small scales where assumed independent of the largest scales of the flow. If we consider cases where the small scales are dependent on the largest scales of the flow, this decreases the size of the probability space associated to the small scales. It does not change the principle of the results presented here, but decreases the span of the maximum dispersion of the ballistic regime. In the limit where the small scales are uniquely defined for one large scales realisation, we fall back into the DNS case.
- **No coupling.** In the case studied here, the particles did not impact the fluid phase. We have seen in the previous section that the reduction of the fluid implies that the unresolved fluid scales are not well known. This uncertainty in the definition of the fluid field translates into an uncertainty of position of the particles. In a case

where the particle retroact on the fluid, this means that the location of the force exerted by the disperse phase on the fluid is not located precisely. This causes even more uncertainty of the fluid field. Thus, following on the first point, in a coupled configuration, we expect an increase of the dispersion of the distribution of the particles in position.

- **Initial particle velocity.** The effect of choosing different fluids was artificially amplified by setting the initial particle velocity at the fluid velocity. In the results presented in the previous sections, the relaxation time scale of the particles was $\tau_p = 1$s. Let us now present what we expect from changing this value.
  - When working with fluid parcels with no inertia $\tau_p = 0$, the ballistic regime corresponds to the ballistic regime of the fluid which is shorter than the ballistic regime of inertial particles. Therefore, fluid parcels are expected to have a shorter initial ballistic regime than the results presented in the previous section.
  - On the contrary, for particles with more inertia, the initial ballistic regime is expected to be longer. Furthermore, if one were to work with thermalised inertial particles, these would be less and less correlated to the fluid as their inertia is high (Février, Simonin, and Squires (2005)). This would tend to decreases and delay the span of the maximum dispersion in the ballistic regime.

Impact on two-way coupling modelling strategy. Now, let us review the impact of these observations on possibilities for modelling two-way coupled two-phase flows.

- After the autocorrelation time scale of the system, an approach involving statistical averaging such as MEF cannot possibly aim at giving a result different than RANS. In this sense, it could still be interesting to derive a time-evolving model which degenerate to RANS after the correlation regime.
- For someone willing to capture non-permanent dynamics, the favoured route seems to compute trajectories of the system, where no averaging is done, but uncertainty is sorted out through random selection.

However let us stress out that this is quite preliminary, as consistent coupled models, even for DNS simulation are still under development today (Zeren (2010), Sec. 2.4.1 and 2.4.2, Horwitz and Mani (2016), Poustis, Senoner, Zuzio, and Villedieu (2019)).

Highlights and conclusions

A numerical study of the EMEF has been presented, based on the use of kinetic simulations of turbulence. The differences between the MEF in a DNS context for the fluid, and the EMEF in the context of reduced fluids, have been investigated:

- The main difference is that the EMEF is always dispersive, even for a delta Dirac distributions.
- The level of initial dispersion of the EMEF is proportional to the uncertainty in the resolved energy of the reduced fluid.
- The long time dispersion of the EMEF is not impacted by the uncertainty in the resolved energy of the reduced fluid, by only by the physical characteristics of the carrier field.

Chapter 10

Evaluation of diffusive closures for LES in the context of the EMEF

In the previous chapter, we have presented the reference behaviour of the EMEF in the context of self-contained fluid reductions based on KS. This is the behaviour we wish for when computing the evolution of inertial particles on a reduced flow field.
Now, the next step is to try to model the dynamics of particles in the context of the EMEF. Unfortunately, we do not have access to the EMEF distribution in the context of the NS equations, because in LES, the sub-grid scales are not known. Furthermore, we have already shown in Sec. 4.2 that computing the evolution of the particles on the reduced fluid alters the behaviour of the disperse phase, but these results were presented in the context of Navier-Stokes equations, and not in our KS context.
This chapter aims at assessing the relevance of diffusive closures for LES in the context of the EMEF. In order to do so, this chapter is divided into three contributions:

- Before performing LES, we first evaluate the effect of fluid reduction in the context of KS, to see the consistency with the real physics encountered when using Navier-Stokes equations for the fluid.
- Then, we investigate what we could expect of Lagrangian diffusive closures, i.e. closures based on the addition of a Wiener process in one equation of evolution of the particles.
- We finally evaluate this class of models for LES under our numerical framework, and we open the discussion to more complex models of the literature.

10.1 Effect of fluid reduction on particle dynamics in KS

For inertial point particle models, the particle dynamics relies on the fluid velocity at the particle location. We have already seen in Sec. 4.2, that altering this fluid velocity alters the particle behaviour. Therefore, the particle evolution on the reduced fluid is different from the particle evolution on the resolved fluid. In this section, we want to assess this impact in the context of KS. The fluid is the one presented in Sec. 6.1. The reductions are the same as those presented in Sec. 10.1. In order to ensure consistency

the fluid and the reduction operation chosen here are the same as in Chap. 9.
We will start by presenting the effect of filtering KS on the dynamic of inertial particles, before observing the impact of inertia on the dynamic of particles on a filtered fluid field.

10.1.1 Impact of fluid reduction on particles of fixed finite inertia

The reduction of the velocity field affects the disperse phase through the fluid velocity seen by the inertial particles. Therefore, we chose to start by presenting the PSD of the fluid velocity seen by inertial particles for different levels of fluid reduction in Fig. 10.1. We can observe the impact of different levels of reduction on the fluid frequencies seen by the particles. Removing the fluid modes of higher frequencies also removes the higher frequencies of the fluid velocity seen by the particles. This result is fully expected and this is just a preliminary step in the assessment of the effect of fluid reduction in our KS context.

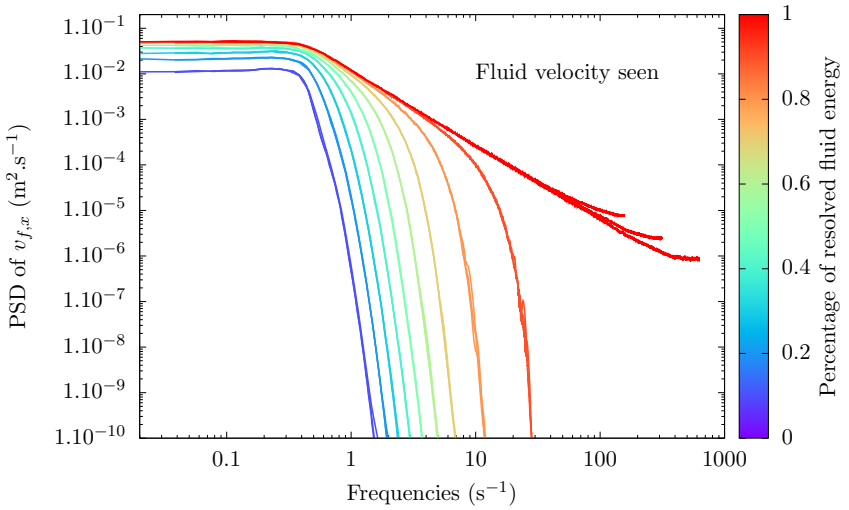

Figure 10.1. Power spectral densities of the fluid velocity seen by an inertial particle of relaxation time τ_p=1s along its trajectory on 240 fields of different resolution. Each PSD is the superposition of 6 PSD of 2^{14} points with Hann windowing of different sampling frequencies in order to get a visualisation of a wide spectrum range.

The fluid velocity seen by inertial particles appears in the acceleration term of Stokes' drag law (Eq. 2.1). Therefore, as a consequence, filtering the fluid velocity field is expected to have an impact on the velocity of inertial particles as we have seen in Sec. 4.2.2 for NS equations. In order to observe this effect, we chose to represent the power spectral densities of the velocity of the particle themselves for different levels of reduction on the frequencies of its velocity in Fig. 10.2. We can observe in Fig. 10.2 that, as higher frequencies are removed in the fluid, they also disappear in the particle trajectories. The less energy in the fluid, the less energy in the particles.
In order to get a more quantitative representation of the impact of fluid reduction,

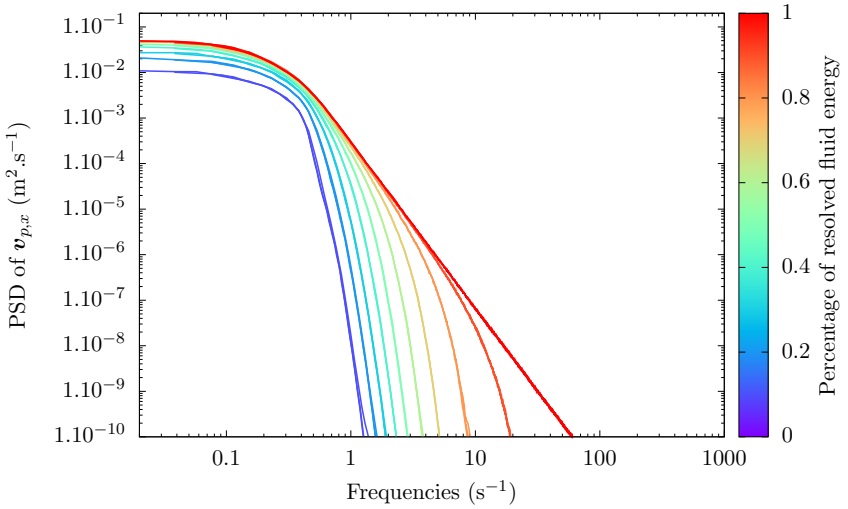

Figure 10.2. Power spectral densities of the velocity of an inertial particle of relaxation time τ_p=1s along its trajectory on 240 fields of different resolution. Each PSD is the superposition of 6 PSD of 2^{14} points with Hann windowing averaged 10 times, of different sampling frequencies in order to get a visualisation of a wide spectrum range.

Fig. 10.3 represents the energy of the fluid velocity seen by the particles (right) and the energy of the particles themselves (left). We can see that, as the resolved fluid energy is decreased, so is the fluid energy seen by the particles. The relation between the fluid energy and the fluid energy seen by the particles is linear. These observations are consistent with the right hand side of Fig. 8.9 representing the energy of the fluid velocity seen by inertial particles according to their inertia. We have seen with Fig. 8.9 that the energy of the fluid velocity seen by inertial particles is independent of inertia of the particles. Therefore, the energy seen by inertial particles is equal to the energy of fluid parcels. We can thus conclude that reducing the energy of the fluid field has a direct impact on the energy of the fluid velocity seen by inertial particles. Let us now focus on the particle velocity variance, represented on the left of Fig. 10.3. We observe that the less energy in the fluid, the less energy in the particles. This observation is consistent with Fig. 4.1 from Fede and Simonin (2006), giving then a first confirmation that reduced simulation in our KS context can give results consistent with realistic Navier-Stokes simulations.

Integrating the velocity velocity of the particles gives the position of the particles. Therefore, we expect an impact of the fluid reduction on the dispersion of inertial particles. The variance of particle position as a function of time for different levels of fluid reduction is represented in Fig. 10.4. We can see on the left hand-side of Fig. 10.4 that fluid reduction does not alter the characteristic regimes of particle dispersion:

- we can always observe an initial ballistic regime where the temporal evolution of the variance of the particular position is quadratic,
- followed by a diffusion regime where the temporal evolution of the variance of the

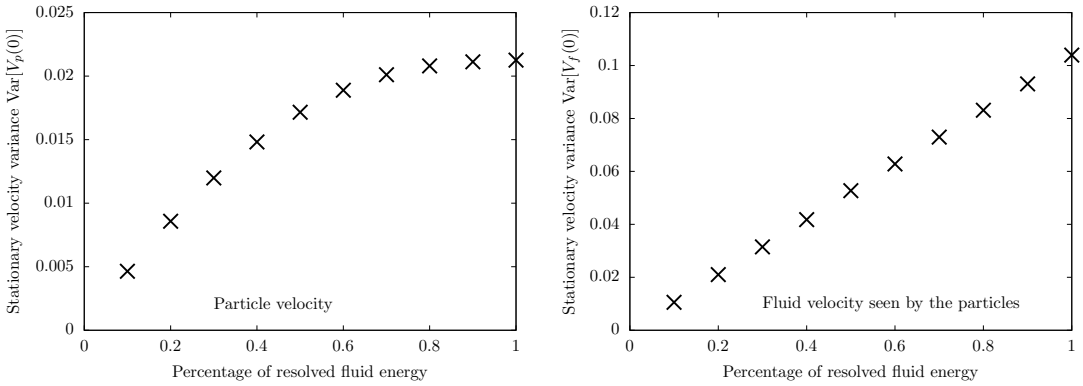

Figure 10.3. Second order moment of particle velocity (on the left) and of fluid velocity seen by particles (on the right) according to fluid resolution (particle relaxation time $\tau_p = 1$s).

particular position is linear.
However, the right hand-side of Fig. 10.4 clearly shows fluid reduction has a strong impact on the level of particle dispersion: the more the fluid is reduced, the less the particles are dispersed. In order to get a more quantitative vision of this phenomenon, the particle dispersion coefficient according to the level of fluid reduction is represented on the left hand-side of Fig; 10.5. We can observe that the less energy in the fluid, the less important the dispersion of the particles, the lower the dispersion coefficient. This is consistent with the observation made with NS equations in Fig. 4.2 from Fede and Simonin (2006).

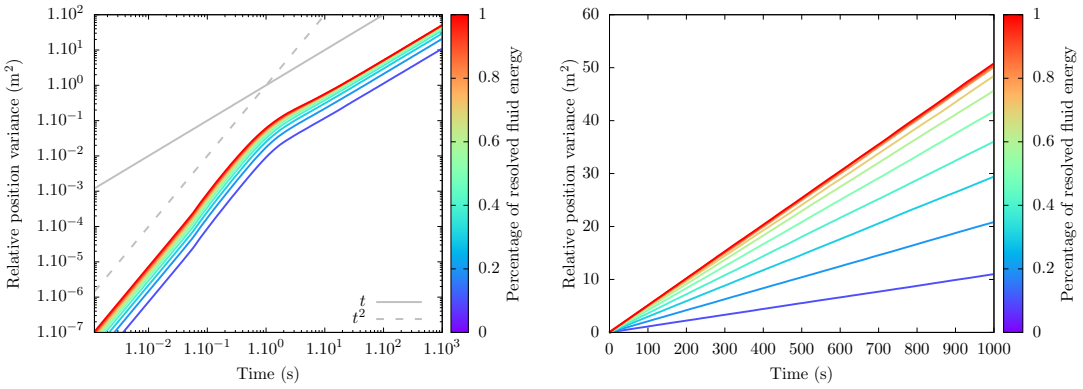

Figure 10.4. Particular dispersion (with logarithmic scaling on the left and with linear scaling on the right) for different levels of fluid resolution. Variance of 1024 particles averaged over 280 different fluid realizations. Particle of relaxation time τ_p=1s.

We have seen in Sec. 1.3.1.3 that diffusion is a function of the particle velocity variance, but also of the autocorrelation time of the particle velocity. Therefore, the autocorrelation time of the particle velocity is represented as a function of the level of fluid reduction on the right hand-side of Fig. 10.5. We observe in this figure that fluid reduction does

not have a significant impact on the particle autocorrelation. Therefore, the impact of fluid reduction on the particle dispersion is solely given by the influence of fluid reduction on the particle velocity variance.

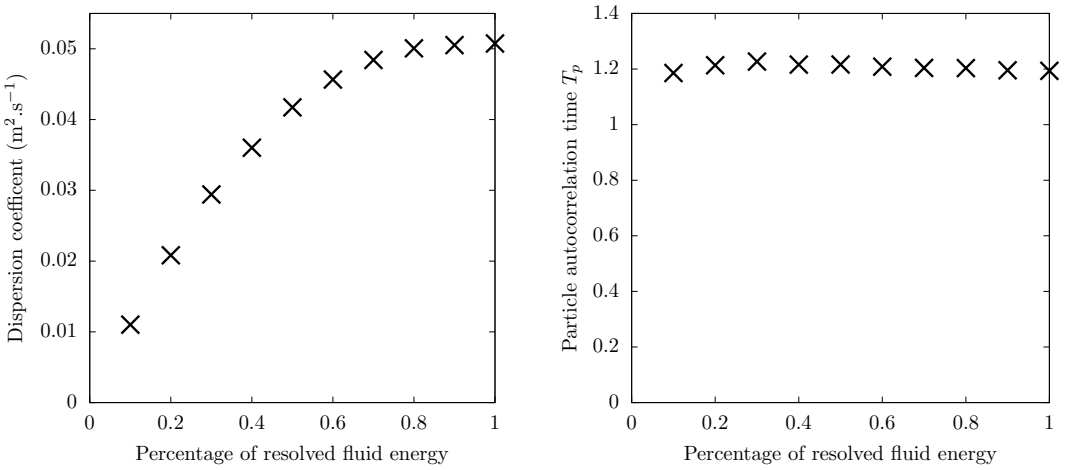

Figure 10.5. On the left, dispersion coefficient.
On the right, Particular autocorrelation time.
Each quantity is represented for different levels of fluid resolution. Variance of 1024 particles averaged over 280 different fluid realizations. Particle of relaxation time τ_p=1s.

We have presented the impact of fluid reduction on the second order moments of inertial particles in the context of KS. We have seen that fluid reduction decreases the variance of the fluid velocity seen by the particles, the variance of the particles and also the dispersion in space of the same particles. However, fluid reduction does not affect the autocorrelation time of the particle velocity. These results obtained with KS are consistent with Fede and Simonin (2006) in the context of the NS equations. Let us now present the effect of inertia on the behaviour of particles on a reduced fluid.

10.1.2 The role of inertia in the impact of fluid reduction of particles

We now present how inertia alters the effect of fluid reduction on the particles dynamics. For this section, we consider a fluid reduction which accounts for 80% of the fully resolved fluid energy. Similarly to the previous section, we will observe successively, the fluid velocity seen by the particles, the velocity of the particles and the dispersion of the particles.
The PSD of the fluid velocity seen by particles of different inertia is presented with and without fluid reduction in Fig. 10.6. We see that particles of all inertia seem affected similarly by the fluid reduction.
Because the fluid velocity seen by the particles influences the fluid velocity of the particles, we have chosen to represent the PSD of the velocity of particles of particles of different inertia, with and without fluid reduction in Fig. 10.7. Lines of the same colour

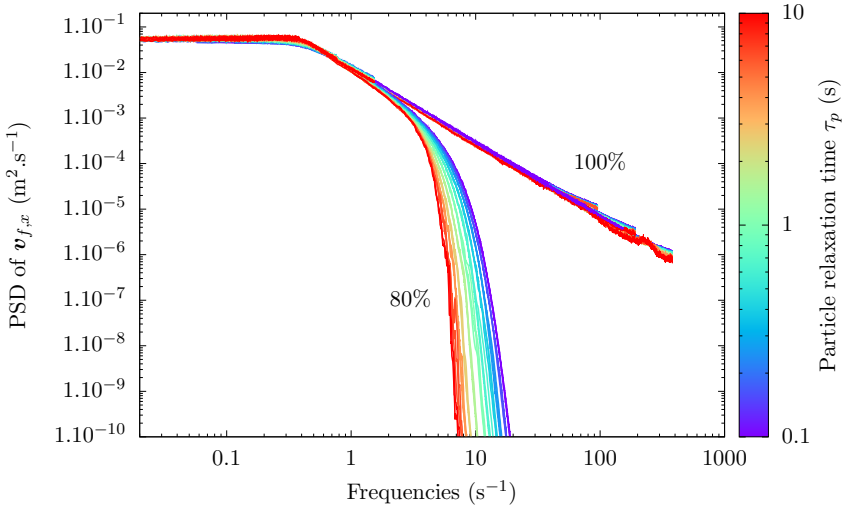

Figure 10.6. Power spectral densities of the fluid velocity seen by an inertial particle of different relaxation times along their trajectory on 240 fields of two resolutions: 100% and 80%. Each PSD is the superposition of 6 PSD of 2^{14} points with Hann windowing of different sampling frequencies in order to get a visualisation of a wide spectrum range.

corresponds to particles of same inertia. When the fluid is reduced, the corresponding PSD shows a lower energy content in the higher wave-numbers.

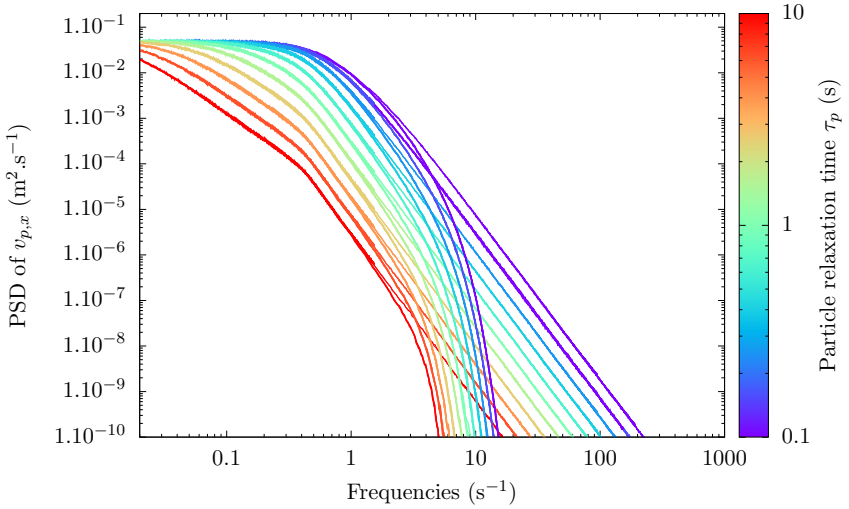

Figure 10.7. Power spectral densities of the particle velocity of inertial particle of different relaxation times along their trajectory on 240 fields of two resolutions: 100% and 80%. Each PSD is the superposition of 6 PSD of 2^{14} points with Hann windowing of different sampling frequencies in order to get a visualisation of a wide spectrum range.

To provide a more quantitative analysis, the influence of fluid filtering on the energy

of the particles of different inertia (left) and the corresponding fluid velocity energy (right) are represented in Fig. 10.8. The blue 'x' correspond to the fully resolved fluid whereas the black '+' correspond to the reduced fluid. We observe that the fluid energy seen by the particles is lower when the fluid is reduced than when it is fully resolved. Furthermore, as seen in the previous section, for a given level of fluid resolution, the fluid energy seen by the particles is independent of inertia. If we now look at the percentage of particle velocity variance on the fully resolved fluid represented by the particle velocity variance after reduction of 20% of the fluid energy for different inertia (left of Fig. 10.8), we can observe that inertia does not influence the proportion of particle energy removed by fluid reduction.

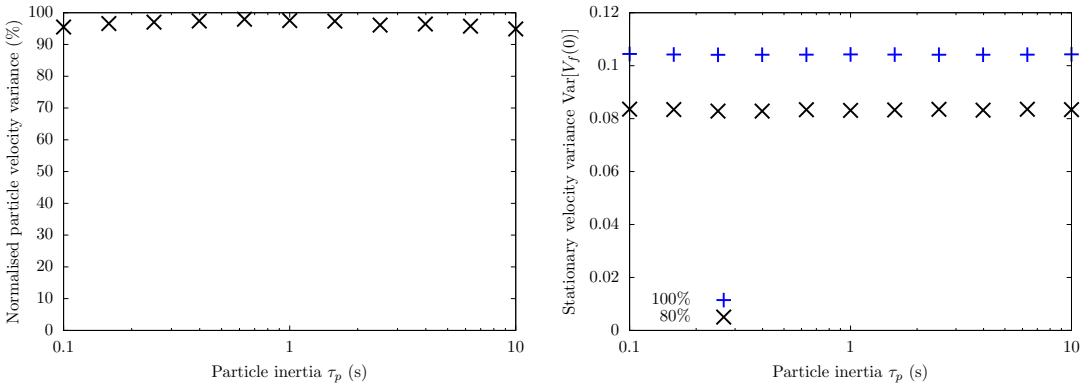

Figure 10.8. Second order moment of particle velocity on the reduced fluid normalised by the second order moment of particle velocity on the fully resolved fluid (on the left) and of fluid velocity seen by particles (on the right) according to particle inertia (100% and 80% fluid resolutions).

We then observe particular dispersion in Fig. 10.9 which represents the temporal evolution of the particle position variance with time for different inertia on the reduced fluid. Fig. 10.9 gives exactly the same behaviour as the one obtained on the fully resolved fluid represented in Figs. 8.7 and 8.8. We can observe on the left-hand side, which offers a representation with a logarithmic scale, the initial ballistic regime, which is quadratic, followed by the diffusion regime, which is linear. Inertia has an impact on the time-span of the ballistic regime. On the right-hand side which presents the same quantities with linear scales, we can observe the inertia impacts the actual level of diffusion of the particles.

The diffusion coefficient for different particle inertia is represented in Fig. 10.10. Comparing with the right-hand side of Fig. 8.8, when filtering only 20% of the total fluid energy, the fluid reduction does not appear to have a significant impact on the diffusion coefficient of inertial particles.

Particle diffusion can be expressed as a function of the particle velocity variance and the particle velocity autocorrelation time. Let us now look at the particle velocity autocorrelation time as a function of inertia on a filtered fluid represented Fig. 10.11. This figure is very similar with the left hand-side of Fig. 8.10 with represents the same

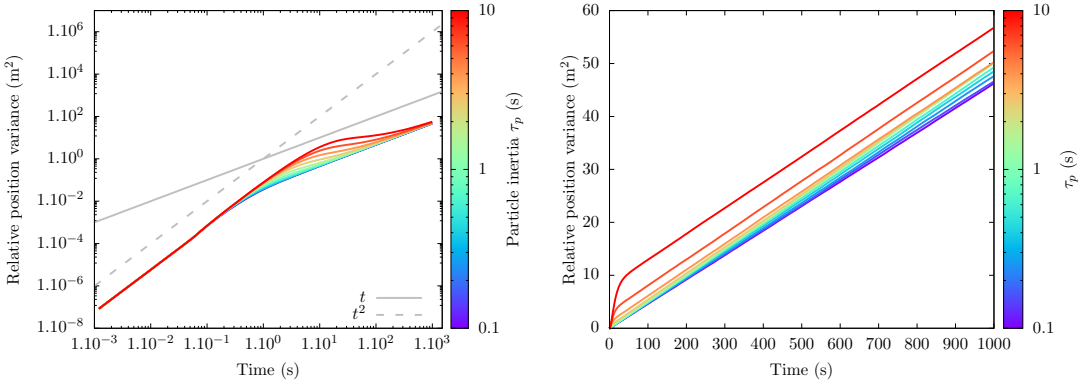

Figure 10.9. Particular dispersion (with logarithmic scaling on the left and with linear scaling on the right) for different levels of particle inertia. Variance of 1024 particles averaged over 280 different fluid realisations. Fluid resolution of 80%.

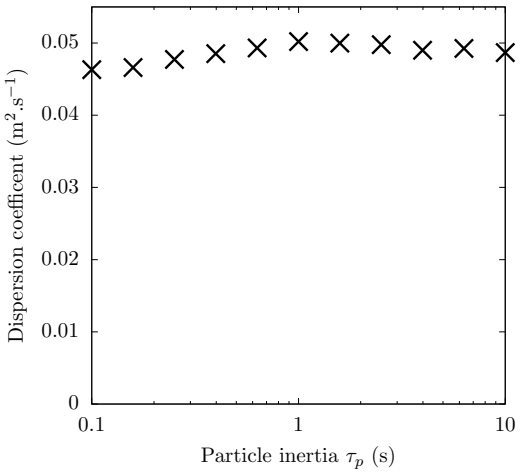

Figure 10.10. Dispersion coefficient for different levels of particle inertia. Variance of 1024 particles averaged over 280 different fluid realisations. Fluid resolution of 80%.

quantity on a resolved fluid. This is very consistent with Fig. 10.10 which shows that filtering has no significant impact on the particle autocorrelation time.

In this section, we have presented the impact of fluid reduction on the dynamics of inertial particles in the context of KS chosen for this work, and we have shown the consistency of our results with the literature based on Navier-Stokes. Therefore, we can consider that our framework can be used for validation of LES particle models. In the next section, we inspect a simple class of closures for the disperse phase from the

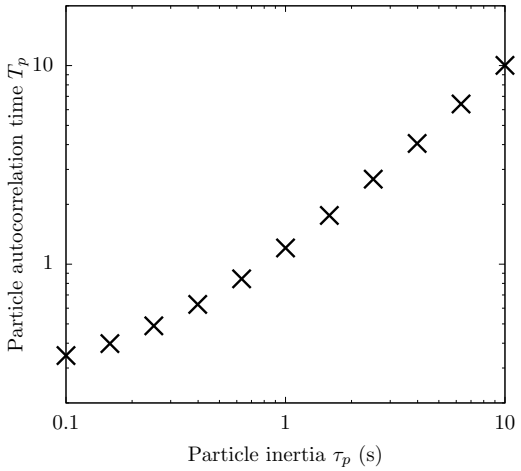

Figure 10.11. Particular autocorrelation time Var $[\boldsymbol{v}_p]$ / $(2.D)$ for different levels of particle inertia. Variance of 1024 particles averaged over 280 different fluid realisations. Fluid resolution of 80%.

literature. We will observe and assess how they affect the dynamics of inertial particles computed on a reduced flow field of KS.

10.2 Theoretical analysis of Lagrangian diffusive closures

Now that we have validated our numerical framework, we can expect to use and validate LES models for particle trajectories. Before going directly to LES, we want to understand the influence of LES closures for particles on the variables of interest: the second order moments of the distribution of the particles. This will allow us to determine what to expect at most from these models, thus enabling us to use them efficiently in order to close the evolution of inertial particles on a reduced fluid flow field. To this end, we perform a theoretical analysis of classical models of the literature, based on the addition of a Wiener process to the particle trajectories, and which differ only by the location of this forcing, as presented in Sec. 4.3.2. We focus on theses models because they are somehow the simplest Lagrangian models in a LES context, and have a strong similarity with classical eddy-dissipation models for gas phase dynamics for instance.
In order to study the effect of the models, let us start by studying the set of equations when $\overline{\boldsymbol{u}}_f = 0$, or equivalently, when the fluid is fully reduced. Corresponding variables

are indexed by 0. When $\overline{\boldsymbol{u}}_f = 0$, all three models share the same generic formulation:

$$\mathrm{d}\boldsymbol{X}_0(t) = \boldsymbol{V}_0(t)\,\mathrm{d}t + \sigma_X \cdot \mathrm{d}\boldsymbol{B}_{t,X}, \tag{10.1a}$$

$$\mathrm{d}\boldsymbol{V}_0(t) = \frac{1}{\tau_V}\left(\boldsymbol{U}_0(t) - \boldsymbol{V}_0(t)\right)\,\mathrm{d}t + \sigma_V \cdot \mathrm{d}\boldsymbol{B}_{t,V}, \tag{10.1b}$$

$$\mathrm{d}\boldsymbol{U}_0(t) = -\frac{1}{\tau_U}\boldsymbol{U}_0(t)\,\mathrm{d}t + \sigma_U \cdot \mathrm{d}\boldsymbol{B}_{t,U}. \tag{10.1c}$$

What distinguishes the three models is the level at which the reduced fluid $\overline{\boldsymbol{u}}_f$ and the Wiener process are added.
In order to study the system of Eq. 10.1, we start by deriving the behaviour of the terms without noise, and then introduce the stochastic process.
Let us note that this class of closures is a change of formalism. When the fluid is fully resolved, it allows to compute physical inertial point particles compatible with the MEF: $\boldsymbol{x}_p(t)$. When the fluid is not fully resolved, it can only be understood as Monte-Carlo sample particles of the EMEF distribution: $\boldsymbol{X}(t)$. Specific equations are introduced in Sec. 4.3.2: Eq. 4.4, Eq. 4.5 and Eq. 4.6.

10.2.1 Solution of the homogeneous deterministic system

Keeping only the deterministic part of the system Eq. 10.1, we get:

$$\mathrm{d}\boldsymbol{x}_0(t) = \boldsymbol{v}_0(t)\,\mathrm{d}t, \tag{10.2a}$$

$$\mathrm{d}\boldsymbol{v}_0(t) = \frac{1}{\tau_V}\left(\boldsymbol{u}_0(t) - \boldsymbol{v}_0(t)\right)\,\mathrm{d}t, \tag{10.2b}$$

$$\mathrm{d}\boldsymbol{u}_0(t) = -\frac{1}{\tau_U}\boldsymbol{u}_0(t)\,\mathrm{d}t. \tag{10.2c}$$

By writing $z_0 = [\boldsymbol{x}_0, \boldsymbol{v}_0, \boldsymbol{u}_0]$, one gets:

$$\mathrm{d}z_0 = \mu z_0\,\mathrm{d}t, \tag{10.3}$$

with

$$\mu = \begin{pmatrix} 0 & 1 & 0 \\ 0 & -\frac{1}{\tau_V} & \frac{1}{\tau_V} \\ 0 & 0 & -\frac{1}{\tau_U} \end{pmatrix}. \tag{10.4}$$

Therefore:

$$z_0(t) = e^{\mu t} z_0(0). \tag{10.5}$$

As a reminder:

$$\mu = PDP^{-1}, \tag{10.6}$$

with the diagonal matrix D and transfer matrix P:

$$D = \begin{pmatrix} 0 & 0 & 0 \\ 0 & -\frac{1}{\tau_V} & 0 \\ 0 & 0 & -\frac{1}{\tau_U} \end{pmatrix}, \quad P = \begin{pmatrix} 1 & 1 & 1 \\ 0 & -\frac{1}{\tau_V} & -\frac{1}{\tau_U} \\ 0 & 0 & -\frac{\tau_V - \tau_U}{\tau_U^2} \end{pmatrix}. \tag{10.7}$$

We thus get:

$$e^{\mu t} = P \begin{pmatrix} 1 & 0 & 0 \\ 0 & e^{-\frac{t}{\tau_V}} & 0 \\ 0 & 0 & e^{-\frac{t}{\tau_U}} \end{pmatrix} P^{-1}. \tag{10.8}$$

Now that we have solved the deterministic part of the system Eq. 10.1, let us add some noise.

10.2.2 Solution of the homogeneous stochastic system

By addition of a Wiener process to the deterministic system (10.2) one gets:

$$\mathrm{d}Z_0 = \mu Z_0 \,\mathrm{d}t + \sigma \mathrm{d}B, \tag{10.9}$$

with $\sigma \in \mathbb{R}^3$, which integrates as:

$$Z_0(t) = e^{\mu t} Z_0(0) + \int_0^t e^{\mu(t-s)} \sigma \mathrm{d}B(s). \tag{10.10}$$

The mean evolution of $Z_0(t)$ is given by:

$$\mathrm{d}\mathbb{E}\left[Z_0(t)\right] = \mu \mathbb{E}\left[Z_0(t)\right] \,\mathrm{d}t. \tag{10.11}$$

The covariance matrix $\rho(t) = \mathbb{E}\left[Z_0(t) Z_0^\top(t)\right]$ has the following behaviour:

$$\mathrm{d}\rho = \left(\mu\rho + \rho\mu^\top + \sigma\sigma^\top\right) \,\mathrm{d}t, \tag{10.12}$$

$$\rho(t) = \int_0^t e^{(t-s)\mu} \sigma\sigma^\top e^{(t-s)\mu^\top} \mathrm{d}s. \tag{10.13}$$

Now, let us look at the dynamics of the system, with the assumption that the noise is not correlated (σ is diagonal with diagonal $(\sigma_X, \sigma_V, \sigma_U)$):

$$
\begin{aligned}
\rho_{11} &= R_{11} + R_{12} + R_{13} + R_{21} + R_{22} + R_{23} + R_{31} + R_{32} + R_{33},\\
\rho_{12} &= -\frac{R_{12} + R_{22} + R_{32}}{\tau_V} - \frac{R_{13} + R_{23} + R_{33}}{\tau_U},\\
\rho_{13} &= \frac{\tau_V - \tau_U}{\tau_U^2}\left(R_{13} + R_{23} + R_{33}\right),\\
\rho_{22} &= \frac{R_{22}}{\tau_V^2} + \frac{R_{23} + R_{32}}{\tau_V \tau_U} + \frac{R_{33}}{\tau_U^2},\\
\rho_{23} &= -\frac{\tau_V - \tau_U}{\tau_U^2}\left(\frac{R_{23}}{\tau_V} + \frac{R_{33}}{\tau_U}\right),\\
\rho_{33} &= \frac{\left(\tau_V - \tau_U\right)^2}{\tau_U^4} R_{33},
\end{aligned}
\tag{10.14}
$$

with

$$
\begin{aligned}
R_{11} &= \left(\sigma_X^2 + \tau_V^2\sigma_V^2 + \tau_U^2\sigma_U^2\right) t + R_{11}(0),\\
R_{12} &= \tau_V^2\left(\frac{\tau_U^2\sigma_U^2}{\tau_V - \tau_U} - \tau_V\sigma_V^2\right)\left(1 - e^{-\frac{t}{\tau_V}}\right) + R_{12}(0)e^{-\frac{t}{\tau_V}},\\
R_{13} &= \frac{\tau_U^4\sigma_U^2}{\tau_V - \tau_U}\left(1 - e^{-\frac{t}{\tau_U}}\right) + R_{13}(0)e^{-\frac{t}{\tau_U}},\\
R_{22} &= \frac{\tau_V^3}{2}\left(\sigma_V^2 + \frac{\tau_U^2\sigma_U^2}{\left(\tau_V - \tau_U\right)^2}\right)\left(1 - e^{-2\frac{t}{\tau_V}}\right) + R_{22}(0)e^{-2\frac{t}{\tau_V}},\\
R_{23} &= -\frac{\tau_V^2\tau_U^4\sigma_U^2}{\left(\tau_V + \tau_U\right)\left(\tau_V - \tau_U\right)^2}\left(1 - e^{-t\frac{\tau_V + \tau_U}{\tau_V\tau_U}}\right) + R_{23}(0)e^{-t\frac{\tau_V + \tau_U}{\tau_V\tau_U}},\\
R_{33} &= \frac{\tau_U^5\sigma_U^2}{2\left(\tau_V - \tau_U\right)^2}\left(1 - e^{-2\frac{t}{\tau_U}}\right) + R_{33}(0)e^{-2\frac{t}{\tau_U}}.
\end{aligned}
\tag{10.15}
$$

The set of Eq. 10.14 corresponds to the analytical evolution of the moments of the distribution of the solutions of the system Eq. 10.9. It allows to analyse the influence of each of the parameters of the model, without having to run countless numerical simulations. With these expressions at hand, one of the quantities of particular interest that we have consistently observed throughout this work is the asymptotic long time behaviour of these second order moments. We present them in the next section.

10.2.3 Long time consistency

Now that we have derived the evolution of the second order moments of the solution of the system Eq. 10.9, we are able to focus on any specific property of these solutions. For instance, one aspect of particular interest for physical systems is the asymptotic limit for long times. This limit is given by:

$$\begin{aligned}
\rho_{11} &\underset{t\to\infty}{\sim} \left(\sigma_X^2 + \tau_V^2\sigma_V^2 + \tau_U^2\sigma_U^2\right) t + \rho_{11}(0),\\
\lim_{t\to\infty} \rho_{12} &= \frac{\tau_V^2\sigma_V^2}{2} + \frac{\tau_U^2\sigma_U^2}{2},\\
\lim_{t\to\infty} \rho_{13} &= \frac{\tau_U^3\sigma_U^2}{2\left(\tau_V+\tau_U\right)},\\
\lim_{t\to\infty} \rho_{22} &= \frac{\tau_V}{2}\sigma_V^2 + \frac{\tau_U^2\sigma_U^2}{2\left(\tau_V+\tau_U\right)},\\
\lim_{t\to\infty} \rho_{23} &= \frac{\tau_U^2\sigma_U^2}{2\left(\tau_V+\tau_U\right)},\\
\lim_{t\to\infty} \rho_{33} &= \frac{\tau_U\sigma_U^2}{2}.
\end{aligned} \tag{10.16}$$

With the limits given by Eqs. 10.16 we are able to understand the ability of each order of modelling, given respectively by Eq. 4.4, Eq. 4.5 and Eq. 4.6, to reproduce the long time asymptotic behaviour of the system of reference.

- With the first order model, we have only one variable, σ_{X1}, thus it is possible to get an asymptotic equivalent of ρ_{11} for long times.
- With the second order model, we have two variables, τ_{V2} and σ_{V2}, thus it is possible to get an equivalent of ρ_{11} and ρ_{22} towards infinity.
- With the third order model, we have three variables, τ_{V3}, τ_{U3} and σ_{U3}, thus it is possible to get an equivalent of ρ_{11}, ρ_{22} and ρ_{33} towards infinity.

In order to get a given long time behaviour for particle dispersion, one has to chose one of the three models given that $\sigma_{X1}^2 = \tau_{V2}\sigma_{V2}^2 = \tau_{U3}\sigma_{U3}^2$. It is the same for the particle velocity variance, which can be identical for the two and three variable models, given that $\tau_{V2} = (\tau_{V3} + \tau_{U3})$.
Once all the different orders of modelling have been scaled to give the same long time behaviour, let us compare numerically how they behave in the next section.

10.2.4 Numerical illustration

In this section, we propose to observe numerical illustrations of each order of modelling, in order to understand how their dynamics differ from each other. To do so, we perform Lagrangian simulations with imposed variances, and we do statistics over 30720 particles. The three orders of modelling have been chosen such that they have the same long time asymptotic behaviour in ρ_{11}, ρ_{22} and ρ_{33} where applicable. The particle position variance for the three orders of modelling is represented in Fig. 10.12. It is interesting

to note that when the third order of modelling has a characteristic time scale of the modelled fluid $\tau_{U3} = 1$s and a characteristic relaxation time for the particles $\tau_{V3} = 1$s, we get the same long time asymptotic values with the second order model for ρ_{11} and ρ_{22} when $\tau_{V2} = \tau_{V3} + \tau_{U3}$, meaning $\tau_{V2} = 2$s. Thus, $\tau_{V2} = 2$ is not an intrinsic physical property of the particles, but rather a composite term given by both the particle and unresolved fluid characteristics.

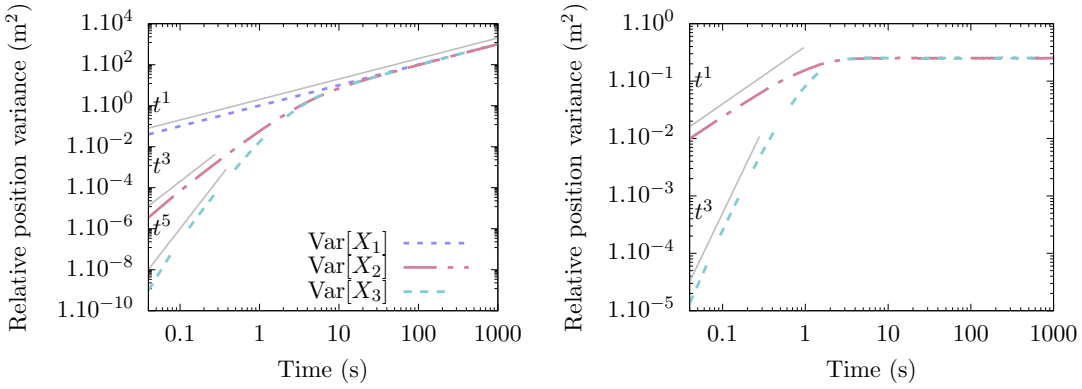

Figure 10.12. Position variance (left) and velocity variance (right) of model III with $\sigma_{U3} = 1$,$\tau_{V3} = 1$ and $\sigma_{V3} = 1$, model II with with $\sigma_{V2} = 0.5$ and $\tau_{V2} = 2$ and model I with $\sigma_{X1} = 1$. Integration of 30720 Monte-Carlo particles with Euler-Maruyama scheme.

After having assessed the long time behaviour of the three orders of modelling, let us now observe their asymptotic equivalent as t goes to zero. If we focus on the particle position variance ρ_{11}, we get Eq. 10.17:

$$\begin{aligned}
\rho_{11,I} &= \sigma_X^2 t, \\
\rho_{11,II} &= \frac{1}{3}\sigma_V^2 t^3 + o\left(t^4\right), \\
\rho_{11,III} &= \frac{1}{20}\sigma_U^2 \frac{t^5}{\tau_{V3}^2} + o\left(t^5\right).
\end{aligned} \tag{10.17}$$

What is interesting is that the asymptotic equivalent of the first order model as t goes to zero is linear. As the number of variables increases, the order of the asymptotic equivalent as t goes to zero increases linearly: the second order model has an asymptotic equivalent of order three as t goes to zero and the third order model has an asymptotic equivalent of order five as t goes to zero. Interestingly, in the case of inertial particles evolving on a resolved fluid (Fig. 1.5) the particle variance has an asymptotic equivalent as t goes to zero of order two. Thus, it does not seem possible to reproduce the initial transport behaviour with any of these models. However, the asymptotic long time diffusive behaviour is perfectly reproduced by all the models presented.
We also represent the PSD of the position and the velocity of the different orders of modelling where applicable in Fig. 10.13. Similarly to physical particle trajectories

(Fig. 8.12), the energy content decreases with increasing frequencies. The decrease in the spatial PSD is directly related to the order of the model. The first order model, the asymptote follows a slope in t^{-2}, the second order model a slope in t^{-4} and the third order model a slope in t^{-6}. Remarkably, none of these model reproduces the reference slope in $t^{-5/3}$ given for physical particles.

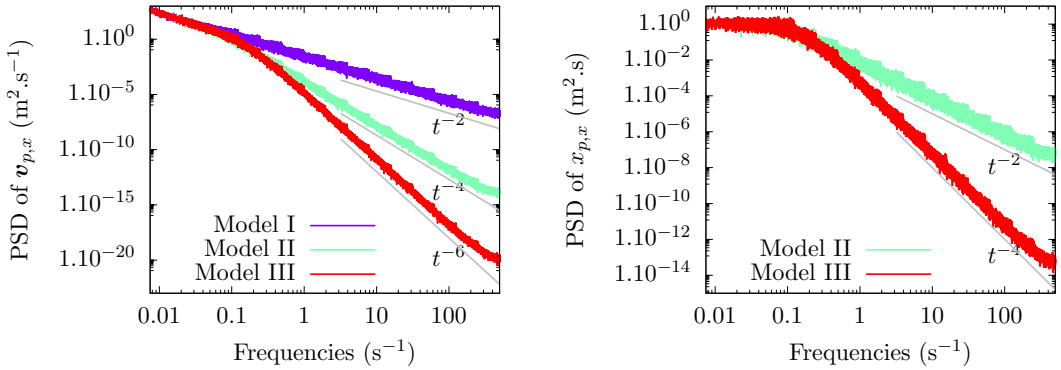

Figure 10.13. Power spectral density in position (left) and velocity (right) of model III with $\sigma_{U3} = 1$,$\tau_{U3} = 1$ and $\sigma_{V3} = 1$, model II with with $\sigma_{V2} = 0.5$ and $\tau_{V2} = 2$ and model I with $\sigma_{X1} = 1$. Integration of 30720 Monte-Carlo particles with Euler-Maruyama scheme.

In this section, we have presented the expected behaviour of the different orders of modelling. We have first derived analytical expressions for the second order moments of the disperse phase. We have then observed numerical simulations, focusing particularly on the asymptotic behaviour for long times and as t goes to zero. We have also presented the PSD in space and velocity of particle trajectories. These observations were done without any underlying fluid flow field in order to apprehend the properties of the homogeneous system of equations. In the next section, we will present numerical simulations of the same models in the context of the reduced flow field given by KS.

10.3 Evaluation of Lagrangian diffusive closures in our framework

Now that we have validated the use of KS, and we have assessed what to expect for diffusive closures, here we want to assess the models in practice, i.e. by performing LES in our KS context, and under the EMEF. We will observe the class of diffusive closures presented in the second section, to see if they helps to reproduce the behaviour of reference of the distribution of particles when only the reduced flow field is available. We have seen in the right hand-side of Fig. 4.1, representing the proportion of energy of the disperse phase preserved after the fluid reduction, that in the context of NS presented by Fede and Simonin (2006), reducing the fluid energy by 14% could lower the particle energy by 17% for St=0.19. However, in the context of KS presented in this work, we can observe in Fig. 10.3 representing the particle velocity variance for different amounts

of fluid resolution, that low levels of fluid reduction lead to a very weak effect on the disperse phase: 30% of reduction of the energy of the fluid only leads to 5% less energy for the disperse phase. With only 5% less energy for the disperse phase, it is difficult to precision of the different closures presented in this section. Therefore, in order to be in a more realistic setting for assessing the effects of the closures on the disperse phase, in this section, the reference fluid filtering is 50%, which leads to 20% less energy for the disperse phase. Note that 50% of fluid reduction is high with respect to the standard order of magnitude advised by Pope for LES simulations which is around 80%.
As a starting point, let us present the dispersion of inertial particles under different formalisms in Fig. 10.14:

- When computing physical deterministic point particle trajectories on one fluid under the DNS formalism, the point dispersion is null. This is the MEF dispersion of a Dirac distribution.
- When considering the EMEF distribution, DNS particles from a single point are dispersed with time. In the EMEF presented Fig. 10.14, 50% of the energy of the fluid stays identical across realisations.
- When reducing the fluid to 50% of its energy, both the MEF and the 50%-EMEF give the same result: the line with the label 50% resolved. This is because the fluctuating fluid part of the 50%-EMEF corresponds to the 50% of fluid energy removed when reducing the fluid.

The objective of the stochastic models is not to fit exactly every single DNS trajectory. It is impossible because the formalism is different. The DNS trajectories of physical particles are deterministic and tractable whereas stochastic trajectories of sample particles are only an intermediate step in order to compute a distribution, the reference distribution in the context of LES being the EMEF distribution.

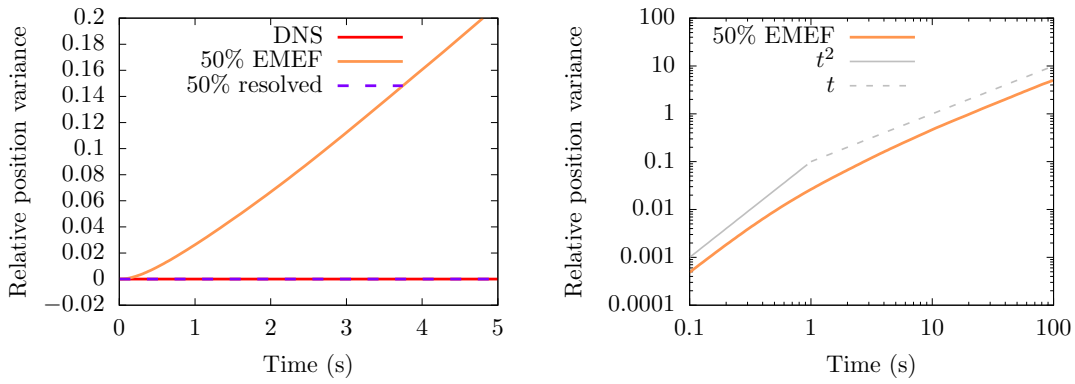

Figure 10.14. Comparison of time evolution of the sample variance of particle relative positions: DNS, 50% EMEF and when 50% of the fluid is resolved. Linear scale (left), logarithmic scale (right). Initial particle velocity set to fluid velocity.

Now, let us try to recover the behaviour of the EMEF from the 50%-EMEF with the models presented in Sec. 10.2. The second order moments of the particle distribution with the different stochastic models presented earlier is shown in Fig. 10.15. Let us

introduce this figure:

- The DNS distribution is a Dirac along all variables. Therefore, its second moment is null.
- The reference distribution is the EMEF distribution corresponding to the reduction operation chosen for the fluid. Here, the fluid underwent a 50% sharp spectral cut-off. The reference EMEF distribution is represented with a black line in Fig. 10.15.
- Here we have set the different closures only with constant parameters. Therefore, we have calibrated them in order to match an asymptotic long time behaviour.
- The higher the order of the model, the more dynamic state variables are represented. Other variables are not part of the dynamical system and do not need to be represented to get its evolution, but they can still be modelled independently. This modelling is not done here, and only state variables are represented.
- The first order model only reproduces the dynamics of the distribution in position. The second order model reproduces the dynamics of the distribution in position and velocity. The third order model considers particle position, particle velocity, and fluid velocity seen by the particle as state variables.

From this figure, we can conclude that:

- none of the models give a correct transient behaviour for any of the state variables. As it is this transient behaviour which differentiates the different levels of spatial filtering and statistical filtering, one can understand why not much attention is given to this aspect for closures in one-way coupled flows.
- The asymptotic long time behaviour is respected for particle velocity and fluid velocity seen by the particles for models II and III. This does not come as a surprise as closure coefficients have been tuned to match this behaviour.
- The asymptotic long time behaviour of the particle position has the correct trend for all models. However, the precise value at any given time has an offset caused by the poor reproduction of the initial ballistic regime.

Now, let us look at the frequency components of the particle trajectories Fig. 10.16. The reference here in black is the PSD of DNS particle trajectories. This is because the EMEF is a specific distribution built with DNS particles. It does not change the frequency components of the particle trajectories. Particles on the reduced fluid see a strong alteration in their energy spectrum. Models aim at reducing the gap between the particle behaviour on the reduced fluid and the particle behaviour on the DNS fluid. None of the models exactly reproduces the DNS behaviour. This is because standard diffusion models only give access to negative powers of two for their high frequencies asymptotes and the DNS high frequency asymptote is a rational number. Bypassing this limitation would require the use of fractional Brownian motion, which is significantly more advanced: not commonly used for industrial applications and severely more computationally expensive (Letournel (2022)). However, given this limitation, the third order model gives a pretty good approximation of the DNS frequency content.
It is nonetheless important to remember that third order modelling technique involves a characteristic time scale of 0.081s in the specific case chosen here, and that integration

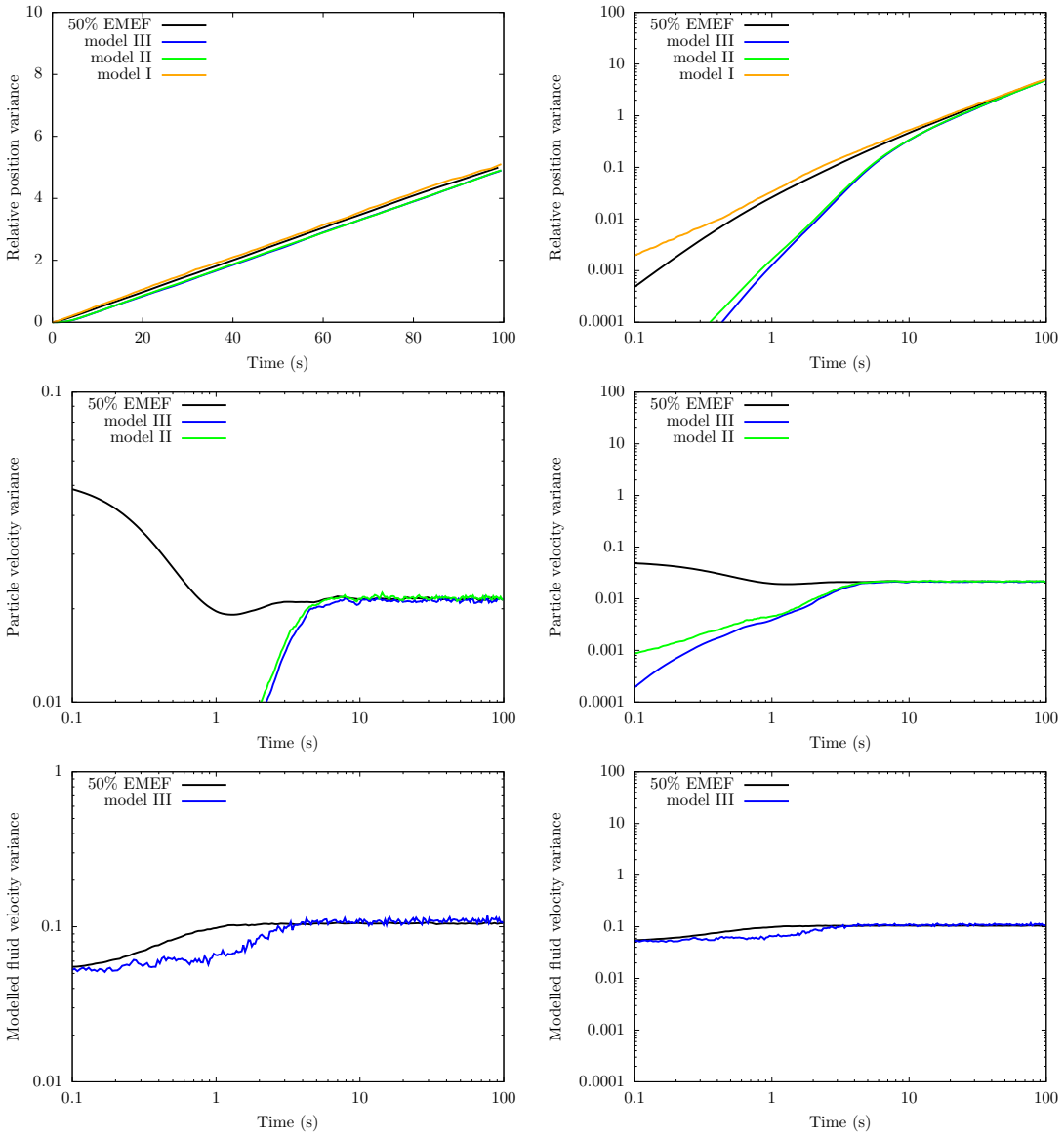

Figure 10.15. Temporal evolution of particle variance in relative position, velocity and modelled fluid velocity (respectively on the first, second and third line) with a linear scaling on the left hand side and a logarithmic scaling on the right hand side. Are represented, the 50% EMEF (reference) and three orders of modelling when 50% of the fluid is resolved.

of the stochastic differential equation requires an explicit scheme. Therefore, the third order model requires the computation of time scales which are one order of magnitude lower than the lower frequency modes of the reduced fluid (around 0.3s).
In this section, we have shown how the use a simple class of diffusive models offers the possibility to recover the long time asymptotic behaviour of the second order moments of

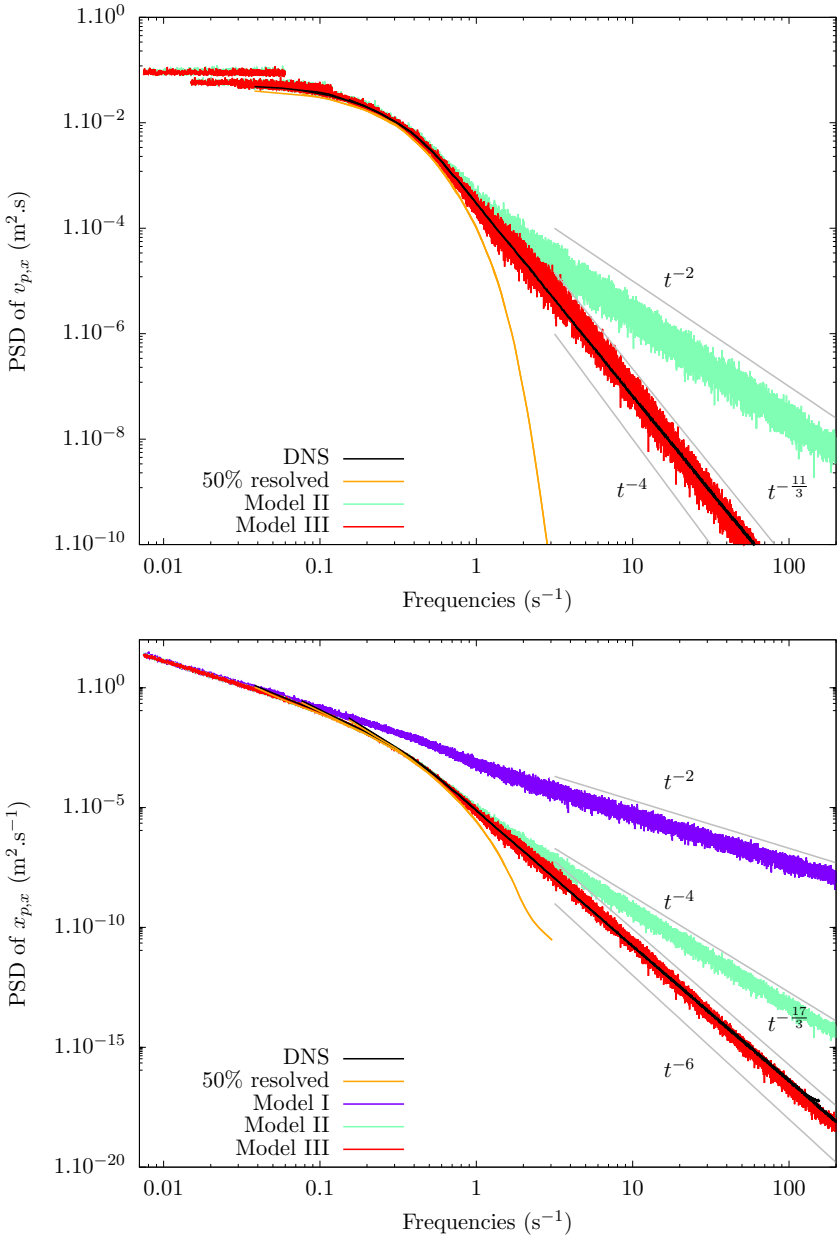

Figure 10.16. Power spectral density of particle position (top) and velocity (bottom). Are represented, DNS (reference), 50% filtered and three orders of modelling when 50% of the fluid is resolved.

the distribution of the particles. The higher the order of the model, the more moments of the disperse phase distribution can be reproduced. However, this class of diffusive closures still possesses some intrinsic limitations which make the reproduction of a step response difficult and prevent them from having the correct energy spectrum.

10.3.1 More advanced closures

The closures that we have presented in the previous section are simplistic compared to the literature because they are considering constant coefficient. These models are perfectly adapted when the level of energy reduction of the fluid is stable. This is the case in the context of KS that we have chosen for this work. However, in practice, when the average fluid characteristics change with space and time, it can be useful to adapt this coefficient to the local conditions of the flow field. Therefore, some models based on the second order model (Eq. 4.5), propose to adapt the energy of the Brownian force to the surrounding fluid. The resulting relations usually take the form $\sigma_{v,II'} \propto k_{\mathrm{SGS}}/\tau_t$. Let us consider three examples of such closures for τ_t taken from Bini and Jones (2008):

- Bini1: $1/\tau_t = |\boldsymbol{v}_p|\Delta^{-\frac{1}{3}}$
- Bini2: $1/\tau_t = \sqrt{k_{\mathrm{SGS}}}\Delta^{-\frac{1}{3}}$
- Bini3: $1/\tau_t = \left(\Delta/\sqrt{k_{\mathrm{SGS}}}\right)^{2\alpha-1}\tau_p^{-2\alpha}$

One of the key challenges resides in computing k_{SGS}. According to the fluid reduction strategy chosen, it can be readily available, which is the case when the reduction model encompasses an evolution equation for k_{SGS}, or it has to be estimated. In our case, because we have access to the whole fluid, k_{SGS} was estimated as

$$\frac{1}{2}\cdot\sum G\left(\boldsymbol{u}_f\left(t,\boldsymbol{x}_p(t)\right) - G\left(\boldsymbol{u}_f\left(t,\boldsymbol{x}_p(t)\right)\right)^2\right). \tag{10.18}$$

Because all of these closures are defined respective to a constant to be set by the user, it is easy to tune them for a specific case where they will obviously match the asymptotic behaviour. However, the modelling accuracy provided remains identical to model II. Therefore, in order to challenge these models a bit more, we have chosen to test them for different fluid resolutions. All the second order models were fine tuned to give the correct asymptotic particle energy when 50% of the fluid is filtered. Keeping this tuning constant, we have then changed the level of fluid filtering to see the robustness of each model. The Fig. 10.17 represents the asymptotic particle energy of all the second order models, fined tuned at 50% of fluid filtering, for various levels of fluid resolution. The reference value is given by the 50% EMEF represented with a dashed line. All models give the correct energy for the disperse phase when 50% of the fluid energy has been removed. This is to be expected because the parameters of each of the models have been tune to match this value. However, when the fluid reduction is different from 50%, the models start to give values which do not correspond to the EMEF. Interestingly, models with $\sigma_{v,II'}$ variable are more stable to off design conditions than the static model.

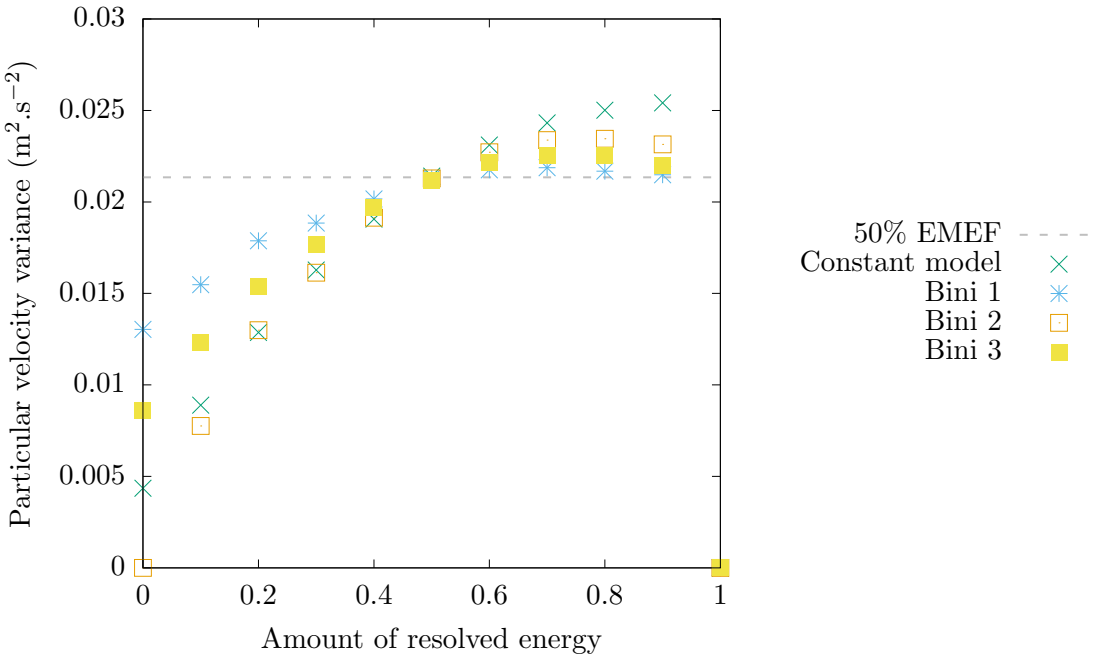

Figure 10.17. Particular kinetic energy according to the amount of resolved energy for different second order models.

Highlights and conclusions

In this chapter, we have benchmarked Lagrangian diffusive models under the EMEF using KS:

- We have shown that diffusive models reproduce very well the long time behaviour of the second order moments of the distribution of the disperse phase.
- However, they cannot reproduce the initial transport regime correctly.
- This difficulty of simple diffusive models to reproduce the correct transient dynamics appears very clearly in their inability to reproduce the PSD of particle trajectories in turbulence .

In order to better capture the behaviour of particles in turbulence, more elaborate models are required. It could be interesting to explore the use of fractional Brownian motion in order to better reproduce the PSD of particles in turbulence (Letournel (2022)).

Conclusion

In this PhD work, we have investigated the definition of a statistical description of turbulent particle-laden flows that is consistent with two-way coupling and large eddy simulation. To this aim, a comprehensive bibliographic review has highlighted the weaknesses of the available formalisms in the literature, with a focus on the Mesoscopic Eulerian Formalism of Février et al. (2005). Following some suggestions of the authors, we have rigorously constructed an Extended Mesoscopic Eulerian Formalism, which considers a random space not only composed of the particles but also composed of the unresolved scales of turbulence, conditioned to a unique realisation of the resolved fluid scales. For the sake of evaluating the impact of such an extended probability space, we have proposed to use synthetic fluids to avoid the resolution of Navier-Stokes equations, and to give an explicit control on the realisations of the gas phase. We have carefully analysed the numerical convergence of our fluid with respect to its parameters, as well as the numerical convergence of particle trajectories and statistics. We have finally used this numerical framework to validate the impact of the Extended MEF on the measured statistics, showing a clear dependency in the initial transport part but a weak impact on the terminal diffusion regime. We have also benchmarked a class of diffusive closures, showing intrinsic limitations in terms of spectral description of the particle trajectories. At the very end, we can emphasise on some key achievements of this work.

Main constructions

A statistically-consistent formalism

In this work, we have given a rigorous theoretical framework to the notion of reduction for two-phase flows (Chap. 5.1), from the perspective of dynamical systems. This strategy is not the most common in the community. It has made possible the precise definition a formalism able to extend the MEF to non-injective fluid reductions: the EMEF (Chap. 5.2). This strategy has been suggested in Février, Simonin, and Squires (2005), but never developed any further. One of the key difficulty has been to find a framework in which to perform actual simulations of this formalism.

A numerical framework for investigation

To investigate the proposed formalism, we have crafted an original numerical set-up (Chap. 6). The numerical setup relies on Kinematic Simulations. It is a standard technique used for mimicking turbulence and studying the behaviour of inertial particles in turbulence, which has not been used so far for studying the impact of conditional averaging on inertial particle distributions. This new setup has been thoroughly validated and characterised (Chap. 7 and 8). Eventually, this has led us to actually study numerical simulations of the EMEF thanks to this unique numerical set-up (Chap. 9). The numerical results have helped us characterise the behaviour of the EMEF.

Main conclusions

An unaffected terminal diffusion regime

The diffusion regime is reached when particles have lost memory of their initial conditions. This terminal regime is the one that is targeted by all diffusive models for particles, scalars, turbulence... Our study has demonstrated that this long-time diffusion regime is not affected by the chosen formalism. This conclusion is of primary importance for the sake of re-validating existing models in the spirit of our formalism, as it would mean that all these models can still be validated in the classical way, i.e. using a unique fluid instead of a full collection of fluids.

A high sensitivity of the initial transport regime

As opposed to the MEF, the distribution of the EMEF experiences some dispersion, even when the initial position of the inertial particles is perfectly known. This dispersive behaviour is controlled for short times by the energy of probability space associated to the fluid reduction. Whereas for the long-time behaviour, there is no impact of the chosen formalism, this initial regime is highly impacted. This is somehow fully expected, as the level of dispersion is directly related to the level of "uncertainty" in the formalism: where the MEF is not able to disperse an initial Dirac distribution, the EMEF can because of its ensemble of probable fluids. One would say that, as all models are validated on the diffusion regime, there is no need to worry. Unfortunately this initial regime is potentially the main regime encountered by droplets in a combustion chamber, as they could have no time to reach this long-time regime before being evaporated. Furthermore, during this transport phase, the two-way coupling between the two phases may be more intense because of the non-equilibrium, and thus requires a specific attention in terms of applications.

A intrinsic limitation of diffusive closures for spectral representation

We have finally evaluated the use of diffusive closures for LES. We have theoretically and numerically highlighted that, even if such models can control some large-time properties

such as the equilibrium velocity variance, they are intrinsically not able to retrieve the correct spectral behaviour as such, as they could only recover power of 2 exponents for the decay of energy at high frequencies, where the right limit is a fraction of 3. This limitation clearly calls for more advanced models for sub-grid scale forcing. We also recall that these models have been evaluated in a Lagrangian framework, but the implications are the same for their Eulerian counterpart, i.e. their associated Fokker-Planck equation.

Perspectives

Navier-Stokes fluids

One of the main limitations of our work is the use of synthetic fluids. Even if we have proven a strong similarity between our fluid and turbulence, there are still features that we are not able to reproduce, such as intermittency. Moreover, our fluid cannot be coupled, and our final goal is two-way coupled flows. To this aim, would want to use Navier-Stokes equations. In order to use these equations, we have to be able to:

- generate fluids with the same large scales and different small scales: a solution is to use kinematic simulations as an initialisation;
- assess the independence between the largest scales and the smallest scales: see how two different initial solutions sharing the same largest scales evolve with time. However, assuming that the largest scales of the flow fields have the same evolution, independent of the smallest scales is a strong assumption.

While conducting this study, we would have to remember that one synthetic fluid is based on 8 fixed parameters per mode, whereas an homogeneous isotropic turbulent flow, even at low Reynolds would require at least $4 * 64^3 \approx 1M$ degrees of freedom[1]. Therefore, the computational cost with Navier-Stokes simulations can become too high, and we would have to envision the use of higher order statistic instead of a simple random sampling, in order to limit the number of required fluids.

Two-way coupled cases

Even if the large-scale independence is generally assumed in the one-way coupled case, it is not necessarily the case when their is a two-way coupling between the particles and the carrier phase. Three scenarios can be envisaged:

- Particles affect the carrier phase only at scales smaller that the cut-off length scale of the reduction operator. In this kind of a case, the two-way extension is straightforward, as long as small scale fluctuations do not affect large scales of the flow.
- Particles affect the carrier phase at all scales, but with negligible variations at large scales between realisations. In this scenario, the conditioning simulations to the largest-scales of the flow is possible.

[1] Velocity and pressure at each point

- Particles affect the carrier phase at all scales, with substantial variations at all scales between realisations. In this case, considering the EMEF in the scope of resolving large-scale while modelling small scales is not possible, and we would have to redefine the ensemble-averaging by considering also the large scales.

More advanced LES closures for particles

Finally, because we have shown that diffusive closures are not expected to retrieve the right spectral behaviour of particles, we need to use more advanced model, such as the one of Gorokhovski and Zamansky (2018). More precisely, advanced statistics, such as intermittency, are mandatory to validate models of the literature, as this is an important trends of developed turbulent flows. This property has several definitions if seen from a mathematical or a physical perspective. Investigating the ability of stochastic Lagrangian models to reproduce it will be investigated in the thesis of Letournel (2022).

Scientific Outreach

The present thesis has been founded by the DGA and supervised by Vincent Plana.

Publications (Mathematics community - names in alphabetical order):

- Goudenèege, L., A. Larat, J. Llobell, M. Massot, D. Mercier, O. Thomine, and A. Vié (2019). Statistical and probabilistic modeling of a cloud of particles coupled with a turbulent fluid. ESAIM: *Proceedings and Surveys* 65, 401-424. (p. 78, 104)

Papers in preparation:

- Mercier, D., A. Vié, M. Massot *Influence of probability space on Large Eddy Simulation of turbulent particulate flows*, Journal of Fluid Mechanics
- Mercier, D., A. Vié, M. Massot *A review of diffusive closures and their limits for inertial particles in Large Eddy Simulation of turbulent particulate flows*, Flow, Turbulence and Combustion

References

Akbari, G. and N. Montazerin (2013). A-priori study of subgrid-scale models for the flow field in the rotor exit region of a centrifugal turbomachine. *International Journal of Heat and Mass Transfer 66*, 423–439. *(p. 77)*

Anez, J., A. Ahmed, N. Hecht, B. Duret, J. Reveillon, and F. X. Demoulin (2019). Eulerian–Lagrangian spray atomization model coupled with interface capturing method for diesel injectors. *International Journal of Multiphase Flow 113*, 325 – 342. *(p. 6)*

Armenio, V., U. Piomelli, and V. Fiorotto (1999). Effect of the subgrid scales on particle motion. *Physics of Fluids 11*(10), 3030–3042. *(p. 60)*

Baddeley, A. (2007). Spatial Point Processes and their Applications. *Lecture notes in Mathematics 1892*, 1–75. *(p. 42)*

Balachandar, S. and J. K. Eaton (2010). Turbulent Dispersed Multiphase Flow. *Annual Review of Fluid Mechanics 42*(1), 111–133. *(p. 32)*

Balachandar, S., K. Liu, and M. Lakhote (2019). Self-induced velocity correction for improved drag estimation in Euler–Lagrange point-particle simulations. *Journal of Computational Physics 376*, 160 – 185. *(p. 7)*

Bardos, C., F. Golse, and C. D. Levermore (1993). Fluid dynamic limits of kinetic equations II convergence proofs for the Boltzmann equation. *Communications on Pure and Applied Mathematics 46*(5), 667–753. *(p. 20)*

Batchelor, G. K. (1952). Diffusion in a field of homogeneous turbulence: II. the relative motion of particles. *Mathematical Proceedings of the Cambridge Philosophical Society 48*(2), 345–362. *(p. 66)*

Bec, J. (2003). Fractal clustering of inertial particles in random flows. *Physics of Fluids 15*(11), 81–84. *(p. 87)*

Bec, J., L. Biferale, M. Cencini, A. Lanotte, S. Musacchio, and F. Toschi (2007). Heavy particle concentration in turbulence at dissipative and inertial scales. *Physical review letters 98*(8), 084502. *(p. 87)*

Bec, J., L. Biferale, A. Lanotte, A. Scagliarini, and F. Toschi (2010). Turbulent pair dispersion of inertial particles. *Journal of Fluid Mechanics 645*, 497–528. *(p. 87)*

Bini, M. and W. P. Jones (2007). Particle acceleration in turbulent flows: A class of nonlinear stochastic models for intermittency. *Physics of Fluids 19*(3), 035104. *(p. 67)*

Bini, M. and W. P. Jones (2008). Large-eddy simulation of particle-laden turbulent

flows. *Journal of Fluid Mechanics 614*, 207–252. *(p. 7, 66, 79, 170)*

Bini, M. and W. P. Jones (2009). Large Eddy Simulation of an evaporating acetone spray. *International Journal of Heat and Fluid Flow 30*(3), 471 – 480. *(p. 8)*

Bishop, C. J. and Y. Peres (2016). *Fractals in Probability and Analysis*, Volume 162. Cambridge University Press. *(p. 113)*

Botto, L. and A. Prosperetti (2012). A fully resolved numerical simulation of turbulent flow past one or several spherical particles. *Physics of Fluids 24*(1), 013303. *(p. 40)*

Buckmaster, T. and V. Vicol (2019). Convex integration and phenomenologies in turbulence. *EMS Surveys in Mathematical Sciences 6*(1), 173–263. *(p. 22)*

Capecelatro, J. and O. Desjardins (2013). An Euler–Lagrange strategy for simulating particle-laden flows. *Journal of Computational Physics 238*, 1–31. *(p. 7, 41)*

Capecelatro, J., O. Desjardins, and R. O. Fox (2016a). Strongly coupled fluid-particle flows in vertical channels. I. Reynolds-averaged two-phase turbulence statistics. *Physics of Fluids 28*(3), 033306. *(p. 78, 80)*

Capecelatro, J., O. Desjardins, and R. O. Fox (2016b). Strongly coupled fluid-particle flows in vertical channels. II. turbulence modeling. *Physics of Fluids 28*(3), 033306. *(p. 80)*

Chadil, M.-A., S. Vincent, and J.-L. Estivalèzes (2019). Accurate estimate of drag forces using particle-resolved direct numerical simulations. *Acta Mechanica 230*(2), 569–595. *(p. 40)*

Chan, T. F., G. H. Golub, and R. J. LeVeque (1982). Updating formulae and a pairwise algorithm for computing sample variances. In *COMPSTAT 1982 5th Symposium held at Toulouse*, pp. 30–41. Springer. *(p. 96)*

Chaouat, B. (2017). The state of the art of hybrid RANS/LES modeling for the simulation of turbulent flows. *Flow, Turbulence and Combustion 99*(2), 279–327. *(p. 54)*

Chapman, D. R. (1979). Computational aerodynamics development and outlook. *AIAA journal 17*(12), 1293–1313. *(p. 25)*

Chapman, S., T. G. Cowling, and D. Burnett (1939). *The mathematical theory of non-uniform gases: an account of the kinetic theory of viscosity, thermal conduction and diffusion in gases*. Cambridge university press. *(p. 20)*

Chassaing, P., R. Antonia, F. Anselmet, L. Joly, and S. Sarkar (2002). *Variable density fluid turbulence*. Kluwer Academic Publishers. *(p. 21)*

Cheneau, B. (2019, February). *Étude numérique de la dynamique de combustion dans un bruleur diphasique turbulent à deux étages*. Ph. D. thesis, Université Paris-Saclay, CentraleSupélec, EM2C. *(p. 3, 10)*

Chiodi, R. and O. Desjardins (2017). A reformulation of the conservative level set reinitialization equation for accurate and robust simulation of complex multiphase flows. *Journal of Computational Physics 343*, 186 – 200. *(p. 5)*

Cordesse, P. (2020). *Contribution to the study of combustion instabilities in cryotechnic rocket engines: coupling diffuse interface models with kinetic-based moment methods for primary atomization simulations*. Ph. D. thesis, Université Paris-Saclay. *(p. 6)*

Cordesse, P., A. Remigi, B. Duret, A. Murrone, T. Ménard, F. X. Demoulin, and M. Massot (2020). Validation strategy of reduced-order two-fluid flow models based on a hierarchy of direct numerical simulations. *Submitted to Flow Turbulence and Combustion*. *(p. 6)*

Crowe, C., M. Sommerfeld, and Y. Tsuji (1998). *Multiphase Flows with Droplets and Particles*. CRC Press. *(p. 31)*

Danforth, C. M. (2020). Mathematics of planet earth. *(p. 29)*

de Chaisemartin, S. (2009). *Modèles eulériens et simulation numérique de la dispersion turbulente de brouillards qui s'évaporent*. Ph. D. thesis, École Centrale Paris. *(p. 9, 44, 94)*

Drew, D. and S. Passman (1999). Theory of multicomponent flow. *(p. 20, 28, 31)*

Drui, F., A. Larat, S. Kokh, and M. Massot (2019). Small-scale kinematics of two-phase flows: identifying relaxation processes in separated- and disperse-phase flow models. *Journal of Fluid Mechanics 876*, 326–355. *(p. 6)*

Dubrulle, B. (2019). Beyond Kolmogorov cascades. *Journal of Fluid Mechanics 867*, P1. *(p. 37)*

Eaton, J. K. (2009). Two-way coupled turbulence simulations of gas-particle flows using point-particle tracking. *International Journal of Multiphase Flow 35*(9), 792–800. *(p. 81)*

Eaton, J. K. and J. R. Fessler (1994). Preferential concentration of particles by turbulence. *International Journal of Multiphase Flow 20*, 169–209. *(p. 44)*

Einstein, A. (1905). On the motion of small particles suspended in liquids at rest required by the molecular-kinetic theory of heat. *Annalen der physik 17*, 549–560. *(p. 41)*

Emre, O. (2014). *Modeling of spray polydispersion with two-way turbulent interactions for high pressure direct injection in engines*. Ph. D. thesis, École Centrale de Paris. *(p. 80)*

Emre, O., R. O. Fox, M. Massot, S. De Chaisemartin, S. Jay, and F. Laurent (2014). Towards Eulerian modeling of a polydisperse evaporating spray under realistic internal-combustion-engine conditions. *Flow, turbulence and combustion 93*(4), 689–722. *(p. 80)*

Essadki, M., S. de Chaisemartin, F. Laurent, and M. Massot (2018). High Order Moment Model for Polydisperse Evaporating Sprays towards Interfacial Geometry Description. *SIAM Journal on Applied Mathematics 78*(4), 2003–2027. *(p. 6, 9)*

Essadki, M., F. Drui, S. de Chaisemartin, A. Larat, T. Ménard, and M. Massot (2019). Statistical modeling of the gas–liquid interface using geometrical variables: Toward a unified description of the disperse and separated phase flows. *International Journal of Multiphase Flow 120*, 103084. *(p. 6, 9)*

Eswaran, V. and S. B. Pope (1988). An examination of forcing in direct numerical simulations of turbulence. *Computers & Fluids 16*(3), 257–278. *(p. 61)*

Eyink, G. L. (2007-2008). Turbulence theory, lecture notes. *(p. 32, 36, 114)*

Falkovich, G., K. Gawedzki, and M. Vergassola (2001). Particles and fields in fluid turbulence. *Reviews of modern Physics 73*(4), 913. *(p. 32, 36, 113)*

Farge, M. (1992). *Evolution des théories sur la turbulence développée*. Seuil. *(p. 26, 31, 106)*

Fede, P. and O. Simonin (2006). Numerical study of the subgrid fluid turbulence effects on the statistics of heavy colliding particles. *Physics of Fluids 18*(4), 045103. *(p. 60, 61, 62, 63, 64, 153, 154, 155, 165)*

Fede, P., O. Simonin, P. Villedieu, and K. D. Squires (2006). Stochastic modeling of the turbulent subgrid fluid velocity along inertial particle trajectories. In *Proceedings of the Summer Program*, pp. 247–258. Center for Turbulence Research. *(p. 67)*

Fefferman, C. L. (2006). Existence and smoothness of the Navier-Stokes equation. *The millennium prize problems 57*, 67. *(p. 22)*

Ferry, J. and S. Balachandar (2001). A fast Eulerian method for disperse two-phase flow. *International journal of multiphase flow 27*(7), 1199–1226. *(p. 69)*

Ferry, J. and S. Balachandar (2002). Equilibrium expansion for the Eulerian velocity of small particles. *Powder Technology 125*, 131–139. *(p. 69)*

Ferziger, J. H. and H. G. Kaper (1973). Mathematical theory of transport processes in gases. *American Journal of Physics 41*(4), 601–603. *(p. 20)*

Février, P., O. Simonin, and K. D. Squires (2005). Partitioning of particle velocities in gas–solid turbulent flows into a continuous field and a spatially uncorrelated random distribution: theoretical formalism and numerical study. *Journal of Fluid Mechanics 533*, 1–46. *(p. v, 10, 12, 13, 14, 45, 48, 49, 79, 80, 81, 119, 149, 173)*

Fox, R. O. (2003). *Computational models for turbulent reacting flows*. Cambridge University Press. *(p. v)*

Fox, R. O. (2014). On multiphase turbulence models for collisional fluid–particle flows. *Journal of Fluid Mechanics 742*, 368–424. *(p. 80)*

Freedman, D., R. Pisani, and R. Purves (1978). *Statistics*. WW Norton & Co. *(p. 124)*

Frisch, U. (1995). *Turbulence: The legacy of A. N. Kolmogorov*. Cambridge university press. *(p. 37)*

Frisch, U. and G. Parisi (1985). Turbulence and predictability of geophysical flows and climate dynamics, proceedings of the international school of physics"enrico fermi," course lxxxviii, varenna, 1983. *(p. 113)*

Fung, J. C. H., J. C. Hunt, N. Malik, R. Perkins, J. C. Vassilicos, A. A. Wray, J. C. Buell, and J. Bertoglio (1991). Kinematics of small scale motions in homogeneous isotropic turbulence. In *Advances in Turbulence 3*, pp. 422–434. Springer. *(p. 87)*

Fung, J. C. H., J. C. R. Hunt, N. A. Malik, and R. J. Perkins (1992). Kinematic simulation of homogeneous turbulence by unsteady random fourier modes. *Journal of Fluid Mechanics 236*, 281–318. *(p. 65)*

Fung, J. C. H. and J. C. Vassilicos (1991). Fractal dimensions of lines in chaotic advection. *Physics of Fluids A: Fluid Dynamics 3*(11), 2725–2733. *(p. 87)*

Fung, J. C. H. and J. C. Vassilicos (1998). Two-particle dispersion in turbulent like flows. *Physical Review E 57*(2), 1677. *(p. 87, 103, 106, 113)*

Fung, J. C. H. and J. C. Vassilicos (2003). Inertial particle segregation by turbulence. *Physical Review E 68*(4), 046309. *(p. 87, 103)*

Garnier, E., N. Adams, and P. Sagaut (2009). *Large Eddy Simulation for compressible*

flows. Springer. *(p. 56)*

Golse, F. and L. Saint-Raymond (2004). The Navier–Stokes limit of the Boltzmann equation for bounded collision kernels. *Inventiones mathematicae 155*(1), 81–161. *(p. 20)*

Gorokhovski, M. and R. Zamansky (2014). Lagrangian simulation of large and small inertial particles in a high Reynolds number flow: Stochastic simulation of subgrid turbulence/particle interactions. In *Proceedings of the Summer Program, Center for Turbulence Research, Stanford University*, pp. 37–46. *(p. 67)*

Gorokhovski, M. and R. Zamansky (2018). Modeling the effects of small turbulent scales on the drag force for particles below and above the Kolmogorov scale. *Physical Review Fluids 3*(3), 034602. *(p. 37, 60, 176)*

Goudenège, L., A. Larat, J. Llobell, M. Massot, D. Mercier, O. Thomine, and A. Vié (2019). Statistical and probabilistic modeling of a cloud of particles coupled with a turbulent fluid. *ESAIM: Proceedings and Surveys 65*, 401–424. *(p. 80, 106)*

Hairer, E., S. P. Nørsett, and G. Wanner (1987). *Solving ordinary differential equations I: Nonstiff problems*. Springer. *(p. 118, 119)*

Hannebique, G., P. Sierra, E. Riber, and B. Cuenot (2013). Large Eddy Simulation of reactive two-phase flow in an aeronautical multipoint burner. *Flow, Turbulence and Combustion 90*(2), 449–469. *(p. 6)*

Heinz, S. (2003). *Statistical mechanics of turbulent flows*. Springer Science & Business Media. *(p. 54, 66)*

Hinze, J. O. (1975). *Turbulence*, Volume 218. McGraw-Hill. *(p. 128, 132)*

Homann, H., J. Bec, and R. Grauer (2013). Effect of turbulent fluctuations on the drag and lift forces on a towed sphere and its boundary layer. *Journal of Fluid Mechanics 721*, 155–179. *(p. 40)*

Horwitz, J. and A. Mani (2016). Accurate calculation of Stokes drag for point–particle tracking in two-way coupled flows. *Journal of Computational Physics 318*, 85–109. *(p. 7, 13, 41, 149)*

Hunt, J., J. Buell, and A. Wray (1987). Big whorls carry little whorls. In *Proceedings of the Summer Program*. *(p. 87, 90, 92)*

Ijzermans, R., E. Meneguz, and M. W. Reeks (2010). Segregation of particles in incompressible random flows: singularities, intermittency and random uncorrelated motion. *Journal of Fluid Mechanics 653*, 99–136. *(p. 87, 90, 91)*

Innocenti, A., C. Marchioli, and S. Chibbaro (2016). Lagrangian filtered density function for LES-based stochastic modelling of turbulent particle-laden flows. *Physics of Fluids 28*(11), 115106. *(p. 68)*

Ireland, P. J. and O. Desjardins (2017). Improving particle drag predictions in Euler–Lagrange simulations with two-way coupling. *Journal of Computational Physics 338*, 405 – 430. *(p. 7, 41)*

Italian Agency For New Energy Technologies (2006). DNS, LES and RANS Comparison. *(p. 55)*

Kaufmann, A., M. Moreau, O. Simonin, and J. Helie (2008). Comparison between Lagrangian and mesoscopic Eulerian modelling approaches for inertial particles

suspended in decaying isotropic turbulence. *Journal of Computational Physics 227*, 6448–6472. *(p. 50)*

Khan, M., X. Luo, F. Nicolleau, P. Tucker, and G. Lo Iacono (2010). Effects of LES sub-grid flow structure on particle deposition in a plane channel with a ribbed wall. *International Journal for Numerical Methods in Biomedical Engineering 26*(8), 999–1015. *(p. 65)*

Knorps, M. and J. Pozorski (2018). Fractal-based modelling of subfilter scales in LES with heavy particles. 13th Workshop on Synthetic Turbulence Models. *(p. 65)*

Kolmogorov, A. N. (1941). The local structure of turbulence in incompressible viscous fluid for very large Reynolds numbers. In *Proceedings of the USSR Academy of Sciences*, Number 4 in 30, pp. 299–303. *(p. 27, 30, 31, 36)*

Kolmogorov, A. N. (1962). A refinement of previous hypotheses concerning the local structure of turbulence in a viscous incompressible fluid at high Reynolds number. *Journal of Fluid Mechanics 13*(1), 82–85. *(p. 37)*

Kraichnan, R. H. (1970). Diffusion by a random velocity field. *Physics of Fluids 13*(1), 22–31. *(p. 87, 99)*

Kramer, P. R. (2001). A review of some monte carlo simulation methods for turbulent systems. *Monte Carlo Methods and Applications 7*(3/4), 229–244. *(p. 64)*

Kuerten, J. (2006). Subgrid modeling in particle-laden channel flow. *Physics of Fluids 18*(2), 025108. *(p. 65)*

Lancien, T., K. Prieur, D. Durox, S. Candel, and R. Vicquelin (2018). Large Eddy Simulation of light-round in an annular combustor with liquid spray injection and comparison with experiments. *Journal of Engineering for Gas Turbines and Power 140*(2), 021504. *(p. 9, 10)*

Landau, L. D. and E. M. Lifshitz (1959). *Course of theoretical physics*. Pergamon Press. *(p. 32)*

Lanford, J. A. Oscar, E. (1981). The hard sphere gas in the Boltzmann-Grad limit. *Physica A: Statistical Mechanics and its Applications 106*(1-2), 70–76. *(p. 20)*

Langevin, P. (1908). On the theory of brownian motion. *Comptes rendus de l'Académie des Sciences 146*, 530533. *(p. 65)*

Langford, J. A. and R. D. Moser (1999). Optimal LES formulations for isotropic turbulence. *Journal of Fluid Mechanics 398*, 321–346. *(p. 77)*

Laurent, F., A. Vié, C. Chalons, R. O. Fox, and M. Massot (2013). A hierarchy of Eulerian models for trajectory crossing in particle-laden turbulent flows over a wide range of Stokes numbers. *Center for Turbulence Research Annual Research Briefs 2012*, 193. *(p. 50)*

Lebowitz, J. L. (1995). Microscopic reversibility and macroscopic behavior: Physical explanatoins and mathematical derivations. In *25 Years of Non-Equilibrium Statistical Mechanics*, pp. 1–20. Springer. *(p. 20)*

L'Ecuyer, P. (2015). Random number generation with multiple streams for sequential and parallel computing. In *Winter Simulation Conference (WSC), 2015*, pp. 31–44. IEEE. *(p. 95)*

Leparoux, J., R. Mercier, V. Moureau, and H. Musaefendic (2018). Primary atom-

ization simulation applied to a jet in crossflow aeronautical injector with dynamic mesh adaptation. In *14th Triennal International Conference on Liquid Atomization and Spray Systems. (p. 5)*

Leray, J. (1933). *Etude de diverses équations intégrales non linéaires et de quelques problèmes que pose l'hydrodynamique*. Gauthier-Villars. *(p. 22)*

Leray, J. (1934a). Essai sur les mouvements plans d'un fluide visqueux que limitent des parois. *Journal de Mathématiques Pures et Appliquées 13*, 331–418. *(p. 22)*

Leray, J. (1934b). Sur le mouvement d'un liquide visqueux emplissant l'espace. *Acta mathematica 63*, 193–248. *(p. 22)*

Leslie, D. C. (1973). *Developments in the Theory of Turbulence*. Clarendon Press Oxford. *(p. 26)*

Lesne, A. and M. Laguës (2012). *Scale invariance: From phase transitions to turbulence*. Springer Science & Business Media. *(p. 24, 27)*

Letournel, R. (2022). *Modélisation et simulation d'écoulements turbulents fortement chargés en particules: modélisation statistique et méthodes de moments*. Ph. D. thesis, CentraleSupélec. *(p. 37, 43, 167, 171, 176)*

Letournel, R., F. Laurent, M. Massot, and A. Vié (2020). Modulation of homogeneous and isotropic turbulence by sub-Kolmogorov particles: Impact of particle field heterogeneity. *International Journal of Multiphase Flow 125*, 103233. *(p. 11, 13, 43)*

Lions, P. L. and N. Masmoudi (2001). From the Boltzmann equations to the equations of incompressible fluid mechanics, II. *Archive for Rational Mechanics and Analysis 158*(3), 195–211. *(p. 20)*

Mandelbrot, B. B. (1974). Intermittent turbulence in self-similar cascades: divergence of high moments and dimension of the carrier. *Journal of Fluid Mechanics 62*(2), 331–358. *(p. 113)*

Marchioli, C. (2017). Large-eddy simulation of turbulent dispersed flows: a review of modelling approaches. *Acta Mechanica 228*(3), 741–771. *(p. 64, 78)*

Marchioli, C., M. V. Salvetti, and A. Soldati (2008). Appraisal of energy recovering sub-grid scale models for large-eddy simulation of turbulent dispersed flows. *Acta mechanica 201*(1-4), 277–296. *(p. 65)*

Masi, E. and Simonin (2014). Algebraic-Closure-Based Moment Method for unsteady Eulerian simulations of non-isothermal particle-laden turbulent flows at moderate Stokes numbers in dilute regime. *Flow Turbulence and Combustion 92*(1-2), 121–145. *(p. 50)*

Maxey, M. (1987). The gravitational settling of aerosol particles in homogeneous turbulence and random flow fields. *Journal of Fluid Mechanics 174*, 441–465. *(p. 87)*

McComb, W. D. (1990). *The physics of fluid turbulence*. Oxford Engineering Science Series. *(p. 77)*

Ménard, T., S. Tanguy, and A. Berlemont (2007). Coupling level set/VOF/ghost fluid methods: Validation and application to 3D simulation of the primary break-up of a liquid jet. *International Journal of Multiphase Flow 33*(5), 510–524. *(p. 40)*

Meneveau, C. and K. Sreenivasan (1987). The multifractal spectrum of the dissipa-

tion field in turbulent flows. *Nuclear Physics B-Proceedings Supplements 2*, 49–76. *(p. 113)*

Mesquita, L. C. C., A. Vié, and S. Ducruix (2018, June). Large Eddy Simulations of a two-phase staged swirling burner using an Euler-Lagrange approach: validation of the injection strategy. In *Proceedings of the ASME Turbo Expo 2018*, Oslo, Norway. *(p. 6)*

Minier, J.-P. and E. Peirano (2001). The PDF approach to turbulent polydispersed two-phase flows. *Physics reports 352*(1), 1–214. *(p. 66, 84)*

Minier, J.-P., E. Peirano, and S. Chibbaro (2004). PDF model based on Langevin equation for polydispersed two-phase flows applied to a bluff-body gas-solid flow. *Physics of Fluids 16*(7), 2419–2431. *(p. 67)*

Minier, J.-P. and C. Profeta (2015, Nov). Kinetic and dynamic probability-density-function descriptions of disperse turbulent two-phase flows. *Physical Review E 92*, 053020. *(p. 36, 65, 67)*

Mols, B. and R. Oliemans (1998). A turbulent diffusion model for particle dispersion and deposition in horizontal tube flow. *International journal of multiphase flow 24*(1), 55–75. *(p. 66)*

Monin, A. and A. Yaglom (1971). *Statistical Fluid Mechanics: Mechanics of Turbulence*, Volume 1. MIT Press, Cambridge. *(p. 31)*

Moreau, M., O. Simonin, and B. Bédat (2010). Development of gas-particle Euler-Euler LES approach: a priori analysis of particle sub-grid models in homogeneous isotropic turbulence. *Flow, turbulence and combustion 84*(2), 295. *(p. 69, 78)*

Movaghar, A., M. Linne, M. Herrmann, A. Kerstein, and M. Oevermann (2018). Modeling and numerical study of primary breakup under diesel conditions. *International Journal of Multiphase Flow 98*, 110 – 119. *(p. 5)*

Murray, S., M. Lightstone, and S. Tullis (2016). Single-particle Lagrangian and structure statistics in kinematically simulated particle-laden turbulent flows. *Physics of Fluids 28*(3), 033302. *(p. 87, 99)*

Naumann, Z. and L. Schiller (1935). A drag coefficient correlation. *VDI Zeitung 77*, 318–323. *(p. 40, 61)*

Nicolleau, F. and A. A. E.-A. Aly (2012). Can kinematic simulation predict Richardson's regime? In *New Approaches in Modeling Multiphase Flows and Dispersion in Turbulence, Fractal Methods and Synthetic Turbulence*, pp. 43–57. Springer. *(p. 92)*

Nicoud, F. and F. Ducros (1999). Subgrid-scale stress modelling based on the square of the velocity gradient. *Flow Turbulence and Combustion 62*(3), 183–200. *(p. 57)*

Nicoud, F., H. B. Toda, O. Cabrit, S. Bose, and J. Lee (2011). Using singular values to build a subgrid-scale model for Large Eddy Simulations. *Physics of Fluids 23*, 085106. *(p. 57)*

Onsager, L. (1949). Statistical hydrodynamics. *Il Nuovo Cimento (1943-1954) 6*(2), 279–287. *(p. 113)*

OpenFoam (2008). Simulation of an Homogeneous Isotropic Turbulence. *(p. 53)*

Pai, M. G. and S. Subramaniam (2009). A comprehensive probability density function

formalism for multiphase flows. *Journal of Fluid Mechanics 628*, 181–228. *(p. 81)*

Pai, M. G. and S. Subramaniam (2012). Two-way coupled stochastic model for dispersion of inertial particles in turbulence. *Journal of Fluid Mechanics 700*, 29–62. *(p. 80)*

Pandya, R. and F. Mashayek (2002). Two-fluid large-eddy simulation approach for particle-laden turbulent flows. *International Journal of Heat and Mass Transfer 45*(24), 4753–4759. *(p. 68)*

Paulhiac, D. (2015). *Modélisation de la combustion d'un spray dans un brûleur aéronautique*. Ph. D. thesis, Université de Toulouse. *(p. 7)*

Peterson, V. L., J. Kim, T. L. Holst, G. S. Deiwert, D. M. Cooper, A. B. Watson, and F. R. Bailey (1989). Supercomputer requirements for selected disciplines important to aerospace. *Proceedings of the IEEE 77*(7), 1038–1055. *(p. 52)*

Pope, S. (2000). *Turbulent flows*. IOP Publishing. *(p. 20, 26, 27, 31, 33, 51, 52, 54, 55, 56, 61, 65, 82, 85, 88, 108, 113)*

Pope, S. (2010). Self-conditioned fields for large-eddy simulations of turbulent flows. *Journal of Fluid Mechanics 652*, 139–169. *(p. v, 54, 77, 80, 148)*

Pope, S. and E. S. Ching (1993). Stationary probability density functions: An exact result. *Physics of Fluids A: Fluid Dynamics 5*(7), 1529–1531. *(p. 42)*

Poustis, J.-F., J.-M. Senoner, D. Zuzio, and P. Villedieu (2019). Regularization of the Lagrangian point force approximation for deterministic discrete particle simulations. *International Journal of Multiphase Flow 117*, 138–152. *(p. 7, 41, 149)*

Press, W., B. Flannery, S. Teukolsky, and W. Vetterling (1989). *Numerical recipes*, Volume 3. Cambridge University Press. *(p. 95)*

Providakis, T., L. Zimmer, P. Scouflaire, and S. Ducruix (2012). Characterization of the Acoustic Interactions in a Two-Stage Multi-Injection Combustor Fed With Liquid Fuel. *Journal of Engineering for Gas Turbines and Power 134*(11), 111503–8. Cat. A. *(p. 3)*

Ray, B. and L. R. Collins (2014). A subgrid model for clustering of high-inertia particles in large-eddy simulations of turbulence. *Journal of Turbulence 15*(6), 366–385. *(p. 65)*

Reeks, M. W. (1977). On the dispersion of small particles suspended in an isotropic turbulent fluid. *Journal of Fluid Mechanics 83*(3), 529–546. *(p. 66)*

Reeks, M. W. (1980). Eulerian direct interaction applied to the statistical motion of particles in a turbulent fluid. *Journal of Fluid Mechanics 97*(3), 569–590. *(p. 87)*

Reeks, M. W. (1991). On a kinetic equation for the transport of particles in turbulent flows. *Physics of Fluids A: Fluid Dynamics 3*(3), 446–456. *(p. 68, 84)*

Reeks, M. W., D. C. Swailes, and A. D. Bragg (2018). Is the kinetic equation for turbulent gas-particle flows ill posed? *Physical Review E 97*(2), 023104. *(p. 36, 63, 126)*

Renaud, A., S. Ducruix, and L. Zimmer (2017). Bistable behaviour and thermoacoustic instability triggering in a gas turbine model combustor. *Proceedings of the Combustion Institute 36*(3), 3899–3906. *(p. 3)*

Reynolds, O. (1883). XXIX. An experimental investigation of the circumstances which

determine whether the motion of water shall he direct or sinuous, and of the law of resistance in parallel channels. *Philosophical Transactions of the Royal Society of London 174*, 935–982. *(p. 24, 32)*

Reynolds, O. (1895). On the dynamical theory of incompressible viscous fluids and the determination of the criterion. *Philosophical Transactions of the Royal Society of London. A 186*, 123–164. *(p. 30)*

Richardson, L. F. (1922). *Weather prediction by numerical process*. Cambridge University Press. *(p. 24, 26, 113)*

Richardson, L. F. (1926). Atmospheric diffusion shown on a distance-neighbour graph. *Proceedings of the Royal Society of London. Series A, Containing Papers of a Mathematical and Physical Character 110*(756), 709–737. *(p. 32, 36)*

Rüemelin, W. (1982). Numerical treatment of stochastic differential equations. *SIAM Journal on Numerical Analysis 19*(3), 604–613. *(p. 93)*

Sabat, M. (2016). *Modèles euleriens et méthodes numériques pour la description des sprays polydisperses turbulents.* Ph. D. thesis, École Centrale Paris. *(p. 50)*

Sabat, M., A. Vié, A. Larat, and M. Massot (2019). Statistical description of turbulent particle-laden flows in the very dilute regime using the anisotropic gaussian moment method. *International Journal of Multiphase Flow 112*, 243–257. *(p. 45, 50)*

Sagaut, P. (2006). *Large Eddy Simulation for incompressible flows: an introduction*. Springer Science & Business Media. *(p. 53, 54, 56)*

Salvetti, M. V., C. Marchioli, and A. Soldati (2006). On the closure of particle motion equations in large-eddy simulation. In *Direct and Large-Eddy Simulation VI*, pp. 311–318. Springer. *(p. 65)*

Sanjosé, M., J.-M. Senoner, F. Jaegle, B. Cuenot, S. Moreau, and T. Poinsot (2011). Fuel Injection Model for Euler-Euler and Euler-Lagrange Large-Eddy Simulations of an evaporating spray inside an aeronautical combustor. *International Journal of Multiphase Flow 37*(5), 514–529. *(p. 6)*

Scholl, S. (2016). Exact signal measurements using FFT analysis. *(p. 96)*

Scotti, A. and C. Meneveau (1999). A fractal model for Large Eddy Simulation of turbulent flow. *Physica D: Nonlinear Phenomena 127*(3), 198 – 232. *(p. 65)*

Shotorban, B. and S. Balachandar (2007). A Eulerian model for large-eddy simulation of concentration of particles with small Stokes numbers. *Physics of Fluids 19*(11), 118107. *(p. 65, 66, 69, 78)*

Shotorban, B. and F. Mashayek (2006). A stochastic model for particle motion in large-eddy simulation. *Journal of Turbulence 7*, N18. *(p. 67)*

Smagorinsky, J. (1963). General circulation experiments with the primitive equations. I: The basic experiment. *Monthly Weather Review 91(3)*, 99–164. *(p. 57)*

Spinoza, B. (1842). *Oeuvres de Spinoza*, Volume 1. Charpentier. *(p. 51)*

Stafford, C., D. Swailes, and N. Chakraborty (2016). Particle dispersion in inhomogeneous turbulence: An analysis of PDF-based models. In *9th International Conference on Multiphase Flow (ICMF 2016)*. Newcastle University. *(p. 87)*

Stokes, G. G. (1851). *On the effect of the internal friction of fluids on the motion of*

pendulums, Volume 9. Pitt Press. *(p. 13, 40)*

Struchtrup, H. (2005). *Macroscopic transport equations for rarefied gas flows*. Springer. *(p. 20, 21, 42)*

Subramaniam, S. (2013). Lagrangian–Eulerian methods for multiphase flows. *Progress in Enerergy and Combustion Science 39*(2–3), 215–245. *(p. 45)*

Taylor, G. I. (1921). Diffusion by continuous movements. *Proceedings of the London Mathematical Society 2*(1), 196–212. *(p. 32, 33, 37, 66, 84, 85, 106, 125, 142, 143)*

Tchen, C. (1959). Diffusion of particles in turbulent flow. In *Advances in Geophysics*, Volume 6, pp. 165–174. Elsevier. *(p. 66, 132)*

Tchen, C.-M. (1947). *Mean value and correlation problems connected with the motion of small particles suspended in a turbulent fluid*. Ph. D. thesis, Delft University of Technology. *(p. 128)*

Temam, R. (1991). Approximation of attractors, Large Eddy Simulations and multiscale methods. *Proceedings: Mathematical and Physical Sciences 434*(1890), 23–39. *(p. 23)*

Temam, R. (2001). *Navier-Stokes equations: theory and numerical analysis*, Volume 343. American Mathematical Soc. *(p. 21, 22, 30, 51, 52)*

Tenneti, S., R. Garg, and S. Subramaniam (2011). Drag law for monodisperse gas–solid systems using particle-resolved direct numerical simulation of flow past fixed assemblies of spheres. *International journal of multiphase flow 37*(9), 1072–1092. *(p. 81)*

Thomson, D. and B. Devenish (2005). Particle pair separation in kinematic simulations. *Journal of Fluid Mechanics 526*, 277–302. *(p. 87, 92)*

Vaudor, G., T. Ménard, W. Aniszewski, M. Doring, and A. Berlemont (2017). A consistent mass and momentum flux computation method for two phase flows. Application to atomization process. *Comput. & Fluids 152*, 204–216. *(p. 5)*

Vié, A., S. Jay, B. Cuenot, and M. Massot (2013). Accounting for Polydispersion in the Eulerian Large Eddy Simulation of the Two-Phase Flow in an Aeronautical-type Burner. *Flow, Turbulence and Combustion 90*(3), 545–581. *(p. 6)*

Vignat, G., S. P. R., D. Durox, A. Vié, A. Renaud, and S. Candel (2020). A joint experimental and LES characterization of the liquid fuel spray in a swirl injector. In *Proceedings of the ASME Turbo Expo 2020*, London, UK. *(p. 6)*

Vinkovic, I., C. Aguirre, M. Ayrault, and S. Simoëns (2006). Large-eddy simulation of the dispersion of solid particles in a turbulent boundary layer. *Boundary-layer meteorology 121*(2), 283. *(p. 67)*

Wang, L.-P. and M. R. Maxey (1993). Settling velocity and concentration distribution of heavy particles in homogeneous isotropic turbulence. *Journal of Fluid Mechanics 256*, 27–68. *(p. 87)*

Wang, Q., X. Zhao, and M. Ihme (2019). A regularized deconvolution model for subgrid dispersion in Large Eddy Simulation of turbulent spray flames. *Combustion and Flame 207*, 89–100. *(p. 65)*

Yakhot, V. and S. A. Orszag (1986). Renormalization group analysis of turbulence. I.

basic theory. *Journal of scientific computing 1*(1), 3–51. *(p. 77)*

Yamamoto, Y., M. Potthoff, T. Tanaka, T. Kajishima, and Y. Tsuji (2001). Large-eddy simulation of turbulent gas–particle flow in a vertical channel: effect of considering inter-particle collisions. *Journal of Fluid Mechanics 442*, 303–334. *(p. 60)*

Zaichik, L. I. (1999). A statistical model of particle transport and heat transfer in turbulent shear flows. *Physics of Fluids 11*(6), 1521–1534. *(p. 68)*

Zaichik, L. I., O. Simonin, and V. Alipchenkov (2009). An Eulerian approach for Large Eddy Simulation of particle transport in turbulent flows. *Journal of Turbulence 10*, N4. *(p. 68)*

Zamansky, R., F. Coletti, M. Massot, and A. Mani (2014). Radiation induces turbulence in particle-laden fluids. *Physics of Fluids 26*(7), 071701. *(p. 42)*

Zamansky, R., F. Coletti, M. Massot, and A. Mani (2016). Turbulent thermal convection driven by heated inertial particles. *Journal of Fluid Mechanics 809*, 390–437. *(p. 7, 13, 78, 80)*

Zeigarnik, B. (1927). On the retention of completed and uncompleted activities. *Psychologische Forschung 9*, 1–85. *(p. iii)*

Zeren, Z. (2010). *Modélisation Lagrangienne stochastique des écoulements gaz-solides turbulents avec couplage inverse en Turbulence Homogène Isotrope stationnaire.* Ph. D. thesis, INPT. *(p. 41, 80, 128, 149)*

Zhang, Z., D. Legendre, and R. Zamansky (2019). Model for the dynamics of microbubbles in high-Reynolds-number flows. *Journal of Fluid Mechanics 879*, 554–578. *(p. 67)*

Zhou, Z., S. Wang, and G. Jin (2018). A structural subgrid-scale model for relative dispersion in large-eddy simulation of isotropic turbulent flows by coupling kinematic simulation with approximate deconvolution method. *Physics of Fluids 30*(10), 105110. *(p. 65)*

Zwick, D. and S. Balachandar (2017, sep). Accurate signal reconstruction for higher order Lagrangian–Eulerian back-coupling in multiphase turbulence. *Fluid Dynamics Research 49*(5), 055507. *(p. 41)*

Zwick, D. and S. Balachandar (2020). A scalable euler–lagrange approach for multiphase flow simulation on spectral elements. *The International Journal of High Performance Computing Applications 34*(3), 316–339. *(p. 41)*

Nomenclature

Latin characters

$\bullet'$	fluctuating part of $\bullet$ in the context of a reduction operator
$\bullet^{-1}$	when $\bullet$ is a function, corresponds to the inverse of $\bullet$
$\bullet^{\leftarrow}$	pre-image of $\bullet$
$\overline{\bullet}$	reduced variable $\bullet$
$\bullet_x$, $\bullet_y$, $\bullet_z$	Cartesian components of the vector $\bullet$
$\bullet^{\top}$	transpose of matrix $\bullet$
$\nabla_{\boldsymbol{v}}$	notation for $\left(\partial_{\boldsymbol{v}_x}, \partial_{\boldsymbol{v}_y}, \partial_{\boldsymbol{v}_z}\right)$
$\nabla_{\boldsymbol{x}}$	notation for $(\partial_x, \partial_y, \partial_z)$
$\boldsymbol{a}_n$	amplitude of mode n in KS
$a_p^{(q)}$	position in phase space for a particle q
$\boldsymbol{a}_f$	measurable set of fluid flow fields
$\boldsymbol{a}_p$	measurable set of phase space for a particle
A	Phase space
A_f	set of fluid flow fields
A_p	phase space for the particles
$\mathcal{A}_f$	set of measurable sets of fluid flow fields
$\mathcal{A}_p$	set of measurable subsets of phase space for the particles
B	bassin of attraction
C_0	Richardson's constant
C_S	Smagorinsky constant
$\mathrm{d}\bullet$	differential of $\bullet$

$d\boldsymbol{B}_t$	3D Wiener process increment
d_p	particle diameter
$\mathrm{d}_t \bullet$	derivative of $\bullet$
D	diffusion coefficient
D	diagonal matrix
D_{red}	reduced dynamical system
D_{ref}	dynamical system of reference
$D_{\mathrm{red,s-c}}$	self-contained reduced dynamical system
$\partial_\bullet$	partial derivative with respect to the variable $\bullet$
Kn	Knudsen number
$\boldsymbol{e}$	event
E	numerical integration error
$E(\kappa)$	average fluid energy density spectrum
$E_{continuous}$	reference continuous average fluid energy density spectrum for KS
$\mathcal{E}$	set of events
$\mathfrak{E}$	enstrophy
$\mathbb{E}$	expectancy
f	distribution of the MEF
f_{all}	joint distribution of the fluid and the particles
$f_{\mathrm{all},\boldsymbol{a}_f}$	conditional distribution of the particles on the set of fluids $\boldsymbol{a}_f$
$f_{\boldsymbol{a}_f}$	average distribution of the particles averaged over the set of fluids $\boldsymbol{a}_f$
$f_{\boldsymbol{a}_f}^{(q)}$	marginal distribution of the particle q on the set of fluids $\boldsymbol{a}_f$
f_{EE}	mesoscopic density
$f_{\mathrm{macroscopic}}$	characteristic frequency of the macroscopic problem
$f_{\mathrm{microscopic}}$	characteristic frequency of the microscopic problem
f_{NCM}	normalised counting measure
f^{N_p}	product distribution of N_p particles
$f_{q,\mathrm{DPS}}$	fine-grain distribution of the particle q
$f_{\boldsymbol{u}_f}$	distribution of the MEF on the fluid $\boldsymbol{u}_f$

G	arbitrary reduction operator of the fluid field
G_{LES}	LES reduction operator of the fluid field
G_{Re}	RANS reduction operator of the fluid field
$\mathfrak{G}$	arbitrary reduction operator
k	reference energy of KS
k'	normalised KS reference energy
k_0	normalisation factor for KS energy
k_{SGS}	sub-grid scale energy
$\ell_{\text{mean free path}}$	mean free path of fluid molecules
$\ell_{\text{physical length}}$	characteristic physical length scale of the problem
L	length scale of the largest turbulent eddies
L	bound in the curvature of a field
L_*	characteristic length scale
log	natural logarithm
$\mathcal{M}_k$	moment of f of order k in the velocity direction
n	index
n_0	dimensionless particle number density
n_η	dimensionless particle number
N_p	number of particles
$\mathcal{N}$	normal distribution
$\mathcal{N}^{\mathrm{R}}$	folded normal distribution
$\widehat{\mathrm{N}}_f$	statistical number of fluids
N_{LE}	number of large eddy realisations
$\widehat{\mathrm{N}}_p$	statistical number of particles
N_{SE}	number of small eddy realisations
N_κ	number of modes in KS
$\| \bullet \|$	norm 2 of $\bullet$
p_f	Fluid pressure
P	transfer matrix

$\mathbb{P}$	probability measure
$\mathbb{P}_t$	probability measure transported at time t
PSD*$(u_{p,x})$	model of the PSD of $u_{p,x}$
$q \in [\![1, \mathrm{N}_p]\!]$	index for the particles
$R(\boldsymbol{u}_f)$	$G((\boldsymbol{u}_f \cdot \nabla_{\boldsymbol{x}})\,\boldsymbol{u}_f) - (\overline{\boldsymbol{u}}_f \cdot \nabla_{\boldsymbol{x}})\,\overline{\boldsymbol{u}}_f$
$R_{(\boldsymbol{V}_p)}$	primitive of the autocorrelation of $\boldsymbol{V}_p$
$\mathbb{R}$	real numbers
$\mathrm{Re} = \frac{U_* L_*}{\nu}$	Reynolds number
$\mathrm{Re}_t = \frac{\boldsymbol{u}_f L_t}{\nu}$	turbulent Reynolds number
s	element of time
s_{ref}	position in the phase space of reference
s_t	global state variable of the two-phase flow system in phase space at time t
$\mathcal{S}_{\mathrm{ref}}$	phase space of reference
S	element of surface
S_{ij}	resolved deformation tensor
$\mathrm{St}_{\mathrm{large}}$	Stokes number based on the largest scales of the flow
$\mathrm{St}_{\mathrm{small}}$	Stokes number based on the smallest scales of the flow
$\mathrm{St}_\eta = \frac{\tau_p}{\tau_\eta}$	Stokes number based on the Kolmogorov scale
t	time
t_0	reference time
t_{01}, t_{02}	initial times
$\int$	integral
T_*	characteristic time scale
T_L	Lagrangian autocorrelation time
U_*	characteristic velocity scale
$\boldsymbol{U}_3$	random variable of the fluid velocity seen for the third order model
$\boldsymbol{u}_0$	fluid velocity variable of the homogeneous system
$\boldsymbol{u}_1$, $\boldsymbol{u}_2$	arbitrary fluid velocity fields
$\boldsymbol{u}_f(t, \boldsymbol{x})$	Eulerian fluid velocity

$\boldsymbol{u}_f, t$	Eulerian fluid velocity field at time t
$\boldsymbol{v}$	variable representing the velocity in phase-space
$\boldsymbol{v}_0$	velocity variable of the homogeneous system
$\boldsymbol{v}_{f@p}\,(t)$	fluid velocity around a particle
$\boldsymbol{v}_f\,(t)$	fluid velocity at the particle position
$\boldsymbol{v}_p$	particle velocity
Var	variance
$\boldsymbol{V}_2$, $\boldsymbol{V}_3$	random variable of the particle velocity
	for the second and third order model
$\boldsymbol{V}_p$	random variable of the particle velocity
$\boldsymbol{x}$	variable representing the position in phase-space
$\boldsymbol{x}_0$	position variable of the homogeneous system
$\boldsymbol{x}_{01}$, $\boldsymbol{x}_{02}$	initial positions
$\boldsymbol{x}_p$	particle position
$\boldsymbol{X}_1$, $\boldsymbol{X}_2$ et $\boldsymbol{X}_3$	random variable of the particle position respectively
	for the first, second and third order model
$\boldsymbol{X}_p$	random variable of the particle position
$\boldsymbol{x}_{p,0}$	particle position at time t_0
$\boldsymbol{x}_{p,t_0,\boldsymbol{x}_{p,0}}$	position at t of the particle which was in $\boldsymbol{x}_{p,0}$ at t_0
$\boldsymbol{x}_{p,\Delta t}$	particle position integrated with a time step Δt
z_0	global variable of the deterministic homogeneous system
Z_0	global variable of the stochastic homogeneous system

Greek characters

$\delta_\bullet$	delta measure at $\bullet$
Δ	normalised convolution kernel
$\Delta_{\boldsymbol{x}}$	Laplacian according to the variable $\boldsymbol{x}$
ε	rate of dissipation of turbulent kinetic energy
ϵ	small positive value
η	Kolmogorov length-scale
θ	parameter
$\left(\widehat{\theta}_n\right)_{n\in\mathbb{N}}$	sequence of estimators of the parameter θ
κ	wave-number
κ_0	lowest wave-number
κ_{EI}	wave-number between the energy-containing range and the inertial sub-range
κ_{ID}	wave-number between the inertial sub-range and the dissipation range
$\kappa_{\max}$	maximum of the wave-number range
$\kappa_{\min}$	minimum of the wave-number range
$\boldsymbol{\kappa}_n$	wave-vectors of KS
κ_η	wave-number at Kolmogorov length-scale
μ_f	fluid cinematic viscosity
ν_f	Fluid dynamic viscosity
ν_{SGS}	turbulent viscosity
ρ	covariance matrix
ρ_f	Fluid density
ρ_p	particle density
σ	vectorial brownian energy
σ_1, σ_2, σ_3	brownian energy respectively of the first, second, and third model
τ_p	characteristic time of the particle
τ_t	characteristic time-scale of sub-grid scale fluctuations
τ_u	autocorrelation time of the fluid velocity seen along a particle trajectory

τ_{U3}	characteristic time of the fluid velocity seen of the third order model
τ_v	autocorrelation time of a particle velocity
τ_{V2}, τ_{V3}	characteristic time of the velocity of the second and third order model
τ_η	characteristic time scale associated to Kolmogorov length-scale
ϕ	particle mass loading
φ_n	phase of the mode in KS
Φ	evolution function of a dynamical system
Φ_f	evolution function for the Navier-Stokes equations
Φ_{ref}	flux of the dynamical system of reference
$\Phi_{\text{red,s-c}}^{\mathcal{S}_{\text{ref}},\mathfrak{G},\Phi_{\text{ref}}}$	flow adapted to a self-contained reduction operator
$\Phi_{\text{red,inj}}^{\mathcal{S}_{\text{ref}},\mathfrak{G}}$	flow adapted to an injective reduction operator
Φ_t	function giving the state of the fluid and the particles after a time t
ω	pulsation
ω	realisation
$\boldsymbol{\omega}$	fluid vorticity vector
ω_f	fluid realisation
ω_n	pulsation of the mode in KS
Ω	set of possible outcomes

Abbreviations

CO	Carbon Monoxide
DNE	Does Not Exist
DNS	Direct Numerical Simulation
EMEF	Extended mesoscopic Eulerian Formalism
EM2C	Laboratoire Énergétique Moléculaire et Macroscopique, Combustion
HIT	Homogeneous Isotropic Turbulence
KS	Kinematic Simulation
LES	Large Eddy Simulation
MEF	Mesoscopic Eulerian Formalism

MPI	Message Passing Interface
NDF	Number Density Function
NCM	Normalised Counting Measure
LE	Large Eddies
NOx	Nitrogen Oxide
NS	Navier-Stokes
PBE	Population Balance Equation
PDF	Probability Density Function
PSD	Power Spectral Density
RANS	Reynolds Averaged Navier-Stokes
RK4	Runge-Kutta of order four
SE	Small Eddies
URANS	Unsteady Reynolds Averaged Navier-Stokes

Appendix

Synthèse en Français

Le spray de carburant constitue un des éléments clefs des moteurs aéronautiques. Afin de reproduire fidèlement le comportement de tels moteurs par simulation numérique, la modélisation de sprays de carburant aux gouttes de tailles variées est d'importance primordiale. Parmi les différentes stratégies envisageables, les méthodes de moment eulériennes offrent une option très intéressante car en s'intéressant directement à la distribution de gouttes de la phase dispersée, elles permettent naturellement de représenter l'évolution de statistiques convergées. Ces méthodes sont déjà utilisées avec succès pour reproduire des tendances macroscopiques telles que la forme de la flamme. Il reste toutefois de nombreux défis à relever afin d'améliorer le niveau de précision et de prédiction de ces méthodes.
Parmi ces challenges, le couplage réciproque entre le spray et la phase gazeuse constitue un élément majeur. En effet, les méthodes de moments utilisées pour la simulation de sprays de chambres de combustion reposent souvent sur le formalisme mésoscopique eulérien formalisé par Février et al. (2005). Ce formalisme envisage la distribution de gouttes de carburant correspondant à une seule réalisation de la phase gazeuse. Le fluide porteur est supposé unique et connu, de sorte qu'une telle approche n'est principalement envisageable que dans un contexte où la phase dispersée ne rétroagit pas sur la phase gazeuse.
Le travail proposé au cours de cette thèse s'attaque à cette limitation et propose une dérivation étendue du formalisme mésoscopique eulérien. Cette dérivation permet de prendre en compte certains cas de couplage entre la phase dispersée et la phase gazeuse grâce à une approche de simulations aux grandes échelles (LES). Cette solution est particulièrement adaptée aux cas où la phase dispersée agit principalement sur les plus petites échelles de la phase gazeuse. Comme le suggère Février et al. (2005), c'est un scénario qui apparaît très pertinent au regard de ce qui est souvent observé en pratique. C'est pourquoi, dans la lignée de Fox (2003) et de Pope (2010), nous sommes amenés à considérer une moyenne conditionnelle du spray par rapport aux éléments résolus de l'écoulement. Cette approche permet de concilier, au sein d'une formulation aux grandes échelles, la vision moyenne du brouillard de gouttes conditionnée à une unique réalisation des grandes échelles du fluide porteur, comme dans le formalisme mésoscopique eulérien classique, et un couplage fort entre la phase dispersée et le fluide à petite échelle. Afin

d'étudier cette construction originale et difficile à approcher de façon pratique, un environnement numérique basé sur des simulations cinématiques a été développé. Les simulations cinématiques permettent de maîtriser l'espace de probabilité associé à l'ensemble des fluides turbulents, ce qui n'aurait pas été possible avec les solutions des équations de Navier-Stokes. Cet outil de simulation a été validé consciencieusement afin d'assurer la convergence des quantités d'intérêt pour l'étude proposée : notamment les moments d'ordre deux de la distribution de particules, ainsi que le contenu fréquentiel de leurs trajectoires. Cet outil a ensuite permis d'évaluer numériquement le comportement du formalisme proposé, en variant le niveau de réduction du champ fluide, de DNS à RANS. On observe alors que dès que l'on travaille avec un champ porteur réduit, ce nouveau formalisme introduit un effet diffusif sur la trajectoire de particules ponctuelles. Pour des temps asymptotiquement longs, les caractéristiques de cette dispersion sont entièrement pilotées par les propriétés du champ turbulent. En revanche, pour les temps courts, cette dispersion est directement impactée par le niveau de réduction du champ fluide. Cette observation est particulièrement intéressante car les gouttes de carburant d'une chambre s'évaporent très rapidement et sont principalement impactées par le régime initial. Pour conclure ce travail, quelques fermetures diffusives pour la phase dispersée, qui sont adaptées au nouveau formalisme que nous avons introduit, sont étudiées et quelques perspectives quant à la simulation d'écoulement diphasiques couplés aux grandes échelles sont présentées.

université PARIS-SACLAY

ÉCOLE DOCTORALE
Sciences mécaniques et énergétiques, matériaux et géosciences (SMEMAG)

Titre: Simulation aux grandes échelles d'écoulements à phase dispersée avec prise en compte du couplage inverse: un formalisme statistiquement cohérent

Mots clés: spray, turbuelnce, simulation aux grandes échelles, couplage, formalisme mésoscopique eulérien, simulation cinématique

Résumé: La simulation de sprays de carburant est d'importance primordiale pour reproduire fidèlement le comportement des moteurs aéronautiques. À cette fin, les méthodes de moment eulériennes sont déjà été utilisées avec succès pour reproduire des tendances macroscopiques telles que la forme de la flamme. Pour les améliorer, il reste toutefois de nombreux challenges, tels que la prise en compte du couplage entre le spray et la phase gazeuse. En effet, le formalisme mésoscopique eulérien formalisé par Février et al. (2005) s'appuie sur une moyenne d'ensemble du spray conditionnée à une réalisation de la phase gazeuse pleinement résolue. Une telle approche est envisageable principalement dans un contexte où la phase dispersée ne rétroagit pas sur la phase gazeuse. Le travail proposé au cours de cette thèse s'attache à étendre le formalisme mésoscopique eulérien pour prendre en compte certains cas de couplage entre la phase dispersée et la phase gazeuse grâce à une approche de simulations aux grandes échelles (LES). Cette solution est particulièrement pertinente car comme le suggère Février et al. (2005), il est souvent observé que la phase dispersée agit en priorité sur les plus petites échelles de la phase gazeuse. C'est pourquoi, dans la lignée de Fox (2003) et Pope (2010), nous sommes amenés à considérer une moyenne conditionnelle du spray par rapport aux éléments résolus de l'écoulement. Afin d'étudier cette construction originale et difficile à approcher de façon pratique, un environnement numérique basé sur des simulations cinématiques a été développé. Les simulations cinématiques permettent de maîtriser l'espace de probabilité associé à l'ensemble des fluides turbulents, ce qui n'aurait pas été possible avec des solutions des équations de Navier-Stokes. Cet outil de simulation a été validé consciencieusement afin d'assurer la convergence des quantités d'intérêt pour l'étude proposée : notamment les moments d'ordre deux de la distribution de particules, ainsi que le contenu fréquentiel de leurs trajectoires. Cet outil a ensuite permis d'évaluer numériquement le comportement du formalisme proposé, en variant le niveau de réduction du champ fluide, de DNS à RANS. On observe alors que dès que l'on travaille avec un champ porteur réduit, ce nouveau formalisme introduit un effet diffusif sur la trajectoire de particules ponctuelles. Pour des temps asymptotiquement longs, les caractéristiques de cette dispersion sont entièrement pilotées par les propriétés du champ turbulent. En revanche, pour les temps courts, cette dispersion est directement impactée par le niveau de réduction du champ fluide. Cette observation est particulièrement intéressante car les gouttes de carburant d'une chambre s'évaporent très rapidement et sont principalement impactées par le régime initial. Pour conclure cette étude, nous étudions quelques fermetures diffusives pour la phase dispersée qui sont adaptées au nouveau formalisme que nous avons introduit et nous présentons quelques perspectives quant à la simulation d'écoulement diphasiques couplés aux grandes échelles.

Title: Large eddy simulation of coupled dispersed phase flows: a statistically-consistent formalism.

Keywords: spray, turbulence, large eddy simulation, coupling, mesoscopic Eulerian formalism, Kinematic Simulation

Abstract: The simulation of the polydisperse fuel sprays is of tremendous importance for high-fidelity descriptions of aeronautical burners. To this end, the Eulerian Moment Methods are an interesting strategy, because of their intrinsic statistical convergence. Such methods have been successfully used to represent macroscopic trends such as the flame shape, but there are still some issues to be tackled in order to increase their level of fidelity and prediction. Among them, the two-way coupling between the spray and the gas phase is critical. Indeed, moment methods used to simulate sprays in burners are often based on the Mesoscopic Eulerian Formalism (MEF) of Février et al. (2005), which considers the ensemble-averaged statistics of the disperse phase conditioned to a unique gas phase. This conditioning is required in order to solve the gas phase without any ensemble averaging such as in RANS methods. Unfortunately, if the disperse phase affects the gas phase, this conditioning may be at least impossible and at most strongly restricted. In this context, the present work investigates the development of a statistical description in the case of a reduced vision of the gas phase, such as the Large Eddy Simulation (LES), and when two-way coupling is taking place between the two phases. This solution is interesting for two-way coupled disperse phase flows, as the retro-coupling can occur at the smallest scales of the flow, with limited impact on the largest scales, as suggested by Février et al. (2005). Beyond the usual description of LES, following Pope (2010) and Fox (2003), we consider a statistical framework of LES under which the statistics are taken as ensemble-averaged over the possible unresolved features. To investigate this solution, a numerical framework using synthetic turbulence is developed, based on a superposition of analytic modes. By doing so, the distribution of modes can be easily controlled, thus enabling the generation of fields with identical large scales. This framework is carefully evaluated to ensure statistical and numerical convergence of the measures of interest, such as particle dispersion. Our formalism is then investigated, focusing on the impact of choosing this framework compared to the initial MEF, from the DNS to the RANS limit. We show that the choice of the formalism has a negligible impact on the diffusion regime of particles in turbulence, but still has a clear impact on the initial transport regime, during which all physics could happen in spray combustion. We finally investigate Lagrangian LES models of the literature in this framework and propose some perspective toward two-way LES of turbulent particulate flows.

Université Paris-Saclay
Espace Technologique / Immeuble Discovery
Route de l'Orme aux Merisiers RD 128 / 91190 Saint-Aubin, France